Single hole spins in silicon quantum dots

Scott Douglas Liles

A thesis in fulfilment of the requirements for the degree of
Doctor of Philosophy

UNSW
AUSTRALIA

School of Physics
Faculty of Science
University of New South Wales

August 2019

Thesis/Dissertation Sheet

Surname/Family Name	:	**Liles**
Given Name/s	:	**Scott Douglas**
Abbreviation for degree as given in the University calendar	:	**PhD**
Faculty	:	**Science**
School	:	**Physics**
Thesis Title	:	**Single hole spins in silicon quantum dots**

Abstract 350 words maximum: (PLEASE TYPE)

Single hole spins in silicon quantum dots are emerging as a promising candidate for use in spin qubit applications. However, experimental studies of single-hole spins have been hindered by challenges in fabricating stable hole-based devices. Particularly, it has been challenging to define silicon quantum dots that are capable of operating down to the last hole. The primary motivation for reaching the last hole is that the fundamental properties of quantum dots, such as the orbital momentum, g-factor, and spin coherence time, are strongly dependent on the total charge occupation. Reaching the last hole allows systematic and reproducible studies of the physical properties of hole spin states. These studies are therefore fundamental for optimising single-hole spins towards spin qubit applications.

In this thesis we perform electrical studies of planar silicon MOS quantum dot devices. These devices include an adjacent charge sensor, allowing direct measurement of the number of holes on the quantum dot. We demonstrate an extremely stable single and double quantum dot, that is suitable for excited-state and magnetic spectroscopy measurements

Next, we characterise the orbital shell structure of a planar silicon MOS quantum dot. The results show that the first six holes occupy the Fock-Darwin orbitals with spin filling consistent with Hund's rule. The hole-hole Coulomb interaction energy is found to be large, approximately 90\% of the orbital energy, which has the potential to complicate hole spin-orbital states in quantum dots containing many holes.

We then isolate a single hole in a known orbital state and study the Land\'e g-tensor. These results show that the hole g-tensor is primarily defined by the symmetry of the electrostatic confinement profile. We find the g-tensor orientation can be electrically controlled, and that the effective g-factor can be modulated to take any value between 0 and 4. Finally, we develop a 3D Luttinger model of the single hole quantum dot in order to quantitatively explain the physical origin of the observed g-tensor modulation.

Overall this thesis demonstrates a step towards fully characterised single hole spins for use in spin qubit application.

FOR OFFICE USE ONLY Date of completion of requirements for Award:

ORIGINALITY STATEMENT

‘I hereby declare that this submission is my own work and to the best of my knowledge it contains no materials previously published or written by another person, or substantial proportions of material which have been accepted for the award of any other degree or diploma at UNSW or any other educational institution, except where due acknowledgement is made in the thesis. Any contribution made to the research by others, with whom I have worked at UNSW or elsewhere, is explicitly acknowledged in the thesis. I also declare that the intellectual content of this thesis is the product of my own work, except to the extent that assistance from others in the project's design and conception or in style, presentation and linguistic expression is acknowledged.’

Signed

Date 09/09/19

INCLUSION OF PUBLICATIONS STATEMENT

UNSW is supportive of candidates publishing their research results during their candidature as detailed in the UNSW Thesis Examination Procedure.

Publications can be used in their thesis in lieu of a Chapter if:

- The student contributed greater than 50% of the content in the publication and is the "primary author", ie. the student was responsible primarily for the planning, execution and preparation of the work for publication
- The student has approval to include the publication in their thesis in lieu of a Chapter from their supervisor and Postgraduate Coordinator.
- The publication is not subject to any obligations or contractual agreements with a third party that would constrain its inclusion in the thesis

Please indicate whether this thesis contains published material or not.

☐ *This thesis contains no publications, either published or submitted for publication (if this box is checked, you may delete all the material on page 2)*

☒ *Some of the work described in this thesis has been published and it has been documented in the relevant Chapters with acknowledgement (if this box is checked, you may delete all the material on page 2)*

☐ *This thesis has publications (either published or submitted for publication) incorporated into it in lieu of a chapter and the details are presented below*

CANDIDATE'S DECLARATION

I declare that:

- I have complied with the Thesis Examination Procedure
- where I have used a publication in lieu of a Chapter, the listed publication(s) below meet(s) the requirements to be included in the thesis.

Name	Signature	Date (dd/mm/yy)

COPYRIGHT STATEMENT

Signed …….....

Date 09/09/19 …….....

AUTHENTICITY STATEMENT

Signed …….....

Date 09/09/19 …….....

"Just think, would you want to open a cake factory where every cake has a random number of eggs?"

Australian Proverb.

Abstract

Single hole spins in silicon quantum dots are emerging as a promising candidate for use in spin qubit applications. However, experimental studies of single-hole spins have been hindered by challenges in fabricating stable hole-based devices. Particularly, it has been challenging to define silicon quantum dots that are capable of operating down to the last hole. The primary motivation for reaching the last hole is that the fundamental properties of quantum dots, such as the orbital momentum, g-factor, and spin coherence time are strongly dependent on the total charge occupation. Reaching the last hole allows systematic and reproducible studies of the physical properties of hole spin states. These studies are therefore fundamental for optimizing single-hole spins towards spin qubit applications.

In this thesis we perform electrical studies of planar silicon MOS quantum dot devices. These devices include an adjacent charge sensor, allowing direct measurement of the number of holes on the quantum dot. We demonstrate an extremely stable single and double quantum dot, that is suitable for excited-state and magnetic spectroscopy measurements

Next, we characterise the orbital shell structure of a planar silicon MOS quantum dot. The results show that the first six holes occupy the Fock-Darwin orbitals with spin filling consistent with Hund's rule. The hole-hole Coulomb interaction energy is found to be large, approximately 90% of the orbital energy, which has the potential to complicate hole spin-orbital states in quantum dots containing many holes.

We then isolate a single hole in a known orbital state and study the Landé g-tensor. These results show that the hole g-tensor is primarily defined by the symmetry of the electrostatic confinement profile. We find the g-tensor orientation can be electrically controlled, and that the effective g-factor can be modulated to take any value between 0 and 4. Finally, we develop a 3D Luttinger model of the single hole quantum dot in order to quantitatively explain the physical origin of the observed g-tensor modulation. Overall this thesis demonstrates a step towards fully characterised single hole spins for use in spin qubit application.

General Introduction

Building artificial atoms using holes

Electricity is usually considered to be the flow of negatively charged electrons. However, this is not always true. In a special class of materials, known as semiconductors, electricity is sometimes carried by a different type of particle. These particles are called holes, and they carry a positive charge. Although they sound unfamiliar, holes are used in half of all semiconductor electronics. Today, the state-of-the-art in electronics is artificial atoms: nano-scale transistors so small they behave like man-made atoms. Artificial atoms harness the quantum behavior of individual electrons, and can be used to develop a new generation of computers, known as quantum computers. However, despite over 50 years of research, almost all technological developments have focused on electron-based electronics. There is still very little understanding of holes. Could it be possible to build an artificial atom out of holes?

This thesis involves studying the properties of holes using tiny nano-scale transistors. With precise control over the electromagnetic environment we have, for the first time, isolated one individual hole using silicon Metal-Oxide-Semiconductor (MOS) technology. This is a huge step in bringing the understanding of holes back on par with electrons. Using these devices we have studied the unique properties of artificial atoms that are made using holes, instead of electrons. Our results show that hole artificial atoms have very different properties to electron artificial atoms. By understanding and harnessing the unique properties of holes, we will have more tools to develop new and exciting semiconductor electronic devices. Holes, which sound like nothing, may just be the thing that future computers are made of.

List of Publications

Journal Articles

Liles, S. D., Li, R., Yang, C. H., Hudson, F. E., Veldhorst, M., Dzurak, A. S., and Hamilton, A. R. (2018). Spin and orbital structure of the first six holes in a silicon metal-oxide-semiconductor quantum dot. Nature communications, 9(1), 3255.

Conference Presentations

Jin, I. K. Liles, S. D., *et. al.*. Strong electric control of a single hole g-factor. Poster. Silicon Quantum Electronics, 2019 (*Accepted*), San Sebastián, Spain.

Liles, S. D., *et. al.*. Spin filling and orbital structure of the first six holes in a silicon MOS quantum dot. Oral Presentation. Silicon Quantum Electronics, 2018, Sydney, France.

Liles, S. D., *et. al.*. Spin filling and orbital structure of the first six holes in a silicon MOS quantum dot. Oral Presentation. International Conference on the Physics of Semiconductors (ICPS), 2018, Montpellier, France.

Liles, S. D., *et. al.*. Spin filling and orbital structure of the first six holes in a silicon MOS quantum dot. Oral Presentation. International Conference on Nanoscience and Nanotechnology (ICONN), 2018, Woolongong, Australia.

Liles, S. D., *et. al.*. Spin filling of holes in a silicon quantum dot. Poster. Spin Qubits 3, 2017, Sydney, Australia.

Articles In Preparation

Liles, S. D., Martins, R., Miserev, D. S., Thorvaldson, I. D., Rendell, M., Hudson, F. E., Veldhorst, M., Sushkov, O. P., Dzurak, A. S., Hamilton, A. R. (2019). Electric control of the single hole g-tensor. *Article in preparation.*

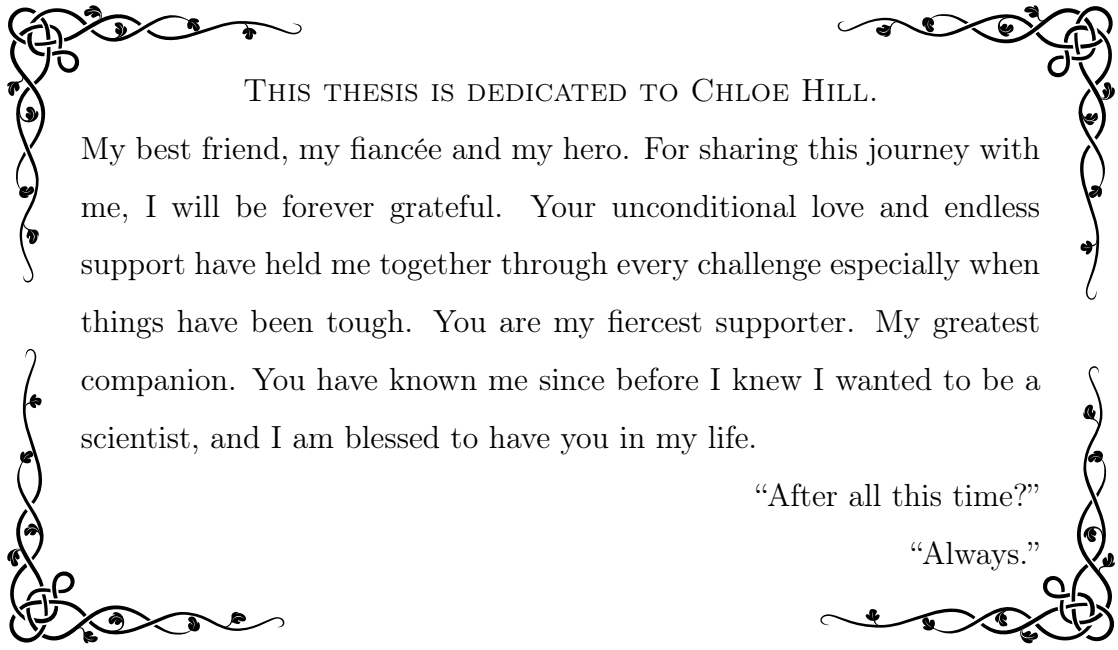

This thesis is dedicated to Chloe Hill.

My best friend, my fiancée and my hero. For sharing this journey with me, I will be forever grateful. Your unconditional love and endless support have held me together through every challenge especially when things have been tough. You are my fiercest supporter. My greatest companion. You have known me since before I knew I wanted to be a scientist, and I am blessed to have you in my life.

"After all this time?"

"Always."

"You could tell by the way he talked, though,
that he had gone to school a long time.
That was probably what was wrong with him."
John Kennedy Toole.

Acknowledgements

The work presented in this thesis was primarily supervised by Professor Alex Hamilton, with significant co-supervision support from Dr Ashwin Srinivasan, Dr Ruoyu Li, and Dr Frederico Martins. All experimental work was conducted on the campus of the University of New South Wales, Sydney.

First of all, I would like to thank my supervisor Prof. Alex Hamilton. His genuine excitement, enthusiasm and optimism sets the culture within the QED group. Thanks to Alex, I have enjoyed 5 years in an environment that is positive, engaging and enriching to anyone who wants to learn to be a scientist. I am grateful for Alex's willingness to share his expertise, and his investment of time and energy into helping me develop as a researcher.

I would like to thank my co-supervisor Dr. Ashwin Srinivasan, who helped guide me through the transition from undergraduate studies to postgraduate research. He is an expert in the clean-room, a calm patient teacher, and I am grateful to have had him as a mentor.

Dr. Ruoyu (Roy) Li is the most talented experimentalist I've had the privilege of working with. I thank him for his unlimited patience and kindness. My most valuable laboratory note books are those that I have filled with sketches of circuit diagrams, software flowcharts and the experimental set-ups, which were designed and explained to me by Roy. It has been humbling to read the future outlook of Roy's PhD Thesis and realize that the work in my thesis follows directly from the significant contributions Roy has made to our group and to this field.

Finally, I offer many thanks to Dr. Frederico Martins, who is an excellent reader. He reads everything, and he reads them well. Even times when I didn't think he was read-

ing something, it turned out he was. If you ever find something that Fred hasn't read (unlikely), you should give it to him, and then the next day if you ask him '*did you read that thing?*' he will tell you that he has read it. Also, Fred is very smart, and also he is very clever. Some people say that Dolphins or Labradors are clever, but they haven't met Fred (as far as I know). So in conclusion, I acknowledge Dr Martins-Male for his generous help, and also, did you know that sometimes Fred has run all the way to Bondi! That is very far, and I would know because occasionally I run to Bronte.

I would like to thank and acknowledge all the current and past members of the QED group: Matt Rendell, Dr. Karina Hudson, Dr. Elizabeth Marcellina, Dr. Daisy Wang, Ik Kyeong Jin, Yonatan Ashlea Alava, Cecilia Bloise, Isaac Vorreiter, Dr. Feixiang Xiang and Dr. Oleh Klochan. The QED group members have always been willing to offer their advice and assistance. I am grateful for the opportunity to work with Ian Thorvaldson, who is the most brilliant student I have encountered.

I am extremely grateful to my project collaborators: Prof. Andrew Dzurak, Dr. Fay Hudson, Dr. Menno Veldhorst, Dr. Henry Yang, Prof. Oleg Sushkov, and Dr. Dmitry Miserev. I would also like to thank members from outside the QED group who have always been willing to offer support and technical advice: Dr. Anderson West, Dr Samuel Bladwell, Dr. Tuomo Tanttu, Dr. Wee Han Lim, Siva Natarajan, Kris Karpinski, Dr. Rodrigo Ormeno and Dr. Jack Cochrane.

As a conservative estimate, I've now spent over 1200 hours teaching physics at UNSW. Teaching has been one of the highlights of my time at UNSW. This is entirely due to the amazing educators in the School of Physics. In particular, I would like to thank A/Prof. Elizabeth Angstmann, who is the most inspiring educator I have encountered. In addition, special thanks go to Tamara Reztsova, Ranji Balalla and Diana Edler, who each provided me an amazing environment when I came through as a student, then again when I joined them as a teacher.

I acknowledge the CSIRO for providing funding in the form of the CSIRO Alumni Scholarship in Physics, which allowed me to travel and study at the Niels Bohr Institute of the University of Copenhagen. I would like to thank the Quantum Devices group for their friendly welcome during my brief stay, and I especially thank A/Prof. Ferdinand

Kuemmeth for sharing his time and expertise.

Outside of research, I would like to thank my parents and my sister for their unconditional support throughout my studies. I am grateful for the distractions from research provided by my friends Bryce, Chris, and Dave. I thank Ali who has always had my back, and when it really mattered, my knee. I also thank Jan for providing context to the phrase *too cold to paddle out*.

Contents

List of Figures

Introduction and outline

"Silicon is the second most abundant element present within the earths crust. Due to its solid state electrical properties it has found prolific use in the modern micro-electronics industry. Historically silicon has been manufactured by compressing 3 million kg of oxygen into a volume of 1 cm^3 and then heating this system to 2 billion Kelvin (3.6 billion Fahrenheit). It is distributed at random by stellar winds, and during supernova explosions."

Thesis Introduction

What is a Quantum Dot?

A semiconductor quantum dot is a small structure capable of trapping an exact and tunable number of electrons or holes. Using modern nano-fabrication techniques it has become possible for some quantum dot systems to trap just one single electron. The size of a quantum dot is such that the trapped charge is confined in all three spatial dimensions. Therefore, quantum dots are a real world example of the textbook quantum mechanics problem, the *'particle in a box'*. The specific size of confinement required for a quantum dot is determined by the Fermi wavelength λ_F. The Fermi wavelength λ_F in semiconductors is typically on the order of tens of nanometers[1]. This size scale is achievable with modern semiconductor processing techniques, and a wide range of studies on quantum dots have been performed beginning, in the 1990's. Studies of quantum dots continue today, as quantum dots are developed for new materials and optimised for specialized applications.

[1]For comparison, the Fermi wavelength in metals is typically less than a nanometer.

How can a quantum dot be formed?

There are a number of ways in which semiconductor quantum dots can be formed. The confinement of a quantum dot is typically achieved through electrostatic potentials or material interfaces, and often includes a combination of both. Electrostatic confinement has the advantage that it can be tuned in-situ, while material based confinement is fixed. The exact symmetry of the quantum dot confinement profile influences the quantized energy spectrum, and therefore can determine the properties of the device.

In Figure 1 we briefly summarize four different examples of semiconductor quantum dots. The quantum dot structure used in this thesis is based on silicon Metal-Oxide-Semiconductor (MOS) technology. This particular structure is shown in the final column labeled planar (2D) quantum dots in Figure 1. The schematic shows the basic operation of a planar quantum dot. A sheet of electrons or holes is formed at the heterojunction interface, indicated by the blue dashed line. This sheet of charge is confined in the vertical direction by the heterointerface band bending. However, the charge is free to move in the other two dimensions, hence the name 2D (or planar) structures. The metal gates are fabricated into specific shapes and are used to deplete the sheet of charge directly below each gate. This is indicated by the scanning electron micrograph image, which shows an example of a MOS device, where a quantum dot is formed at the region indicated by the white circle [1].

Why are quantum dots valuable?

The ability to localize single electrons (or holes) in a controllable structure has significant applications for both fundamental research, and in technological applications. In terms of fundamental research, quantum dots are ideal for investigating the quantum properties of individual charge states, particularly the spin. Prior to the development of quantum dots, spin properties were typically investigated using ensemble averaged measurements. However, quantum dots offer the ability to localize and measure one individual spin state and perform measurements in a controlled manner. This has allowed valuable insight into the underlying spin physics of semiconductor systems.

The ability to control the spin and charge state of a quantum dot has a range of new and novel technological applications. These include the use of quantum dots as extremely

Structure	Dopant based quantum dots	Self assembled quantum dots	Nanowire based quantum dots	Planar (2D) quantum dots
Schematic	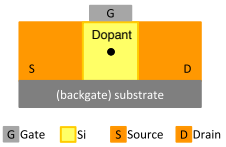	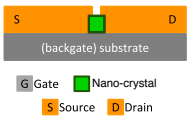	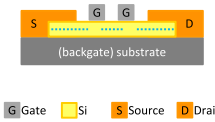	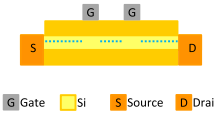
Example of a device	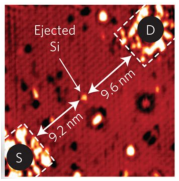	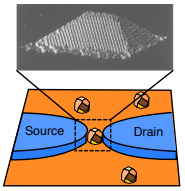	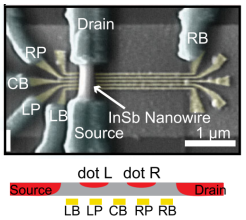	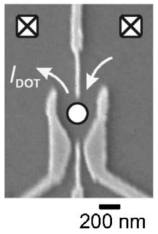
Key Properties	- Deterministically placed dopant atom as quatum dot. - Charges are confined by radially symmetric atomic potential. - Single atom transistor is conceptially beautiful. - Tunnel coupling set primarily by dopant spacing. - Maximum occupation of two charges bound to the dopant. - Extremely low disorder.	- Nano-crystal as a zero dimensional structure. - Confinment symmetry defined by the shape and structure of the nano-crystal. - Hard wall potential as confinement. - Placement and integration of multiple quantum dots is difficult. - Tunnel coupling set primarily by spacing between nano-crystals.	- Material based hard wall confinement in 2D and electrostatic confinement in 1D. - In-situ control of tunnel rate with barrier gates. - Difficult to couple multiple quantum dots across different nanowires. -Interface disorder potential very close to confined charge.	- 2DEG or 2DHG formed at the heterojunction. - Electrostatic control of lateral confinement by surface gates. - Allows wide range of in-situ tunability. - Freedom to fabricate an arbitrary gate patern including multiple adjacent quantum dots or adjacent charge sensors (QPC's or SET's). -Interface disorder potential very close to confined charge.

Figure 1: **Comparison of different quantum dot structures: First column** is for quantum dots formed using single dopant atoms. The example shows a deterministically placed phosphorus atom coupled to a source (S) and (D) contact [2]. **Second column** is for quantum dots formed using zero dimensional material structures. The example image shows a self assemble Ge 'hut' nanocrystal that is deposited on a Si substrate. Source and drain contacts are fabricated for electrical measurements [3, 4]. **Third column** is for quantum dots formed by one dimensional nanostructures. The example shows an InSb nanowire, with a layer a electrostatic gates directly below, which can be used to form the quantum dot [5]. **Fourth column** is for quantum dots formed using two dimensional structures. The example shows an SEM of an AlGaAs/GaAs quantum dot. Light grey gates deplete the 2DEG at the heterointerface and form a quantum dot in the location of the white circle [1]. Schematics are reproduced from [6].

sensitive electrometers [7], for storing quantum information as a qubit[1] [8], for use as artificial atoms [9], or for analogue quantum simulations [10, 11]. A primary motivation for the research in this thesis is the use of quantum dots for storing quantum information by controlling the spin spin state of a trapped electron or hole.

What is the state-of-the-art for single-spin control in quantum dots?

In 1997 Loss & DiVincenzo [8] first proposed that quantum computation can be achieved

[1]Analogous to the bit, which is a unit of classical information used in computing. A qubit (short for quantum bit) is the fundamental unit of quantum information, used for quantum computing.

by using the spin projection of a single-electron in a quantum dot as a qubit. Operation of this type of qubit (typically known as a Loss-DiVincenzo qubit or a single-spin qubit) requires the ability to achieve high fidelity coherent control of a single-electron (or single-hole) spin-state in a quantum dot. Significant progress towards full control of a single-spin was initially made using laterally defined AlGaAs/GaAs quantum dots. In 2000 Ciorga *et al.* [1] demonstrated control of a lateral GaAs quantum dot down to the single electron regime[1]. In 2004 Elzerman *et al.* [12] demonstrated single-shot readout of the single-electron spin state. Following this, in 2006 Koppens *et al.* [13] demonstrated coherent control of a single-electron spin using Electron Spin Resonance (ESR). The ESR was driven using a proximal strip-line to produce an oscillating magnetic field at the quantum dot. It was found that a major challenge for coherent spin control in GaAs quantum dots is the abundance of the magnetic nuclei. The nuclear spins strongly interact with the single electron spin, and this limits the time scale for coherent spin control to tens of nanoseconds in GaAs quantum dots [14, 15].

An attractive way to increase the time scale for coherent spin control is to move to materials with predominately non-magnetic nuclei. This has provided significant motivation for research into quantum dots based in Group IV material systems, since they can be purified to remove nearly all the magnetic isotopes. Silicon MOS based quantum dots are a particularly promising candidate for developing single-spin qubits. This is because they have the potential for integration with the modern micro-electronics industry, which is already based on silicon MOS technology. In 2009 Lim *et al.* [16] demonstrated control of a lateral silicon MOS quantum dot down to the single electron regime. Following this, in 2014 Veldhorst *et al.* [17] achieved coherent control of a single-electron spin for time scales up to 120μs. This showed that by using magnetically quiet materials it is possible to enhance the spin coherence time by a factor of 10^5.

Electron spins in lateral (MOS) silicon quantum dots are an extremely successful system for spin control [6, 18]. The challenge now is scaling the technology up, so that multiple spin states (spin qubits) can be individually controlled on a single quantum device. The technological challenges for scaling up are; (1) maximizing the spin lifetime, (2)

[1]Similar to the stunning results of Tarucha *et al.* [9] who used vertically defined AlGaAs/GaAs quantum dots to show artificial atom shell structure in 1996.

maximizing the speed of coherent spin control, (3) ensuring individual control of multiple spin states, and (4) ensuring that there is controllable coupling between the spin states[1]. In 2015 Veldhorst *et al.* [19] used a lateral (MOS) quantum dot in isotopically purified silicon to achieve coherent control of two coupled spin states with an individual spin control speed of around 400kHz (one full spin rotation every 2.5μs).

A promising way to scale up single-spin qubit systems is to use electric fields to control the spin state, rather than magnetic fields. All-electric spin control has the advantage that quantum dot designs already include local electric gates, which are suitable for addressing individual spin states. This would remove the need for a bulky ESR strip line, and free up space in the design for scaling up to multiple coupled quantum dots. In addition, spin manipulation speed depends on the proximity of the driving field to the spin state. Therefore the local electric gates could provide faster spin control than magnetic manipulation, since the local electric gates are closer to the spin state than the magnetic strip line. However, electron spins in Group IV quantum dots do not intrinsically couple to electric fields.

Hole spins in Group IV quantum dots have recently received significant interest for use as fast scalable single-spin qubits [18]. The enhanced spin-orbit coupling of the valence band allows an intrinsic mechanism for hole spins to couple to electric fields. Using hole spins, instead of electrons, can potentially keep the advantages of long spin coherence times, and industry compatibility that the Group IV material systems offer, while adding the potential for scalable, fast electric manipulation.

[1](1) defines how long quantum information can be stored using a spin state. (2) defines the time required to control the spin state. Together criteria (1) and (2) can be used to determine how many spin control operations can be performed before the quantum information is lost. (3) is important for scalability since it should be possible to selectively control each spin on a device with multiple quantum dots. (4) is required in order to achieve the entangled states necessary for quantum computation.

What is the state-of-the-art for single hole-spin control in Group IV quantum dots?

The majority of the research into single-spin qubits has focused on electron spin states. Recently, there have been a number of promising experimental developments for hole spins confined in Group IV quantum dots[1]. The most significant recent developments have been the demonstration of rapid all-electric control of hole spins quantum dots based on silicon nanowires by Maurand *et al.* [20, 21] (2016), germanium hut-wires by Watzinger *et al.* [22–24] (2018), and germanium MOS devices by Hendrickx *et al.* [25, 26] (2019). Hole spins have been shown to have spin control rates up to 150MHz (one full spin rotation in 7ns), which demonstrates the potential of single-hole spins for use as fast scalable spin-qubits. While these recent experiments have shown a improvement in the spin control speed, the coherence time of hole spins has been found to be short, on the order of several hundred nanoseconds. Determining the underlying mechanisms that lead to this short spin coherence times, even in group IV quantum dots, is an open question for hole spin physics.

These recent experiments have shown the high potential that hole-spins have for spin qubit applications. However, there still remains fundamental gaps in the understanding and technology of hole based quantum dots. While it is now standard for n-type MOS quantum dots to reach the last electron regime, it has proven a challenge to reach the last hole regime in identical MOS devices [27–29]. The previously mentioned hole-spin manipulation experiments of Maurand *et al.*, Watzinger *et al.* and Hendrickx *et al.* have been performed in the few-hole regime, where the absolute number of holes occupying the quantum dot is unknown. While this is not inherently a draw-back, most electron spin-qubit experiments have operated in the one electron regime [6, 30].

Reaching the last hole regime would allow two key advantages; (1) it becomes possible to isolate a single hole and perform a systematic study the spin properties, and (2) it is possible to sequentially add holes back into the quantum dot in order to characterise the quantum dot orbital structure and observe hole-hole interaction effects. Studies of quantum dot orbital structures and the single electron spin physics have provided

[1]These have been reviewed in the opening literature review sections of chapters 2, 3 and 4 of this thesis.

significant insight and have been key in the development of electron spin qubits in silicon quantum dots [6] (as discussed in the previous subsection). However, since it remains a challenge to isolate a single hole in silicon, many questions about the underlying spin physics of holes remain unanswered.

What new information does this thesis produce?

There are three primary questions that we address in this thesis:

(1) - Is it possible to isolate one single hole in a silicon MOS quantum dot?

(2) - What is the orbital shell structure for holes in silicon MOS quantum dots?

(3) - What are the underlying physical properties of a single-hole spin?

To address these questions we study the electrical and magnetic properties of p-type silicon MOS quantum dots. We demonstrate operation down to the last hole, allowing the isolation of one single hole, thereby achieving for p-type MOS technology what has been achieved for n-type quantum dots more than 10 years earlier [16, 31]. A full set of electrical characterisation measurements is included, which demonstrates that these devices offer a stable and tunable platform for hole spin control. Experimental operation down to a single hole provides access to a range of valuable spectroscopic measurements. We study the orbital spectrum of the hole quantum dot, and characterise the sequence that hole spins fill into the quantum dot. Finally, we have characterised the 3D Landé g-factor anisotropy of a singly occupied hole quantum dot and developed a theoretical model to describe a single hole spin in a silicon quantum dot. This provides new understanding of the underlying spin-orbit physics of holes spin states. This thesis presents a systematic study of the fundamental physics of single hole spins in silicon quantum dot devices, and demonstrates a step forwards for the technology available to p-type quantum electronic devices.

Thesis Outline

Chapter 1 provides the background information and concepts relevant for the experimental work of this thesis.

Chapter 2 reports the first operation of a silicon MOS single quantum dot down to the last hole.

Chapter 3 reports spectroscopic measurements characterising the orbital shell structure and the spin filling sequence of a single hole quantum dot.

Chapter 4 reports an experimental characterisation of the single hole Landé g-tensor, and includes a theoretical model to support the analysis of the underlying physics for single hole spin states.

Chapter 5 concludes this thesis by providing a summary of the key results, an outlook, and suggestions for future work.

Chapter 1

Background information

"Despite what you may have been told,
holes are not simply heavy electrons."
Alex Hamilton

Introduction

In this chapter we provide the background information relevant to the experimental results presented in chapters 2, 3 and 4. In section 1.1 we introduce fundamental electrostatic properties of quantum dots. In section 1.2 we discuss the operation and optimisation techniques employed in quantum dot charge sensing. In section 1.3 we introduce the background details of the orbital physics involved in quantum dots. In section 1.4 we discuss spin-qubits, which are a primary motivation for studying spins in quantum dots. Finally in section 1.5 we summarize the main difference between hole and electron spin states in silicon devices. This background chapter concludes with Table 1.2, where we compare the observed spin properties of electrons and holes in recent experiments.

1.1 Electrical transport properties for quantum dots

One of the most fundamental techniques to characterise semiconductor quantum dots is to observe the transport through the device. In this section we provide the background information related to electrical transport in single and double quantum dot devices. In section 1.1.1 we introduce the constant interaction model and the key parameters for understanding the electrostatic response of a quantum dot. In section 1.1.2 we discuss the fundamental details of transport through a single quantum dot. In section 1.1.3 we discuss how transport measurements can provide spectroscopic insight into quantum dot orbital structure. Finally, in section 1.1.4 we review transport through two quantum dots in series.

1.1.1 Constant interaction model

The fundamental properties of electrical transport through a quantum dot can be understood in terms of the discrete quantized energy levels. These energy levels are defined by two factors: the charging energy due to Coulomb interactions, and the discrete single particle energies of the quantized system. The constant interaction model is a model that describes the electrostatic response of the quantum dot energy levels. In the constant interaction model it is assumed that the two factors (the capacitive Coulomb interactions and the single particle energy levels) are independent. In this section we focus on the Coulomb interactions, and the corrections due to the single particle energy spectrum are discussed in section 1.3.

A schematic circuit digram of a single quantum dot is shown in Figure 1.1(a). The total energy of the quantum dot can be controlled using voltages applied to the Source V_S, the Drain V_D and the Gate (or gates) V_G, which capacitively couple to the charges confined in the quantum dot (C_S, C_D, and C_G respectively). The energy spectrum of the dot can be modelled by treating the system as an capacitor with an integer charge occupation. This simplified electrostatic model is known as the constant interaction model. The

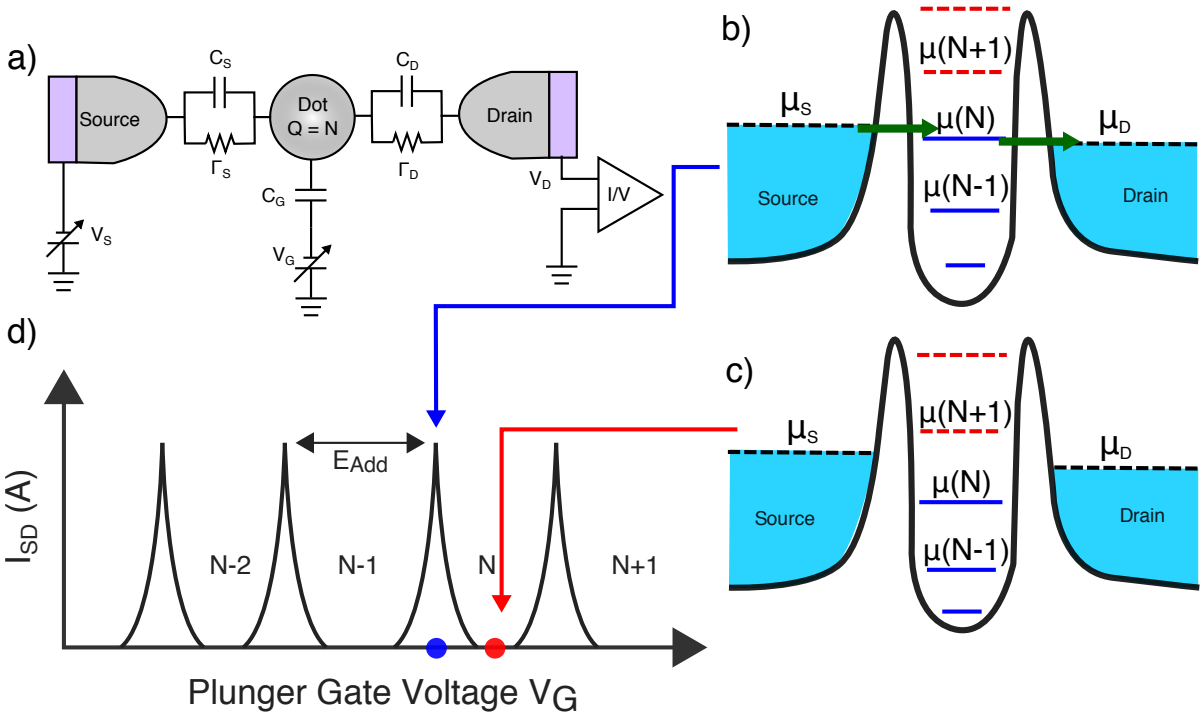

Figure 1.1: **Single quantum dots and Coulomb blockade:** (**a**) Shows an electrostatic model of a single quantum dot coupled to a source and drain ohmic contact. A source-drain bias $V_{SD} = V_S$-V_D can drive a current, which is then monitored using a current (I/V) preamplifier. Tunneling between the dot and contacts is represented by resistor and tunnel rates Γ_i. (**b**) Shows a schematic of the electrochemical potential levels when the N^{th} quantum dot level μ_N lies in the small source-drain bias window ($\mu_S - \mu_D$). A source-drain current can pass via tunneling onto and off the μ_N quantum dot level, as indicated by the green arrows. (**c**) Here the quantum dot chemical potential has been tuned such that the total charge of the dot is fixed at N. In this configuration the source-drain current is Coulomb blocked. (**d**) Schematic of the source-drain current I_{SD} for a quantum dot as a function of the plunger gate voltage V_G. Blue and red dots indicate the V_G that corresponds to the schematic of (b) and (c) respectively. Reproduced from [30].

energy of a single quantum dot (shown in Figure 1.1(a)) $U(N)$ is given by,

$$U(N) = \frac{(-|e|(N - N_0) + C_S V_S + C_D V_D + C_G V_G)^2}{2C} + \sum_N E_{n,l}(B) \qquad (1.1)$$

where N is the number of charges confined in the dot, N_0 is the background charge offset, and C is the total capacitance given by $C = C_S + C_D + C_G$. The last term in Equation 1.1 is the sum over all occupied single-particle energy levels to include orbital and spin effects to the constant interaction model. This model gives a ladder of discrete energy levels identified by the charge occupation.

The electrochemical potential $\mu(N)$ of the dot can be calculated from the energy difference between two consecutive energy levels. Based on the constant interaction model

(Equation 1.1),

$$\begin{aligned}\mu(N) &= U(N) - U(N-1) \\ &= (N - N_0 - \frac{1}{2})E_C - \frac{E_C}{|e|}(C_S V_S + C_D V_D + C_G V_G) + E_N \qquad (1.2) \\ &= (N - N_0 - \frac{1}{2})E_C - (\alpha_S V_S + \alpha_D V_D + \alpha_G V_G) + E_N, \qquad (1.3)\end{aligned}$$

where $E_C = e^2/C$ and is known as the Coulomb charging energy. In Equation 1.3 we introduce the parameter $\alpha_i = eC_i/C$, where α_i is the lever arm of gate i and has units of J/V. The electrochemical potential of the quantum dot is linear in the applied voltages. Due to this linearity in V_i, the electrochemical potential is the most convenient parameter for discussing quantum dot quantized states.

The spacing between the consecutive ground state electrochemical potentials is called the addition energy E_{add}. The addition energy varies with different charge occupation, where E_{add}(N) is the energy required to add one more electron to an N-electron quantum dot. Based on the constant interaction model the addition energy is given by

$$E_{add}(N) = \mu(N+1) - \mu(N) = E_C + \Delta E(B) \qquad (1.4)$$

where $\Delta E(B)$ is the energy separation between the quantum levels occupied by the (N+1)th and the Nth charges. $\Delta E(B)$ can have a magnetic field dependence when spin or orbital effects are considered[1]. $E_{add}(N)$ is a useful parameter to monitor since it contains the Coulomb interaction contribution (E_C), plus the quantum confinement contribution ($\Delta E(B)$). Therefore differences in E_{add} for different N can indicate if consecutive charges are added into the same or different orbital levels. Similarly, monitoring the effect of a magnetic field on a specific $E_{add}(N)$ can be used to determine the spin state of the quantum dot. These effects are discussed in more detail in section 1.3.2.

[1] See section 1.3 for further discussion.

1.1.2 Low bias regime and Coulomb blockade

Electrical transport through a single quantum dot can be understood in terms of the ladder of quantum dot electrochemical levels, and the window due to the difference between source and drain electrochemical potentials (μ_S and μ_D respectively). The difference between μ_S and μ_D opens a range of energies, referred to as the source-drain bias window ($\Delta E_{SD} = \mu_S - \mu_D$). In most experiments $\mu_D = eV_D = 0$ and $\mu_S = \mathrm{e}V_S$, hence the bias window is typically tuned experimentally using only V_S.

We begin by considering the linear response regime where the bias window is small enough that only one of the quantum dot levels can be aligned within the bias window at a time. In this case, if $\mu_{dot}(\mathrm{N})$ is within the source-drain bias window $\mu_D \leq \mu_{dot} \leq \mu_S$ a source-drain current can flow. This current flows by carriers tunneling from the source, onto the $\mu_{dot}(\mathrm{N})$ level, then finally from the dot into the drain. This configuration is schematically shown in Figure 1.1(b). When there are no quantum levels available within the source-drain bias window, the total charge of the dot is fixed, and the current is blocked. This is known as Coulomb blockade and is shown schematically in Figure 1.1(c).

In Figure 1.1(d) we show a schematic of the current through a single quantum dot as a function of gate voltage V_G. Sweeping V_G shifts the ladder of μ_{dot} levels through the narrow source-drain bias window. As consecutive μ_{dot} levels move through the source-drain bias window, the current periodically shows discrete peaks followed by regions where the current is Coulomb blocked. The spacing between consecutive peaks is proportional to the addition energy E_{add} defined in Equation 1.4. The width of each individual peak is defined by two factors: the width of the source-drain bias window, and any broadening of the discrete electrochemical levels (for example thermal broadening of source or drain Fermi distributions, or finite lifetime effects).

The Coulomb blockade of a single quantum dot for low source-drain bias can be used to determine the energy scales of a quantum dot. Coulomb blockade measurements typically include: counting the number of Coulomb peaks to determine the discrete charge occupation, extracting the addition energy from the Coulomb peak spacing, or

determining the reservoir charge temperature using the Coulomb peak width [32, 33]. Coulomb blockade measurements are a primary analysis tool used throughout this thesis.

1.1.3 High bias regime and excited state spectroscopy

We now consider the case where the source-drain bias window is large enough for multiple quantum dot levels to be accessible for tunneling from the source. In Figure 1.2 we show a schematic of the source-drain current I_{SD} through a single quantum dot device for a large source-drain bias window ($\Delta E_{SD} = \mu_S - \mu_D$). Inset (i) of Figure 1.2 shows the initial case where V_G has been tuned such that $\mu_S = \mu$(N). At this point ($\alpha_G V_G = 0$) I_{SD} increases from zero since charge can flow between the source and drain via tunneling onto the μ(N) ground state. Inset (ii) of Figure 1.2 shows the case where the μ(N) excited state (green line) is within the bias window. Similarly, inset (iii) of Figure 1.2 shows the case where the second μ(N) excited state is available for tunneling from the source.

The presence of an additional levels within the bias window can increase the source-drain current I_{SD}[1]. However, the exact profile of I_{SD} with respect to V_G depends on the coupling between the individual quantum levels and the leads. Typically, I_{SD} is largest when a quantized level is aligned μ_S, and this is shown schematically in Figure 1.2. The structure of I_{SD} shown in Figure 1.2 is defined by the alignment of the quantum dot energy levels within the source-drain bias window. Therefore observing the structure in I_{SD} as a function of V_G allows spectroscopic measurements of the quantum dot excited states [30].

For the schematic profile of I_{SD} in Figure 1.2 we have shown the case where the source-drain bias window (eV_{SD}), is less than the addition energy ($E_{add}(N)$). For this case the quantum dot will be in Coulomb blockade when $eV_{SD} < \alpha_G V_G < E_{add}(N)$. Inset (iv) of Figure 1.2 schematically shows the Coulomb blockade region for a high source-drain bias window. Although the two μ(N) excited states (green lines) are within the bias window, the μ(N) ground state is below μ_D, and the total charge of the dot is Coulomb blocked at N. Since the charge is fixed at N, the μ(N) excited states are not accessible, and I_{SD}

[1]Provided the tunnel coupling is weak enough for additional levels to have an impact on the tunnel rate. A more detailed discussion is presented in section 3.7.1 and Figure 3.13.

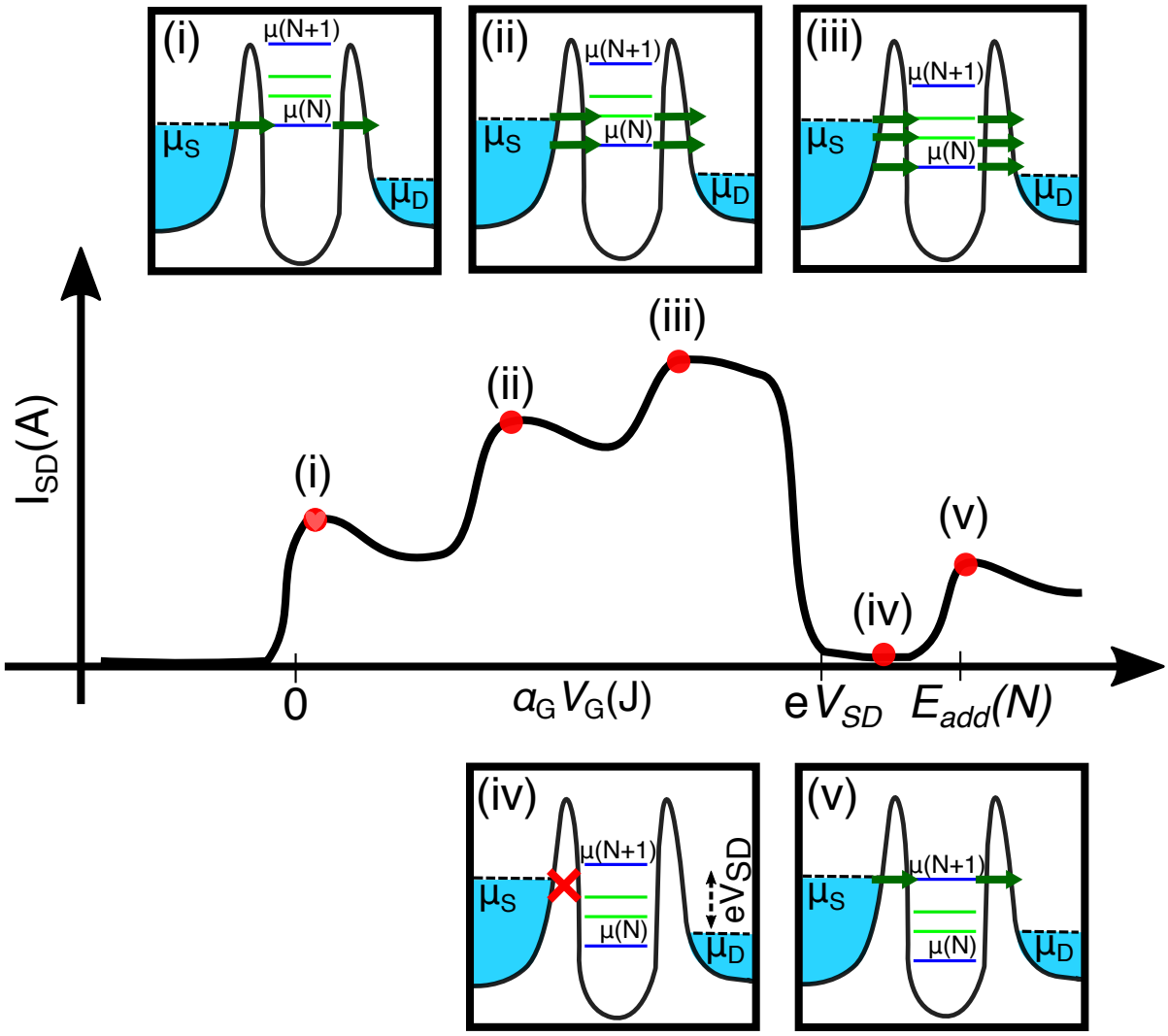

Figure 1.2: **High bias excited state spectroscopy:** This figure shows a schematic of I_{SD} as a function of V_G when a large source-drain bias $V_{SD} = V_S - V_D$ is applied. The x-axis is the quantum dot gate voltage V_G, which has been scaled to units of energy using the lever arm α_G and offset so that the μ(N) ground state aligns with the zero point of electrochemical potential. The insets show the alignment of the quantum dot levels as V_G shifts the ladder of quantum dot electrochemical potentials. Dark blue lines indicate ground state levels, and the green lines are the N excited states. Green arrows highlight the tunneling paths available. eV_{SD} is the energy of the source-drain bias window and $E_{add}(N)$ is the energy required to add the (N+1)th charge to the quantum dot.

drops to zero. Coulomb blockade will be lifted once $\alpha_G V_G = E_{add}$ since a current will flow through the μ(N+1) ground state, as shown in inset (v) of Figure 1.2.

1.1.4 Transport in double quantum dots

In this section we discus the electrical transport properties when two quantum dots are connected in series, known as a double quantum dot. An electrostatic model of a double

quantum dot is shown in Figure 1.3(a). The most significant additions from the single quantum dot model is the effect of mutual capacitance between the two dots C_M, and the additional cross capacitance of V_{g2} on Dot 1 parameterized as $C_{1,2}$ (and V_{g1} on Dot 2, $C_{2,1}$). It is possible to apply the constant interaction model, similar to the single dot case in section 1.1.1, and this is discussed in detail in the reviews of Van der Wiel *et al.* [34] and Hanson *et al.* [30]. However, the explicit mathematical form of the double dot constant interaction model is not relevant for this thesis[1].

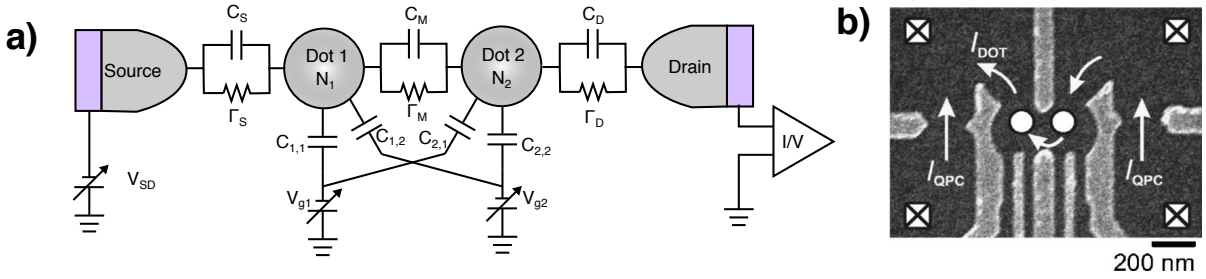

Figure 1.3: **Schematic of a double quantum dot:** (**a**) Shows an electrostatic model of a double quantum dot. N_1 and N_2 are the charge occupations of Dot 1 and Dot 2 respectively. The inter-dot tunnel rate is represented as Γ_M, and the inter-dot capacitive coupling is C_M. (**b**) This SEM shows a typical MOS double quantum dot structure. Crossed boxes are ohmic contacts, and white circles show the location of the two quantum dots. Reproduced from [35].

An example of a real double quantum dot structure is shown in Figure 1.3(b). This shows a Scanning Electron Microscope (SEM) image of a typical lateral double quantum dot [35]. Here the grey metal gates deplete electrons at the GaAs/AlGaAs interface below and allow the formation of two quantum dots, indicated by the white circles. Transport through the double quantum dot occurs as indicated by the arrows and label I_{DOT}.

The transport properties of double quantum dots are typically analyzed using a charge stability diagram. A charge stability diagram is a 2D map identifying the charge state of each dot (N_1, N_2) as a function of the two plunger gate voltages V_{g1} and V_{g2}. In Figure 1.4(a) we show a schematic charge stability diagram for two quantum dots with no mutual coupling ($C_M = 0$). The text indicates the charge occupation of each quantum dot (N_1, N_2) while the nearly-vertical and nearly-horizontal lines indicate the N_1 and N_2 charge transitions respectively. The slope of the charge transitions is due to the cross capacitance of V_{g1} on Dot 2 and V_{g2} on Dot 1 respectively. The color scale indicates the

[1]For example see Equation (32) in [30].

source-drain current I_{SD} for the double quantum dot in low bias regime. In the low bias regime I_{SD} can only occur when energy levels of both dots lie within the bias window. When $C_M = 0$, I_{SD} can only occur at the charge transition intersections, shown by the blue circles.

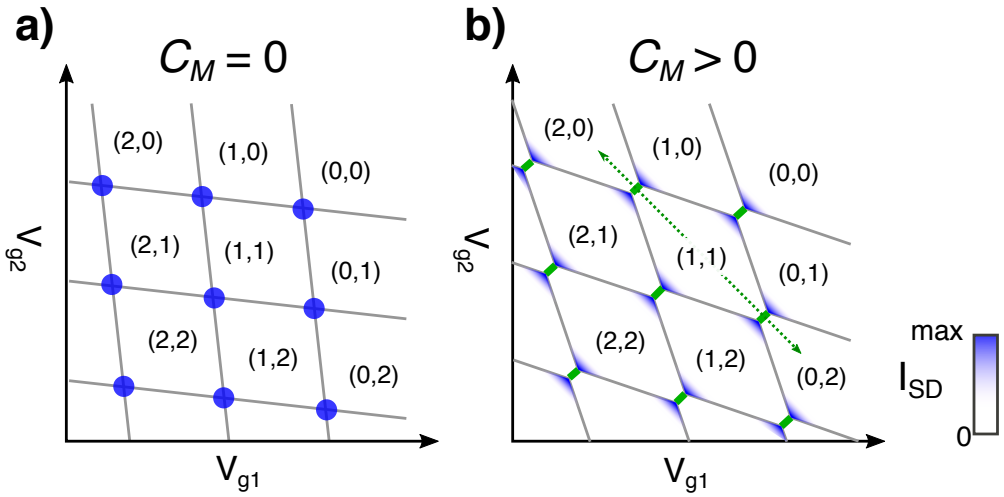

Figure 1.4: **Schematic double dot charge stability diagrams:** (**a**) When the inter-dot capacitive coupling C_M is zero the double dot stability diagram forms a tilted checkerboard. Vertical (horizontal) grey lines show the Dot 1 (Dot 2) charge transition regions, where the tilt is due to the coupling of Dot 1 (Dot 2) with V_{g2} (V_{g1}). Text indicates the (N_1, N_2) charge occupation. (**b**) When the inter-dot capacitive coupling C_M is non-zero the double dot stability diagram forms into a honeycomb pattern. Solid green lines indicate the inter-dot transitions, and dashed green lines indicate translations in (V_{g1}, V_{g2}) that maintain constant total charge occupation of the double dot system (N_1 + N_2). The blue color scale highlights regions on the stability diagram where a source-drain current I_{SD} is typically observed. Figure is modified from [30].

In Figure 1.4(b) we show a schematic charge stability diagram when mutual coupling between the two dots is included ($C_M > 0$). The effect of mutual coupling separates the charge transition intersections (blue points in Figure 1.4(a)) into 'triple points'. This is a result of the change in electrostatic energy of one dot when charge is added to the other dot. The triple points are the only location on the low bias double dot stability diagram where I_{SD} can occur as indicated by the color scale (discussed further in section 1.1.4). The separation of the triple points is determined by the mutual inter-dot capacitance C_M. The line connecting two adjacent triple point is known as the inter-dot transition (solid green lines). Translating across an inter-dot transition (indicated by the dashed green line) shuffles charge between the two quantum dots while the total charge of the double quantum dot remains fixed.

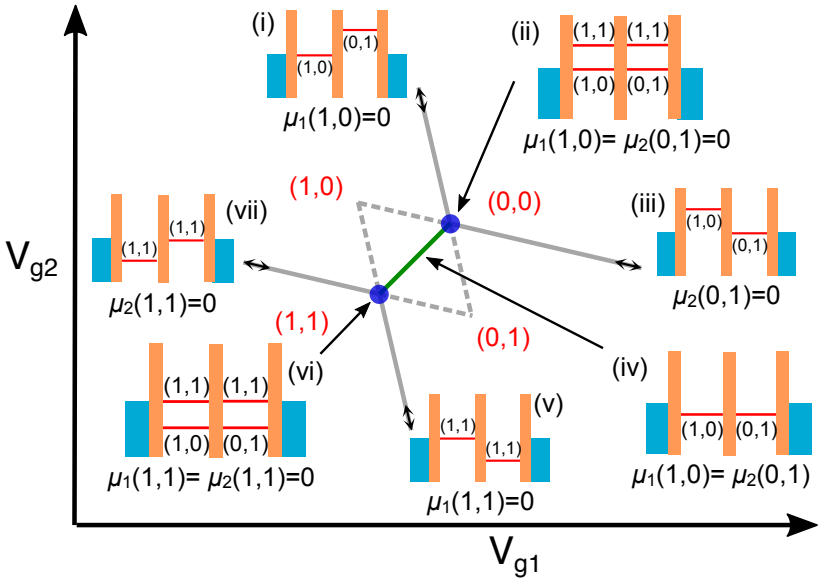

Figure 1.5: **Schematic charge stability diagram at the (0,0)-(1,1) transition for realistic C_M:** The grey lines mark the boundaries of the different charge transitions and red text highlights the charge occupation (N_1, N_2). Insets schematically show the alignment of levels for the indicated regions. The blue dots highlight the triple points. The solid green line is the inter-dot transition, where the (1,0) and (0,1) ground states are degenerate. This schematic is for small source-drain bias $\mu_S \approx \mu_D \approx 0$ and $C_M > 0$. Figure is modified from [30].

We now discuss the alignment of the electrochemical potential levels around a set of triple points in a double dot charge stability diagram. In Figure 1.5 we show a schematic of the (1,0) to (0,1) region of the charge stability diagram for a low source-drain bias window. We use this charge configuration for simplicity, however the general model can be applied to any (N_1, N_2) ground state charge configuration. Solid grey lines indicate the regions in the (V_{g1}, V_{g2}) profile where the total charge on the double dot will change. Insets (i),(iii),(v),(vii) schematically show the electrochemical levels at the respective charge transitions.

The triple points are indicated by blue circles in Figure 1.5 and correspond to the positions where the available states in both dots align with the source and drain levels (which we take as approximately zero for low bias regime). Inset (ii) shows the schematic of the upper triple point where $\mu_1(1,0) = \mu_2(0,1) = 0$, while inset (vi) shows the schematic of the lower triple point where $\mu_1(1,1) = \mu_1(1,1) = 0$. For low source-drain bias, the triple points are the only region of a double dot stability diagram when a source-drain current can occur.

The inter-dot transition is indicated by the solid green line in Figure 1.5. This region of the charge stability diagram is particularly interesting for the double quantum dot systems. Translations across the inter-dot transition will shuffle a single electron between the left and right quantum dot, while keeping the total charge of the double dot constant. Further, along the inter-dot transition the (1,0) and (0,1) energy levels are degenerate, as shown in inset (iv). Therefor, at the inter-dot transition it is possible for one electron to simultaneously occupy both quantum dots. This can have uses in initializing entangled states for quantum computing [8], or for simulating molecular bonding [10, 11].

In this section we have discussed the main features of electrical transport for a double quantum dot. Specifically, we have considered the low bias regime. In the case of high source-drain bias the triple points evolve into a pair of so called bias triangles. As with single quantum dots, studies of double transport in the high bias regime can provide spectroscopic information about the double quantum dot system. However, these measurements are not relevant to this thesis. For further discussion of these effects see reviews of Van der Wiel *et al.* [34] and Hanson *et al.* [30].

1.2 Charge sensing measurements of semiconductor quantum dots

The two most common all-electrical techniques for studying a quantum dot are (1) measurements of the transport through the system, or (2) sensing of the total charge occupation of the quantum dot using a coupled electrometer. In section 1.1 we discussed the main properties of quantum dots with respect to transport measurements. Charge sensing can be used to extract the same information as transport measurements. In section 1.2.1 we briefly outline the advantages of using a charge sensor over transport measurements. The experimental techniques for charge sensing are then discussed, with section 1.2.2 detailing the basic operation, section 1.2.3 outlining how excited state spectroscopy is performed and section 1.2.4 introducing methods to optimize charge sensor operation. All measurements of quantum dots presented in the experimental results of

this thesis employ the charge sensing techniques discussed here.

1.2.1 How charge sensor improves quantum dot characterisation

Charge sensing measurements require an extremely sensitive electrometer to be coupled to the charge state of the quantum dot [36, 37]. This requirement demands additional circuit design and fabrication. However, charge sensing enables experiments that would be difficult or impossible using standard transport measurements. A major advantage of using a charge sensor is that this lifts the source-drain tunnel rate requirements. Transport measurements are limited to a minimum tunnel rate, otherwise the source-drain current is undetectable. For example, when the tunnel rates are of order 1MHz the source-drain current will be only 0.2pA, which is reaching the limit of most experimental signal-to-noise demands.

Charge sensing does not require current to flow through the quantum dot. Thus, charge sensing can monitor quantum dots operating down to very weak coupling between the confined charge and a lead. This is valuable for reaching the last charge regime of a quantum dot, since tunnel rates typically drop significantly as the quantum dot approaches the last charge. In addition charge sensing of a quantum dot is non-invasive, as it does not require transport through the quantum dot. Since transport is not required, a charge sensor can monitor the charge state of a quantum dot that is coupled to a single reservoir[1].

1.2.2 How to use a charge sensor

Charge sensing can be performed using any system that shows a strong response to a small change in the local electric field. Commonly used systems for charge sensing are Quantum Point Contacts (QPC) and Single Electron Transistors (SET)[2], since these devices can be extremely sensitive to electric fields. In addition QPCs and SETs are suitable for fabrication directly adjacent to the quantum dot under study, allowing max-

[1] As opposed to transport measurements, where coupling to two reservoirs (source and drain) is required.

[2] In p-type devices Single Hole Transistors (SHT) can be used.

imum capacitive coupling to an adjacent quantum dot. As an example, Figure 1.6(a) shows a double quantum dot device with an adjacent QPC charge sensor. The conductance profile of the QPC is shown in red in Figure 1.6(b). The region indicated by the dashed cross is the optimum configuration for using the QPC as a charge sensor. The rise of the first plateau (indicated by the dashed cross) is extremely steep, causing the QPC current to be extremely sensitive to local electric fields, including the field caused by the number of charges confined in the quantum dot.

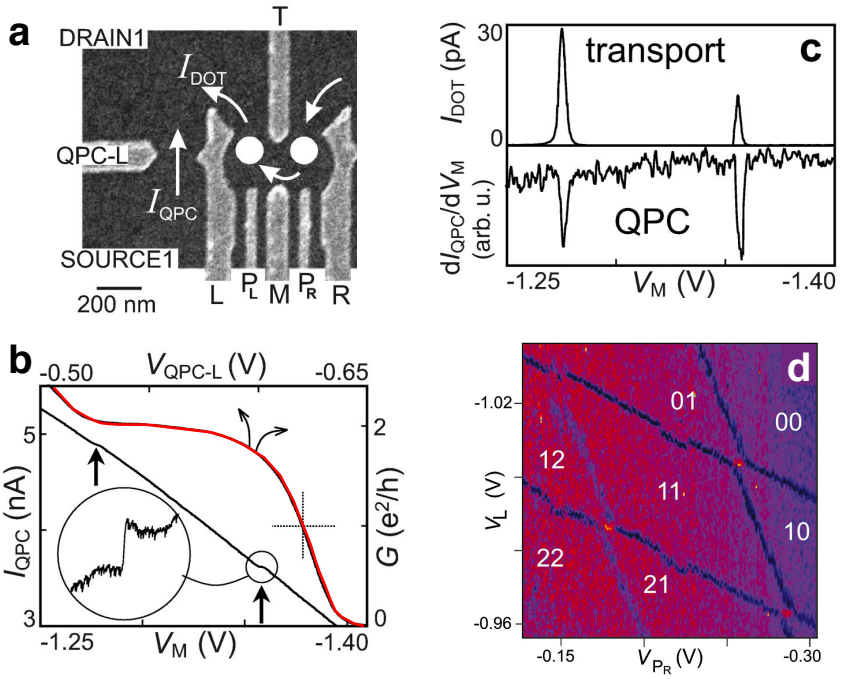

Figure 1.6: **QPC charge sensing:** (**a**) A SEM image of a double quantum dot (two white circles) with an adjacent QPC charge sensor. (**b**) The red data shows the QPC conductance profile (right axis) as a function of V_{QPC-L} (top axis). The dashed cross indicates the region where the QPC is most sensitive to the local electrostatic environment. In this case the most sensitive region is on the rise of the first QPC conductance plateau. To perform charge sensing the QPC is tuned conductance G=e^2/h and the voltage of gate M is swept. The black data shows the QPC current with respect to V_M. (**c**) The top panel shows the transport current though the double dot, while the bottom panel shows the derivative of the black data in (b). The two measurements were taken simultaneously. (**d**) Measurement of a double dot charge stability diagram where the color scale is the derivative of the QPC signal. Text indicates the charge occupation of the left and right quantum dot as N_1N_2. Reproduced from [35].

An example of QPC charge sensing is shown by the black data in Figure 1.6(b). The QPC is configured to the optimal conductance[1] and the gate M voltage is swept over a range that changes the quantum dot occupation by two electrons. The black data shows

[1]This is the region of highest transconductance (dG_{QPC}/dV_{QPC}), which occurs around G = e^2/h.

two discrete steps in QPC current, which are superimposed on a rising background. The rising background is due to the capacitive coupling of the QPC with V_M. Figure 1.6(c) compares the quantum dot transport signal with the derivative of the QPC signal showing that the Coulomb peaks in transport correspond with the spikes in the sensor signal $\mathrm{d}I_{QPC}/\mathrm{d}V_M$. This confirms that the discrete steps in I_{QPC} occur when the total charge of the coupled quantum dot changes by one electron. Finally, in Figure 1.6(d) the QPC charge sensor has been used to observe the charge stability diagram of the double quantum dot. The color scale of Figure 1.6(d) is $\mathrm{d}I_{QPC}/\mathrm{d}V_M$, and the clear honeycomb pattern of a double quantum dot can be observed. Overall, in this section we have introduced the fundamental features and typical operation of a charge sensor.

1.2.3 How to use a charge sensor for excited state spectroscopy

In section 1.1.3 we have shown how excited state spectroscopy can be performed using transport measurements. In this thesis charge sensing measurements are employed rather than transport measurements. In this section we discuss how excited state spectroscopy measurements can be performed using charge sensing methods.

The charge sensor spectroscopy technique used in this thesis was first demonstrated by Elzerman *et al.* [38] in 2004. Figure 1.7(a) shows a SEM image of a device studied by Elzerman *et al.* The device is a single lead (reservoir) quantum dot with an adjacent QPC charge sensor[1]. Spectroscopy of the excited states is performed by applying a continuous square pulse of amplitude $V_P > 0$ to the plunger gate. The tunnel rate onto the quantum dot depends on the number of states that are energetically accessible during the load phase of the square pulse. This change in tunnel rate effects the average charge occupation of the quantum dot, and this is observed in the charge sensor signal. This pulse technique is often referred to as pulse-bias spectroscopy.

Figure 1.7(b) shows the results of the pulse-bias spectroscopy measurement obtained by

[1]Here the quantum dot is only connected to a single lead and so this device is referred to as a single-lead quantum dot. For comparison, transport measurements require two leads, a source and a drain. Single lead quantum dots have advantages for some applications since coupling to the leads can degrade the performance of quantum dots. Hence, minimizing the number of leads coupled to the quantum dot can be desirable to enhance performance of quantum dot devices, particularly in qubit applications [30].

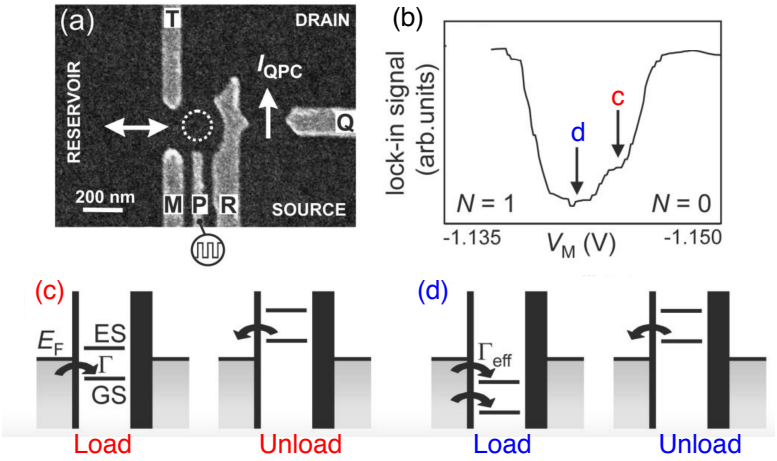

Figure 1.7: **Pulse-Bias spectroscopy:** (**a**) SEM image of a single-lead (reservoir) quantum dot with an adjacent QPC charge sensor. Electrons are confined in a quantum dot indicated by the dashed circle. A continuous square wave of amplitude V_P is applied to the gate labeled P. (**b**) The charge sensor signal (y-axis) as the dot is swept across the N=0 to N=1 charge transition. (**c-d**) Schematics of the Ground State and Excited State levels during the load and unload phase of the square pulse. The level configuration corresponds to the V_M indicated by the c and d labels in (b).

Elzerman *et al.* [38]. Here the y-axis is the sensor signal, the x-axis is the voltage of the M gate (V_M), and the measurement is performed while a continuous square pulse of amplitude V_P=6mV is applied to the P gate. Initially in the N=0 region the sensor signal shows an approximately constant value with respect to V_M. This is because no quantum dot levels are accessible in the pulse window, and so the average charge occupation of the quantum dot is fixed over the pulse period. As V_M is made more negative, the $\mu(1)$ ground state becomes accessible for tunneling during the load phase of the square pulse (as indicated in Figure 1.7(c)). At the V_M voltage indicated by the label c the square pulse changes quantum dot charge occupation between N=1 (load) and N=0 (unload). This changes the time averaged charge occupation of the quantum dot, which is reflected in the charge sensor signal. When the $\mu(1)$ excited state becomes available for tunneling the effective tunnel rate (Γ_{eff}) increases (as indicated in Figure 1.7(d). This changes the average charge occupation of the quantum dot[1] and can be observed as additional structure in the sensor signal. Finally, the charge sensor signal returns to the background level once the $\mu(1)$ ground state falls bellow the pulse window and the quantum dot occupation remains Coulomb blocked at N=1.

[1]When an excited state is available the load time will be shorter since there are two possible states. However, *in general* the unload period will remain unchanged. Hence the dot spends more time (on average) in the N=1 state when additional excited state levels are available for tunneling.

The results of Figure 1.7(b) demonstrate how excited state spectroscopy can be performed using a finite amplitude pulse technique. The pulse-bias technique is analogous to the high-bias transport spectroscopy technique[1]. The advantage of pulse-bias spectroscopy is it provides access to time domain measurements. If the pulse period is shorter than the tunneling time ($1/\Gamma_{\text{eff}}$) then no signal can be observed, and the tunnel rate can be deduced [38]. Alternatively, if the sensor bandwidth exceeds the tunnel rate then single charge tunneling event can be observed in real time using a single shot charge sensor measurement [39].

1.2.4 How to get the most out of a charge sensor

Optimal operation of a charge sensor involves maintaining the sensor in the configuration where it is maximally responsive to the local electrostatic environment. During experiments several factors can cause the sensor shift away from the optimal configuration. The most common effect is due to cross capacitance of the sensor with the array of gates used to control the dot. Unexpected effects such as random charging events or drifts of voltage sources can similarly displace the charge sensor from optimal configuration. When the maximal sensitivity can be identified by a specific sensor parameter (for example the sensor conductance), digitally controlled feedback techniques can be employed to maintain optimal sensor performance [40].

In this thesis we use a dynamic feedback compensation technique developed by Yang *et al.* [40] to optimize our charge sensing measurements. In this section we describe how dynamic feedback compensation significantly improves charge sensor operation. Figure 1.8(a) shows a SEM of the silicon quantum dot device studied by Yang *et al.*. The device has a single quantum dot (bottom) coupled to a Single Electron Transistor (SET) charge sensor (top). Figure 1.8(b) shows transport through the quantum dot I_D (black), which exhibits as series of Coulomb peaks as the dot plunger gate V_{PD} is swept. The current through the charge sensor (I_S) is simultaneously measured (purple data in Figure 1.8(b)). Initially the charge transitions are clear in I_S. However, as V_{PD} is reduced the

[1]For example compare the structure of the charge sensor signal in Figure 1.7(b) to the structure in I_{SD} in Figure 1.2.

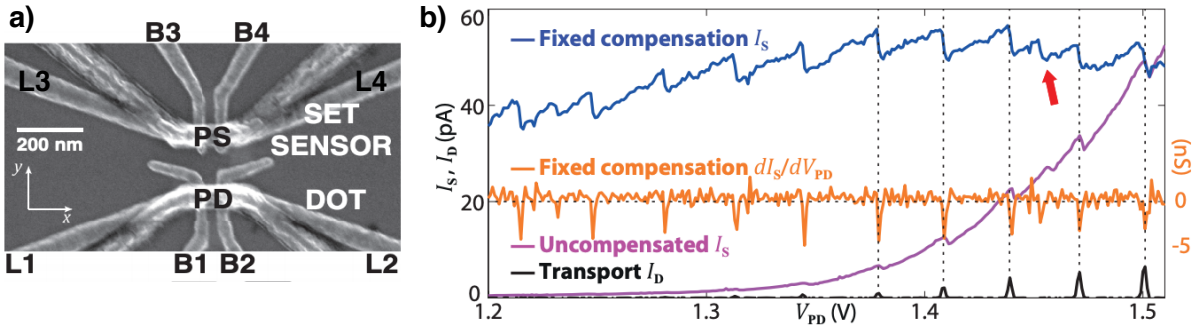

Figure 1.8: **Charge sensor compensation:** (**a**) A SEM image a silicon MOS quantum dot device (bottom) with an adjacent SET charge sensor (top). (**b**) Transport through the quantum dot I_D (black) shows Coulomb peaks as the dot plunger gate V_{PD} is swept. The current through the SET sensor I_S (purple) shows charge transition signals superimposed on a decaying background. The charge transition signals are the discrete jumps in I_S, and they correspond with the Coulomb blockade peaks in I_D. The decaying I_S can be compensated by adding a fixed linear correction (using V_{PS}) as shown in the blue data. The derivative of the compensated I_S is shown in yellow. Reproduced from [40].

sensor shifts away from the most sensitive region and eventually pinches off. This results in non-uniform amplitude of charge transition signals, and limits the range of sensor operation.

The drift in I_S can be corrected by applying a fixed linear compensation to one of the sensor gates. The blue data in Figure 1.8(b) shows I_S when a compensation is applied to maintain the sensor current at approximately 50pA, and the yellow trace shows the numerical derivative of the blue data. The compensation is achieved by incrementally stepping the voltage applied to the sensor plunger gate V_{PS} after each measurement. The use of compensation on the sensor has clear advantages and significantly improves the sensor operation. When compensation is applied all charge transitions have approximately the same amplitude. This allows Yang *et al.* to identify that the transition indicated by the red arrow is likely related to a charge trap, and not the quantum dot[1]. Further, the compensation prevents the sensor from pinching off allowing operation over a larger range of V_{PD} without the need for retuning.

The compensation used in Figure 1.8(b) is a fixed increment in V_{PS}. Yang *et al.* note that the compensation can be further improved using a dynamic feedback method, which takes I_S as the feedback signal and incrementally adjusts feedback gate V_{PS} after each measurement. The advantage of a dynamic feedback is that it is more robust to changes

[1]Based on the difference in the amplitude compared with other transitions.

in the sample, such as random 'jumps due to charge trap movement. In this thesis all experimental results of the quantum dot charge state are performed using dynamic feedback charge sensing[1].

1.3 Quantum dots as artificial atoms

In section 1.1 we discussed the electrostatic properties of quantum dots with reference to the constant interaction model. Here we introduce the discrete orbital energy spectrum that arises due to the spatial confinement. This orbital spectrum give rise to *atom-like* properties of quantum dots, and justifies the label of quantum dots as artificial atoms. In this thesis we focus on quantum dots based on silicon MOS structures. Therefore, this section focuses on the unique atom-like properties of 2D quantum dots.

In section 1.3.1 we introduce the orbital structure of a well defined 2D quantum dot, which has become known as the Fock-Darwin energy spectrum. We then discuss the grounds state (section 1.3.2) and excited state (section 1.3.2) spin filling sequence for the Fock-Darwin orbital shells. This spin filling sequence can be understood in terms of Hund's Rules. Finally, we conclude this section by introducing two relevant factors that strongly influence the quantum dot orbital structure and spin filling. These are the effect of the conduction band degenerate valley states (section 1.3.4), and Spin-Orbit Interactions (section 1.3.5).

1.3.1 Energy spectrum of a 2D quantum dot

In this subsection we define the main features of the orbital shell structure for two-dimensional quantum dots. When a quantum dot is based on a two-dimensional structure[2] lateral surface gates are typically used to electrically confine charge. The shape of 2D quantum dots can be considered disk-like, where the diameter is much larger than the vertical thickness[3]. When the lateral confinement is electrically defined it can be consid-

[1] Unless explicitly stated otherwise.

[2] See Figure 1 for comparison of different dimensional quantum dot structures.

[3] For a disk-like quantum dot the 2D sub-band spacing should be much larger than the energy separation of the lateral energy levels.

ered a soft boundary, which can be approximated as a harmonic oscillator confinement. For the case of circularly symmetric 2D harmonic confinement, the energy spectrum at zero magnetic field is given by

$$E_{n,l} = (2n + |l| + 1)\hbar\omega_0, \tag{1.5}$$

where n(=0,1,2...) is the radial quantum number, $l(= 0, \pm1, \pm2...)$ is the angular momentum number and ω_0 defines the confinement oscillator frequency.

The energy spectrum of Equation 1.5 gives rise to a series of orbital levels separated[1] by $\hbar\omega_0$. The occupancy of each level can be determined by considering the number of degenerate states[2]. The lowest energy level (n, l)=(0,0) has two-fold degeneracy and is occupied by a Pauli spin-pair. The second orbital-shell can contain up to four charges due to the degeneracy of the (0,1)=(0,-1) energy levels. The third shell has triple orbital degeneracy since the (0,2)=(0,-2)=(1,0) energy levels and can hold six electrons. This shell structure is known as the Fock-Darwin spectrum [41, 42] and is often described with *magic numbers* N = 2, 6, 12, ..., which label the total occupation at which each consecutive orbital shell is full.

The most common experimental technique used to study the atom-like properties of quantum dots is extracting the addition energy E_{add} (see Equation 1.4). The addition energy is the energy needed to add an extra charge to a quantum dot, and is analogous to the electron affinity (or ionization energy) of atoms. As with the ionization energy in atoms, the addition energy of artificial atoms shows orbital structure. However, it is necessary to know the absolute charge occupation of a quantum dot in order to use the structure observed in E_{add} to characterise orbital structure of an artificial atom. Therefore it is vital that a quantum dot can reach the last charge, since this allows the study of E_{add} starting from zero charge.

The Fock-Darwin orbital shell filling has been observed in the addition energy of quantum dots with well defined 2D confinement[3]. Figure 1.9(a) shows the transport measurement

[1] In a typical experiment with a 2D quantum dot $\hbar\omega_0$ is on the order of a few meV.

[2] Keeping in mind that each (n, l) state can hold two charges with opposite spin.

[3] As an example see references for vertical GaAs quantum dots [9], lateral GaAs quantum dots [1] and lateral (MOS) silicon quantum dots [16].

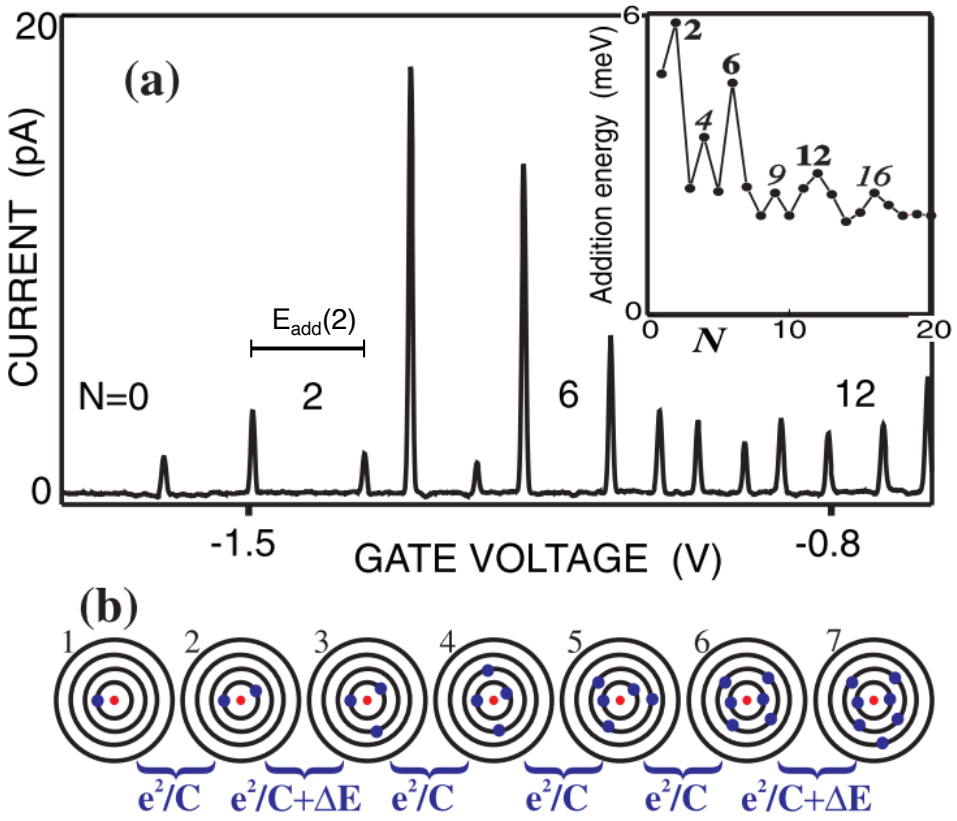

Figure 1.9: **Shell Structure of a 2D atom:** (**a**) Transport measurement of a vertically defined GaAs quantum dot. The absolute charge occupation is identified with text labeled N. As an example the N=2 addition energy $E_{add}(2)$ is shown. Inset shows the addition energy for the first 20 electrons. Bold text highlights the magic number shell filling. Smaller spikes in the addition energy occur at N=4, 9 and 16 as a result of Hund's rule spin filling (see section 1.3.2). (**b**) Schematic of the shell structure of a 2D circularly symmetric artificial atom. Reproduced from [43].

of a single quantum dot down to the last electron [43]. The inset in Figure 1.9(a) shows the addition energy, which is extracted by measuring the spacing between consecutive Coulomb peaks. The addition energy show distinct spikes at N = 2, 6 and 12 consistent with the Fock-Darwin magic numbers. Figure 1.9(b) schematically shows the shell structure of a 2D artificial atom. This indicates that when an orbital shell is full the addition energy includes both the Coulomb charging energy e^2/C and the energy required to occupy the higher orbital ΔE.

In the case that the 2D confinement is parabolic but not circularly symmetric the shell filling will depart from the Fock-Darwin *magic number* shell structure. The 2D non-

symmetric harmonic confinement is given by

$$V(x,y) = \frac{1}{2}m\omega_x^2 x^2 + \frac{1}{2}m\omega_y^2 y^2 \tag{1.6}$$

where ω_x and ω_y define the x and y axis harmonic oscillator frequencies respectively. In this case the four-fold degeneracy of the second orbital shell is lifted by the energy $\Delta E = (\omega_x - \omega_y)\hbar$. This splitting of the second orbital shell can be described by non-degenerate p_x and p_y orbitals. Similarly the higher shells will also be influenced by asymmetries in the lateral confinement. Observation of the orbital shell filling can therefore provide insight into the spatial confinement profile of a quantum dot[1] [44, 45].

1.3.2 Ground state spin filling of Fock-Darwin orbitals

In this section we introduce the spin-filling sequence of the Fock-Darwin orbital shells. The spin filling sequence can be understood in terms of three main effects: (1) The Pauli exclusion principle, which forbids two charges with equal spin from occupying the same orbital; (2) The Zeeman effect[2], which splits the energy between the spin-up and spin-down states by $\Delta E_Z = 2|E_Z| = g^*\mu_B B$; and (3) the Coulomb interaction energy (exchange energy), which can lead to a difference in energy between states with symmetric or anti-symmetric orbital wavefunctions.

First we briefly introduce the primary technique for spin-state spectroscopy. Spin states are typically identified by observing the evolution of energy levels as a magnetic field is applied. These experiments are referred to as magnetospectroscopy measurements. The approached used in this thesis is to observe the evolution of the addition energy E_{add} when a magnetic field is applied in the plane of the 2D charge[3]. The change in addition energy with respect to a magnetic field is given by

$$\frac{\delta E_{add}}{\delta B} = g^*\mu_B[\Delta S_Z(N) - \Delta S_Z(N-1)], \tag{1.7}$$

[1] If the shell filling is consistent with the *magic numbers* this can indicate a symmetric confinement, while variations from the *magic numbers* can indicate an asymmetric confinement.

[2] Where g^* is the effective g-factor, μ_B is the Bohr magneton constant and B is the magnitude of the applied magnetic field.

[3] In-plane fields are used to reduce the coupling the magnetic field to orbital states.

where $\Delta S_Z(N) = S_Z(N) - S_Z(N-1)$ and $S_Z(N)$ is the spin of the dot with N charges. Since adding one charge changes $S_Z(N)$ by $\pm\frac{1}{2}$, this give three possible magnetic dependencies of E_{add},

$$\frac{dE_{\rm add}}{dB} = \begin{array}{ll} +g^*\mu_B & \text{for} \quad \downarrow\uparrow \\ -g^*\mu_B & \text{for} \quad \uparrow\downarrow \\ 0 & \text{for} \quad \uparrow\uparrow \text{ or } \downarrow\downarrow \end{array} \tag{1.8}$$

where the first and second arrow depicts the spin filling sequence of the $(N+1)^{th}$ and N^{th} holes respectively[1]. The spin filling sequence can be determined by observing the slope of E_{add}(N) with respect to B, starting from the N=1 charge state. Similarly, the spin filling sequence can be determined from the magnetic evolution of states in excited state spectroscopy measurements. Alternatively, magnetic fields can be used to identify the orbital filling sequence using Pauli exclusion principle [9, 43].

We now outline the ground state spin-filling sequence observed for the Fock-Darwin spectrum. Since the first orbital of the Fock-Darwin spectrum is two-fold degenerate the first two charges form a Pauli spin pair. The first charge fills the lowest energy Zeeman state of the $(n, l) = (0, 0)$ orbital and the second charge fills into the quantum dot with opposite spin[2]. The second orbital has four-fold degeneracy. It has been found that the third electron has $(n, l, S_Z) = (0, +1, \downarrow)$ and the fourth electron fills the quantum dot with $(n, l, S_Z) = (0, -1, \downarrow)$ [1, 9].

The spin filling sequence of the third and fourth charges is consistent with Hund's rule in atomic physics, which states that electrons fill into atomic orbital such that the net spin is maximized. The alignment of the spin for the third and fourth charges is due to a reduction in the interaction energy when the third and fourth charges occupy different orbitals. This reduction in energy can be observed in the addition energy measurements of Figure 1.9, where there is a reduction of E_{add} for adding the fourth and sixth electrons,

[1]There are several assumptions made to simplify this equation. First we have assumed that the effective g-factor of consecutive levels is the same. This may not be the case in systems with strong spin-orbit interactions. Secondly, ground state transitions of S_Z larger than $1/2$ can occur when strong interaction effects are present between charges in the quantum dot [30].

[2]By convention we take spin-down ($\downarrow$) as aligned with the external magnetic field, and spin-up ($\uparrow$) as anti-aligned with the external magnetic field. The Zeeman effect splits spin states by $\Delta E_Z = 2|E_Z| = g\mu_B B$. The lowest energy Zeeman state will be either spin-down (aligned with B) or spin-up (anti-aligned with B) depending on the g-factor. For example the electron g-factor is negative in GaAs and positive in Si.

and an increase in E_{add} for the adding the fifth electron. The spin filling for higher Fock-Darwin shells continues in this way, following Hund's rules for atomic physics based on the degeneracy of the 2D orbitals.

1.3.3 Excited states of a few charge single quantum dot

In section 1.3.2 we discussed the ground state spin filling. Here we focus on the excited states of the N=1 and N=2 charge configurations.

A quantum dot with just one charge forms a basic single spin system. To determine the energy levels we consider the orbital energy $E_{orb} = \hbar\omega_0$ and the Zeeman energy of a single spin $E_z = g\mu_B B/2$. The first four energy states of a single spin systems are

$$E_{\downarrow,0} = -E_z \tag{1.9}$$

$$E_{\uparrow,0} = +E_z \tag{1.10}$$

$$E_{\downarrow,1} = -E_z + E_{orb} \tag{1.11}$$

$$E_{\uparrow,1} = +E_z + E_{orb} \quad , \tag{1.12}$$

where $E_{S_Z,l}$ represents the energy of one charge with spin orientation $S_Z = (\uparrow \text{ or } \downarrow)$ occupying an orbital with angular momentum l. At zero magnetic field the energy separation between the ground state and the first excited state will be E_{orb}.

We now consider the two charge system. A quantum dot with two charges will always have a spin singlet $|S\rangle$ as the ground state at zero magnetic field [46]. The first excited states of the two-charge quantum dot are the spin triplets $(|T_+\rangle, |T_-\rangle, |T_0\rangle)$. At zero magnetic field the three triplet states are degenerate. However in the presence of a magnetic field the triplets are split based on their different spin components $S_Z = +1$ for $|T_+\rangle$, $S_Z = 0$ for $|T_0\rangle$, and $S_Z =$ -1 for $|T_-\rangle$. For the triplet states, the two charges occupy different orbitals. The antisymmetry of the orbital wavefunctions and the occupation of different orbital shells reduces the Coulomb energy for the triplet states. This reduction in energy can be included in the model using the term E_K. The modified singlet triplet energy spacing can then be defined as $E_{ST} = E_{orb} - E_K$. The first four states of the

two-charge system are,

$$\begin{aligned} E_S &= E_{\downarrow,0} + E_{\uparrow,0} + E_C \\ &= E_C \qquad (1.13) \\ E_{T_-} &= E_{\downarrow,0} + E_{\downarrow,1} + E_C - E_K \\ &= -2E_Z + (E_{orb} - E_K) + E_C \\ &= -2E_Z + E_{ST} + E_C \qquad (1.14) \\ E_{T_+} &= +2E_Z + E_{ST} + E_C \qquad (1.15) \\ E_{T_0} &= E_{\downarrow,0} + E_{\uparrow,0} + E_{ST} + E_C \\ &= E_{ST} + E_C \quad , \qquad (1.16) \end{aligned}$$

where E_C is the Coulomb charging energy.

The first take away of these equations is that at zero magnetic field the spacing between the N=2 ground state and first excited state is $E_{ST} = E_{orb} - E_K$ and not $E_{orb} = \hbar\omega_0$. Excited state spectroscopy for N=1 will allow insight into the single particle energy spectrum. However, for all higher charge occupations the Coulomb interaction E_K will influence the excited state spectrum. This provides a motivation for reaching the last charge, in order to measure the single particle energy spectrum without interactions. The second take away of these equation is that if we compare E_S with E_{T_-} we can see that the N=2 ground state can be a triplet state if $2E_Z > E_{ST}$. It is possible to determine E_{ST} using by observing the Zeeman energy required to induce a singlet to triplet ground state transition[1]. This form of magnetospectroscopy is used in combination with pulse bias spectroscopy in this thesis.

Figure 1.10(a) shows the energy level spectrum defined by Equations 1.13-1.16. The purpose of Figure 1.10(a) is to illustrate the energy spectrum of a two charge quantum dot, and to highlight the transitions available for the N=1 to N=2 occupation. The colored lines indicate transitions that are available based on spin conservation. We highlight that this schematic is for GaAs where the g-factor is negative, hence the spin-

[1] In addition, the ability to polarize the ground state has applications in spin-based technology [47].

up at $|T_+\rangle$ are the lowest in energy[1].

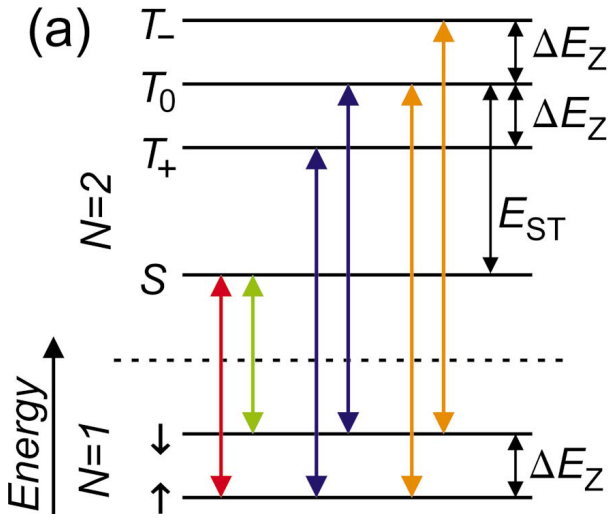

Figure 1.10: **Two-charge spin states:** (**a**) Shows the energy level spectrum available at the N=1 to N=2 charge transition for a GaAs quantum dot. These are the energy levels described in Equations 1.13-1.16. The colored lines indicate transitions that are available based on spin conservation. The horizontal dashed line indicates that the total charge state of the quantum dot has changed from N=1 to N=2. Crossing the dashed line adds E_C energy to the quantum dot. Note that this schematic is for electrons in GaAs where the g-factor is negative, hence the ↑ and $|T_+\rangle$ are the lowest in energy. Reproduced from [47].

1.3.4 Valley states in silicon quantum dots

In the previous sections of this introduction we have discussed the orbital structure of 2D quantum dots (section 1.3.1) and discussed the spin filling sequence into these orbitals (section 1.3.2 and section 1.3.3).Electrons in silicon quantum dots have an additional level of complexity due to the presence of valleys in the silicon conduction band. However, when the valley states are well defined, they can be exploited for use in new technology [6]. The challenge is that valley physics is complex, and relies on atomic scale properties. Therefore substantial differences in valley properties are observed between nominally identical devices. In this section we discuss the main aspects of valley physics for silicon MOS quantum dots[2]. We conclude by discussing that the additional complexity introduced by conduction band valley states provides a motivation for studying

[1]The orbital excited state structure can be complicated for silicon due to the degeneracy of the valley states. See section 1.3.4 for further discussion.

[2]For a more detailed review see Zwanenburg *et al.* [6].

valence band holes in silicon quantum dots, since valley states are not present in the valence band.

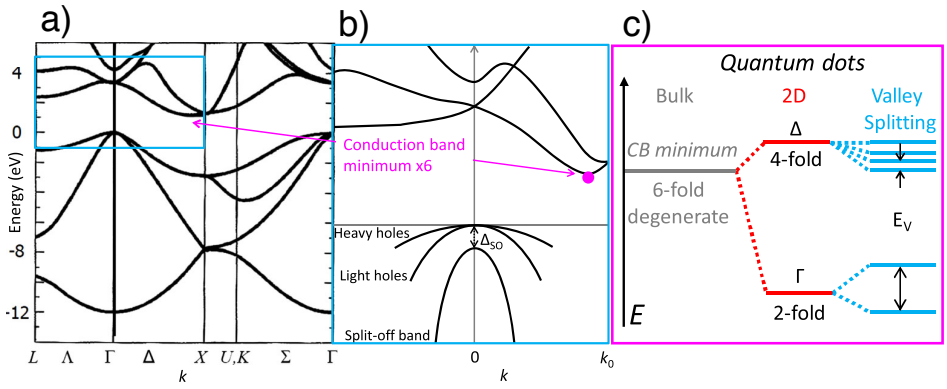

Figure 1.11: **Silicon Band structure and valley degeneracy:** (**a**) This figure shows the bulk silicon band structure. The pink arrow indicates the Conduction Band (CB) minima, which occurs at k≠0. (**b**) Zoom of the region indicated by the blue rectangle in (a). (**c**) Schematic diagram of the splitting of valley states for bulk (grey), 2D (red) and quantum dots (blue). In bulk the CB minimum has 6-fold degeneracy. however, in 2D structures the 6-fold degeneracy is lifted by strain. The splitting between the 2-fold Γ level and the 4-fold Δ level is typically tens of meV [48]. The degeneracy of the 2D valley states is further lifted by electric confinement. Typical splitting of the Γ levels is 0.1-1meV [49]. Silicon band diagram is reproduced from [50], schematic reproduced from [6] .

The band structure of bulk silicon has a conduction band minimum at a non-zero momentum. This gives rise to six degenerate valley states in the conduction band, as shown in Figure 1.11(a-b). While the valleys do not significantly influence conventional electronics, the presence of degenerate ground states plays a critical role for quantum electronics. In quantum electronic devices the valley degeneracy is typically broken by various effects. For electrons in a 2D quantum well the in-plane strain splits the six valley states into a 2-fold degenerate ground state (Γ valleys) and a 4-fold degenerate excited state (Δ valleys), as shown schematically in Figure 1.11(c). The typical splitting between the Γ and Δ valleys is on the order of tens of meV [48]. Electric confinement of a quantum dot then lifts the degeneracy of the Γ valleys, with typical valley splitting of order 0.1-1 meV. However, the exact magnitude of the Γ valley splitting is determined by atomic scale details of individual devices. The variability and complexity of valley physics introduces a challenge for engineering reproducible silicon quantum dots towards specific applications, such as qubits.

Qubit applications require quantum dots with a robust two level energy state that is well separated from higher energy excitations. Valley states complicate the energy spectrum

by introducing an additional degree of freedom. The relevant energy scales to consider are the valley splitting E_V and the orbital energy ΔE. When the E_V is large compared to ΔE the electrons occupy the well defined orbital levels n=1,2,3 and the lowest energy valley state V1. Alternatively if ΔE is large compared to E_V then four electrons sequentially fill into the Γ valley states V1 and V2 with orbital number n=1, followed by the V1 and V2 states with orbital number n=2. These two trivial cases are shown schematically in Figure 1.12(a) and (b).

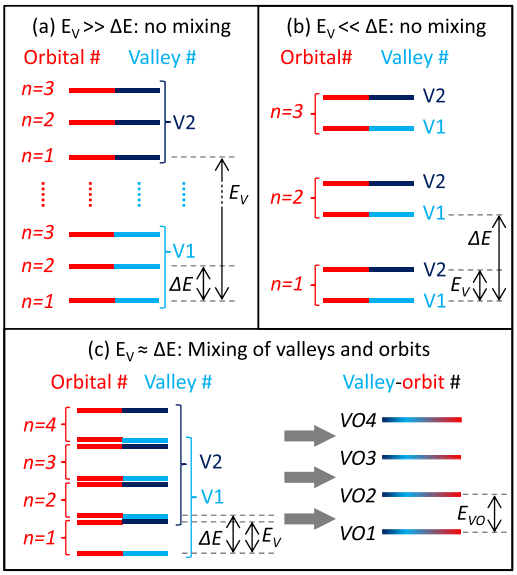

Figure 1.12: **Valley-orbit mixing in silicon:** (**a-b**) Schematic of the energy levels when the valley splitting and orbital energy are not comparable. The orbital number is given by n, and the two non-degenerate Γ valley states are indicated by valley numbers V1 and V2. (**c**) When E_V and ΔE are comparable the orbital and valley states hybridize into valley-orbit states. The valley-orbit states become the relevant single particle states indicated by VO1, VO2,... which are separated in energy by E_{VO}. Reproduced from [6].

Valley and orbit states can hybridize into mixed single particle levels, and this complicates the orbital shell structure of electron quantum dots in silicon. The effects of hybridization can be most clearly observed when the valley splitting is comparable to the orbital energy, as shown in Figure 1.12(c). Mixed single particle states are known as valley-orbit states, and the relevant splitting is the valley-orbit splitting E_{VO}. The valley-orbit mixing and valley-orbit splitting are determined by complex atomic scale phenomena, and understanding the physical mechanisms remains a topic of active research. The bulk silicon valence band is not complicated by degenerate valley states.

The bulk silicon valence band is not complicated by degenerate valley states. This has

provided a motivation for studying hole states in silicon quantum dots. At the valence band maximum the Heavy Holes (HH) and Light Holes (LH) are degenerate, as shown in Figure 1.11(b). However, electrical confinement lifts the degeneracy of the Heavy and Light Holes based on the different effective masses, with typically LH-HH splitting on the order of a few to tens of meV[1]. This allows p-type silicon quantum dots have to have a Heavy Hole ground state [28]. Pure heavy holes in silicon quantum dots are expected to occupy the well known Fock-Darwin orbital states, without the complexity of additional valley mixing. This would allow p-type quantum dots the have the simple and well defined energy structure observed in GaAs, while maintaining the advantages of silicon as a material system. However, there have been no studies of the orbital shell structure for holes in 2D silicon quantum dots that can be used to confirm this prediction.

1.3.5 Spin-Orbit Interaction

A wide range of non-trivial spin effects can be observed when the spin and orbital degrees of freedom are coupled together [51]. Any effect that couples the spin and orbital momentum is referred to as a Spin-Orbit Interaction (SOI). In this section we describe the two primary types of spin-orbit interaction that effects both electrons and holes in semiconductor quantum dots. Specifically these are the Dresselhaus effect and the Rashba effect. The focus is to provide a qualitative description of these main effects, with insight into their physical origins. For full details see Winkler [51].

In atomic physics the Spin-Orbit Interaction (SOI) arises as a relativistic correction due to the motion - or *orbit* - of an electron in a static electric field. The electric field $\vec{E}$ produces an internal magnetic field proportional to $\vec{E} \times \vec{p}$, where $\vec{p}$ is the electrons momentum. This internal magnetic field acts on the spin state, and the strength of the interaction depends on the orbital momentum. Hence, the presence of electric fields can mediate the spin-orbit coupling.

In solid state devices the Spin-Orbit Interaction (SOI) experienced by both electrons and holes arises from two distinct types of electric field[2]. The first case occurs due

[1] This is discussed further in section 1.5.1.

[2] Holes have an additional Luttinger Spin-Orbit Interaction (SOI), which doesn't occur for electrons.

to Bulk Inversion Asymmetry (BIA) of the atoms in the crystal lattice. The Spin-Orbit Interaction (SOI) produced by Bulk Inversion Asymmetry (BIA) is known as the Dresselhaus effect [51]. The strength of the Dresselhaus effect is determined by the crystal lattice and basis. Bulk silicon has a diamond lattice with no BIA, hence there is no Dresselhaus SOI in bulk silicon [6][1]. The Dresselhaus effect is present in zinc-blende crystals such as GaAs, and is stronger for heavier atoms since heavier atoms produce a larger atomic electric field.

The second case of semiconductor Spin-Orbit Interaction (SOI) is due to Structural Inversion Asymmetry (SIA) of the confinement potential. The Spin-Orbit Interaction (SOI) produced by Structural Inversion Asymmetry (SIA) is known as the Rashba effect [51]. The strength of the Rashba SOI is determined by the asymmetry of the confinement potential, defined by $\nabla \cdot V(\vec{r})$. This can lead to interesting since the confinement symmetry is typically tunable in MOS quantum dot devices. This allows the strength of the Rashba spin-orbit coupling to be tuned in-situ [51]. In devices with symmetric confinement the Rashba SOI is suppressed regardless of the mixing between bands.

Both the Rashba and Dresselhaus effects mix the spin states between the valence and conduction bands. As such, the strength of the both Spin-Orbit Interaction effects is determined by the band gap. In materials with a small band gap, such as InAs and InSb the mixing between conduction and valence bands is large resulting in strong SOI for typical devices. Alternatively, in silicon the large band gap strongly suppresses mixing between the conduction band and the valence band, resulting in extremely weak Rashba SOI.

Typically the Luttinger SOI is the larger than BIA and SIA for Holes. This is discussed in more detail in section 1.5.2.

[1]However, there is evidence for the interface-Dresselhaus effect, which arises due to BIA at the Si/SiO_2 oxide [52]. This interface-Dresselhaus effect occurs since the SiO_2 inherently sets an interface orientation breaking the spatial invariance of the bulk. The interface-Dresselhaus effect produces a coupling that is identical to the typical bulk Dresselhaus effect and scales based on the proximity of the charge to the interface.

1.4 Single-spin qubits

A major application for semiconductor quantum dots is their use in quantum computation technology. Quantum computation aims to use quantum states to perform algorithms that are either not possible or not feasible for classical computers. The basic unit of quantum information - a *quantum bit* - is known as a *qubit*. While classical bits must either be in the '0' or '1' state, a qubit can exist in superposition of the '0' and '1' states. The current state-of-the-art in quantum computational technology to determine the optimum physical implementation of a qubit, with a focus on scaling up to multi-qubit structures. The success in fabrication and the well defined quantized energy levels makes semiconductor quantum dots ideal for use as qubits. Implementing and optimizing quantum dots as reliable qubits continues to be a major field of research in quantum information technology.

There are three main physical qubits that can be implemented using semiconductor quantum dots: charge qubits [53, 54], singlet-triplet qubits [14, 15] and single-spin qubits [8]. The single-spin qubit (sometimes known as the Loss-DiVincenzo qubit [8]) is the most relevant to this thesis. The basis states of a single-spin qubit are the spin down $|\downarrow\rangle$ and spin up $|\uparrow\rangle$ Zeeman spin states of a quantum dot. It is possible to define a spin qubit in a quantum dot containing a large number electrons (or holes), however the most intuitive spin qubit is formed by a single electron in a static magnetic field. This provides a motivation for reaching the last charge in quantum dot systems, since the most promising spin qubit experiments have been performed using quantum dots containing just one electron [17, 19, 55].

1.4.1 Single-spin qubit time scales

The parameters used to determine the suitability of a qubit to store quantum information are the relaxation time, and the coherence time. The relaxation time T_1 is the time scale over which an excited state decays to the ground state. In spin qubits T_1 corresponds to the time scale for the spin to relax from the higher energy Zeeman state to the lowest energy Zeeman state. This relaxation involves a change in energy and angular

momentum, which is typically dissipated through the phonon bath or nuclear spin bath. The behavior of T_1 can then be understood in terms of: (1) the density of states of the nuclear spin bath, (2) the density of states of the phonons, (3) the hyperfine coupling (mediating the nuclei-electron spin coupling), and (4) the spin orbit coupling strength (mediating the spin-phonon coupling). In typical spin-qubit experimental conditions the Zeeman splitting of the spin states is large enough to suppress relaxation via the nuclei spin bath, and relaxation is primarily via spin-phonon coupling mediated by the spin-orbit interaction.

The phase coherence time T_2 describes the timescale over which quantum phase information can be preserved. In spin qubits this corresponds to how long a coherent superposition of the $|\downarrow\rangle, |\uparrow\rangle$ basis states can be preserved. The quantum phase for a spin qubit is defined by the phase of the Larmor spin precession. Quantum phase randomization in spin qubits is primarily due to fluctuations and inhomogeneity in the nuclei spin bath, which alters the spin precession frequency by changing the local magnetic field. Therefore developing spin qubits in materials with an extremely low density of magnetic nuclei or weak hyperfine coupling has been a major focus for enhancing spin qubit coherence times [6, 18].

Phase decoherence mechanisms can be considered to have components occurring on two different time scales: (1) The quasi-static component, which is constant over one measurement but may vary between consecutive measurements[1]; and (2) the fluctuating component, which varies over the course of a single measurement. Due to these two components measurements of the spin decoherence time are extremely sensitive to the way the measurements are performed. The decoherence time time, labeled as T_2^* is the free precession phase coherence time observed over a set of different measurements. Therefore T_2^* is sensitive to the variations of the quasi-static component, which changes between measurements. It is possible to significantly enhance the measured decoherence time by using spin *refocusing* techniques.

Spin *refocusing* techniques dynamically decouple the spin from the quasi-static dephasing

[1]The most common quasi-static component is the slowly varying background nuclei spin bath [6, 30, 56].

sources [57]. Using dynamical decoupling methods can enhance the observed decoherence time by several orders of magnitude [14, 56]. The spin coherence time that has been measured using a dynamic decoupling technique is typically presented as T_2^i, where the text $'i'$ indicates the particular protocol used. For example, in single-spin qubits Hahn echo (T_2^{Hahn}) or CPMG (T_2^{CPMG}) techniques are commonly used to *refocus* the spin. Using *refocusing* techniques it can be possible to enhance the observed decoherence time up to the fundamental limit given by $T_2 \leq 2T_1$ [30, 58].

A key challenge for qubit systems is to maximize the relaxation time, and the coherence time. Silicon is a particularly attractive system for maximizing the T_1 and T_2 of spin qubit systems. Natural silicon contains 95% non-magnetic nuclei, and can be purified to nearly 100% non-magnetic nuclei. The absence of a nuclear spin bath suppresses spin relaxation and phase randomization. In addition, electrons in silicon experience very weak Spin-Orbit Interactions (SOIs), which limits the spin coupling to phonons and charge noise. Due to these favorable properties electrons in silicon quantum dots can achieve an extremely long T_2^* and high fidelity manipulation[1]. In the next section we introduce the methods to produce spin manipulation in semiconductor quantum dots.

1.4.2 Spin manipulation

Electrons in quantum dot based spin qubits can be manipulated using Electron Spin Resonance ESR. This involves applying an oscillating magnetic field perpendicular to a static magnetic field. Coherent spin rotations between the $|\uparrow\rangle$ and $|\downarrow\rangle$ qubit basis states are driven when the frequency of the oscillating magnetic field matches the Zeeman energy of the spin split states ($\hbar f_{osc} = g\mu_B B$). The frequency of the spin rotations is known as the Rabi frequency (f_{Rabi}) and is proportional to the square root of P, where P is the power of the driving field at the qubit site. Typically spin-qubits driven by ESR can experience f_{Rabi} up to several MHz [13, 17, 55].

While ESR can be used to drive long lived, highly coherent spin qubits [19], there are

[1] A T_2^* of 120μs, T_2^{CPMG} up to 28ms and control fidelity of 99.6% has been observed by Veldhorst *et al.* [17] in a single spin-qubit based on a silicon MOS quantum dot. Recently in a two-qubit silicon MOS control fidelities of up to 98% have been observed (Huang *et al.* 2019 [55]).

some challenges in scalability. It is difficult to address individual spins in a multi-qubit device, since producing localized magnetic fields is challenging. Generally an oscillating magnetic field is produced using a bulky proximal strip line, and this takes up space on a device and requires additional fabrication. There are additional challenges related to the qubit operation speed ($1/f_{Rabi}$). The maximum Rabi frequency is limited since high power magnetic fields generated by a strip line produce heat, which will degrade qubit performance. Each of these effects is a challenge for scaling up spin qubits towards the multi-qubit systems needed for quantum computing.

Spin qubits driven by electric fields are a potential solution to overcome the challenges in the scalability of spin qubits. All-electric driving of the spin states is known as Electric Dipole Spin Resonance (EDSR) and has been demonstrated in 2007 by Nowack *et al.* [59]. Recently Hendrickx *et al.* [25] have achieved all electric spin manipulation for spin qubits with f_{Rabi} exceeding to 100MHz and qubit control fidelities of 99.3%. This demonstrates the potential for fast scalable qubit control and there currently considerable research interest in developing EDSR based spin qubits.

The challenge of using electric fields to control spin states is that the magnetic moment of a free electron (or hole) spin does not intrinsically couple to electric fields. Electric manipulation must be mediated via a physical mechanism that allows an oscillating electric fields to produce an oscillating *effective* magnetic field. There are three main ways to achieve this in semiconductor devices: (1) using the intrinsic Spin-Orbit Interaction (SOI), where an oscillating electric field can produce an effective oscillating internal magnetic field [60]; (2) using g-Tensor Modulation Resonance (g-TMR), where electric field oscillations can induce an oscillating Landé g-factor [61, 62]; or (3) Using a micro-magnet, where electric fields can spatially displace the wavefunction through a non-uniform magnetic field [63]. The first two approaches (SOI and g-TMR) can be mediated by an intrinsic spin orbit coupling[1]. There has been an increase in research of systems with strong spin-orbit coupling due to their potential for use as scalable spin-qubits[2].

[1] In contrast the micro-magnetic approach requires the inclusion of bulky micro-magnet in the fabrication process. This reduces one of the advantages of electric manipulation, which was the ability to remove the bulky ESR strip line.

[2] This approach, including the underlying physical mechanisms is discussed in much more detail in the literature review of Chapter 4.

In this section of the thesis we have outline the main aspects of spin qubits and detailed how they are related to semiconductor quantum dots. The research presented in Chapters 2, 3, and 4 of this thesis is focused on understanding the fundamental physics of hole spins in silicon quantum dots. A primary motivation for enhancing the understanding of hole spin states is to determine the feasibility of implementing hole spins as spin qubits. In the following section we will discuss the current state of silicon hole spin physics.

1.5 Holes in silicon quantum dots

So far in this introduction we have discussed physics that applies to both electrons and holes in silicon quantum dots. In this section we highlight some of the main aspects that distinguish hole from electron based quantum dots in silicon. In section 1.5.1 we introduce the background physics of the silicon valence band. In section 1.5.2 we introduce the 4x4 $\boldsymbol{k}\cdot\boldsymbol{p}$ model known as the Luttinger model, which describes the lowest energy valence band states. Finally, in section 1.5.3 we present a high level summary of the key factors that distinguish holes from electrons in quantum dot applications.

1.5.1 Valence band states in silicon

The spin physics of holes varies from electrons since holes occupy the valence band rather than the conduction band. The valence band is made from atomic p-orbitals[1] (l=1) and the hole states can therefore have total angular momentum[2] of J=1/2 or J=3/2. These two states (J=1/2 and J=3/2) are split in energy due to spin-orbit coupling, where the splitting is known as the spin-orbit gap (Δ_{SO}). The $J = 1/2$ states have just one projection of the total orbital momentum $j_z = \pm 1/2$, however the J=3/2 bands has two projections defined by $j_z = \pm 3/2$ and $j_z = \pm 1/2$. Overall this gives rise to the three distinct energy levels in the valence band, which are shown schematically in Figure 1.13(a) (red, blue and purple).

The spin-orbit gap (Δ_{SO}) is typically much larger than the energy scales in semiconductor

[1] Recall that the atomic shell filling of silicon is [Ne]$3s^2 2p^2$.

[2] $J = L + S$, where $L = 1$ for the valence band and $S = 1/2$ is the spin angular momentum.

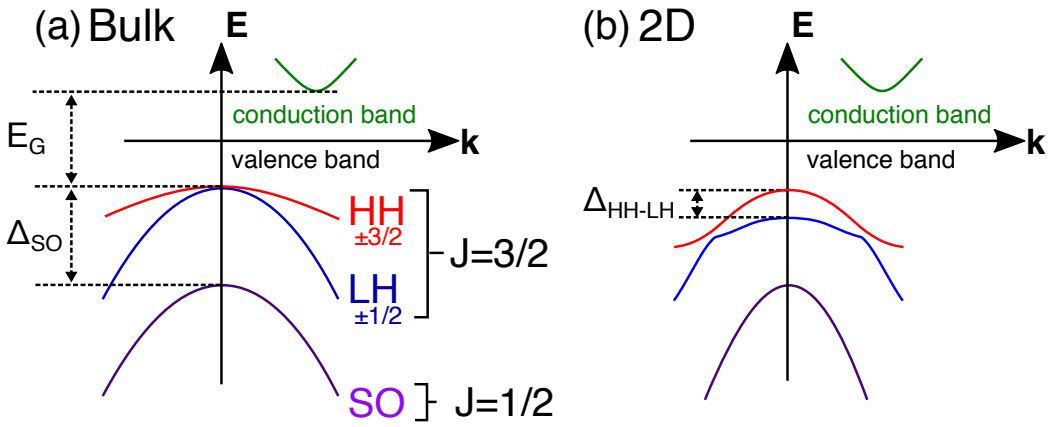

Figure 1.13: **Schematic of silicon valence band:** (**a**) Schematic of the bulk silicon band structure. The valence band has three distinct energy levels; Heavy Holes (HH, red), Light Holes (LH, blue) and the Split-Off band (SO, purple). The distinct total angular momentum (J) and projections (j_z) are identified for each band. (**b**) Schematic of the silicon band structure when 2D confinement has been imposed. The 2D confinement lifts the degeneracy of the HH and LH bands, with HH moving to higher energy. The LH and HH states experience an avoided crossing due to the mixing of HH and LH states. The effects of confinement on the conduction band have been discussed in section 1.3.4. Figure modified from [64].

quantum devices, and the J=1/2 band can be neglected since it is generally unoccupied[1]. Therefore, it is the $J = 3/2$ states that are primarily considered in the hole physics of semiconductor quantum dots. Since these states have $J = 3/2$, they are conventionally referred to as having effective spin S=3/2. The two $J = 3/2$ bands have different effective masses. Therefore, these two bands are known as the Heavy Hole (HH, $j_z = \pm 3/2$) and Light Hole bands (LH, $j_z = \pm 1/2$). These Heavy and Light hole bands are degenerate at the valence band maximum (k=0). In the next section we discuss a model for these 4 low energy valence band states ($j_z = \pm 1/2$ and $j_z = \pm 3/2$).

1.5.2 Luttinger Model of the Valence band

Full $\boldsymbol{k}\cdot\boldsymbol{p}$ models can successfully describe the semiconductor band structure including the effects of non-parabolically, spin-splitting, and electric and magnetic field induced effects [51, 65]. However, these full $\boldsymbol{k}\cdot\boldsymbol{p}$ models also require solving large 14x14 matrices. Typically in semiconductor quantum devices only the low energy valence band states are occupied, making it unnecessary to solve the full 14x14 matrices in order to describe

[1] Δ_{SO} = 40meV in silicon and Δ_{SO} = 341meV in GaAs [51]. Typical energy scales for electrically addressable quantum dots are 0.1 to 20meV.

the underlying valence band physics. The Luttinger model is a 4x4 $\boldsymbol{k}\cdot\boldsymbol{p}$ model used to describe low energy hole spectrum in cubic semiconductors [51, 66]. The general form of the Luttinger Hamiltonian (H_L) has three main contributions, which are given by

$$\begin{aligned} H_L = &\quad \text{(Kinetic)} + \text{(Spin-orbit)} + \text{(Cubic Crystal Symmetry)} \\ H_L = &\quad H_K + H_{SO} + H_C \\ H_L = &\quad \left(\gamma_1 + \frac{5}{2}\gamma_2\right)\frac{\boldsymbol{\pi}^2}{2m} - \frac{\gamma_3}{m}(\boldsymbol{\pi}\cdot\boldsymbol{J})^2 + \frac{\gamma_3-\gamma_2}{m}(\pi_x^2 J_x^2 + \pi_y^2 J_y^2 + \pi_z^2 J_z^2) \end{aligned} \quad (1.17)$$

where γ_i are Luttinger material parameters (see Table 1.1), $\boldsymbol{\pi}$ = $\boldsymbol{k}$ - e$\boldsymbol{A}$ is the long momentum, $\boldsymbol{A}$ is the vector-potential, axes x, y and z are oriented along the crystal axes [1,0,0], [0,1,0] and [0,0,1] respectively, m is the bare electron mass, and $\boldsymbol{J} = (J_x, J_y, J_z)$ is the hole angular momentum (spin 3/2). In the following sections we discuss the main physical effects that are described in this Luttinger model.

Material composition in Luttinger model

The effects of the material composition are included in the Luttinger Hamiltonian by the Luttinger parameters $\gamma_{1,2,3}$ and κ. In this thesis we have focused on silicon. However, the valence band of other materials can be described by including the relevant Luttinger parameters. A summary of the relevant bulk Luttinger parameters is included in Table 1.1.

	γ_1	γ_2	γ_3	κ
Si	4.29	0.34	1.45	-0.42
GaAs	6.98	2.06	2.93	1.2
InAs	20.4	8.3	9.1	8.78
InSb	37.1	16.5	17.7	15.6
Ge	13.4	4.24	5.69	3.41

Table 1.1: **Bulk Luttinger parameters**: See Winkler [51] Table D.

Effective mass in the Luttinger model

The Luttinger Hamiltonian gives the effective mass[1] of the Heavy Holes (HH) and Light Holes (LH) as,

$$m^{HH} = \frac{m}{\gamma_1 - 2\gamma_2} = 0.28m, \quad m^{LH} = \frac{m}{\gamma_1 + 2\gamma_2} = 0.20m \tag{1.18}$$

where m is the free electron mass, and γ_i are the bulk Luttinger parameters. The specific numbers given in Equation 1.18 are for silicon.

When 2D confinement is introduced the difference in the effective masses lifts the degeneracy of the Heavy and Light hole bands at the valence band maximum. A schematic of the 2D valence band structure is shown in Figure 1.13(b). The result of 2D confinement is that the ground state of a 2D Hole Gas is the Heavy Hole states (at k≈0). The magnitude of the Heavy Hole Light Hole splitting (Δ_{HH-LH}) at k=0 depends on the strength of the 2D confinement, and is typically on the order of 4-10meV in 2D systems. For a simple square well confinement the splitting between the first (n=1) Heavy Hole and Light Hole states can be given as

$$\begin{aligned} \Delta_{HH-LH} = & \quad \frac{\pi^2 n^2 \hbar^2}{2m_{LH} d^2} - \frac{\pi^2 n^2 \hbar^2}{2m_{HH} d^2} \\ = & \quad \frac{2\gamma_2 \pi^2 \hbar^2}{m d^2} \end{aligned} \tag{1.19}$$

where d defines the square well width, and the masses are taken from Equation 1.18. As a rough estimate in silicon for a square well of width 10nm, $\Delta_{HH-LH} \sim 5$meV.

The Light Hole states are typically unoccupied for low energy scales. However, for k≠0, the different curvature of the bands brings the Heavy Hole and Light Hole bands together allowing mixing. This mixing can influence the hole spin physics [51] by effecting the angular momentum of a hole state. The magnitude of the HH-LH mixing will depend on Δ_{HH-LH} and the Fermi momentum, however it can be electrically controlled by tuning the 2D confinement potential (analogous to changing d in Equation 1.19). It is the

[1]Here we show the perpendicular effective mass for growth direction [001]. See Ref [51] Equations 4.33 for directional dependence of effective masses.

HH-LH mixing that causes the avoided crossing of the bands, shown schematically in Figure 1.13(b).

Luttinger spin-orbit coupling

Valence band holes in silicon experience an enhanced spin-orbit coupling compared to electrons. This enhanced spin-orbit coupling is due to the p-orbital (l=1) nature of the valence band holes and is included in the Hamiltonian as as the Luttinger spin-orbit term

$$H_{SO} = -\frac{\gamma_3}{m}(\boldsymbol{\pi} \cdot \boldsymbol{J})^2. \tag{1.20}$$

In silicon the Luttinger Spin-Orbit Interaction (SOI) is strongest spin-orbit coupling term acting on the hole states[1]. For holes confined in silicon quantum dots, the Luttinger SOI captures the 3D orbital symmetry of the confinement. This allows anisotropic spin-orbit coupling to arise based on anisotropy in the orbital confinement profile.

The enhanced spin-orbit coupling of holes in silicon has been experimentally observed by studying the spin-orbit length (λ_{SO}). The spin-orbit length is a useful parameter since it defines the distance a charge must travel for the spin-orbit interaction to produce a π rotation of the spin[2]. Holes in silicon MOS quantum dots have spin-orbit lengths measured to be 110nm [28]. This is comparable to the strength of the spin-orbit coupling of electrons in small band gap systems such as InAs (λ_{SO} = 127nm [67]). The large spin-orbit coupling experienced by valence band holes provides motivation for their implementation as all-electric spin qubits[3]. Holes in silicon MOS based quantum dots are particularly promising due to the Heavy Hole ground state with no valley degeneracy and the advantages of silicon MOS fabrication. However, there are limited experimental studies of hole spin-orbit coupling interactions in these devices. There still remains many open questions regarding the complex spin-orbit coupling of holes states.

[1] Dresselhaus and Rashba spin-orbit coupling are suppressed in silicon due to the large band-gap and lattice structure.

[2] Shorter spin-orbit lengths (λ_{SO}) occur for systems with stronger net spin-orbit interaction strengths.

[3] See the Literature review presented in Chapter 4 for further details.

Cubic crystal symmetry in the Luttinger model

The effect of the cubic lattice symmetry is described by the term

$$H_C = \frac{\gamma_3 - \gamma_2}{m}(\pi_x^2 J_x^2 + \pi_y^2 J_y^2 + \pi_z^2 J_z^2). \tag{1.21}$$

To determine the significance of this term it is useful to compare the magnitude of the H_C coefficient with the H_{SO} coefficient. This can be parameterized by considering the value of

$$\eta = \frac{\gamma_3 - \gamma_2}{\gamma_3}. \tag{1.22}$$

In systems such as InAs $\eta = 0.1$ and the H_C term can be ignored or treated as a perturbation. However, in silicon $\eta = 0.77$ and H_C can introduce crystal based anisotropy to the Hamiltonian.

Zeeman splitting in the Luttinger model

To complete the model of the valence band Hamiltonian it is necessary to include the effect of an external magnetic field $\boldsymbol{B}$. The simplest magnetic response comes from the Zeeman effect,

$$H_Z = \ -g\mu_B \boldsymbol{B} \cdot \boldsymbol{J} \tag{1.23}$$

where $\boldsymbol{J}$ is the hole 'spin 3/2' and the g is the g-factor. The bulk g-factor is given by $g = 2\kappa$. Typically the Zeeman effect is characterised by observing the linear in $\boldsymbol{B}$ splitting of an energy level. The Zeeman effect is then parameterized by the g-factor, which can be extracted from the slope dE/dB. In this sense, the experimental g-factor is defined by all the linear in $\boldsymbol{B}$ terms in the Hamiltonian, where the total Hamiltonian is given

$$\begin{aligned} H = &\quad H_L + H_Z \\ H = &\quad H_K + H_{SO} + H_C + H_Z \end{aligned}$$

In addition to the Zeeman term (H_Z), magnetic fields also enter into the Luttinger Hamiltonian (H_L) through the vector potential in the long momentum $\boldsymbol{\pi} = \boldsymbol{k} - e\boldsymbol{A}$. The Luttinger Spin-Orbit (H_{SO}) and cubic asymmetry (H_C) terms can both introduce linear in B terms to the total Hamiltonian, which will modify the effective g-factor. As a simple example we can consider vector potential $\boldsymbol{A} = (B_z y, 0, 0)$ which defines the magnetic field $\boldsymbol{B} = (0, 0, B_z)$. Then the spin orbit Hamiltonian becomes

$$\begin{aligned} H_{SO} = & \quad \frac{\gamma_3}{m}(\boldsymbol{\pi} \cdot \boldsymbol{J})^2 \\ = & \quad \frac{\gamma_3}{m}\left((k_x - eB_z y)J_x + k_y S_y + k_z J_z\right)^2 . \end{aligned} \tag{1.24}$$

If we collect the terms that are linear in B in Equation 1.24, then the spin-orbit contribution to the *effective Zeeman*[1] splitting is given by,

$$\begin{aligned} H_{SO}^Z = & \quad -\frac{2ye\gamma_3}{m}(\boldsymbol{k} \cdot \boldsymbol{J})B_z J_x \\ = & \quad g_{SO}^* \mu_B B_z J_x \\ \text{where} & \\ g_{SO}^* = & \quad -\frac{4y\gamma_3}{\hbar}(\boldsymbol{k} \cdot \boldsymbol{J}). \end{aligned} \tag{1.25}$$

This highlights how the Luttinger Spin-Orbit Hamiltonian can modify the effective hole g-factor[2]. Similarly the Cubic term H_C can produce linear in B terms, which can further modify the effective hole g-factor. This discussion of the hole g-factor is continued in Chapter 4 of this thesis, where we present an experimental and theoretical study of the g-factor for a single hole in a silicon MOS quantum dot.

[1] The terms in Equation 1.24 that have no B dependence contribute a constant energy shift, and the terms that are quadratic in B are small and can be neglected.

[2] The observed effective g-factor will be given by the tensor sum of the Zeeman g-factor g and the spin orbit g-factor g_{SO}^*.

1.5.3 Comparison of spin properties in different group IV quantum dot structures.

In section 1.5.1 and section 1.5.2 we have discussed some of detailed underlying physics that distinguishes hole spin states from electron spin states. In this final section we present a summary of the different properties of holes and electrons in silicon quantum electronic devices. The summary is presented in Table 1.2. The focus is primarily on differences in spin properties with a focus on spin-qubit applications. Three distinct device categories are presented in Table 1.2: electrons in MOS quantum dots, which currently are the most successful spin-qubit systems; holes in MOS quantum dots, which are a promising candidate and the focus of this thesis; holes in germanium quantum dots, which have shown amazing progress in the recent year achieving all electric qubit operations in Ge MOS [25] and Ge hut wires [23].

1.5.4 Conclusion of background for holes in quantum dots

In sections 1.5.1, 1.5.2, and 1.5.3 we have covered the background physics for hole quantum dots that is relevant for the experimental chapters of this thesis. Each Chapter of this thesis begins with a literature review. In Chapter 2 we present a review of the development of hole based quantum dots in silicon MOS structures. In Chapter 3 we cover the literature for spectroscopy measurements of hole quantum dots in a range of materials and quantum dot structures. Finally, in Chapter 3 we review the physical mechanisms that are related to g-tensor modulation in semiconductor quantum dots.

Table 1.2: Summary of electron and hole properties relevant for spin-qubit applications. All values are electrically measured values.

Property	**Electrons**	**Holes in Silicon**	**Holes in Germanium**	
	MOS devices	MOS devices	MOS Devices	Nanowire devices
Effective mass	$0.19m_e$	$m^{HH} = 0.28m_e$	(0.05-0.1)m_e [68]	$0.044m_e$ [69]
Mobility ($cm^2V^{-1}s^{-1}$)	$10^4 - 10^5$	$10^3 - 10^4$ [a]	10^6 [68]	10^2 [71]
Ground state degeneracy	Two valley states $\Delta_{\text{V1-V2}}$=(0.1-1)meV	$\Delta_{HH-LH} \approx 5 - 10$meV [51]	$\Delta_{HH-LH} \approx 30$meV [26]	$\Delta_{HH-LH} \approx$ tens to hundreds of meV [72]
Spin-Orbit Interactions	Negligible	Strong $\lambda_{SO} = 110$nm[28]	Strong $\lambda_{SO} = 127$nm [69]	
Landé g-factor	2±0.01 [52][b]	Anisotropic and tunable, $\cdot g_{\text{MOS}} = (0.2 - 4)$[c] $\cdot g_{NW} = (1.6 - 2.6)$ [73],[104]	Anisotropic and tunable, Not fully studied. $g \approx 0.3$ [25]	Anisotropic and tunable, $g = (0 - 4.5)$ [72], [129]
Spin manipulation	·Magnetic via ESR, ·Electric via EDSR using a micro-magnet [63]	All-electric using strong intrinsic SOI		
Rabi Frequency	ESR up to 500kHz [55], EDSR up to 30MHz [74]	EDSR up to 60MHz [20] for CMOS nanowire.	EDSR up to 100MHz [25]	EDSR up to 140MHz [23]
T_1	Up to 2s [75], sensitive to $\Delta_{\text{V1-V2}}$	Not measured	(6±3)μs [26]	Ge Hut: 90μs [24] SiGe NW: 600μs [76]
T_2^*	120μs for MOS device, 20μs with micro-magnet, [17], [74][d]	(60 ± 1)ns [20] for CMOS nanowire	Up to 800ns [25]	Ge Hut: 130ns [23] SiGe NW: 190ns [77]
T_2	28ms for MOS device, 3ms with micro magnet, [17], [74]	(245 ± 14)ns [20], for CMOS nanowire	Up to 2μs [25]	Not measured

[a] Typically μ_e/μ_h is around 3-5 in ambipolar silicon MOS devices [70].
[b] Weakly modulated by interface SOI [52].
[c] See Chapter 4 of this thesis.
[d] In both cases an isotopically purified silicon sample is used.

Chapter 2

Single and double quantum dots in silicon MOS structures

Abstract

Hole quantum dots in many materials are attracting attention for uses in spin based applications, such as spin qubits. While single electrons confined in planar Si quantum dots are one of the most successful electron spin-qubit systems, there has been limited study of single holes in identical 2D structures. To date, no-one has presented measurements of a stable 2D hole quantum dot in silicon operating down to the last hole, which is the most widely used regime for spin-based quantum computation applications. In this chapter we present such measurements of a hole quantum dot device. Confirmation of the absolute charge occupation is possible since the device includes an adjacent charge sensor. We present a full set of characterisation measurements demonstrating that this is device structure allows stable, well defined single hole quantum dots, suitable for spin based applications. Finally, we tune the device to the double quantum dot regime, and present measurements of a 2D Metal-Oxide-Semiconductor (MOS) silicon double quantum dot. These results represent a significant step forward in the understanding, fabrication, and potential applications of p-MOS quantum electronic devices.

Publication

The results presented in this chapter appear in the article and supplementary material of: Liles, S. D., Li, R., Yang, C. H., Hudson, F. E., Veldhorst, M., Dzurak, A. S., and Hamilton, A. R. (2018). Spin and orbital structure of the first six holes in a silicon metal-oxide-semiconductor quantum dot. Nature communications, 9(1), 3255.

2.1 Chapter introduction

The spin states of electrons confined in semiconductor quantum dots form a promising platform for quantum computation [6, 8, 30]. Recent studies of silicon complementary MOS (CMOS) qubits have shown coherent manipulation of electron spin states with extremely high fidelity [17]. However, manipulation of single electron spins requires large oscillatory magnetic fields to be generated on-chip, making it difficult to address individual qubits when scaling up to multi-qubit devices [13, 17]. In addition, electron spins experience a strong hyperfine coupling to the nuclei spin of the host crystal, which limits spin coherence times [14]. While coherence time can be significantly improved by using isotopically purified material systems such as silicon [17], the isolation of electron spins makes it difficult to perform fast operations, thereby sacrificing operation speed for coherence time.

Hole spins in semiconductor quantum dots are attracting significant attention as candidates for fast, highly coherent spin qubits [78, 79]. These two key factors for qubit operation, coherence and speed, can be enhanced due to the unique spin properties of valence band holes. Hole spins are predicted to have long coherence times due to the weak hyperfine coupling to nuclear spins [80, 81]. Optical studies of hole quantum dots suggest a 10 to 100 times enhancement of T_2^* over electron spins [82, 83]. By significantly suppressing a leading source of decoherence, p-type materials may provide highly coherent spin qubit systems. Hole spin based qubits have been demonstrated to have rapid operation times [20, 22], due to the inherently strong spin-orbit coupling[1], which allows

[1]While Spin-Orbit Coupling (SOC) will decrease the decoherence time via charge noise, the SOC also enables orders of magnitude decrease in gate operations time. ESR driven spin qubits have typical

spin states to be controlled locally with electric fields applied to gate electrodes [59, 60, 84, 85]. Hole spins therefore provide a highly scalable system of easily addressable, fast qubits.

Despite these promising properties, hole based quantum dots still face technological challenges that have been overcome in electron systems more than a decade ago [6]. Planar silicon CMOS quantum dots are amongst the most promising semiconductor system to implement spin qubits. This type of device is suitable for high frequency spin manipulation experiments [59], and is optimized for scalability up to many qubits [86, 87]. However, creating a planar silicon CMOS quantum dot capable of confining a single hole has been a challenge [28, 29, 70, 88]. Previous studies of planar silicon-based hole quantum dots have used transport measurements to study the addition spectrum of the quantum dot [28, 29, 88]. However, as these devices approach the few hole regime, the tunnel barriers become extremely opaque, and the transport signal falls precipitously. This has hampered studies of hole quantum dots containing one and two holes, which is the most widely used regime for spin-based quantum computation applications.

In this chapter we present an experimental study of a surface-gated silicon metal-oxide-semiconductor quantum dot capable of reaching the last hole. Confirmation that the device can reach the single hole regime is possible since the device incorporates a charge sensor. In addition, we demonstrate a double hole quantum dot operating in the last hole regime. These results are a promising step towards developing hole quantum dots towards spin based application such as spin qubits. Finally, we note that these hole quantum dots are formed using same planar geometry that has already proven highly successful for electron spin qubits [17, 19, 59].

gate times of around 1μs [17], while electrically driven spin-orbit qubits have shown gate times around 10ns [22] (See Table 1.2) . The key factor is the ratio of spin decoherence time to the gate operation time. Experiments are still required to quantify the decrease in decoherence time for hole spins due to charge noise.

2.2 Literature review - Single spins in silicon MOS quantum dots

Semiconductor quantum dots are a rich and interesting research field. For quantum physicists, quantum dots can act as artificial atoms or molecules, allowing access to a quantum mechanics lab on a semiconductor chip. In addition, quantum dots can serve as platforms for new applications and technology. In particular, the electrically addressable quantum dots are ideal for spintronics, and spin based quantum information applications, since the quantum dot serves as an ideal structure to confine and manipulate individual spins. In this literature review I will discuss the development of silicon MOS quantum dot structures towards spin based applications. The focus of this review is to highlight the significance of reaching the last hole in a silicon MOS quantum dot within the context of the silicon MOS semiconductor technology.

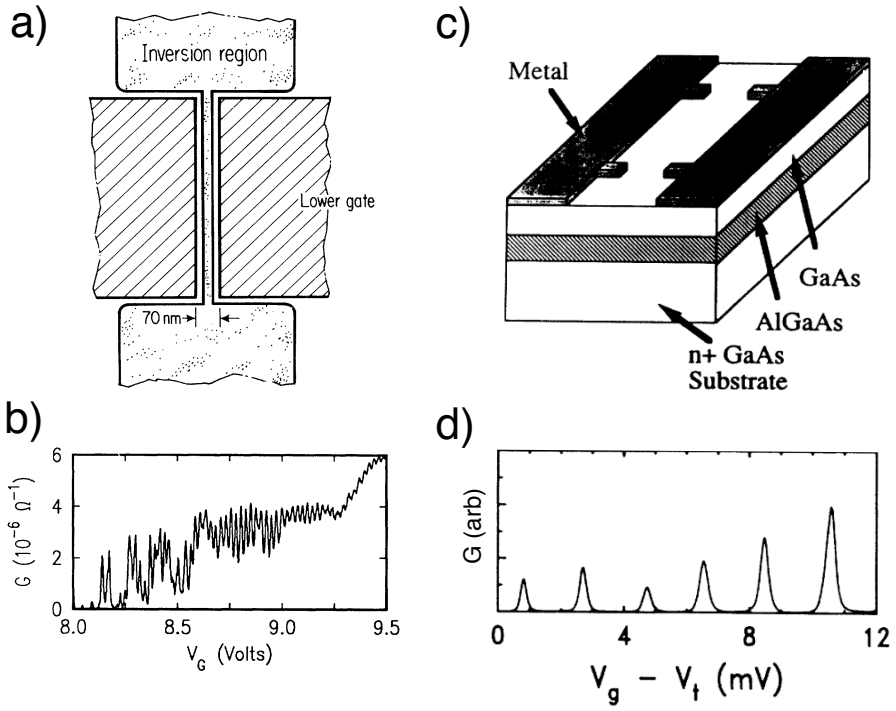

Figure 2.1: **Early examples of Coulomb blockade in Si and GaAs:** (**a**) Shows the layout of the silicon based device studied by Scott-Thomas *et al.*. Accidental quantum dots form due to disorder in the narrow silicon channel. (**b**) Shows the conductance oscillations due to Coulomb Blockade, measured as as function of the Lower gate voltage. Reproduced from [89]. (**c**) Shows the schematic layout of the GaAs/AlGaAs quantum dot device studied by Meirav *et al.*. (**d**) Shows the conductance as a function of the gate bias above threshold, with clear well defined Coulomb blockade. Reproduced from [90].

A defining feature of a quantum dot is the ability to observe Coulomb blockade. The first evidence of Coulomb blockade in a semiconductor was observed in 1989 using a Si/SiO_2 MOSFET device [89]. Figure 2.1(a) shows a schematic of the device, which consists of a one dimensional etched silicon channel. Reproducible periodic oscillations in the conductance of the device are shown in Figure 2.1(b). These conductance oscillations are due to the formation of a quantum dot along the narrow one-dimensional channel. The current becomes blockaded by the repelling force of adding more electrons to the quantum dot. In these early silicon devices the charge islands were formed by disorder effects where electrons are confined into 'puddles' of trapped charges by impurities in the material.

From 1990 significant progress in the understanding and measurement of quantum dots was made using GaAs as a material system. In addition to the well developed nano-technology for GaAs nano-electronics, the low disorder allowed fabrication of reliable, reproducible and highly controllable quantum dot devices. Figure 2.1(c) shows the schematic of an early GaAs MOS quantum dot, and Figure 2.1(d) shows the high quality of the Coulomb blockade. GaAs quantum dots were of high enough quality to act as artificial atoms and in 1996 Tarucha *et al.* observed orbital shell structure [9]. Further successes allowed measurements of Pauli spin blockade [91], where the current through a device is blocked based on the spin configuration of a double quantum dot. Finally in 2006 Koppens *et al.* showed ESR measurements of electrons confined in GaAs planar structures [13, 59].

In addition to demonstrating the progress of GaAs based quantum dots, the ESR measurements also highlighted a key challenge that limits GaAs as a material for spin based applications. The spin coherence time of electrons in GaAs was found to be limited to tens of nanoseconds due to the abundance of magnetic nuclei [14]. The magnetic moment of the Ga and As nuclei interact with the electron spins via the strong hyperfine coupling, leading to decoherence. Dynamical decoupling mechanisms can extend the electron spin coherence times [56, 92, 93], however the low concentration of magnetic nuclei in silicon provided motivation for large scale research focus on silicon as a base material for quantum dots.

2.2.1 Electrons in silicon MOS quantum dots

In this subsection I discuss the key developments using silicon MOS quantum dots to confine electrons[1]. Here we particularly focus on the development of these systems for spin based electronic applications, such as spin-qubits.

In order for quantum dots in a particular material to be full developed towards spin based applications there are four broad criteria the devices should be able to fulfill. These criteria are;

1 - Controllable demonstration of Coulomb blockade.

2 - Control of the absolute charge occupation.

3 - Ability to readout the spin state.

4 - Ability to manipulate the spin state.

1 - Controllable Coulomb Blockade: The first observation of Coulomb blockade in a semiconductor occurred in 1989 using a planar silicon MOSFET device [89], and by 1999 controllable Coulomb blockade was achieved by Simmel *et al.* [94] in silicon MOS quantum dots. Figure 2.2(a) shows a vertical schematic of the device studied by Simmel *et al.* [94]. This device employed a multi-layer structure with a large metallic upper gate used to form a 2DEG, while two lower gates deplete the 2DEG and form a controllable quantum dot. The upper oxide layer was 80nm and the lower oxide layer was 20nm thick. The surface layout of the device is shown in Figure 2.2(b) showing the conceptual idea of deliberately forming an electron island, between the source and drain 2DEG regions.

Silicon quantum dots improved as technology of multilayer gates was developed. Fujiwara *et al.* [96] (2006) and Angus *et al.* [95] (2007) each studied a well defined quantum dot with tunable tunneling barriers. An example of the device layout used by Angus *et al.* (2007) is shown in Figure 2.2(c). The major improvement on previous silicon MOS quantum dots is the significant decrease in the oxide thickness. Thin oxide reduces the impact of disorder at the SiO_2 interface on the confinement profile, allowing the formation

[1]For a full reference of all silicon quantum dot structures such as self assembled, nanowires and dopant quantum dots see Zwanenburg *et al.* [6].

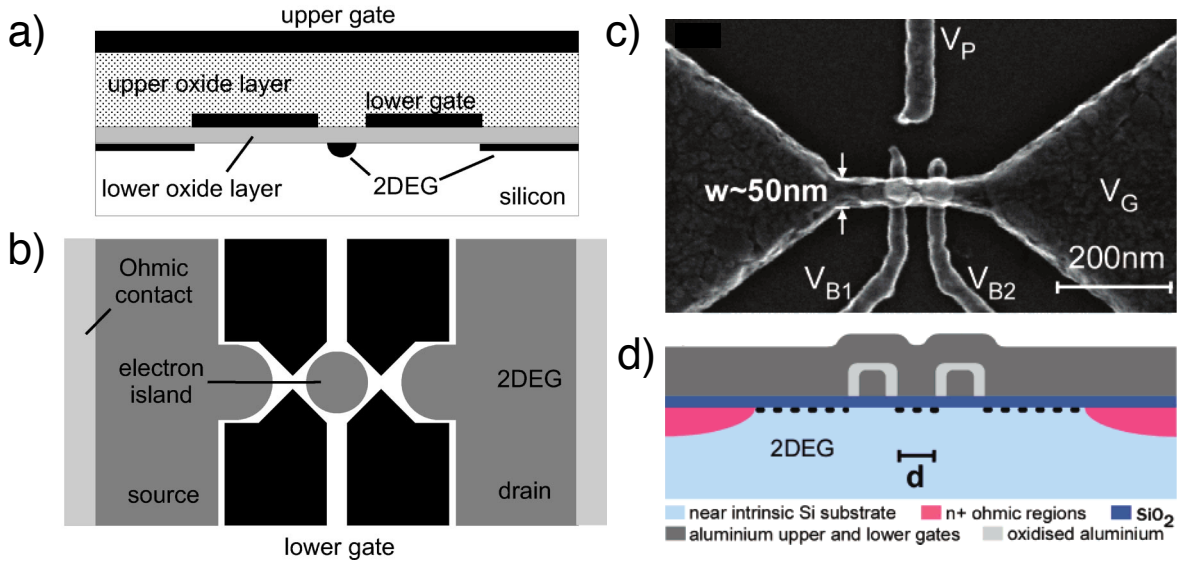

Figure 2.2: **Multi-layer silicon MOS quantum dots:** (**a**) Schematic of the multilayer silicon MOS quantum dot studied by Simmel *et al.* in 1995. An upper gate forms a 2DEG, while the lower gates form the electron Island as demonstrated in (b). The upper oxide layer is 80nm thick and the lower oxide layer is 20nm thick. Reproduced from [94]. (**c**) SEM image of the multilayer devices studied by Angus *et al.* in 2007 with (**d**) showing the corresponding vertical schematic. Here the thickness of the SiO_2 and the oxidized aluminum are both several nanometers thick. The scale bar labeled d represents the lower gate separation, which is less than 40nm. Reproduced from [95].

of well defined, tunable quantum dots[1]. Angus *et al.* use a 5nm thick SiO_2 layer, while the multilayer stack of aluminum gates is insulated by an AlOx layer that is only several nanometers thick. This extremely thin oxide allows the gates to be placed very close to the 2DEG, providing excellent control of the dot tunnel barriers and chemical potential. An SEM of the layout of these MOS quantum dots is shown in Figure 2.2(d). In 2009 Lim *et al.* used these multilayer devices to observe silicon electron quantum dots reaching the few hole regime. However, a key challenged remained with these structures; the quantum dot chemical potential was controlled by the same gate which forms the 2DEG lead. This limited the range of operation of the quantum dot, and made reaching the last electron difficult.

This subsection demonstrates the major developments allowing controllable Coulomb blockade of electron MOS quantum dots in silicon. Coulomb blockade indicates the

[1]Scott-Thomas *et al.* [89] show that the disorder effects in silicon MOS devices are strong enough to form quantum dots even when there is no electrostatic gates present. The thin oxide used by Angus *et al.* allows the gates to provide a strong electric confinement, overpowering the effects of the SiO_2 interface disorder. Thin oxide (on the order of a few nanometers) is not necessary for GaAs quantum dot devices due to the low disorder of the samples.

ability to isolate an island of charge within a quantum dot and is an important step towards development of spin based electronics. However, the experiments presented in this subsection have all been in the many electron regime, where the absolute number of electrons is unknown. This makes interpretation of the physical properties such as energy structures and magnetic response challenging, since the quantum dot charge and orbital configuration is unknown and therefore cannot be reproduced across multiple devices. The next step forward in the technology is to demonstrate control of the absolute number of charges on the dot.

2 - Control of the absolute charge occupation: The ability to control the absolute charge occupation hinges on the ability to fully deplete all charges from the dot[1]. Observations of silicon quantum dots reaching the last electron were demonstrated by Liu *et al.* [31] (2008) and Lim *et al.* [16] (2009). Lim *et al.* (2009) achieved this control by adding an additional layer of aluminum gates. An SEM of the device by Lim *et al.* (2009) is shown in Figure 2.3(a), and a schematic is shown in 2.3(b). The key feature was the addition of the P gate, allowing the dot chemical potential to be tuned independently of the 2DEG leads. Evidence that the last electron has been reached is shown in 2.3(c). As the number of electrons decreases, the charging energy increases, which is typical of the few electron regime. Finally no additional Coulomb diamonds are observed, confirming the last electron has been reached (therefore labeled N = 0).

The results of Liu *et al.* [31] (2008) and Lim *et al.* [16] (2009) show confirmation of the last electron through charge transport measurements. Typically charge transport measurements do not provide strong confirmation that the last charge has been reached. This is because additional transitions can be missed as a result of the tunnel barriers becoming opaque. In cases where transport measurements are used to determine the occupation, supporting results are typically required to confirm the last hole has been reached. Lim *et al.* [98] characterised the spin and valley state using magnetic field spectroscopy, and found the results consistent with the device last electron. Confirmation of the absolute charge occupation is most convincing when the device incorporates an

[1]Confirmation that the last hole has been depleted typically requires a charge sensor. However, in cases with large clear source-drain current it is possible to observe full depletion of the dot in Coulomb diamonds.

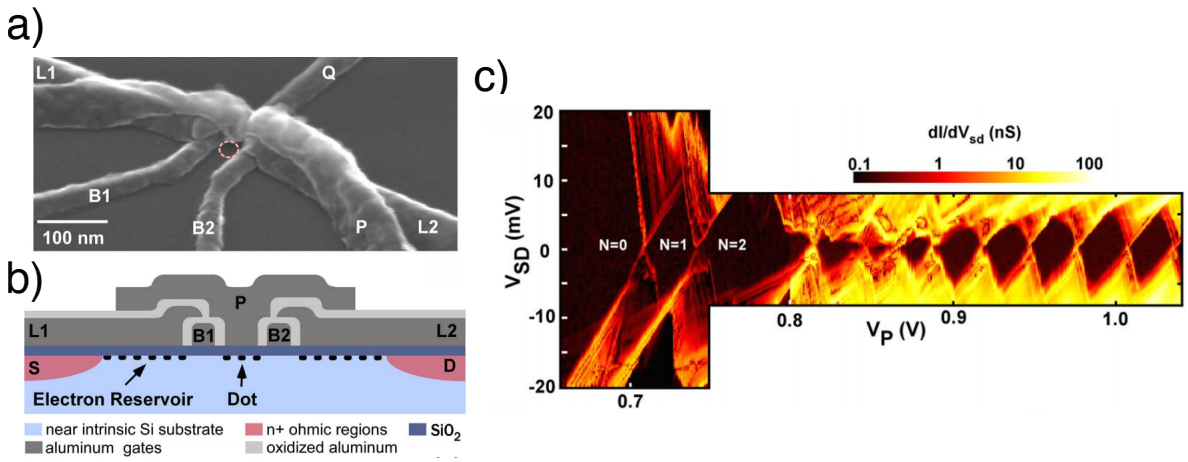

Figure 2.3: **Single electron silicon MOS quantum dots:** (**a**) SEM of the device studied by Lim *et al.* and (**b**) corresponding vertical schematic. The advantage of this device is that the gates L1 and L2 can form a 2DEG, while the P-gate acts as an independent plunger gate, allowing fine control of the quantum dot potential. (**c**) Shows the Coulomb diamonds, which confirm the dot has reached the last electron. Assignment of N=0 is due to no more transitions being observed even for very large source-drain. Reproduced from [16].

adjacent charge sensor.

This subsection highlights the developments allowing silicon MOS quantum dots to reach the last electron regime. The key feature was the implementation of a separate plunger gate to control the quantum dot. Reaching the last charge is a major step towards developing spin based electronics, since it allows access to the absolute number of charges confined in a dot. The ability to know the absolute number of electrons provides a platform for meaningful spectroscopic measurements of spin, valley and orbital states. Lim *et al.* (2011) [98] and Yang *et al.* (2012) [49] used the multilayer silicon MOSFET's to study the behavior of a silicon artificial atoms, providing insight into the valley-orbit states expected in silicon quantum dots.

3 - Ability to readout the spin state: Reading out the spin state of electrons in a quantum dot requires a spin-to-charge conversion mechanism. Pauli spin blockade is a widely used feature of double quantum dots, which can allow spin state readout due to the spin selective transport. Spin measurements of electrons confined in planar silicon quantum dots became possible with the observation of Pauli spin blockade in these devices [31, 99].

4 - Ability to manipulate the spin state: In 2004 Veldhorst *et al.* [17] used an improved design of the multi-layer quantum dots to demonstrate electron spin resonance of single electrons in Si MOSFET quantum dots. The layout is shown in Figure 2.4(a) with a schematic shown to the left. This device is a single lead quantum dot, where the quantum dot is coupled to a single reservoir. The metal gate labeled C (green) provides tight confinement of the quantum dot. The remaining gates (labeled G1 - G4) can act as plunger gates or tunnel barrier, depending on the location of the dot. A single electron transistor (SET) is adjacent to the dot and is used to readout the state of the quantum dot. Finally, an ESR strip line is shown in blue. This device layout highlights the advantages of 2D quantum dots, since all features (strip-line, dot and SET) can be fabricated on the surface, using multiple layers, within several hundred nanometers of each other.

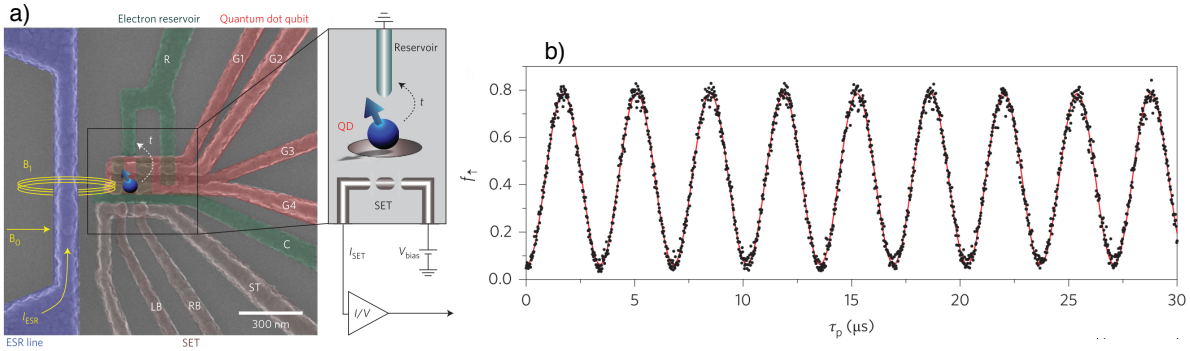

Figure 2.4: **ESR of electrons in Si MOS quantum dots:** (**a**) False color SEM image of the single lead quantum dot device studied by Veldhorst *et al.*. The grey gates labeled ST, LB and LR for the SET. LB and RB are the right and left barrier gates, which are fabricated bellow ST. This allows the formation of a SET in the same way as Angus *et al.* shown in Figure 2.2(d). The remaining gates are described in the main text. Next to the SEM shows a schematic of the typical operation of the device. (**b**) Shows the measurement of ESR for a single electron. Here the y-axis is the electron spin projection and the x-axis is the length of time microwaves are applied for. The black dots are individual measurements. The spin projection oscillates between up and down, at a Rabi period of 4μs and a dephasing time of 120μs. Reproduced from [17].

The results of the ESR measurements performed by Veldhorst *et al.* are shown in Figure 2.4(b). The key result is an observed spin dephasing time, T_2^* of 120μs, which is orders of magnitude improvement on GaAs (T_2^* is of order 10ns [15]) and other semiconductor quantum dots. The reason for such long spin dephasing times is due to the material used. Veldhorst *et al.* use an epitaxially grown isotopically purified ^{28}Si epilayer with

only 800ppm residual concentration of ^{29}Si. Removing the majority of the magnetic ^{29}Si nuclei suppresses the main source of decoherence, allowing long spin lifetimes for electrons in ^{28}Si quantum dots.

2.2.2 Holes in silicon MOS quantum dots

Long spin coherence times and the ability to perform high fidelity spin manipulation positions electrons in silicon MOSFET quantum dots as a leading spin qubit system. However, despite these clear technological successes there are still some challenges and aspects that can be improved. Electron spins are not coupled to electric fields and spin manipulation must be performed by ESR, applying oscillating magnetic fields via adjacent strip-lines (see Figure 2.4(a)). Since the Rabi frequency (spin manipulation frequency) is linear with respect to the square root of the microwave power, the maximum Rabi frequency (f_{Rabi}) for ESR has experimentally imposed limits. The metallic strip-line must be placed away from the quantum dot, which reduces the power received by the dot. Further, since the magnetic field is generated by a alternating current, increasing the microwave power heat's the sample. In contrast, if electrical manipulation of spins is possible, then Electric Dipole Spin Resonance (EDSR [60, 62]) can be driven with the adjacent plunger gates using oscillating voltage, rather than a oscillating current. Hence, the isolation of electron spins from electric fields makes it difficult to perform fast operations, thereby sacrificing operation speed for coherence time.

An attractive solution to these challenges is to use holes instead of electrons. The strong spin-orbit coupling of holes provides a mechanism for electric fields to couple to spin states, allowing fast local spin manipulation, while retaining the advantages of silicon as a material system. In this subsection I will discuss the key developments of p-type MOS quantum dots. I will highlight the development of hole based Si MOS quantum dots along the four technology criteria introduced in the previous section. In particular, I highlight that there have been no previous demonstrations of a silicon MOS quantum dot operating down to the last hole.

1 - Controllable Coulomb Blockade: The first observation of a single hole tran-

sistor was by Leobandung *et al.* in 1995 [100]. Figure 2.5(a) shows a schematic of the device, which uses silicon-on-insulator technology. The quantum dot is formed by etching an abacus shaped bead in the narrow silicon channel. Stable hole quantum dot devices using silicon MOS technology were achieved in 2013 by Li *et al.* [27] and Spruijtenburg *et al.* [29]. These devices used the same multi-layer aluminum gate layouts that had proved successful for electron devices. Figure 2.5(b) shows the schematic used by Li *et al.*, which is exactly same lithography as used by Lim *et al.* [16] to reach the last electron. The only change in the device was the polarity of the ohmic contacts. It is interesting that although n-type devices reached the last electron with this layout, p-type devices were unable to reach the last hole [1]. This is shown by the Coulomb diamonds in Figure 2.5(c). Since the Coulomb diamonds increase in size as hole occupation decreases, it is clear the device has reached the few hole regime. However, the current drops to an unmeasurable level before it is possible to confirm the dot has been fully depleted.
Despite not reaching the last hole, excited states can be clearly observed in the source-drain bias measurements in Figure 2.5(c). Observation of excited state energies can give access to confinement energy of the quantum dot, and can be used to characterise spin properties such as the g-factor. Excited state energies around 800μeV are comparable to the excited state energies of the last few electrons in devices with the same lithography. Given the similar effective mass of electrons and heavy-holes in silicon ($0.19m_e$ and $0.21m_e$ respectively), this suggests that Li *et al.* were close to the last hole. However, the current to drops below the noise level before the last Coulomb diamond can be observed. This suggests that in order to reach the last hole, charge sensing methods must be used. There has been no measurements of a silicon MOS quantum dot reaching the last hole to date[2].

Experiments studying ambipolar quantum dots have provided insight into the differences between the electric properties of hole and electron devices. The first ambipolar silicon quantum dot measurements were performed in 1999 using a silicon-on-insulator device

[1] It is unclear why the identical hole device did not reach the last hole. Recent experimental results suggest that optimal hole quantum dots may require a smaller spacing between gates than electron devices [101].

[2] The last hole regime has been achieved for planar GaAs quantum dots [102], InAs self assembled quantum dots [103], and silicon nanowires quantum dots [104].

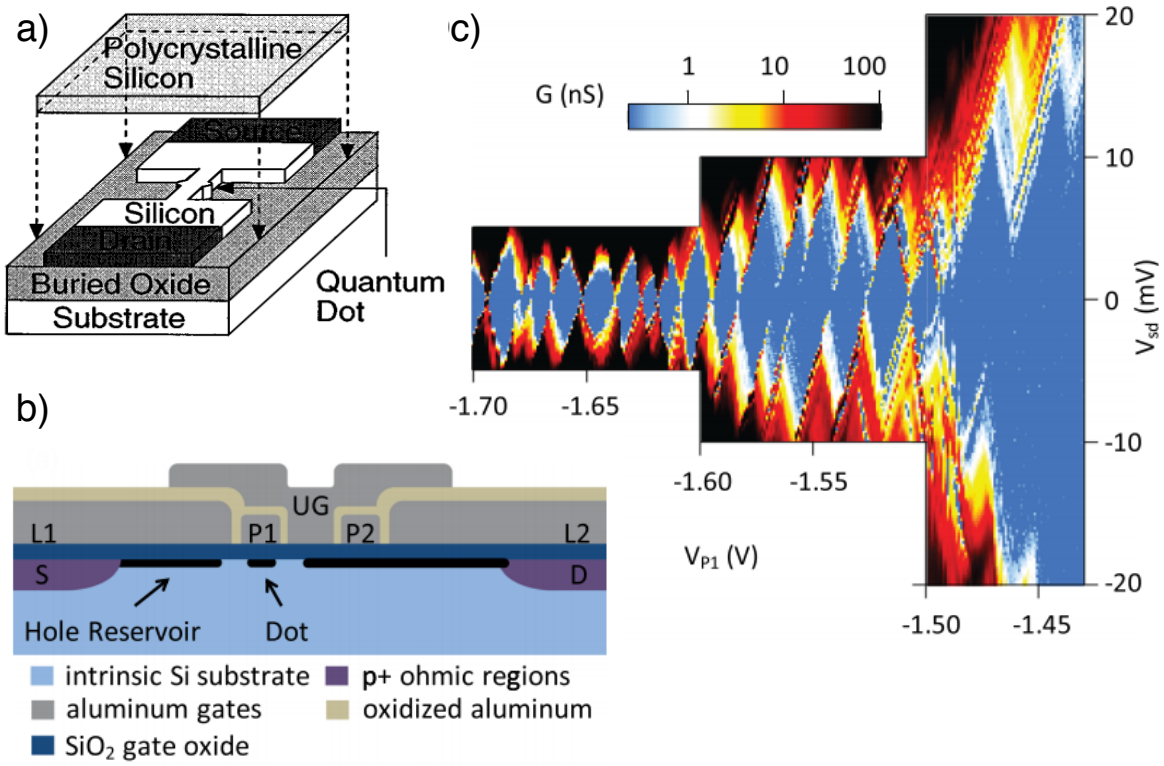

Figure 2.5: **Hole MOS quantum dot development:** (**a**) Schematic of the silicon-on-insulator device studied by Leobandung *et al.* [100]. (**b**) Vertical schematic of the multilayer MOS device studied by Li *et al.*. The lithography is identical to the multilayer devices studied by Lim *et al.* [16], including the nanometer-thin oxide layers. (**c**) Coulomb diamonds observed in the source-drain bias measurements of Li *et al.*. Additional triangles remain for $V_{P1}>$ -1.45V, where the current becomes to weak to measure. Reproduced from [27].

[105]. Further experiments have used ambipolar devices fabricated using the multilayer aluminum gate technique [70, 106, 107]. Figure 2.6 inset (i) shows an example of the ambipolar quantum dot device studied by Mueller *et al.* [107]. The quantum dot is formed by using a two layer aluminum gate stack. Two sets of ohmic contacts are made on either side of the quantum dot, and electrons or holes can flow between the source and drain depending on the polarity of the Lead gate, as shown in insets (ii) and (iii).

The first important result of ambipolar measurements is the difference in MOSFET conduction properties between the two polarities. The black line in Figure 2.6 shows the pinch-off characteristics of the device as a function of the Lead gate voltage. Positive V_{gate} allows for electron conduction, while negative V_{gate} allows for hole conduction. The turn on voltage is around 1.5V for electrons, and around 2.5V for holes. Further, the saturation current for electrons is around 7nA for electrons and 2nA for holes. These

differences in the conductance and turn-on voltage are typical for experiments comparing electrons and holes. Despite the differences, the main experimental result is that the threshold voltage for n-type and p-type conduction is below the oxide breakdown voltage (we have found this to be around 4-5V experimentally), and the current signal is strong enough to observe reproducible Coulomb blockade.

The second important result of ambipolar studies is comparing the properties of an electron and hole quantum dot, formed on exactly the same device. The green and red trace show measurements of the quantum dot Coulomb oscillations for holes and electrons respectively. Despite the differences in conductance and threshold voltage, the n-type and p-type channel show comparable quality Coulomb blockade oscillations. This provides evidence supporting the approach of taking the well establish lithographic designs used for n-type quantum dots and applying it to p-type devices. Translating the same lithography between n-type and p-type devices is often not possible for other hole structures, such as GaAs where the hole and electron effective masses necessarily require different confinement profiles [102, 108, 109].

2 - Controllable of absolute charge occupation: Previous studies of hole MOS quantum dots have not reached the last hole regime [27–29]. While silicon electron quantum dots have strong transport signal even down to the last electron [16, 98], silicon p-type devices typically show lower conductance resulting in weak transport signals. This has made it difficult to confirm the last hole in transport, since the current fall precipitously in the few hole regime, and the last transition cannot be confirmed [27, 29]. This challenge could be overcome by incorporating a charge sensor to silicon hole quantum dot devices.

3 - Ability to readout the spin state: In 2015 Li *et al.* observed Pauli spin blockade of holes using a double quantum dot [28]. An SEM of the device used is shown in Figure 2.7(a). The device is a double quantum dot, where two dots are formed directly under G1 and G2. Figure 2.7(b) shows the double dot stability diagram, with the characteristic honey-comb pattern indicated by black dashed lines. Inset (i) shows the bias triangles

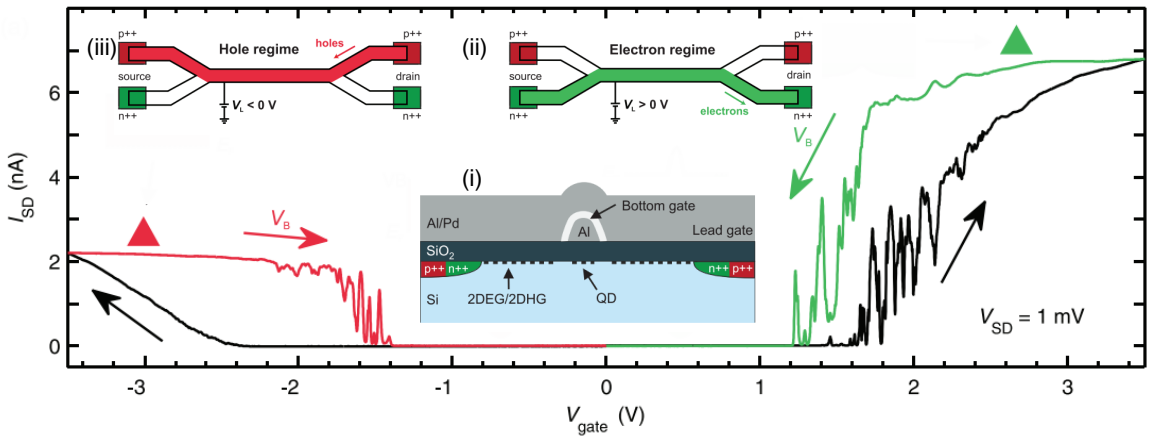

Figure 2.6: **Measurements of ambipolar MOS quantum dots:** Inset (i) shows the schematic of the device, which includes 10nm SiO_2, an Al/Pd Lead gate used to accumulate charge, and a Al bottom gate, which can form a quantum dot below. The device has p-type and n-type ohmic contacts on either side allowing conduction via holes or electron as shown in insets (ii) and (iii). Black data shows the turn on curves where both the the Lead gate and the back gate are ramped together. The n-type channel pinch-off shows Coulomb blockade, while the p-type does not. Mueller *et al.* [107] suggest that negative charge traps at the Si/SiO_2 interface provide a possible explanation for this difference. For small source-drain bias these negative charge traps can act as tunnel barriers to electrons, causing the formation of Coulomb islands. The red and green curves show the Coulomb blockade of the hole and electron quantum dot as a function of bottom gate voltage (Lead gate is held fixed). Colored triangles indicate where the conductance saturates. Reproduced from [107].

for negative source-drain bias. When the bias is reversed the base of the bias triangle has current blocked, consistent with Pauli Spin Blockade [91]. The ability to observe Pauli spin blockade demonstrated a step forward for holes in silicon quantum dots, since Pauli spin blockade is a fundamental technique used to read out the spin state.

4 - Ability to manipulate the spin state: Spin manipulation has not yet been performed for holes in 2D silicon MOS quantum dots. However, recent results using different quantum dot structures have confirmed that holes can have extremely fast spin manipulation times. In 2016 Maurand *et al.* used CMOS etched silicon nanowires [73, 110, 111] to show hole Rabi frequencies of 60MHz [20]. Rabi frequencies reaching 150MHz have been observed using self assembled Ge quantum dots [4, 23, 24] and in Si/Ge MOS quantum dots [25, 26, 112].

Conclusion of holes in silicon MOS quantum dots review

Holes in Si MOS quantum dots have shown the ability to address three of the four key criteria for spin based application. However, the criteria step two, demonstrating a de-

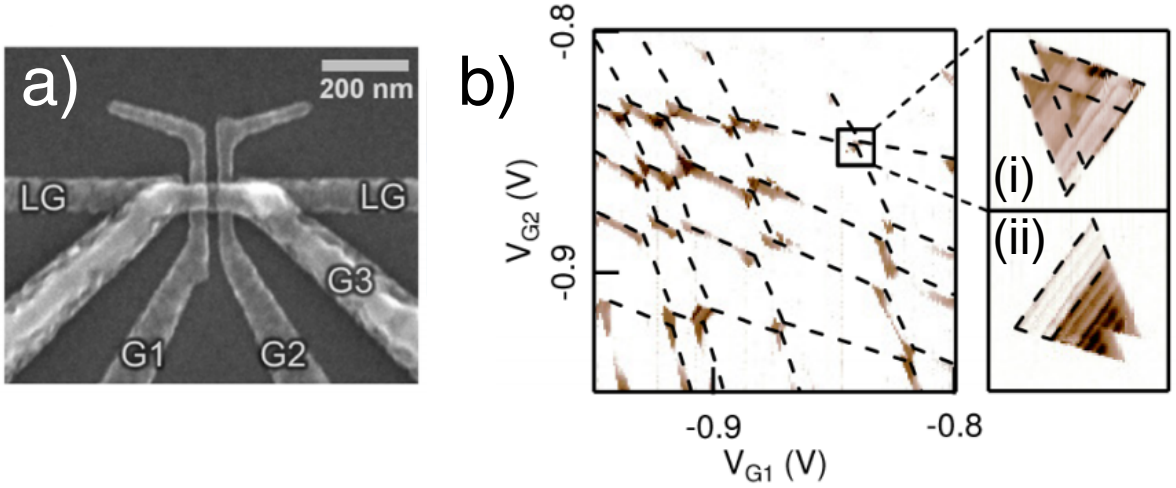

Figure 2.7: **Pauli spin blockade in hole double quantum dots:** (**a**) Shows a SEM of the multilayer p-type double quantum dot studied by Li *et al.*. (**b**) Stability diagram of the double dot, where the x and y axes are the G1 and G2 gate voltage respectively. Here the color scale is the source-drain current. Black dashed lines indicate the honeycomb pattern of a double quantum dot. (i) Shows a zoom of the bias triangle for negative DC source-drain voltage. (ii) Shows the same bias triangle for positive source-drain voltage. The current at the base of the triangle has been blocked by Pauli spin selection rules preventing transport between the two dots. Reproduced from [28].

vice operating down to the last hole, has remained an open challenge. Fulfilling this remaining criteria is the focus of the research presented in this chapter. The motivation for reaching the last hole regime is that from the last hole the absolute charge occupation can be determined. Knowledge of the absolute charge occupation provides valuable context to spectroscopy measurements of spin and orbital states. Ambipolar experiments have shown it is viable to use the same lithography for n-type and p-type silicon quantum dots. Here we draw on the success of the n-type device design used by Veldhorst *et al.* [17] to achieve a single and double hole quantum dot operating down to the last hole.

2.3 Credits for sample fabrication

Unless otherwise stated, all samples studied in this thesis were fabricated by Australia Nanotechnology Fabrication Facility (ANFF) process engineers F.E. Hudson and M. Veldhorst. Design and lithographic layout of the samples has been developed with in collaboration with F.E. Hudson, M. Veldhorst, R. Li, A.R. Hamilton, A. Dzurak, and

S.D. Liles (thesis author).

All measurements presented in this thesis have been performed by S.D. Liles (thesis author). Similarly all analysis and interpretation of results presented in this thesis has been performed by S.D. Liles (thesis author)

2.4 Sample layout and schematic

In this section we outline the key details regarding the fabrication of the Si MOSFET devices studied in this thesis. This includes details of the MOSFET fabrication, Scanning Electron Microscope (SEM) images of the device structure and a brief discussion of the ideal operation of the device.

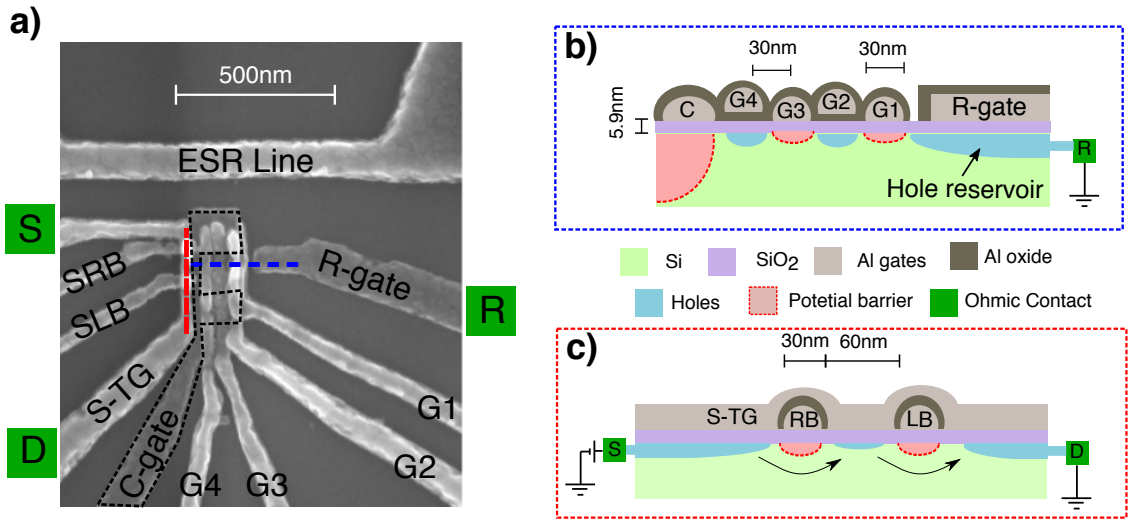

Figure 2.8: **SEM and schematic outline of the device: (a)** Shows the SEM image of a device identical to the devices studied in this thesis. Clockwise, the Aluminum gates are the Electron Spin Resonance (ESR) Line, the Reservoir gate (R-gate), gates 1 to 4 (G1 to G4), the Confinement Gate (C-gate), the Sensor Top Gate (S-TG) and the Sensor Left and Right Barrier gates (SLB and SRB). The green squares labeled 'S', 'D' and 'R' indicate the relative positions of the three p-type ohmic contacts. The black dashed line indicates the shape of the C-gate, which is on the bottom layer. **(b)** Vertical cross section indicated by the blue dashed line in (a). This shows the operation of the device as a double quantum dot. On the right the Reservoir gate accumulates a 2D reservoir of holes at the SiO_2 interface (blue). G1 and G3 are operating as tunneling barriers, indicated by the dashed red regions below. G2 and G4 are in accumulation mode, forming two potential wells at the interface directly below the respective gates. **(c)** Vertical cross section indicated by the red dashed line in (a), showing the sensor operating as a Single Hole Transistor (SHT). S-TG accumulates a sheet of 2D charge at the hetero-junction. The gates SLB and SRB are biased to act as tunneling barriers. SRB and SLB form a single quantum dot in series with the sensor circuit.

All devices studied in this thesis are silicon MOSFET structures. These devices are

fabricated using high resistivity natural (001) silicon as a substrate. All p-type ohmic regions are prepared by boron diffusion. A 5.9nm gate dielectric (SiO_2) is grown by dry oxidation in the active region of the device. Subsequently, the gate pattern is fabricated using multilayer Al-Al_20_3 gate stack technology [27]. These gates are fabricated in several layers. The first layer is the R-gate and C-gate. Layer 2 is gates SLB, SRB, G1 and G3. The final layer is gates G2, G4 and ST. Between each layer the previous layer of gates are exposed to low pressure oxygen plasma to form a several nanometer thin native AlO_x oxide. Fabrication of the multiple layers in this order is important, since it allows the lower level gates to act as depletion gates. The final stage of fabrication is a forming gas (95% N_2 5% H_2) anneal to reduce SiO_2 interface disorder and enhance low temperature performance [95].

Figure 2.8(a) shows the SEM image of a fully fabricated device. The labels in Figure 2.8(a) identify the name for each gate based on the desired function (see caption). In the top of the SEM image the ESR line is visible, although the ESR line was not used for any experiments in this thesis, it demonstrates the flexibility of MOS device layouts. Ohmic contact is achieved by overlapping the respective accumulation gates with a degenerately-doped region far away from the active sample region. The ohmic contacts associated with their relative accumulation gates are shown by the green squares in Figure 2.8(a).

The design of this device is optimized to operate as a quantum dot, with an adjacent charge sensor. An example of typical operation of the quantum dot is shown in Figure 2.8(b). The C-gate provides strong confinement for the quantum dot. In addition to providing confinement the C-gate also ensures there is no current path between the quantum dot and the charge sensor. The R-gate accumulates a 2DHG, which acts as a reservoir of holes connected to the grounded ohmic labeled 'R' (green square). The gates G1 to G4 can be selectively biased to act as accumulation gates or tunnel barriers. Holes from the 2DHG reservoir can tunnel in and occupy the quantum dot based on the finely tuned voltage applied to gates G1, G2, G3, G4 and C.

The second region of the device is the charge sensor circuit. An example of the charge sensor operating as a Single Hole Transistor (SHT) is shown in Figure 2.8(c). The charge sensor circuit consists of the two p-type ohmic contacts 'S' and 'D', which act as the

source and drain of the charge sensor circuit. A current can flow between ohmic contacts S and D, underneath S-TG, with SRB and SLB acting as tunneling barriers. The sensor circuit is isolated from the quantum dot circuit provided the voltage applied to the C-gate is sufficiently depleting. The sensor is adjacent to the quantum dot allowing the sensor current to be maximally sensitive the changes in hole occupation. Further, the orientation of the sensor with respect to the quantum dot gates (G1, G2, G3 and G4) allows the sensor current to be sensitive to not only the total charge of the quantum dot, but also the spatial position. This is because holes accumulated under G1 will be further from the sensor than holes accumulated under G4, and will therefore have a different capacitive effect on the charge sensor.

2.5 Device comparison: from electrons to holes

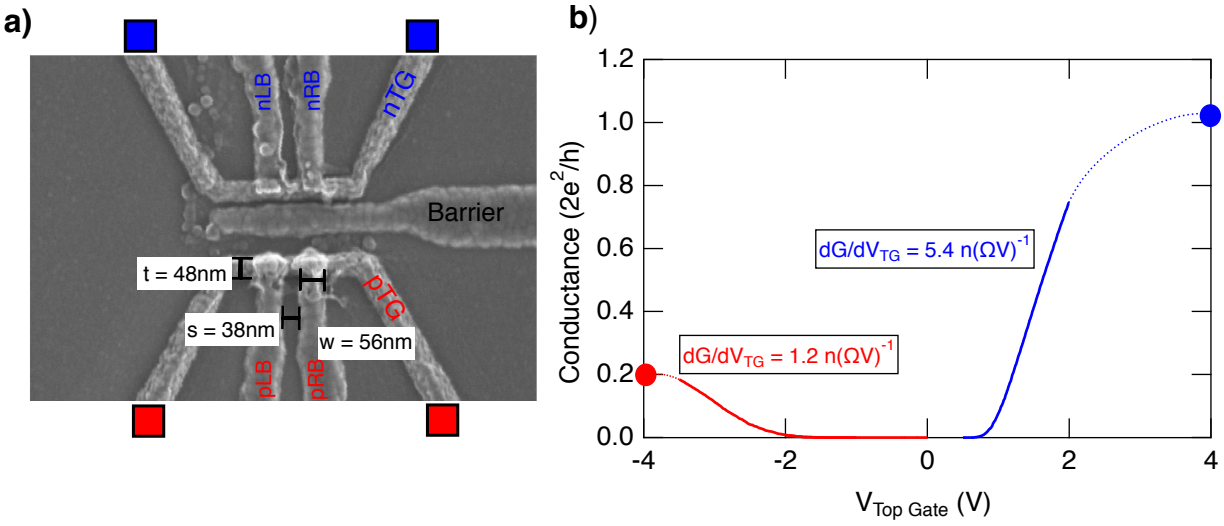

Figure 2.9: **Feasibility tests using ambipolar devices: (a)** A SEM image of the active region of an ambipolar device used for testing. Colored squares indicate the relative location of four ohmic contacts. The red squares indicate p-type regions, while the blue squares indicate the n-type region. The top and bottom circuits are identical and can be separated by the barrier. **(b)** Shows the turn on characteristics of the n-type (blue) and the p-type (red) channels. Here the x-axis is the relevant top gate (nTG for blue data and pTG for red data), while the y-axis is the conductance in units of $2e^2/h$. For both measurements the left and right barrier gates (nRB,nLB,pRB,pLB) are left at 0V. The colored text is the maximum slope for each pinch-off. Solid colored dots indicate the observed conductance when the voltage source was at its limit of |4V| (individual measurements at ±4V from laboratory note book). Dotted lines are a guide to the eye. Measured at 4K. Credit to Anderson West for fabrication of this device.

It is important to determine the feasibility of fabricating multi-layer p-type quantum

dot devices using the same layout schematic as n-type quantum dot devices. Prior to fabricating the batch of p-type devices shown in section 2.4, the channel turn on properties were investigated using basic ambipolar MOS quantum dot devices. Figure 2.9(a) shows an SEM image of the active region of the ambipolar device. The devices consist of four ohmic contacts, two of which are p-type (red squares) and two n-type regions (blue squares). The device consists of two identical circuits. Each has a Top Gate (TG), and a Left and Right Barrier gate respectively (LB and RB). The barrier gates are fabricated underneath the Top Gate in the same way as shown in Figure 2.8(c). This allows a current to flow between the two ohmic contacts when gates TG, RB and LB are appropriately biased.

The turn on characteristics of the p-type and n-type channels are shown in Figure 2.9(b). The key result of Figure 2.9(b) is the distinct difference in the maximum slope of the pinch-off curves, and in the different apparent maximum current. Continuous sweeps are shown over the pinch-off region, and single data point[1] is added indicating the current at ±4V respectively (data is connected by dotted line, which is a guide to the eye). From this data we can calculate the maximum slope and infer the saturation current for n-type and p-type conduction. The maximum slope of the n-type pinch-off is 4.5 times larger than the maximum slope of the p-type pinch-off. If we approximate the system as a MOSFET with $I = \frac{A}{L}\mu ne$, then the ratio of the slopes for identical channel Area (A) and Length (L) can occur from either a difference in hole and electron mobilities (μ) or density of states (dn/dV). For this section we are interested in the slope of the pinch-off since dG/dV is an indicator of how strongly the charge sensor will respond to a change in the charge occupation of a nearby quantum dot.

The n-type saturation conductance is approximately a factor of 5 larger than the p-type saturation conductance. This difference in saturation conductance has often been observed in ambipolar MOSFET devices [70, 106, 107] the origin needs further systematic investigation. Possible explanations include the different doping concentrations of the n-type and p-type regions, the difference in hole and electron mobility (possibly resulting from larger interface roughness for holes), or a difference in the p-type contact resistance.

[1] Recorded in S. Liles laboratory note book. We have found that devices are typically damaged when voltages larger than |4|V are applied.

The turn on voltage for holes is -2V, which is much larger than for electrons (-0.9V). This is likely due to the presence of positively charged Si/SiO_2 traps at the interface [113]. However, it is not significant as this voltage does not exceed the oxide breakdown voltage ($\approx$4.5V). In this section we are interested in the sensor conductance, since this will influence the signal strength and the integration time required for operation of the charge sensor.

We have observed that the p-type and n-type channels show similar pinch-off behavior, and have discussed the quantitative differences. A more detailed discussion of the mechanisms causing these differences is beyond the scope of this section. The primary aim of this section is to compare n-type and p-type MOS devices in-order to asses the suitability of using n-type lithography to make p-type devices. Since the p-type pinch-off slope is smaller than the n-type slope we expect that the p-type charge sensor will be less sensitive the charge of an adjacent quantum dot than an equivalent n-type charge sensor. In addition since the conductance of the p-type channel is less, the p-type charge sensor may require longer integration times than equivalent n-type charge sensors. This longer integration time could mean that single shot measurements are not possible for these p-type devices. Although the p-type channel has a smalled dI/dV and saturation current, the features are still clearly observable showing that this p-type device is viable. In conclusion, these results provide motivation for moving forward to fabrication and characterisation of p-type silicon MOS quantum dot devices.

2.6 Characterising the quantum dot device

Within this section we demonstrate the typical electrical behavior of the quantum dot devices studied in this thesis. The main purpose of this section is to highlight the typical behavior and properties of these silicon p-type MOS quantum dot devices. A major aspect of experimental studies of quantum electronic devices is test and characterisation. This is because these are state-of-the-art devices designed to push forward into previously undeveloped technology. As such, yield of functioning devices can be low[1], and it is par-

[1] On average we have found that about one third of these type devices function as designed. Typically, in devices that are not optimal the issue is an electrical short through the thin oxide between adjacent

ticularly valuable to establish a suite of characterisation measurements and parameters. In this section we present the suite of characterisation measurements used to evaluate the p-type silicon MOS quantum dots. The figures in this section show the typical results of these characterisation measurements, obtained from fully functional devices. Finally, we highlight several specific results that allow the calculation of experimental parameters that will be used in future sections.

2.6.1 Characterising the quantum dot gate characteristics

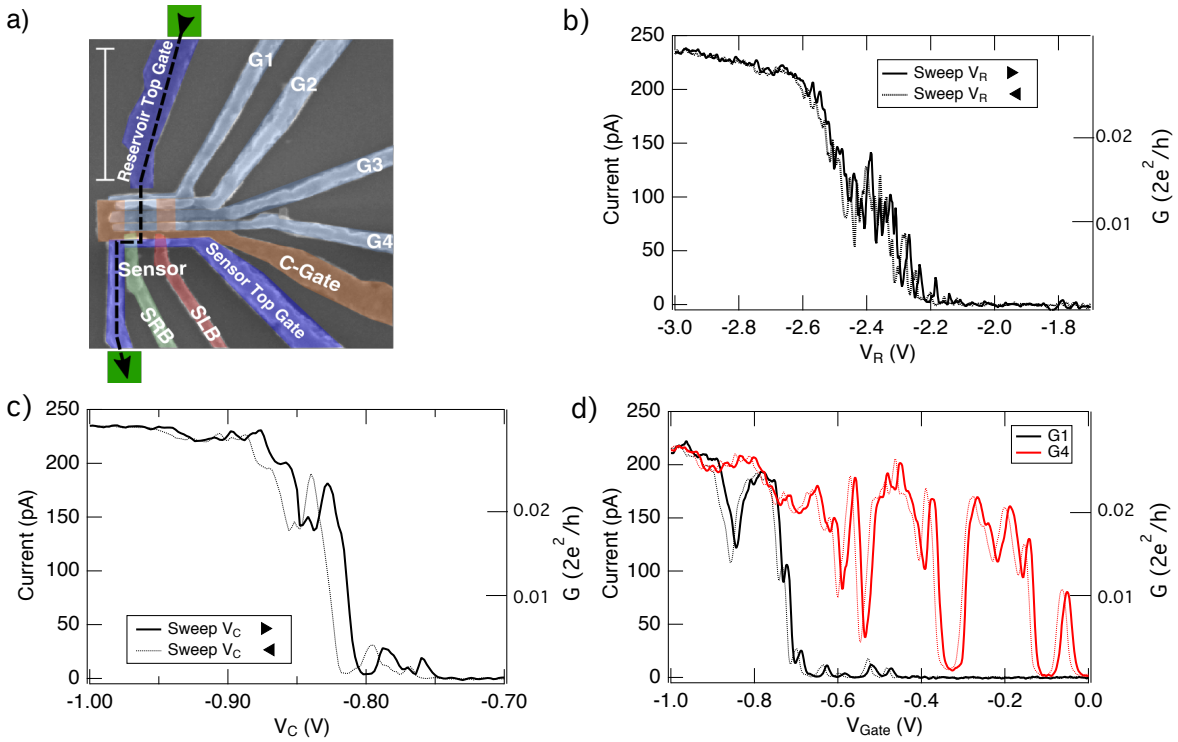

Figure 2.10: **Gate electrode pinch-off characteristics: (a)** False Color SEM image of a typical device. Green squares represent the p-type ohmic contacts and the black dashed line indicates the path of the current. The scale bar is 500nm. **(b)** Pinch-off characteristics of the Reservoir Top gate. All other gates are biased to -3V. In all figures here the solid and dashed curves are for the two different sweep directions, highlighting the reproducibility of the features. The hysteresis is due to filters in the measurement set-up, and the sweep rate is 7mV/s. **(c)** Pinch-off characteristics of the C-gate. The sweep rate is 7mV/s **(d)** Example pinch-off characteristics of two gates G1 and G4, for sweep rate of 20mV/s. All measurements are performed at base temperature of 30mK, with a source drain bias of 100μV. The conductance in units of $2e^2$/h is shown on the right axis of each graph.

The first characterisation measurement performed is to determine the functionality of

overlapping gates.

the quantum dot gates. To check this gate functionality, we investigate the electrostatic pinch-off of the key gates related to forming a quantum dot. Figure 2.10(a) shows the schematic for the first set of measurements. We monitor the current between the ohmic under the Reservoir Top Gate (top green square) and one of the ohmic contacts of the sensor (bottom green square). First we check that a current can be measured between the two ohmic contacts (shown as a black dashed line in Figure 2.10(a)) when all gates are tuned to be sufficiently negative. Typically this occurs when all gates are approximately -3V. This measurement allows confirmation that the two ohmic contacts are operational and the holes can be accumulated across the entire device as required. Typical minimum resistance of these devices is around 250-500kΩ. Similar electron devices, measured in the same way have a resistance of around 10-25kΩ.

We then systematically test the pinch-off of individual electrodes. In Figure 2.10(b) we show the pinch-off of the Reservoir top gate (all other gates are biased to -3V). The measurement of the Reservoir top gate pinch-off is vital since it identifies the V_R voltage required to accumulate a reservoir of 2D holes under the Reservoir Top Gate. In this case we find that V_R should be set to less than -2.8V to accumulate a 2D Hole Gas (2DHG).

The next characterisation measurement is to determine the pinch-off characteristics of the Confinement gate (C-gate). In Figure 2.10(c) we present the pinch-off measurement of the C-gate. The main function of the C-gate is to isolate the sensor and quantum dot regions of the device, and to provide a confinement profile for the quantum dot. The complete pinch-off of the current by V_C=-0.75V demonstrates that the C-gate should be kept more positive than -0.75V during quantum dot experiments, in order to keep the sensor and reservoir 2DHG regions separated.

The final test for this configuration is investigating the pinch-off measurements of the four gates (G1, G2, G3, and G4). The aim of this test is to determine the functionality of each individual dot gate. Due to the size and shape of the C-gate it is necessary to bias the C-gate close to pinch-off, otherwise the current can run along the left edge of the C-gate, and cannot be pinched-off by gate G1 to G4. In Figure 2.10(d) we present typical pinch-off measurements for G1 and G4. The exact profile of each measurement is

strongly influenced by the C-gate voltage, however the key observation of Figure 2.10(d) is that a series of reproducible conductance oscillations, can be observed as a function of G1 and G4, typical of the formation of a large quantum dot, followed by saturation at around 200pA. The oscillations are reproducible as shown by the reverse direction sweep (dotted line in Figure 2.10(d). Measurements for G2 and G3 are qualitatively similar to that of G1 and G4. During these measurements one gate is swept, while all other gates are held at -3V, except the C-gate which is biased to -0.85V.

2.6.2 Characterising the charge sensor

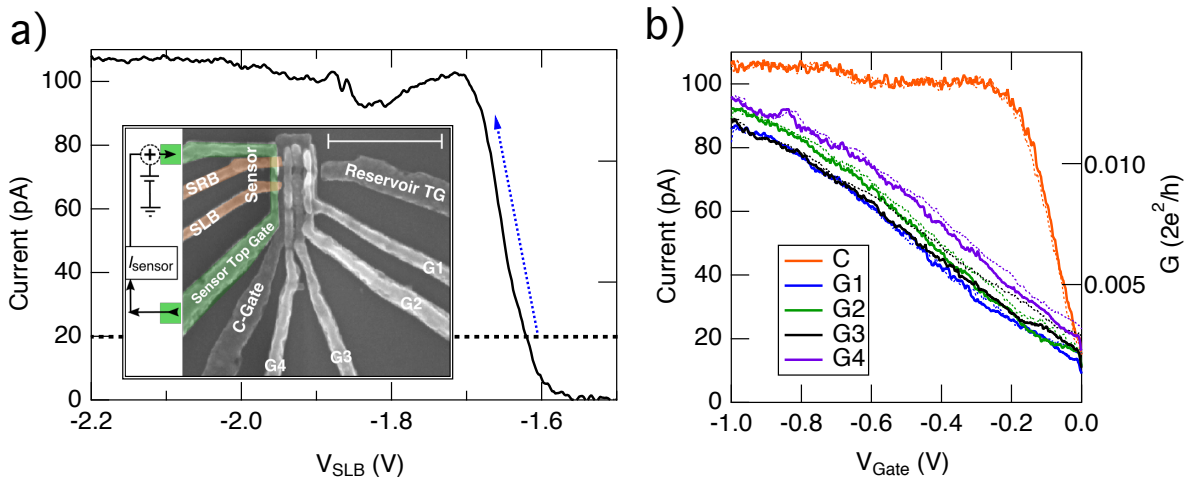

Figure 2.11: **Charge sensor characterisation: (a- inset)** Shows a SEM image with false colors highlighting the gates relevant to the charge sensor. Schematic on the left indicates the measurement of the sensor current, with an AC current being passed through the device between the two ohmic contacts, indicated as green squares. Scale bar is 500nm. **(a)** We show the pinch-off characteristics of the charge sensor as a function of V_{SLB}. Here ST and SRB are tuned to be fully accumulating, and all other gates are at 0V. The horizontal dashed line shows the initial I_{sensor} current used in (b). **(b)** We measure the sensor current when sweeping one gate from 0V to 1V while all other gates are held constant. As each gate is made more negative the sensor current increases, following the same trend as in (a), indicated by the blue dashed line in (a). The C-gate has the largest effect due to its size and proximity to the sensor. G1, G2, G3 and G4 have approximately the same coupling to the sensor. For this data V_{SLB} was set to -1.62V, and the sensor $V_{SD} = 100\mu$V AC. The right axis on each figure shows the conductance in units of $2e^2$/h (a and b have the same axis scale).

The next set of measurements demonstrate the typical operation characteristics of the charge sensor. In the inset of Figure 2.11(a) we present an SEM image of the device with the charge sensor gates highlighted in false color. A 100μV AC voltage is applied to the sensor source ohmic contact and the sensor source-drain current, I_{sensor}, is moni-

tored using standard lock-in techniques. In Figure 2.11(a) we present a typical pinch-off measurement of the sensor current, I_{sensor}, using the voltage applied to the Sensor Left Barrier (SLB).

Typically the optimal operation point of a charge sensor is defined by a particular sensor conductance (or current). Standard operation of a device will involve large voltage sweeps of multiple quantum dot gates. These gates will capacitively couple to the charge sensor, and can cause the sensitivity of the sensor to vary during the measurements. In order to compensate for this effect we calculate the cross capacitance between the Sensor Left Barrier and the relevant dot gates. We tune V_{SLB} to the pinch-off region indicated by the horizontal dashed line in Figure 2.11(a). We then individually sweep the voltage applied to gates C, G1, G2, G3, and G4, and measure the effect on the sensor current. An example of the effect of each gate on the sensor current is presented in Figure 2.11(b). We quantify the cross capacitance in terms of the ratio dV_{gate}/dV_{SLB}, as shown in the Table 2.6.2.

Gate	$\mathbf{dI}_{sensor}/\mathbf{dV}_{gate}$ (Ω^{-1} x10^{-10})	$\mathbf{dV}_{SLB}/\mathbf{dV}_{gate}$
SLB	13.3±0.02	1
C	4.86±0.03	0.365 ± 0.005
G1	0.871±0.003	0.065 ± 0.001
G2	0.865±0.012	0.065 ± 0.001
G3	0.763±0.013	0.057 ± 0.001
G4	0.930±0.012	0.070 ± 0.001

Table 2.1: **Transconductance of the sensor for various gates:** This table summarizes the effect of each gate on the sensor current. The measurement is for the sensor initially tuned to the base of the blue arrow in Figure 2.11 (a). The first column indicates the respective gate. The second column is the transconductance extracted from the linear region in Figure 2.11(a)-(b). The third column is the ratio between the SLB gate and the other respective gates. This ratio can be used to determine the compensation of V_{SLB} required when other gates are shifted.

2.6.3 Pulse bias measurement technique

Charge sensing measurements are performed by monitoring the transconductance of the charge sensor. We experimentally measure the transconductance using the pulse-bias

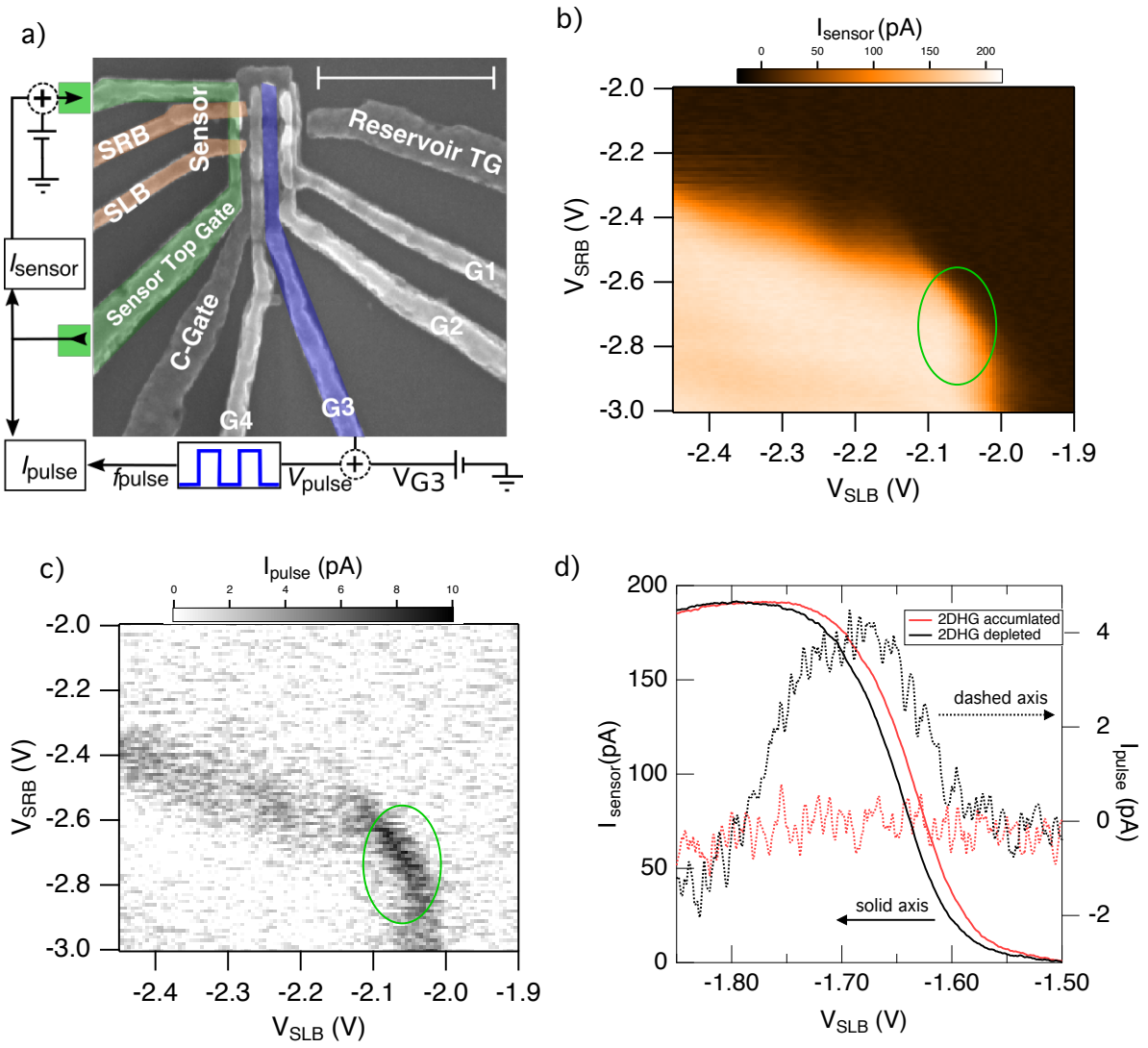

Figure 2.12: **Final characterisation measurements: (a)** A SEM image of a typical device with false colors highlighting the gates related to bias pulse charge sensing measurements. The sensor source-drain signal is measured using two lock-in amplifiers, giving the reading of I_{pulse} and I_{sensor}. A square pulse is added to the DC voltage applied to G3. **(b)** Pinch-off of the sensor current I_{sensor} as a function of the two sensor barrier gates SLB and SRB. **(c)** I_{pulse} measured simultaneously to the measurement in (b). A clear signal can be seen in I_{pulse} in regions where I_{sensor} is rapidly changing. This is indicated by the green ellipse, which is placed in the same location for (b) and (c). The strongest I_{pulse} signal occurs at V_{SLB} = -2.05 and V_{SRB} = -2.61V. **(d)** The Solid curves show the sensor current pinch-off when G3 is depleting (black) and accumulating (red) a 2DHG. The solid curves are measured on the left axis. The dashed curves show the I_{pulse} signal measured simultaneously to the corresponding I_{sensor} measurement (red or black).

measurement technique, which has been fully described in section 1.2.4. Figure 2.12(a) shows a SEM image of the device with gates relevant to charge sensing in false color A 1mV DC voltage and a 100μV AC voltage (f_{sensor} = 77Hz) is applied to the source ohmic. The sensor current, I_{sensor} is monitored using a lock-in referenced to f_{sensor}. To measure the transconductance a square pulse of amplitude V_{pulse} at frequency f_{pulse} is added to the DC voltage of G3. This square pulse modulates the DC sensor current at f_{sensor}. The modulation of the DC sensor current, which we call I_{pulse} is measured by a lock-in which has been reference to f_{pulse}. The signal I_{pulse} is proportional to the transconductance dI_{sensor}/dV_{G3} at a given V_{SLB}.

In Figure 2.12(b) we show the sensor current, I_{sensor}, with respect to the two barrier gates SLB and SRB. This shows a typical corner-corner plot with SLB and SRB able to pinch the current off. We note that it is possible to form a single quantum dot by fine tuning SLB, SRB and ST. However, unlike in n-type samples with the same lithography, the single dot formed in these sensors is not suitable for stable charge sensing. We have found that the single dot formed in the p-type charge sensor is not sensitive to the quantum dot gates G1, G2, G3, or G4. We suspect that in the the sensor dot is formed on either side of the SLB or SRB, and not in the middle as desired. It is likely that the pitch of the sensor barrier gates needs to be optimised for holes in p-type sensors[1].

Figure 2.12(c) shows the measurement of I_{pulse} taken simultaneously to the measurement of Figure 2.12(b). A clear signal in I_{pulse} can be observed at the regions of V_{SLB} and V_{SRB} where I_{sensor} is rapidly changing, indicated by the green ellipse in Figures 2.12(b-c). Evaluating the I_{pulse} signal in this way allows V_{SLB} and V_{SRB} to be tuned to the region of highest transconductance, which is where the sensor is most sensitive to the quantum dot charge state. In all measurements in this thesis chapter the sensor is operated in the region where I_{pulse} is largest.

The final characterisation measurement identifies the voltage ranges at which a 2DHG is formed under gates G1, G2, G3, and G4. This measurement is vital, since once the C-gate has separated the sensor and reservoir gates it is difficult to determine the voltages

[1]The pitch of the sensor SLB and SRB gates used here is identical to that used in n-type SET charge sensors. We suspect that the pitch may need to be adjusted slightly to optimize p-type SHT charge sensing [114].

required to accumulate holes into a quantum dot. In Figure 2.12(d) the solid black line shows the sensor current pinch-off as a function of V_{SLB}. In this measurement all gates G1, G2, G3 and G4 are biased at 0V. The black dashed line in Figure 2.12(d) is the simultaneous measurement of I_{pulse}. A distinct peak in I_{pulse} is observed on the region where I_{sensor} rapidly changes, since I_{pulse} is proportional to $\mathrm{d}I_{sensor}/\mathrm{d}V_{SLB}$.

We then bias G3 to -3V in order to accumulate a 2D Hole Gas (2DHG) below G3. The solid red curve in 2.12(d) shows the sensor pinch-off measured when G3 is -3V. The slope and saturation of the red and black solid curves are the same, with the only difference being the offset to more positive V_{SLB}. The key result can be seen in the measurement of I_{pulse} when V_{G3} has accumulated a 2D Hole Gas (2DHG). The dashed red line shows I_{pulse} measured simultaneously with the solid red data. Despite the similarity of the solid curves, the dashed red and black curves are distinctly different. The reason for the difference is due to the accumulation of the 2DHG. When the 2DHG is accumulated, the holes below G3 screen the square pulse applied to the gate. Thus, the I_{pulse} signal of transconductance is suppressed when a 2DHG is formed. This is a useful measurement for identifying and fine tuning the voltages at the final stages of tuning single lead quantum dot devices. This measurement can be repeated for all dot gates (G1-G4), providing valuable information for the approximate voltages to form a quantum dot. We have found that all gates accumulate at similar voltages, which are typically in the range of 1.5V and 2.5V.

2.7 Measurement of a single-hole quantum dot in the last hole regime

Figure 2.13(a) shows a schematic of the device, and Figure 2.13(b) shows a scanning electron microscope image of a nominally identical device to the one used in this study. This device features a planar hole quantum dot connected to a single reservoir (R) of two-dimensional (2D) holes, with an adjacent charge sensor (SHT). The number of holes on the dot N is controlled with the bias on gate G3, and the charge occupation in the

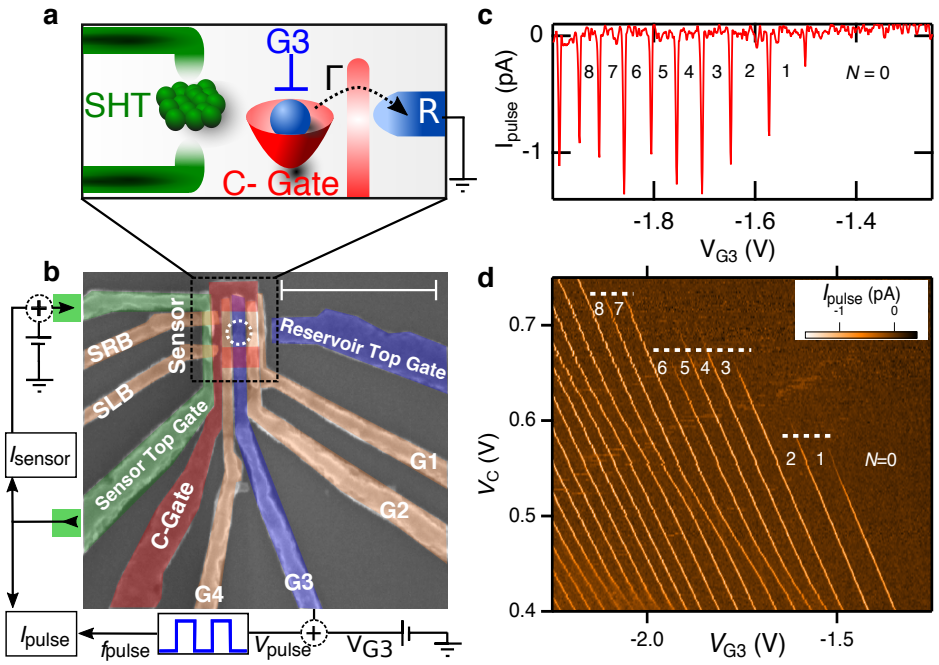

Figure 2.13: **Silicon quantum dot with charge sensor, capable of reaching the last hole:** (**a**) Schematic of the device concept. The device consists of a quantum dot coupled to a single reservoir (R), with an adjacent single hole transistor (SHT) charge sensor. The tunnel rate between the dot and reservoir (Γ) can be tuned using the C-gate voltage (V_{C}), and the dot occupation can be controlled with G3-gate voltage (V_{G3}). (**b**) False-colored scanning electron microscope image of an identical device, with the measurement schematic. The scale bar is 500nm. (**c**) Depletion of the last 10 holes in the quantum dot, showing the V_{pulse} induced signal on the charge sensor measured at $V_{\mathrm{C}} = 0.47$V. (**d**) Charge stability diagram, showing the number of holes on the dot as a function of the confining gate (C-gate) and pulse gate (G3) potentials. The horizontal white lines highlight the disappearance of the charge transition signals in distinct groupings, indicating shell filling (discussed further in Chapter 3). Measurements performed for $V_{\mathrm{pulse}} = 3$mV and $f_{\mathrm{pulse}} = 333$Hz. A slight bending in the lines in the vicinity of ($V_{\mathrm{G3}} = -2$V,$V_C = 0.55$V) is due to coupling to nearby confined charge. The specific gate voltages are V_R = -3.50V, V_{G1} = -3.50V, V_{G2} = -1.01V and $V_{\mathrm{G4}} = 0$V.

dot is monitored using an adjacent charge sensor. The dot-reservoir tunnel rate Γ can be tuned without significantly affecting the dot confinement shape using the bias applied to the C-gate. By measuring the charge occupation with a charge sensor we are able to study hole states even when the tunnel rate between the dot and reservoir is much smaller than can be detected in transport.

When operating the device, the reservoir top gate is negatively biased to accumulate a 2D hole system at the Si/SiO_2 interface below. The quantum dot is defined by positively biasing gates G1, G2, G4, and the C-gate (see caption). G3 acts as the dot plunger gate and is operated in the negatively biased regime. It is possible to operate this device in the double dot regime down to the (0,0) charge state, using gate G2 as the second dot's

plunger gate (in section 2.8 we present more data regarding the double dot configuration).

In order to observe the charge stability diagram for the holes in this quantum dot we employ a pulse-bias technique [38], which allows the charge occupation of the dot to be monitored using an adjacent single hole transistor (SHT) charge sensor. We apply a 1mV DC excitation to the SHT's source ohmic contact (top green square in Figure 2.13(b), and add a continuous square wave of magnitude V_{pulse} and frequency f_{pulse} to gate G3. The modulation of the DC sensor current by V_{pulse}, called I_{pulse}, is sensitive to $dQ_{\text{dot}}/dV_{\text{G3}}$ (as long as $\Gamma > 2f_{\text{pulse}}$). In Figure 2.13(c) we show a measurement of I_{pulse} as V_{G3} is swept. At specific values of V_{G3} a hole is able to tunnel on and off the dot during the positive/negative phase of V_{pulse}. This charge movement decreases the DC sensor current, causing a negative spike in I_{pulse} of width V_{pulse} in the V_{G3} scan. The measurement of Figure 2.13(c) was repeated over a range of V_{C} to produce the charge stability diagram in Figure 2.13(d). The identification of the last hole in the dot is confirmed by the absence of any additional charge transitions beyond the region labeled N=0 in Figure 2.13(d).

2.7.1 Tunnel rate independent measurements

The absolute hole occupation N presented in the previous section is inferred from measurements of I_{pulse} in Figure 2.13(d). However, I_{pulse} is sensitive to the dot tunnel rate Γ [38][1]. Therefor it is possible that additional charge transitions are present, however they remain undetected due to the long tunnel time compared to the pulse frequency f_{pulse}. The sensor conductance, measured via I_{sensor}, is sensitive to the quantum dot charge occupation and is independent of the dot tunnel rate. In this section we present measurements of I_{sensor} allowing confirmation of the absolute hole occupation in a manner that is not limited by tunnel rates.

In Figure 2.14(a) we present a charge stability diagram obtained by measuring I_{pulse} while sweeping V_{G3} and V_{C}. Horizontal dashed lines indicate the values of V_{C} where $\Gamma \sim 2f_{\text{pulse}}$.

[1] If the tunnel time $1/\Gamma$ is longer than $1/2f_{\text{pulse}}$ then hole will not load/unload over the period of the square pulse. Therefore the visibility of the charge transition can be lost as a function of tunnel rate. We note that the tunnel rate between the dot and the reservoir can be controlled using V_C.

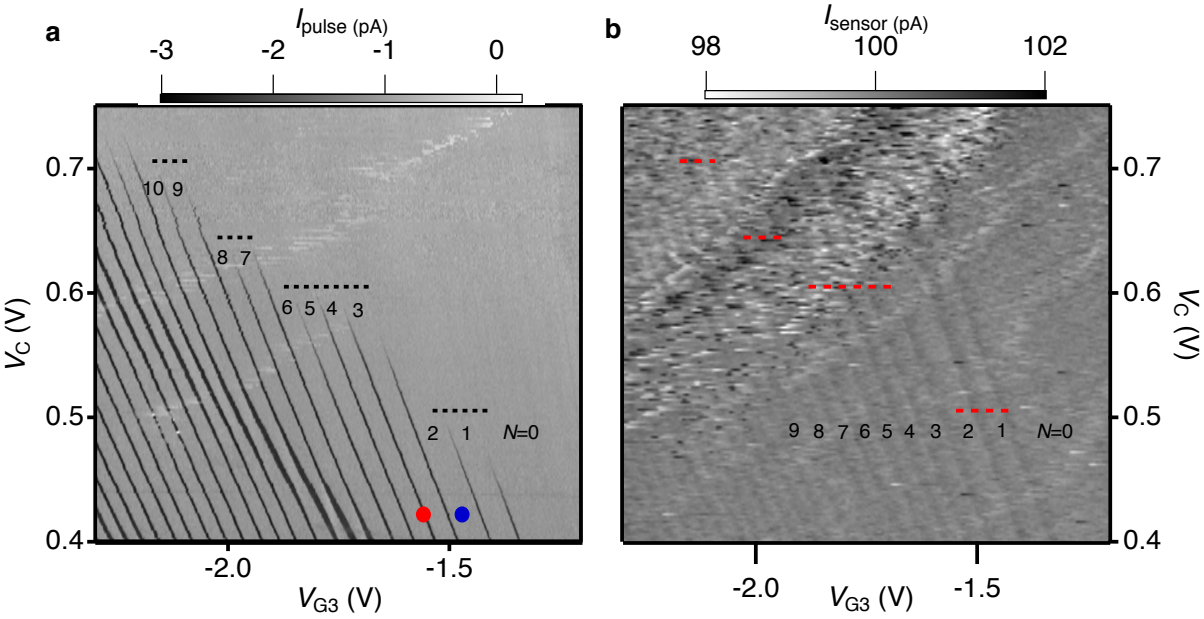

Figure 2.14: **Tunnel rate independent measurements of hole occupation:** (**a**) I_{pulse} charge stability diagram over a larger range than in Figure 2.13(d). The horizontal black lines highlight the disappearance of the charge transition signals, which occurs as V_{C} become more positive causing the tunnel rate for to become much less than f_{pulse} = 333Hz. The red and blue circle represent the device configuration for the red and blue data in Figure 2.15(a). (**b**) Measurement of I_{sensor} obtained simultaneously to the data presented in (a). I_{sensor} is monitored by adding a 50μV AC 77Hz excitation to the sensor source ohmic contact. Horizontal red lines are drawn at the same V_{C} and V_{G3} as the black dashed lines in **a**, highlighting that the I_{sensor} charge transitions are visible well beyond the V_{C} when the I_{pulse} charge transition signals are no longer visible. For both Figures **a** and **b** the experimental parameters are the same as Figure 2.13(d), except V_{G2} = -1.0V. The difference in V_{G2} explains the difference in the position of the black dashed lines between this Figure and the white dashed lines in Figure 2.13(d).

In addition to measuring I_{pulse}, we simultaneously monitor the sensor conductance using a standard lock-in measurement. In Figure 2.14(b) we show the measurement of I_{sensor} obtained simultaneously to the measurement of I_{pulse}. We observe charge transitions in I_{sensor}, which correspond to the same charge transition signals in Figure 2.14(a). In Figure 2.14(b) horizontal lines are drawn at the same values of V_{C} and V_{G3} as in Figure 2.14(a). Each charge transition signal in I_{sensor} continues well beyond the V_{C} at which the corresponding I_{pulse} charge transition is no longer visible. This demonstrates that I_{sensor} is sensitive to charge transitions that have very low tunnel rates. We see no additional charge transitions in I_{sensor} beyond the last transition providing further evidence that the device is operating down to the last hole.

2.7.2 Control of tunnel rates

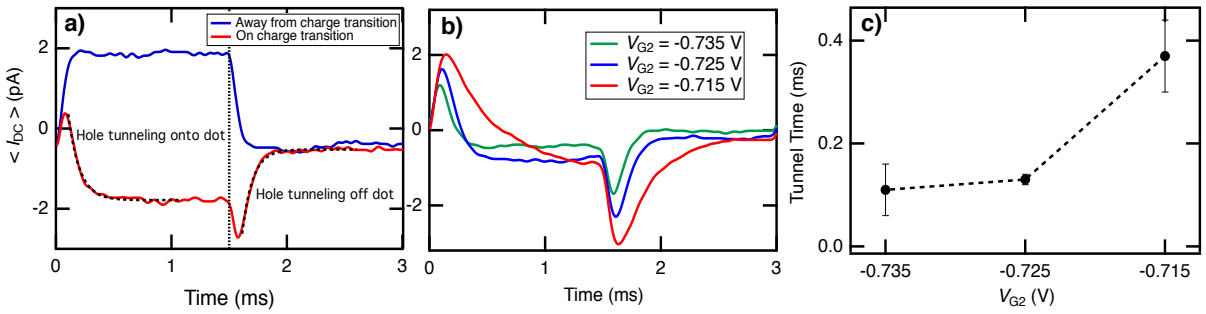

Figure 2.15: **Control of the dot-to-reservoir tunnel rate:** (**a**) $\langle I_{\mathrm{DC}} \rangle$ measured as a function of time while a 3ms square pulse is applied to G3 (V_{pulse} = 3mV). The vertical dotted line separates the x-axis into the load phase (0-1.5ms) of the square pulse and the empty phase (1.5-3ms)of the square pulse. The blue and red lines are measurements when the device is in the configuration shown by the blue and red circles in Figure 2.14(a). The black dashed lines are an exponential fit to the decay of the $\langle I_{\mathrm{DC}} \rangle$ signal. (**b**) $\langle I_{\mathrm{DC}} \rangle$ for progressively more negative V_{G2}, where V_{G2} controls the coupling between the dot and the reservoir. (**c**) The hole tunnel time as extracted from an exponential fit to the decay in $\langle I_{\mathrm{DC}} \rangle$ for each trace in **b**. The error bars are extracted from the standard deviation of the fit to the exponential decay (600 data points).

In this section we demonstrate control of the dot tunnel rate Γ. Figure 2.15(a) compares the DC sensor signal when the device is at a charge transition (red) and away from a charge transition (blue). In Figure 2.15(a) the y-axis is the average DC sensor signal $\langle I_{\mathrm{DC}} \rangle$, which is plotted as a function of time. To obtain $\langle I_{\mathrm{DC}} \rangle$ we perform 1024 single shot measurements over a 3ms square wave, which is applied to G3. $\langle I_{\mathrm{DC}} \rangle$ is the time resolved average of all 1024 single shot measurements. The blue data in Figure 2.15(a) is a measurement of $\langle I_{\mathrm{DC}} \rangle$ when the dot is far away from a charge transition (indicated by the blue circle in Figure 2.14(a). $\langle I_{\mathrm{DC}} \rangle$ follows the shape of the square wave due to capacitive coupling of the sensor conductance to the load and empty phase of the square pulse. The red data in Figure 2.15(a) is the same measurement of $\langle I_{\mathrm{DC}} \rangle$, however the dot is now tuned to be at a charge transition (indicated by the red circle in Figure 2.14(b).

In the load phase, where the square pulse is in the negative phase, $\langle I_{\mathrm{DC}} \rangle$ initially increases as the sensor conductance follows the capacitive coupling. However, when a hole tunnels onto the dot, the additional positive charge causes an exponential decay in $\langle I_{\mathrm{DC}} \rangle$. In the empty phase, where the square pulse is in the positive phase, the reverse of this process occurs. $\langle I_{\mathrm{DC}} \rangle$ exponentially decays due to holes tunneling out from the dot, reducing the positive charge and returning $\langle I_{\mathrm{DC}} \rangle$ to the non-transition value. The width of the

exponential decay in $\langle I_{\mathrm{DC}} \rangle$ results from the average tunnel time of holes over the 1024 single shot measurements.

In Figure 2.15(b) we demonstrate control of the tunnel rate by presenting measurements of $\langle I_{\mathrm{DC}} \rangle$ at three different V_{G2}. As V_{G2} is made more negative the tunnel barrier height between the dot and reservoir is decreased, causing a decrease in the dot to reservoir tunnel time. We extract the tunnel time by fitting an exponential function to the decay in $\langle I_{\mathrm{DC}} \rangle$. In Figure 2.15(c) we plot the extracted tunnel time for V_{G2} = -0.715 V, -0.725 V and -0.735 V, which is found to be 0.37±0.07 ms, 0.13±0.01 ms and 0.11±0.05 ms respectively. This shows the device is tunable and behaves as expected.

2.8 Double quantum dot in the last hole regime

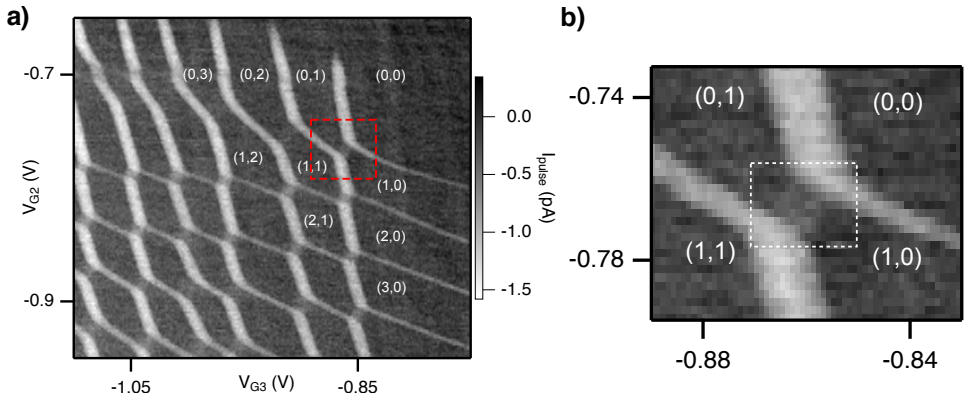

Figure 2.16: **Operation of device as a double quantum dot: (a)** I_{pulse} double dot charge stability diagram for V_{G3} and V_{G2} (V_{pulse} = 10mV, f_{pulse} = 333Hz). White text shows the hole occupation (N_{G2},N_{G3}). **(b)** Zoom- in of the (0,1) to (1,0) charge transition highlighted by the red dashed box in (a). A weak inter-dot signal is visible connecting the two anti-crossed charge transitions, as indicated by the dashed white rectangle.

When V_{G2} is made sufficiently negative G2 no longer behaves as a tunnel barrier, but begins to act as an accumulation gate. In Figure 2.16(a) we show a measurement of I_{pulse} as a function of V_{G2} and V_{G3}. We observe a honeycomb pattern consistent with a double dot charge stability diagram. The absolute hole occupation (N_{G2},N_{G3}), of the double dot can be assigned since we see no additional charge transitions in I_{pulse} or I_{sensor} beyond the region labeled (0,0). The magnitude of the I_{pulse} signal for the G2 dot charge transitions (horizontal lines of the 'honey-comb' pattern) is less than the magnitude of

the I_{pulse} signal for G3 dot charge transitions[1]. This is because G2 is further from the sensor, causing the G2 dot to have a weaker capacitive coupling to the sensor. Finally, in Figure 2.16(b) we show the (0,1) to (1,0) charge transition region. We observed a weak signal in I_{pulse} along the axis between the (0,1) and (1,0) region. This weak signal results from inter-dot charge transitions induced by the square wave. Inter-dot transitions can be seen for many transitions in Figure 2.16(b). These results highlight the full tunability of the the device, in addition to the remarkable electrical stability for a p-type quantum dot[2].

2.8.1 Tuning tunnel rates in the double dot configuration

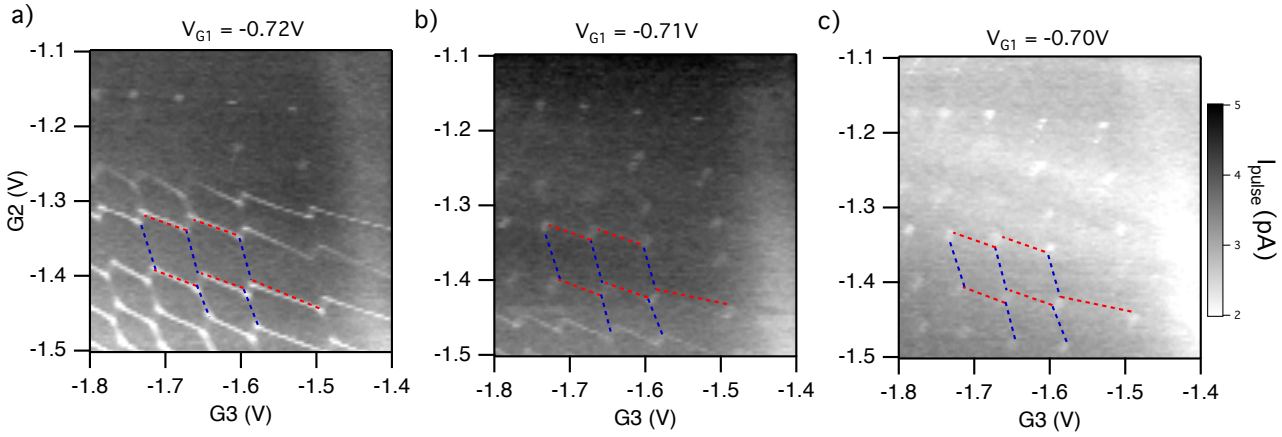

Figure 2.17: **Control of tunnel barrier in double dot regime:** Charge stability diagram when the device is tuned to have a double dot under G2 (y-axis) and G3(x-axis). We present measurements for three different tunneling barrier configurations **(a)** V_{G1} = -0.72, **(b)** V_{G1} = -0.71, and **(c)** V_{G1} = -0.70. In all three figures the red and blue dashed lines highlight the equivalent transitions for reference. This demonstrates the effects of the tunnel barrier, G1, on the inter-dot and charge transition signals.

We now investigate the way the double dot is influenced by changing the tunnel barrier between the dots and the lead. The device has a single reservoir of holes, and the tunnel rate can be controlled by varying V_{G1}. However, the plunger gates for the double dot, G2 and G3, also influence the tunnel rate. In Figure 2.17 the double dot charge stability diagram is presented for three different tunnel barrier tunneling rates. In Figure 2.17(a) when V_{G1} = -0.72V a clear honeycomb structure can be observed, and part of

[1]Notice that the horizontal lines have a weaker amplitude than the vertical lines.

[2]The measurement in Figure 2.16 took approximately 4 hours, and is reproducible over a period of several days.

the structure is highlighted by the red and blue dashed lines. However, in Figure 2.17(a) when V_{G2} > -1.3V (top of image) the charge transition lines become less visible. In contrast the inter-dot signals can be clearly observed even up to V_{G2} = -1.15V. To configure a more opaque tunneling barrier we set V_{G1} = -0.71V and present the stability in Figure 2.17(b). For V_{G1} = -0.71V the charge transition lines can be only observed for V_{G2} <-1.15V. However, the remaining inter-dot signals can clearly be observed. We highlight this by including the red and blue dashed lines on the same transitions as presented in Figure 2.17(a).

Finally, in Figure 2.17(c) we present the double dot stability diagram for V_{G1} = -0.70V. As the tunnel barrier finally becomes too opaque to allow charge transitions at f_{pulse}, however all inter-dot transitions can clearly be observed[1]. We show red and blue dashed lines to demonstrate the honeycomb pattern connecting the inter-dot signals of the double dot. In Figures 2.17 we have not presented the absolute charge occupation, as we have in Figure 2.16. The reason for this is that as V_{G1} is made more positive, an accidental quantum dot forms close to G1, making the absolute charge occupation unclear.

2.9 Conclusion and outlook of Chapter Two

Chapter Two first presents a literature review of silicon MOS quantum dots. This highlights that a fundamental gap has been the inability to form a hole quantum dot where the absolute charge occupation is known. Within this chapter we have presented results of a single and double quantum dot operated down to the last hole regime. In addition to presenting a full electrical characterisation, we demonstrate the tunability of this device by showing control of the tunnel rates for both configurations.

These results present a significant step forward for p-MOS technology. In particular, it would now be possible to perform spectroscopic measurements in a charge configuration that can be reproduced across different devices. This reproducibility is not possible unless the absolute charge occupation is known. Future measurements of interest would

[1]Inter-dot tunnel rates are typically several orders of magnitude larger than dot-to-reservoir tunnel rates [115].

include performing artificial atom type measurements [9], such as observing the hole spin filling and the orbital structure of holes confined in these devices. These results are valuable for assessing the suitability of p-MOS devices for spin based applications.

As a final note we discuss the novelty of these devices. Traditional artificial atom devices have been made using l=0 and s=1/2 ($J = 1/2$) electrons, just like conventional atoms. Here we use l=1 and s=1/2 ($J = 3/2$) electrons (holes) to make an artificial atoms. This can lead to a complex and rich array of spin-orbit properties for hole based artificial atoms. These properties have not been studied in great detail, and p-type artificial atoms provide a valuable opportunity to isolate a single hole for experimental study. These hole-based artificial atoms have potential for alternative ways to perform spin manipulation (using electric fields, rather than magnetic fields [60]), and could potentially exhibit complex spin states as holes fill into the higher orbital of the artificial atom.

Chapter 3

Spectroscopy of single hole quantum dots in silicon MOS structures

Abstract

In this chapter we perform the first spectroscopic measurements of a planar silicon Metal Oxide Semiconductor (MOS) based single hole quantum dot operating in the last hole regime. The spin shell filling sequence is characterised for the first six holes using magneto-spectroscopy, and is consistent with the Fock-Darwin states of a circular two-dimensional quantum dot. At low magnetic field we observe spin filling, which obeys Hund's first rule, while at high magnetic field we observe the singlet triplet transition for the two hole ground state. Finally, we investigate the orbital spectrum using pulse bias spectroscopy and find that hole-hole interaction energy is 90% of the orbital energy. These results provide experimental evidence of the orbital spin physics for silicon surface-gated artificial atoms operating in the last hole regime.

Publication

The results presented in this chapter appear in the article and supplementary material of: Liles, S. D., Li, R., Yang, C. H., Hudson, F. E., Veldhorst, M., Dzurak, A. S., and

Hamilton, A. R. (2018). Spin and orbital structure of the first six holes in a silicon metal-oxide-semiconductor quantum dot. Nature communications, 9(1), 3255.

3.1 Chapter introduction

The majority of research into spin-qubits has focused on electron spins [6, 18, 30]. However, hole spins confined in silicon MOS quantum dots are an gaining attention as an attractive candidate for spin based electronic applications [78, 79]. The valley degeneracy of silicon leads to complex valley-orbit states in electron spin-qubits, which complicates the spin dynamics of these systems and requires some engineering to overcome [19, 75, 116]. Holes, on the other hand, occupy the valence band, which has no valley degeneracy, simplifying the energy states. In addition, the 2D confinement of MOS quantum dots lifts the heavy-hole light-hole degeneracy, leaving heavy hole states as the ground state [51]. In this case it would be expected that the orbital spectrum of holes in silicon MOS quantum dots follows the well defined Fock-Darwin structure, and that the single hole ground state is a well defined spin doublet, similar to the ground state of electrons in well defined GaAs MOS quantum dots [1, 9]. However, challenges in fabrication of hole quantum dots have limited the number of studies of hole quantum dots, and to date, there has been no investigation of the spin and orbital structure of the first few holes in silicon planar quantum dots.

Recent experimental work studying hole spin manipulation in nanowire [20] and self assembled [23] quantum dots has demonstrated extremely fast all electric hole-spin manipulation rates of up to 150MHz. This is significantly faster than spin manipulation times of equivalent electron spin qubits[1], and demonstrates the high potential of holes for spin qubit applications. However, these hole-spin manipulation experiments also demonstrated unexpectedly short spin coherence times, on the order of several hundred nanoseconds. Since these experiments are performed in the few hole regime, the exact state that is being manipulated is unknown, and determining the exact relaxation mech-

[1]Electron spins states driven by ESR have manipulation rates measured up to 0.5MHz [17, 55], and electron spins driven by EDSR (using a micro-magnet) have manipulation rates up to 30MHz [74].

anisms is difficult. Experiments studying the spin properties of electrons have shown that the orbital structure and energy spectrum of the host quantum dot play a significant role in determining spin lifetimes [6, 30, 49, 117]. Often is is possible to improve spin lifetimes by orders of magnitude when details of the orbital and spin structure are well characterised [44, 75]. This demonstrates the need to perform detailed spectroscopic measurements of hole based quantum dots.

In Chapter 2 we demonstrated a single quantum dot operating down to the last hole. Since the absolute charge occupation is known, this makes it possible to perform spectroscopic measurements of a hole quantum dot in a known and reproducible state. In this chapter we present the first spectroscopic measurements of a single hole silicon MOS quantum dot. We observe clear evidence of orbital shell structure in the addition energy and the tunnel rates. Magneto-spectroscopy studies show magic number shell filling consistent with the Fock-Darwin states of a circular two-dimensional quantum dot, with the spin filling sequence of the first six holes consistent with Hund's rule. Next, we use pulse bias spectroscopy to determine that the orbital spectrum is heavily influenced by the strong hole-hole interactions. These results provide a path towards scalable silicon hole-spin qubits.

3.2 Literature review - Spectroscopy measurements of single quantum dots

Semiconductor quantum dots are an exciting candidate for developing new and novel quantum devices. However, in order to fully develop quantum dot devices, it is necessary to gain a full understanding of the underlying physics. Spectroscopic measurements provide valuable information about the energy spectrum and spin-physics. In this literature review we demonstrate examples of spectroscopic measurements in quantum dot devices[1]. In section 3.2.1 we selectively discus several experiments performed using elec-

[1]Particularly we will discus characterisation of the excited state spectrum (see section 1.2.3 and 1.1.3) and the spin filling sequence (see section 1.3.2).

tron based quantum dots[1]. Following this, in section 3.2.2 we review the progress of spectroscopy experiments performed in hole based quantum dots. Hole based quantum dots typically exhibit non-trivial spin and orbital effects, and in this review we have grouped experiments based on the material system. The literature review concludes by highlighting that detailed measurements of the spin and orbital structures are necessary to determine the suitability of hole spins for spin-based semiconductor technology.

3.2.1 Spectroscopy measurements of electron quantum dots

The discrete energy spectrum fundamentally defines the behavior of each quantum electronic device. Experiments characterising the orbital shell structure and spin filling sequence are therefore vital as an initial characterisation measurement of quantum dots. As one of the earliest examples, Tarucha *et al.* [9] have studied GaAs quantum dots and demonstrated the electrons filling into Fock-Darwin orbital shells, with spin filling consistent with Hund's rules. Similar experiments performed by Lim *et al.* [98] using MOS silicon quantum dots have demonstrated the valley-orbit states of electrons in MOS silicon quantum dots. These characterisation measurements are most valuable when performed in devices where the absolute charge occupation is known. This allows results to be reproduced and compared in different devices and by different research groups. The characterisation of orbital shells and spin filling is the foundation by which quantum dot physics can be understood, and different quantum dot device structures can be compared.

Spectroscopy for developing new technology

With a clear understanding of the energy structure of a quantum dot, its possible to determine ways in which the device can be implemented in new technology. An example of a novel spintronic device made possible through spectroscopic analysis is the quantum dot bipolar spin filter. In 2000 Recher *et al.* [118] proposed that the discrete spin resolved energy levels of a quantum dot could be tuned to produce a fully polarized spin current. Hanson *et al.* [47] used a lateral GaAs quantum dot to experimentally realize

[1]These experiments are discussed to demonstrate several key points, and not as a full literature review of electron spectroscopy measurements.

this proposal. In Figure 3.1(d) we show the source-drain bias spectroscopy measurement performed by Hanson *et al.* of the lateral GaAs single quantum dot. This measurement was performed with a 12T magnetic field applied, splitting the spin up and down energy states. The schematic in Figures 3.1(a-c) shows the energy levels of the spin split ground state at the positions labeled 'a', 'b' and 'c' in Figure 3.1(d). In the region labeled 'I' of Figure 3.1(d) the only state available for transport is the spin up state. Hence, in this region the device will act as a spin filter, transmitting only spin up electrons. The device can be moved out of the spin filter regime using only electric fields to shift into location 'b' (using V_G) or to the location 'c' (using V_{SD}).

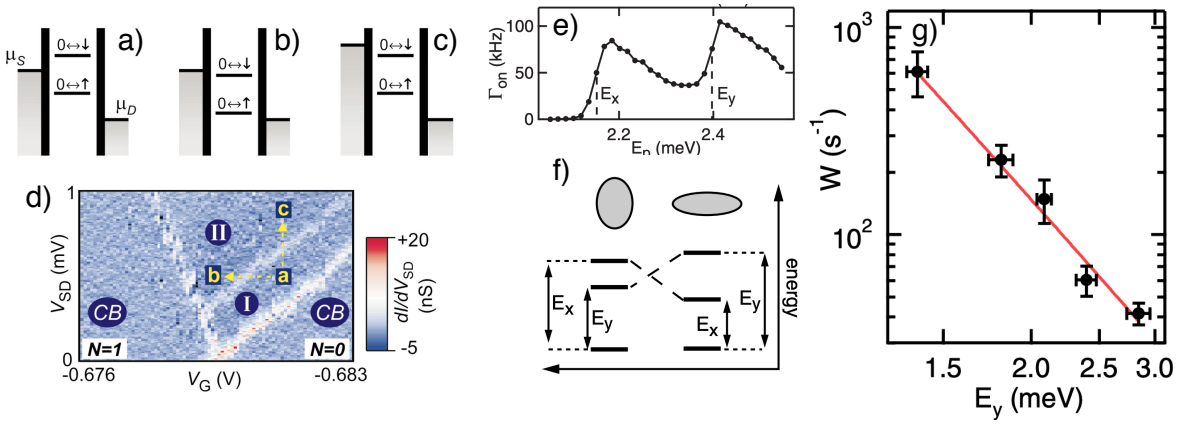

Figure 3.1: **GaAs examples of novel spectroscopy results:** (**a-c**) Energy level diagrams for the spin split ground state of a single electron GaAs quantum dot. Level alignment corresponds to the energy spectrum at the position labeled 'a', 'b' and 'c' in (d). (**d**) Source-drain bias spectroscopy measurement of the N=0 to N=1 transition. 'CB' labels the regions of Coulomb Blockade. (a)-(d) are reproduced from [47]. (**e**) Pulse bias spectroscopy measurement allowing the calculation of the excited state energies E_x and E_y by Amasha *et al.* [44]. The y-axis is the dot tunnel rate, which is enhanced when an excited state is energetically available. (**f**) Schematic of the excited state energies for two different confinement profiles. Left shows a vertically elongated dot where $E_x > E_y$. Electric fields can squeeze the dot confinement into the horizontally elongated configuration where $E_x < E_y$. (**g**) The spin relaxation rate, W, measured for different E_y (where E_y is the closest excited state to the ground state, ie $E_x > E_y$). The spin relaxation rate decreases as the splitting between the ground state and the y-excited state increases. (e)-(g) are reproduced from [47].

Spectroscopy for optimizing spin-qubits

Quantum dots receive considerable and ongoing research interest for their use in quantum information technology. Particularly since quantum dots are an ideal system to host a semiconductor based spin-qubit. In order to optimize qubit operation the key physical parameters should be accurately known, including the internal Hamiltonian, the presence of additional states, and the coupling of the qubit with external electric

and magnetic fields. This information provides the ability to determine the suitability of a qubit system, it gives insight into ways the qubit can be controlled, and allows accurate calculations of qubit dephasing and state leakage. We now discus the importance that spectroscopic measurements have for characterising and optimizing the functionality of quantum dots towards spin qubit technology.

Quantum dots based on GaAs/AlGaAs MOS quantum dots initially emerged as a leading system for spin based quantum computation [18, 30]. In 2008 Amasha *et al.* [44] studied a GaAs lateral quantum dot with tunable orbital confinement. Figure 3.1(e) shows the spectroscopy measurements that allowed Amasha *et al.* to determine the excited state energy spectrum of the device. Figure 3.1(f) shows a schematic of the results, where tuning the gate voltages allows in-situ control of the confinement shape, thereby influencing the excited state (E_x and E_y) energy levels. In these devices, spin relaxation is mediated by spin-orbit coupling, which couples the ground state with the excited states E_x and E_y [119]. Control of the excited state energy affects the coupling between the spin and orbital states, allowing in-situ control of the spin relaxation rate. Figure 3.1(g) demonstrates that characterisation of the excited state spectrum can allow experimental control of the spin relaxation rate by over an order of magnitude.

Silicon based MOS quantum dots are now a leading candidate for spin based quantum information applications [6]. However, the valley degree of freedom introduces complex non trivial physics related to spin qubits [116]. Therefore, spectroscopic measurements that characterise the valley states of silicon quantum dots are valuable. For example, the presence of valley degeneracy can greatly complicate the operation of silicon based qubits [116]. In 2013 Yang *et al.* [75] studied the valley states in a silicon MOS quantum dot. Figure 3.2(a) shows the measured valley splitting on the y-axis as a function of the applied electric field on the x-axis. These results presented in Figure 3.2(a) demonstrate electric control of the valley states.

The magnitude of the valley splitting is shown by Yang *et al.* [75] to have significant consequences on the spin relaxation rate. Figure 3.2(b) shows the spin-valley energy levels as a function of magnetic field. Critically, when the valley splitting (E_{VS}) matches the Zeeman energy (E_Z), the $\nu+$ and $\nu-$ valleys anti-cross. Figure 3.2(c) shows the spin

relaxation rate measured for two different valley splitting energies E_{VS} (green and red). If $E_{VS} > E_Z$ for all magnetic fields, then the spin relaxation follows a B^5 dependency (green data), and the valleys do not anti-cross in the measured range of magnetic field. However, if the E_{VS} is tuned such that $E_{VS} = E_Z$ at some magnetic field, then a distinct enhancement in the spin relaxation rate can be observed (red data, $E_{VS} = E_Z$ at 2.8T). The enhancement, or so called 'hot spot' was an unexpected and unpredicted [75, 80, 120] feature.

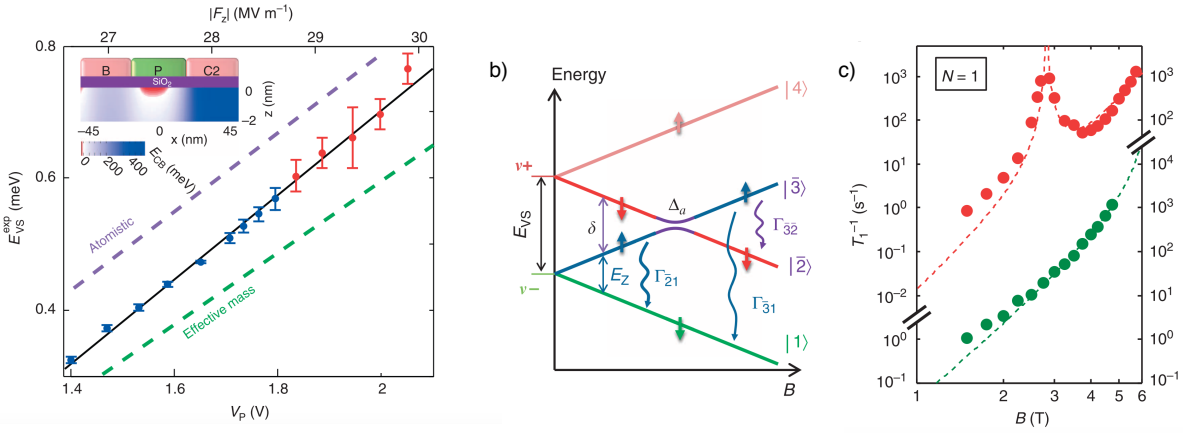

Figure 3.2: **Spin-valley lifetimes in silicon quantum dots:** (**a**) Valley splitting measured as a function of plunger gate voltage V_p (top axis is the calculated magnitude of the interface vertical electric field for a given V_p). Red and blue circles are the measured valley splitting, while the green and purple are the valley splitting calculated using the effective mass and atomistic methods respectively. Top inset shows a schematic of the device and a simulation of the dot location. The dot is formed in the red region, underneath the plunger gate (P), and confined by the gates C2 and B. (**b**) Energy diagram of the single electron spin-valley states as a function of magnetic field. $\nu+$ and $\nu-$ are the two valley states, which anti-cross where the valley splitting is equal to the Zeeman energy. Colored arrows indicate the spin projection of each level, and curved vertical arrows indicate potential relaxation paths. (**c**) Spin relaxation rate as a function of magnetic field for two different E_{VS}. Green is for the case that E_{VS}<E_Z for all magnetic fields. Red is for the case that E_{VS}=E_Z at 2.8T, where a hot spot in the relaxation is observed at the valley crossing. Note the different y-axes scales for the red and green data. Reproduced from [75].

Conclusion of electron spectroscopy

These examples demonstrate the necessity of fully characterising the energy spectrum of quantum electronic systems. In the case of Hanson *et al.* [47] the excited state spectrum provided access to a novel operation mode as a spin filter. The detailed analysis of the excited states and valley states provided insight into the underlying spin physics of the devices studied by Amasha *et al.* [44] and Yang *et al.* [75]. Without this detailed understanding variations in spin lifetimes over the order of several magnitudes could

remain unclear.

3.2.2 Spectroscopy measurements of hole quantum dots

We now focus on measurements studying the energy spectrum and spin states of holes in quantum dots. This results are grouped together based on similar materials and device structures. For each material system we highlight the key results from hole spectroscopy measurements. The focus here is to highlight that holes typically exhibit non-trivial spin and orbital physics. It has not been standard to observe the well defined Fock-Darwin spectrum in hole quantum dot devices.

Holes in InAs quantum dots

One of the earliest electrical studies showing shell filling of holes was performed by Reuter *et al.* [103] in 2005. The device studied by Reuter *et al.* was an InAs self-assembled quantum dot. Reuter *et al.* observed low bias Coulomb blockade down to the last hole, then investigated the evolution of the Coulomb peaks under a magnetic field up to 32T in order to determine the shell structure. Figure 3.3(b) shows the Coulomb peaks as a function of magnetic field with the spin and shell filling indicated in the corresponding insets. The insets on the left indicate the ground state shell filling at 0T, while the insets on the right indicate the filling a 32T. The interesting result is that the N=6 ground state is fully polarized at zero magnetic field, with a half filled p orbital shell and a partially filled d orbital shell (s,s,p,p,d,d). This is distinctly different to electrons in InAs or GaAs quantum dots, which exhibit an unpolarized (s,s,p,p,p,p) N=6 ground state at B=0T. Above 14T the shell filling in Figure 3.3(a) sequence changes due to a crossing of the single particle energy levels.

The shell filling of holes observed by Reuter *et al.* [103] deviates from the expected single particle shell filling sequence, where the s, p and d shells fill in order. The explanation for this anomalous result is due to the enhanced Coulomb interaction experienced by holes in InAs quantum dots. Due to the larger effective mass of holes than electrons in InAs, spatial confinement of holes must be stronger than for electron quantum dots. This results in stronger hole-hole Coulomb interaction, decreasing the ratio between the

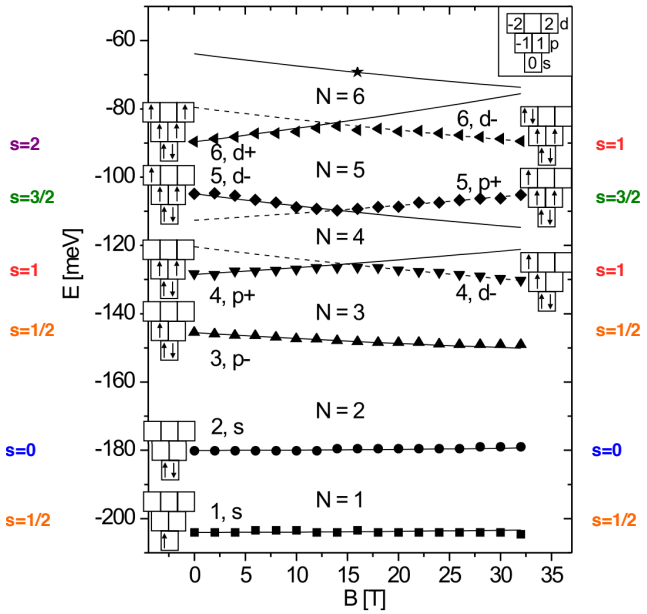

Figure 3.3: **Spin and shell filing of holes in an InAs quantum dot:** The energetic positions of the Coulomb peaks measured by Reuter *et al.* [103]. N is the total number of holes on the quantum dot, and the insets show the occupation of holes into the single particle energy levels before (left) and after (right) the crossing. Colored text indicates the total spin of the quantum dot for low magnetic field (left) and high magnetic field (right).

Coulomb energy and the quantization energy scale. The fifth and sixth holes fill into the d orbital since the strong interaction between tightly confined holes makes the higher momentum d orbital energetically favorable to the half filled p orbital (where the hole wavefunction overlap would be larger).

Holes in GaAs quantum dots

The low disorder and well developed nano-fabrication techniques for GaAs quantum devices allowed extremely well defined electron quantum dots with clear orbital shell structure [1, 9]. Single hole transistors based on GaAs MOS structures have been studied by Klochan *et al.* [121] and Tracy *et al.* [102]. Despite both devices showing excited states in the few hole [121], and the last hole [102] regimes neither works reported observations of Zeeman splitting of the single particle states, which is required to perform magneto-spectroscopy and characterise the spin states.

Wang *et al.* [108] improved on the GaAs MOS design of Klochan *et al.* [121] and studied a well defined single hole dot in GaAs with clear excited states. The evolution of the devices is shown in Figure 3.4(a). Figure 3.4(b) shows the source-drain bias spectroscopy

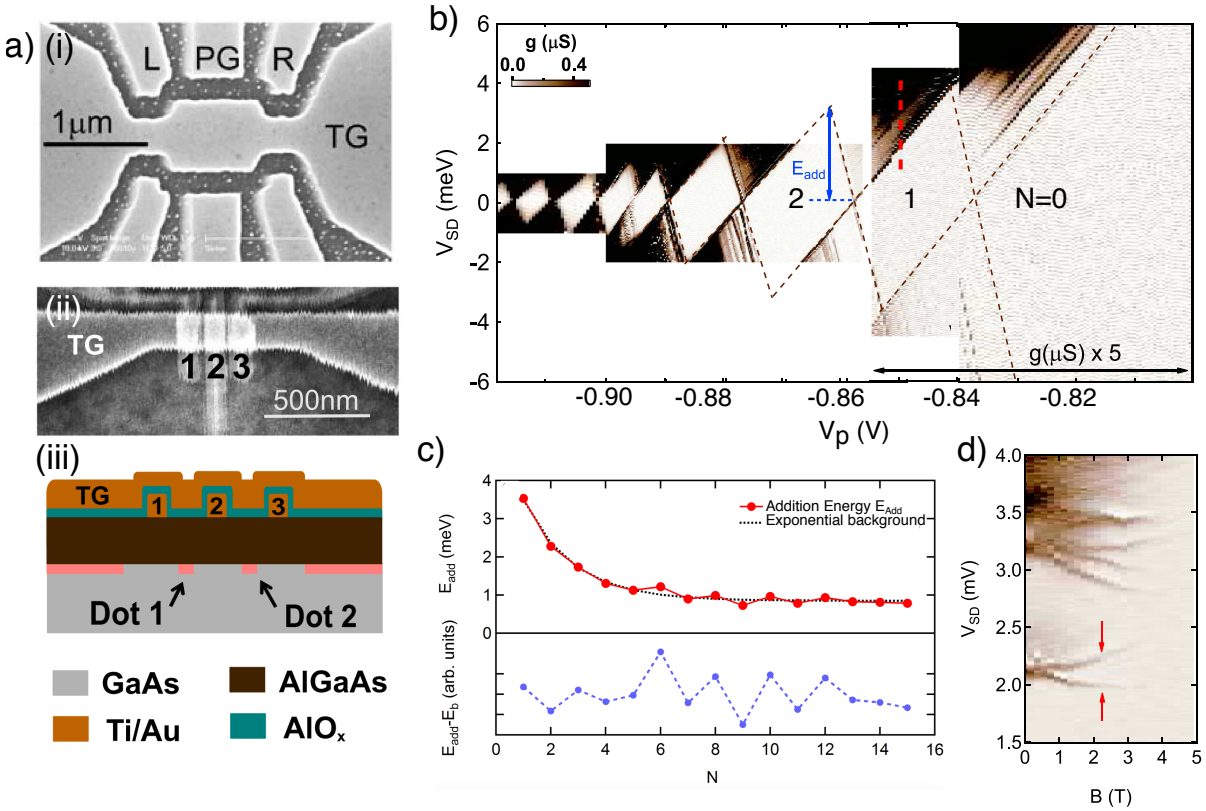

Figure 3.4: **Spin and shell filling of holes in GaAs:** (**a**) Evolution of GaAs hole devices in Hamilton research ground at UNSW. (i) shows SEM of the device studied by Klochan *et al.* [121]. This device includes a single Top Gate (TG) accumulating holes in both the quantum dot and the source and drain regions. Side gates L, PG, and R tune the quantum dot. (ii) Shows a SEM image of the device studied by Wang *et al.* [108]. This device improves on the previous design by including a double layer structure, where depletion gates sit below the accumulating top gate. (iii) Shows a schematic of the double layer device. (**b**) Source-drain bias spectroscopy measurement of a GaAs MOS quantum dot studied by Wang *et al.* [108]. It is likely that all holes are depleted for V_p > -0.83 due to the open Coulomb diamond. (**c**) Top figure shows the raw addition energy measured from (b) in red and an exponential fit to the decay in black. Bottom Figure in blue shows the difference between the background exponential decay and the measured addition energy. The exponential decay in addition energy is due to change is the dot size. There is no evidence for shell filling as no clear increase in addition energy is observed at the 2D magic numbers 2, 6, 12. (**d**) The line cut indicated by the red dashed line in (b) is measured as a function of magnetic field. The ground state splits into a spin pair, while the excited state shows a complex excited state spectrum.

measurements of Wang *et al.* suggesting they were able to reach the last hole. Unlike the measurements of electrons in GaAs [1, 9], the addition energy spectrum observed by Wang *et al.* did not show clear evidence for orbital shell structure, as shown in Figure 3.4(c). To study the spin states, Wang *et al.* measured the evolution of the N=2 ground state and excited states, as indicated by the vertical red dashed line in Figure 3.4(b). The ground state was observed to split into a spin-pair as shown by the red arrows in Figure

3.4(d). Observation of a ground state spin pair is an anomalous result[1]. This could be explained by a non conventional spin filling sequence, or it could be that the dot is not completely emptied of all charges in Figure 3.4(b). Distinguishing these effects could be resolved by implementing a charge sensor to the device. The excited states in Figure 3.4(d) split into four states, which could result from a p-like orbital degeneracy, or could be due to closely spaced 2-fold degenerate excited states. Despite these anomalous shell filling results, Wang *et al.* have observed Pauli spin blockade in the few hole regime of a lateral GaAs MOS double quantum dot. This demonstrates that is a spin dependent orbital structure [109] in the few hole regime. However, it is interesting to note that Wang *et al.* did not observe Pauli spin blockade in the two hole regime, where it has typically been observed in GaAs electron quantum dot devices [30, 91].

Bogan *et al.* [122] have studied the energy spectrum of holes in GaAs double quantum dots. A schematic of the device is shown in Figure 3.5(a). The device is designed to allow both transport measurements (I_{DQD}) and charge sensing (I_{CS}). Bogan *et al.* use transport measurements to extract the energy spectrum of the double quantum dot. Importantly the charge sensor allows absolute confirmation of the hole occupation, which was not possible for Wang *et al.* [108, 109]. Figure 3.5(b) shows the charge stability diagram obtained using the charge sensor. Bogan *et al.* tuned the device to the two hole regime and used high-bias double dot transport measurements to extract the hole energy spectrum. A schematic of the results is shown in Figure 3.5, where the magnetic evolution of the singlet and triplet states has been quantified.

The spectroscopy measurements of Bogan *et al.* [122] have furthered the understanding of the consequence of spin-orbit coupling on single hole quantum dots. Since Bogan *et al.* have characterised the singlet-triplet energy states, it is possible for them to analyze double dot transport with respect to known spin and orbital states. This analysis has demonstrated an anomalous result, which arises due to the strong spin-orbit coupling experienced by holes. In contrast to electron devices, Bogan *et al.* found that the hole spin was not conserved during inter-dot tunneling in GaAs double quantum dot devices. The presence of spin-flip tunneling prevents the formation of Pauli spin blockade, and similar

[1]The N=2 ground state is not expected to split into a spin pair, since the two holes would be expected to form a spin singlet ground state.

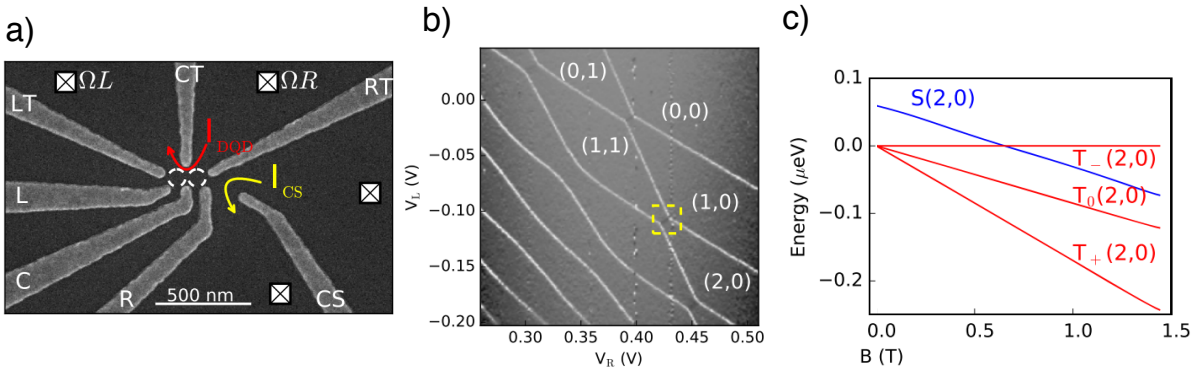

Figure 3.5: **Spectroscopy two hole states in a GaAs double quantum dot:** (**a**) Shows a SEM image of the device studied by Bogan *et al.* [122]. The device consists of a double quantum dot with a charge sensor. Source-drain bias transport measurements can be employed by monitoring the current through the double dot. Importantly, the charge sensor allows confirmation of the absolute hole occupation. (**b**) The charge stability diagram of the double quantum dot device, demonstrating operation down to the last hole. The yellow square indicates the region used to study the energy spectrum of the N=2 quantum dot. (**c**) Schematic of the N=2 energy spectrum, which has been extracted from source drain bias measurement of the double dot.

to Wang *et al.*, Bogan *et al.* do not observe Pauli spin blockade in the two hole regime. The conclusions of Bogan *et al.* are strongly supported thanks to the adjacent charge sensor, which allows the absolute charge occupation to be independently confirmed.

Characterisation of the two hole energy spectrum in GaAs provided the foundation for further analysis of hole spin properties. Using the anomalous non-spin conserving transport combined with the well characterised energy spectrum, Bogan *et al.* [115] developed a novel spin-to-charge conversion protocol[1]. Using this protocol Bogan *et al.* performed the first electrical characterisation of T_1 for single hole spins in GaAs quantum dots. These results have shown that GaAs hole spin relaxation occurs via the phonon-mediated spin–orbit interaction, and T_1 is observed by Bogan *et al.* over a range from 400ns to 60μs with a B^5 dependence.

Holes in silicon quantum dots

We begin this section by discussing planar p-MOS silicon quantum dots, which are the main structure investigated in this thesis[2]. The few hole regime has been reached by

[1]Typical double dot spin-to-charge conversion mechanisms have relied on Pauli spin blockade and spin-conserved inter-dot transport. However, when there is strong spin-orbit coupling spin flip tunneling is possible, and traditional Pauli spin blockade based spin-to-charge cannot be easily implemented. This is a motivation for Bogan *et al.* to implement a novel technique.

[2]In Chapter 1 we present a full literature review for detailing the development of planar p-MOS silicon quantum dots.

in planar single hole silicon p-MOS devices by Li *et al.* [27] and Spruijtenburg *et al.* [29] in (2013). Excited states of the single hole quantum dot were observed by Li *et al.* with energies on the order of 800μeV. Li *et al.* [28] extended their study to double dot devices, where Pauli spin blockade was observed in transport measurements. Using high-bias double dot transport spectroscopy Li *et al.* calculated the spin-orbit strength and characterised the role of spin-orbit interaction in lifting the Pauli spin blockade for silicon hole spins. However, in these measurements the absolute charge occupation is unknown. This introduces a challenge for further analysis, since the extent of hole-hole interactions and the exact orbital profile both remain unknown. These challenges can be overcome by incorporating a charge sensor in the silicon MOS devices. This is exactly the aim of the experimental research in this chapter.

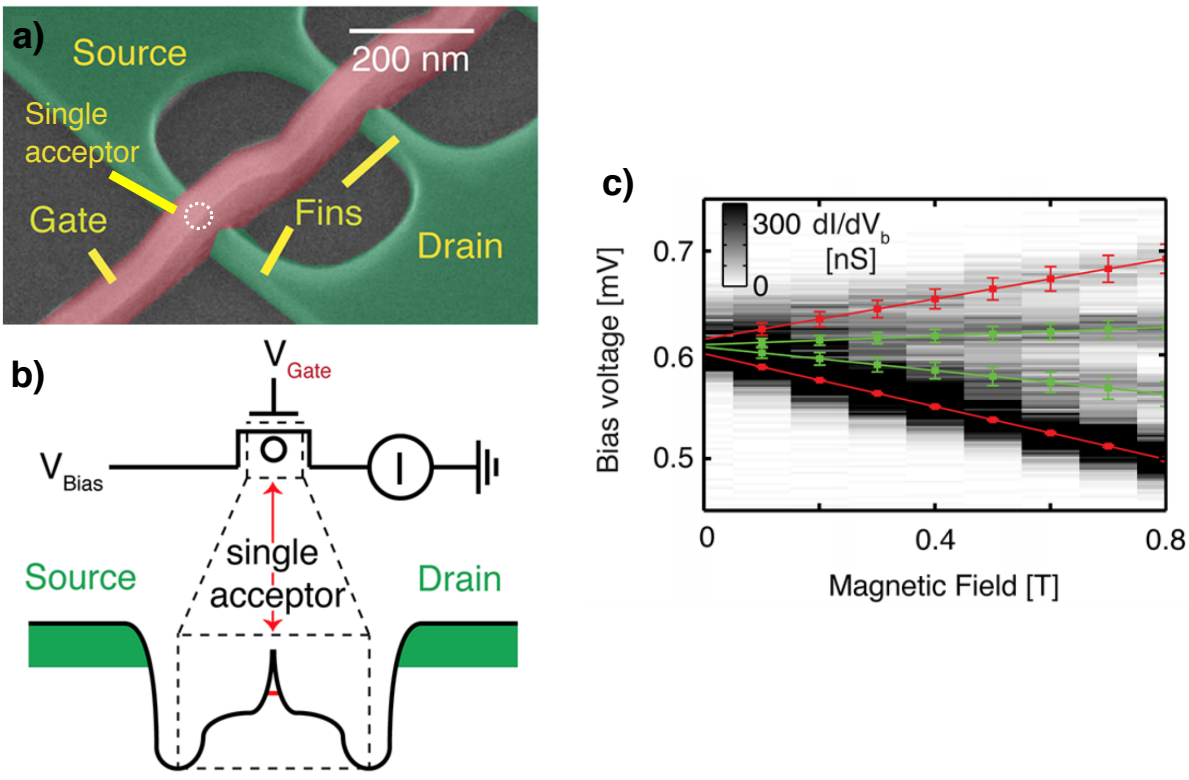

Figure 3.6: **Acceptor quantum dot in silicon:** (**a**) False colour SEM image of the p-type FinFET quantum dot device studied by Van der Heijden *et al.* [123]. This device has two channels formed by the undoped fin regions, with each channel connected to a source and drain p-type region. If a boron atom happens to be present in a 'Fin', it can trap holes and act as a quantum dot. (**b**) Shows a schematic of the single acceptor quantum dot, which can be controlled using the gate. (**c**) Shows source-drain bias spectroscopy of the ground state, where the colour scale is the transconductance. Four distinct states are visible as the spin up and spin down Heavy holes (red) and Light Holes (green). The degeneracy is lifted due to the different g-factors, where $g_{HH} = 0.81$, and $g_{LH} = 0.85$.

We now briefly discuss silicon based single accepter quantum dots. Acceptor dopants provide a distinctly different confinement symmetry to planar MOS and nanowire quantum dots. The confinement symmetry of a quantum dot significantly impacts the energy spectrum. In silicon based single accepter quantum dots spherical symmetry of the confinement is retained, and the Heavy-Hole and Light-Hole states remain degenerate. Van der Heijden *et al.* [123] have studied the energy spectrum of single holes confined to a boron dopant in a silicon MOSFET structure. A schematic of the device is shown in Figure 3.6(a). Van der Heijden *et al.* use magnetospectroscopy measurements to show that the single hole ground state has four-fold degeneracy, and is made of degenerate Heavy Hole and Light Hole states. In planar MOS and 1D nanowire devices the difference in effective mass and confinement lifts the Heavy Hole Light Hole degeneracy [51]. These spectroscopy measurements of Van der Heijden *et al.* confirm that acceptor quantum dots significance that the confinement symmetry has on the orbital spectrum.

Summary of hole spectroscopy review

In these sections we have presented a review of spectroscopic measurements of holes in a range of material systems (InAs, GaAs and Si) and device structures (planar MOS, self assembled, and single dopants). The focus of these sections has been to highlight the non-trivial spin and orbital physics that has been observed in hole based quantum dots. Particularly the focus has been on how spin-orbit interactions, confinement, and different effective masses can lead to the observed orbital spectrum. Readers interested in further spectroscopy studies of holes can consider the following: Si nanowires [104, 111], physically defined Si [124], Si/Ge nanowires [76, 77], Ge hut wires [72], and Ge planar MOS [26].

Prospects for hole-spin qubits

A major motivation for studying hole based quantum dots is due to the favorable properties holes are predicted to have for spin qubit applications [78, 79]. Holes are predicted to be suitable for fast electric manipulation of spin [60], while also having long spin coherence times [80, 81]. Recent experiments by Maurand *et al.* [20], Hendrickx *et al.* [26], and Watzinger *et al.* [22] have each confirmed that hole spins can have Rabi frequen-

cies up to 150MHz[1]. These are promising results, particularly since the observed spin manipulation times are even faster than theoretically predicted [21, 125][2]. However, the ongoing challenge has been to enhance the hole spin coherence times, which are found to be much shorter than expected, on the order of hundreds of nano-seconds. On the one hand, operation speed appears even better than expected, and on the other, spin lifetimes appear shorter. Each of these hole spin manipulation experiments [20, 22, 26] were performed in the few hole regime, where the absolute charge occupation and details of the energy structure are unknown. The success of the hole spin experiments performed by Maurand *et al.*, Hendrickx *et al.*, and Watzinger *et al.* highlights the potential of holes for spin qubit applications. However, the open question of coherence times demonstrates the need to fully characterise and understand the spin properties of these devices through detailed spectroscopic measurements.

3.2.3 Conclusion of literature review

Semiconductor quantum dots exhibit a rich energy spectrum, with well defined devices showing shell structures analogous to atoms. It is often irresistible for physicists to build up periodic tables of artificial atoms [43]. However, quantum dots with a clearly observable and well defined orbital shell structure are not typical and should not be taken for granted. This is particularly true for p-type quantum dots, where a mix of non-trivial properties can influence the spin and orbital structure. The energetic structure of a quantum device plays a key role in the properties, particularly those related to spin. As such, spectroscopic measurements provide vital information allowing physicists and engineers to asses potential uses, and to understand the electronic and magnetic properties of a quantum dot. Finally, in order for spectroscopic measurements to have

[1] These experiments were performed using three different quantum dot structures, Maurand *et al.* [20] studied a CMOS silicon nanowire, Hendrickx *et al.* [25] studied a SiGe MOS quantum dot, and Watzinger *et al.* [22] studied a self assembled Ge quantum dot.

[2] Ares *et al.* [125] predict a maximum Rabi frequency of 100MHz in SiGe quantum dots and Hendrickx *et al.* [25] observe Rabi frequency up to 160Mz in SiGe MOS quantum dots. Crippa *et al.* [21] model the Rabi frequency in Si nanowire quantum dots using g-TMR theory and require a free parameter to fully predict Rabi frequencies. In both cases the unknown mechanism enhancing the Rabi frequency is likely due to spin manipulation via spatial modulation of the wavefunction [60]. While g-TMR can be predicted, spatial modulation of the wavefunction is device specific. See Chapter 4 literature review for further discussion.

context with other results and devices, it is necessary to known the absolute charge occupation.

3.3 Characterising the lever arm

In order to begin studying the energy spectrum of a quantum dot, it is necessary to have a method allowing changes in energy to be measured. In quantum dots the energy levels can be measured using a source-drain bias voltage, which can be directly converted to an energy (see section 1.1.3). Alternatively, it is possible to determine energy scales using the capacitive coupling between the dot and the gates (see section 1.2.3). In this case an experimentally determined coefficient that converts gate voltage to energy is required.

The lever arm α is a linear coefficient allowing a change in gate voltage to be converted to a change in the electrochemical potential $\Delta E = \alpha \Delta V_{\mathrm{G3}}$. Typically in quantum dots, the lever arm α is determined by varying the source-drain bias, and measuring so called Coulomb diamonds in single dot transport. However, since the devices described in this thesis are single lead quantum dot devices, transport measurements through the single dot are not possible. In order to calculate the lever arm we first tune V_{G3} so that the single dot under G3 is on a charge transition (in this case we use the 2nd to 3rd hole transition). We then apply an 8mV sawtooth wave to G3 causing the hole occupation of the dot to shift from two holes to three holes over the sawtooth sweep. The average DC sensor current $\langle I_{\mathrm{DC}} \rangle$ will shift from high to low as the sawtooth sweeps the dot electro-chemical potential across the reservoir chemical potential. The width in V_{G3} of the shift from high to low $\langle I_{\mathrm{DC}} \rangle$ is determined by the Fermi distribution of hole states in the reservoir [32, 33].

In Figure 3.7(a) we show $\langle I_{\mathrm{DC}} \rangle$ for two different fridge mixing chamber temperatures T_{MXC}. The width of the transition in $\langle I_{\mathrm{DC}} \rangle$ is sensitive to the thermal broadening of the reservoir distribution of hole states. We fit $\langle I_{\mathrm{DC}} \rangle$ to the function

$$\langle I_{\mathrm{DC}} \rangle = \frac{I_{\text{peak-to-peak}}}{1 + \exp[\frac{(V_{\mathrm{G3}} - V_0)\alpha e}{k_{\mathrm{B}} T}]} + I_{\text{offset}} = \frac{a}{1 + \exp[\frac{V_{\mathrm{G3}} - b}{c}]} + d \tag{3.1}$$

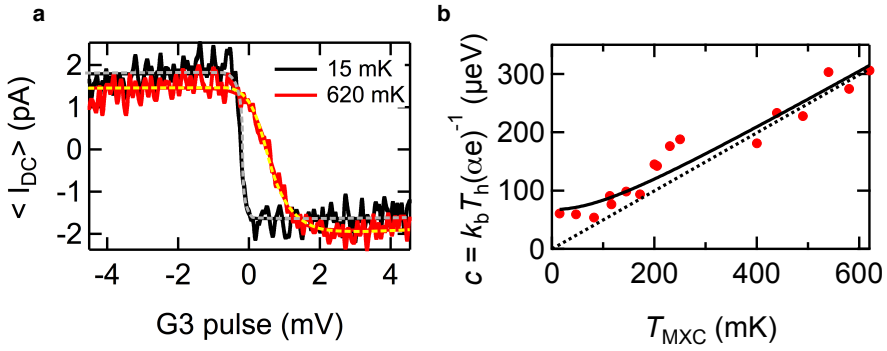

Figure 3.7: **Lever arm calculation:** (**a**) $\langle I_{\rm DC}\rangle$ resulting from an 8mV sawtooth wave applied to G3 at fridge temperatures of 15mK and 620mK. Fit lines are shown in yellow (620mK) and grey (15mK) dashed lines. (**b**) Fitting parameter c (Equation 3.1) as a function of fridge temperate $T_{\rm MXC}$. Typical values for the remaining fitting parameters of Equation 3.1 are approximately constant at $a = 3.6$pA, $b = 0.32$mV, $d = -1.8$pA. $T_{\rm h}$ is the hole temperature temperature, which depends on the hole bath temperature T_0 and the mixing chamber temperature $T_{\rm MXC}$ (Equation 3.3). The solid black line is a fit to Equation 3.3, giving $T_0 = 136\pm25$ mK, and $\alpha = 0.174\pm0.008$ eV/V. The dashed black line is a least squares fit for the data $T_{\rm MXC} > 300$mK. The resulting slope of the dashed black line gives $\alpha = 0.174\pm0.009$ eV/V.

where a, b, c, d are fitting parameters. The smooth dashed lines in Figure 3.7(a) show the fit to the raw data. By comparing the fitting function to the Fermi-Dirac distribution we determine that the parameter

$$c = \frac{k_{\rm B}}{\alpha e}\sqrt{T_0^2 + T_{\rm MXC}^2} \tag{3.2}$$

$$c = \frac{k_{\rm B}}{\alpha e} T_h \tag{3.3}$$

where T_0 is the constant hole bath temperature, and $T_{\rm MXC}$ is the dilution fridge mixing chamber temperature. T_h is the actual hole temperature, which is given by $T_{\rm MXC}$ and T_0 added in quadrature. We extract the lever arm by measuring the temperature dependence of the fitting parameter c.

In Figure 3.7(b) we plot the fitting parameter c as a function of the fridge mixing chamber temperature $T_{\rm MXC}$. On the range of 15mK to 130mK the fitting parameter c is unaffected by changes in the mixing chamber temperature $T_{\rm MXC}$. Above 130mK the fitting parameter c increases linearly with $T_{\rm MXC}$, as shown by the black dashed line in Figure 3.7(b). We extract the hole bath temperature, T_0, to be 136±25 mK. For $T_{\rm MXC}$ above ∼130mK we infer that the hole bath temperature $T_{\rm h}$ is equal to $T_{\rm MXC}$. The G3 lever arm $\alpha_{\rm G3}$ is calculated to be 0.174±0.008 eV/V from fitting the parameter c as a

function of T_{MXC} to Equation 3.3. The G3 lever arm α_{G3} was calculated for the two to three hole charge transition. We use $\alpha_{\mathrm{G3}} = 0.174$ eV/V for all analysis presented in the main text. We note that the lever arm could be dependent on the hole occupation due to additional screening and changes in the dot size. However, the charge transition lines are linear in the V_{G3} V_C phase space shown in Figure 2.14(a)[1]. This indicates that the lever arm remains within the uncertainty range of 0.174±0.008 eV/V for at least the first 12 holes.

3.4 Evidence for orbital structure of single quantum dot

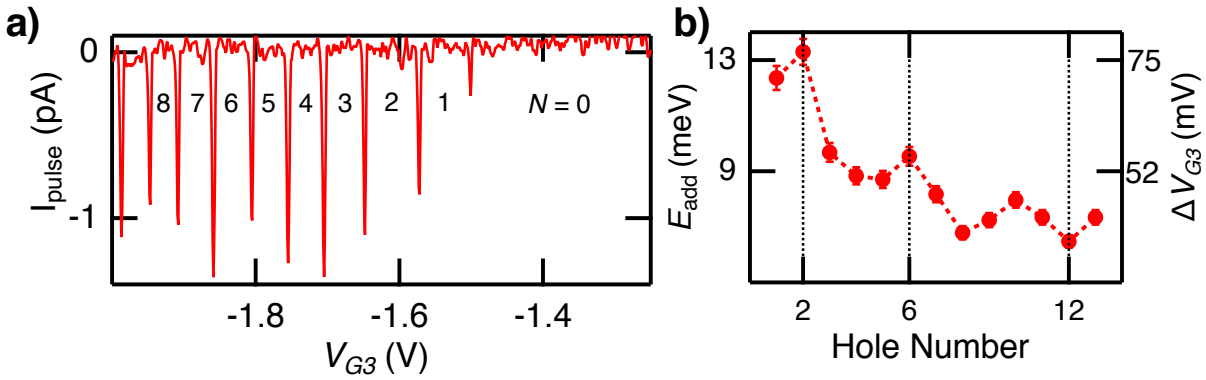

Figure 3.8: **Measurement of the Addition Energy:** (**a**) Coulomb blockade of the single quantum dot reproduced from Figure 2.13(c) in order to provide context. (**b**) The hole addition energy extracted from (**a**), showing peaks at N=2 and 6 consistent with the expected Fock-Darwin 2D shell filling. The error bars result from the standard error in the mean of 20 measurements over a small range of V_{C}. All gate voltages are the same as stated in Figure 2.13(c) caption.

The spacing of the charge transition lines in Figure 3.8(a) provides clear evidence for orbital shell filling of the hole quantum dot[9]. We extracted the addition energy ($E_{\mathrm{add}}(N) = \mu_{N+1} - \mu_N$) by measuring the spacing ΔV_{G3} between consecutive Coulomb peaks, then converted ΔV_{G3} to energy using the lever arm of 0.174 eV V^{-1} (see section 3.3). In Figure 3.8(b) we plot the addition energy E_{add} for increasing hole number. A clear increase in the addition energy is observed for N=2 and N=6, which suggests the

[1]There is a slight kink around (V_{G3}, V_C) = (-1.7, 0.45), however this appears as a result of a nearby confined charge. Later, in Appendix A section A.2.2 we have confirmed that the lever arm is independent of the gate voltages.

orbital shell is full for the second and sixth holes.

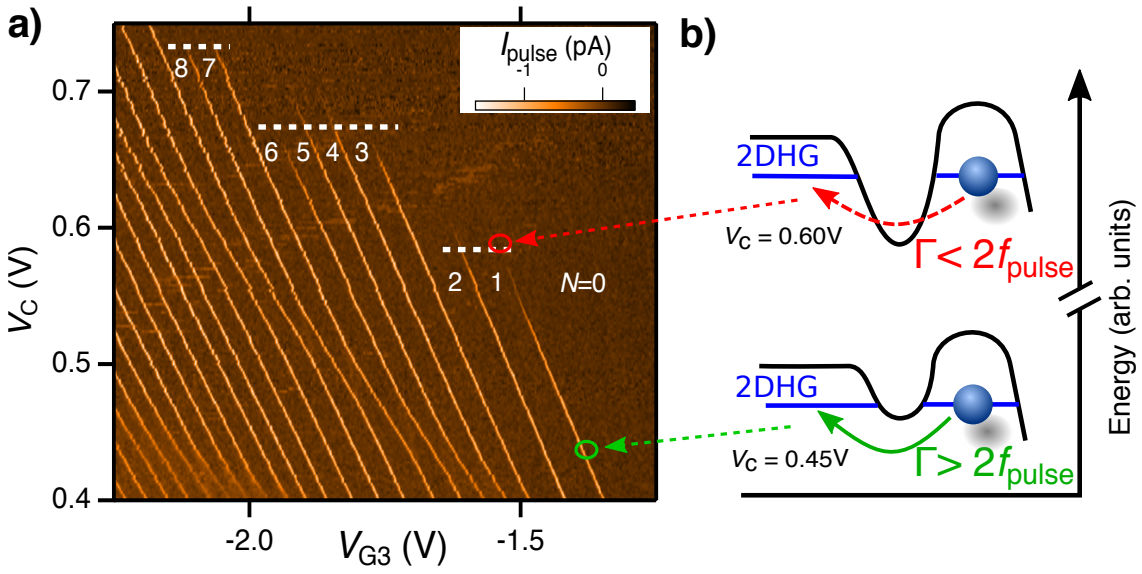

Figure 3.9: **Tunnel rate grouping of the single dot:** (**a**) Charge stability diagram reproduced from Figure 2.13(d) to provide context. The number of holes in the dot are labeled in white text. The horizontal white lines highlight the disappearance of the charge transition signals in distinct groupings, indicating shell filling. (**b**) Schematic diagram depicting the change in the tunnel barrier height between the V_C and V_{G3} configurations indicated by the green and red circle in (**a**). The tunnel rate, Γ, between the dot and the 2D hole gas (2DHG) is influence by changing V_C, causing the charge transition signals to disappear when the tunnel time becomes comparable to the period of the pulses applied to G3. See methods section for additional experimental parameters.)

Further evidence for orbital shell filling is given by the stair-like disappearance of charge transition signals. In Figure 3.9(a) we reproduce the charge stability diagram of the single hole quantum dot. The stair-like disappearance of charge transition signals is highlighted by the dashed horizontal white lines in Figure 3.9(a). Along each vertical charge transition line the measured signal decreases as V_C is made more positive. As V_C becomes more positive the tunnel barrier becomes more opaque, and subsequently the tunnel rate from the dot to the reservoir Γ decreases. The charge sensor transition is no longer visible when $\Gamma < 2f_{pulse}$, as shown schematically in Figure 3.9(b). When a hole in the dot occupies a higher energy orbital shell, its wavefunction span increases, which increases the tunnel rate. Hence, the charge sensor transition signals should lose visibility at more positive V_C for holes in higher orbitals. A statistical analysis of the visibility of the charge transition lines (see section 3.4.1) shows that the N=(1,2), (3,4,5,6) and (7,8) charge transitions become unmeasurable with the pulsed gate technique at almost the same V_C (dashed lines in Figure 3.9(a)). The groupings suggest that these holes fill

the same orbital state, with similar tunnel rates in the same orbital level.

The observation of a shift in addition energy and tunnel rate suggest the first two holes fill into the first orbital, and the next four holes fill into the second orbital. This shell filling is consistent with the Fock-Darwin orbital structure for a 2D parabolically confined quantum dot [41, 42]. Beyond N=6 the observed orbital filling departs from the so-called 2D magic numbers, which may reflect a loss of circular symmetry of the parabolic confinement for higher hole occupation, since the higher orbital hole wavefunctions are more sensitive to a non-circular confinement profile. Other possibilities include many-body effects [1], which further reduce the energy spacing between different shells.

3.4.1 Statistical analysis of tunnel rate groupings

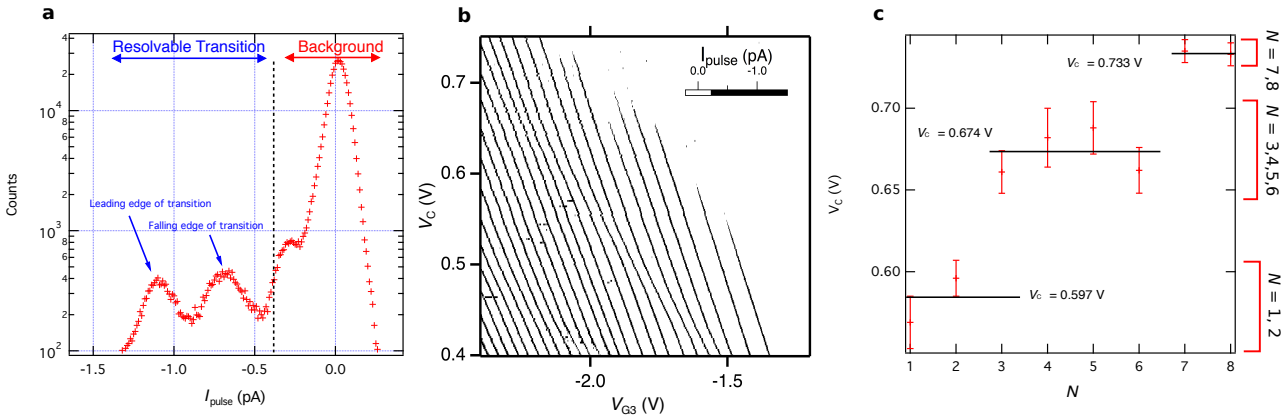

Figure 3.10: **Charge transition histogram and groupings: (a)** Histogram of the data presented in the charge stability diagram of Figure 3.9. The x-axis shows bin centers for values of measured I_{pulse}, while the y-axis shows the number of counts within the bins. The horizontal blue arrow labeled 'Resolvable Transition' highlights the values of I_{pulse} that correspond to charge transition signals, while the horizontal red arrow labeled 'Background' highlights the values of I_{pulse} that correspond to background signal. The peak centered at approximately 0pA is the background signal. The two peaks at -1.1pA and -0.7pA can be identified from the data as the rising and falling edges of the pulse-detected charge transition. **(b)** The charge stability diagram from Figure 3.9(a) shown with with binary colour scale. For the charge transition signal, I_{pulse} < -0.22pA, data is shown as black, while for the background single, I_{pulse} > -0.22pA, data is shown as white. This allows the extraction of the background signal and easy identification of the loss of visibility of each charge transition. **(c)** The extracted values of V_C (with uncertainty) at which each transition loses visibility There is a clear overlap of the N = (1,2) the N=(3,4,5,6) and N = (7,8). The horizontal black lines highlight this overlap, and are draw at the same respective V_C as Figure 3.9(a). The red brackets on the right side highlight the groupings. The error bars are the deviation in the mean V_C value at which the charge transition is no longer visible

In Figure 3.9(a) horizontal white lines are drawn to highlight the stair-like disappearance of the charge transition visibility. The specific V_C at which the horizontal lines are drawn

has been determined by extracting the value of V_C at which the charge transition signal in I_{pulse} is no longer distinguishable from the background signal.

In order to determine a value of I_{pulse} that characterizes the loss of visibility, we take a histogram of the data presented in the charge stability diagram of Figure 3.9(a). In Figure 3.10(a) we show this histogram with I_{pulse} on the x-axis and number of counts on the y-axis. The analysis of 3.10(a) shows three clear distributions. The largest distribution is the background signal, centered at I_{pulse} approximately 0pA. The two other distributions, centered at I_{pulse} = -1.1pA and I_{pulse} = -0.7pA make up the rising and falling edges of the detectable charge transition signal respectively. The blue arrow labeled 'Resolvable Transition' marks the range of I_{pulse} = (-0.15,-0.22)pA, which corresponds to the range of I_{pulse} readings where a charge transition is detected. To demonstrate this, in Figure 3.10(b) we plot the charge stability diagram with a binary color scale, with black for values of I_{pulse} indicated by the blue horizontal arrow in Figure 3.10(a) (transition) and white for any value of I_{pulse} outside this range (background).

Based on the distribution of I_{pulse} we are able to extract a value of V_C at which the signal is no longer visible. The error bars are determined from the width of the distributions, and the observed decay in I_{pulse}. Figure 3.10(c) shows the extracted values of V_C for the charge stability diagram in Figure 3.10(b). The horizontal black lines in 3.10(c) correspond to the horizontal lines drawn in Figure 3.9(a). The distinct groupings are highlighted by the red brackets on the right of Figure 3.10(c). There is no overlap between the distinct groupings, demonstrating the effect of orbital shell filling.

3.5 Magnetospectroscopy of first six charge states

To determine the spin structure of the hole quantum dot, we study the magnetic field dependence of the addition energy for N=1 to 6 holes. The slope of the N^{th} addition energy $E_{\mathrm{add}}(N)$ with respect to B depends on the relative spin orientation of the $(N+1)^{th}$

and N^{th} hole, with three distinct possibilities:

$$\frac{dE_{\text{add}}}{dB} = \begin{array}{ll} +\left(\frac{g_N^*+g_{N+1}^*}{2}\right)\mu_B & \downarrow\uparrow \\ -\left(\frac{g_N^*+g_{N+1}^*}{2}\right)\mu_B & \uparrow\downarrow \\ \pm\left(\frac{g_{N+1}^*-g_N^*}{2}\right)\mu_B & \uparrow\uparrow \; or \; \downarrow\downarrow \end{array} \tag{3.4}$$

where the first and second arrow depicts the spin filling sequence of the $(N{+}1)^{th}$ and N^{th} holes respectively. We have the average of the two effective g-factors since E_{add} measures the spacing between the N^{th} and $(N{+}1)^{th}$ energy levels, which can occupy different orbitals and have different g-factors. Notice that the third term will be zero provided that $g_N^* = g_{N+1}^*$, and can be non-zero when $g_N^* \neq g_{N+1}^*$.

3.5.1 Addition energy magnetospectroscopy measurements

In Figures 3.11(a−e) we show the addition energy, $E_{add}(N) = \mu_{n+1} - \mu_n$ for the first six holes as a function of in-plane magnetic field B. In all figures we observe a distinct change in the slope of dE_{add}/dB at 2.7T, and so we refer to $|B|$<2.7T as the low field region, and $|B|$>2.7T as the high field region. For all data we observe that in both the low and high field region of Figures 3.11(a−e) the data is linear in B. This is consistent with the expected behavior of Equation 3.4 allowing the spin filling sequence to be determined[1].

In order to infer the spin configuration of the dot for different hole occupations we first consider the N=1 spin state. The N=1 spin will be aligned with the in-plane magnetic field B, and we assign this as 'spin down'. The relative spin orientation of the first six holes can then be determined by observing the slope of the addition energies in Figures 3.11(a-e) and comparing the results with Equation 3.4.

As an example of how the spin orientation is inferred, we first discuss in detail the $E_{add}(1)$ measurement shown in Figure 3.11(e). The N=1 hole fills as spin down (aligned with

[1]We use an in-plane magnetic field allowing the addition energy behavior to be well described by Zeeman effects only. It is expected that the hole density is approximately 10^{12} cm^{-2}, and the thickness of the 2D layer is of the order of 5nm. This thickness is less than the in-plane magnetic length for all data presented in this work. Therefore, we consider in-plane magnetic field induced orbital effects to be negligible. Orbital effects would appear as a non-linear effect in the addition energy.

the magnetic field), this is shown as the black arrow in the upper left inset of Figure 3.11(e). In the range 0<B<2.7T we observe that the addition energy increases. This is consistent with the N=2 hole spin anti-aligned with the N=1 spin, and the addition energy is increasing due to the Zeeman effect. We represent the N=2 spin orientation with a red arrow in the upper left inset of Figure 3.11(e). At 2.7T the distinct change in slope suggests a change in the orientation of the N=2 spin state. For B>2.7T the $\mathrm{d}E_{add}/\mathrm{d}B$ is approximately zero, consistent with the N=1 and N=2 spins now both aligned with the magnetic field[1]. Due to Pauli's exclusion principle the N=2 hole must now occupy a different orbital state to the N=1 hole. Evidence from section 3.4 has shown that the first orbital level has only 2-fold degeneracy, hence the N=2 state must occupy a higher momentum orbital than the N=1 state. The relative spin orientation and orbital occupation for |B|>2.7T is represented in the lower right inset of Figure 3.11(e).

For the higher hole occupations we emphasize that the slope of the addition energy depends only on the on two highest energy hole spins that are occupied. For example consider the magnetospectroscopy measurement of $E_{add}(3)$ presented in Figure 3.11(c). In the low field region the slope $\mathrm{d}E_{add}/\mathrm{d}B$ is approximately zero, suggesting the N=3 and N=4 hole are spin aligned. Measurements of $E_{add}(2)$ determined that the N=3 hole has spin down (the N=3 state is the orange arrow in Figure 3.11(a-c), so the N=4 hole must also be spin down at low magnetic field (the N=4 state is the green arrow in Figure 3.11(a-c). Consecutive filling of spins with the same alignment is consistent with the N=3 and N=4 states occupying degenerate p_x and p_y orbitals. The inset of 3.11(c) has two grey arrows representing the spin and orbital level occupied by the N=1 and N=2 holes. We present both the N=2 and N=1 states as grey in 3.11(c) since they are indistinguishable in the measurement of $E_{add}(3)$.

[1]When both spins have the same alignment and g-factor the Zeeman effect will not influence the addition energy. We note that the slope is close to, but not exactly zero. This is due to the difference in g-factors between the $1s$ and $2p$ orbital and is discussed below in section 3.5.2.

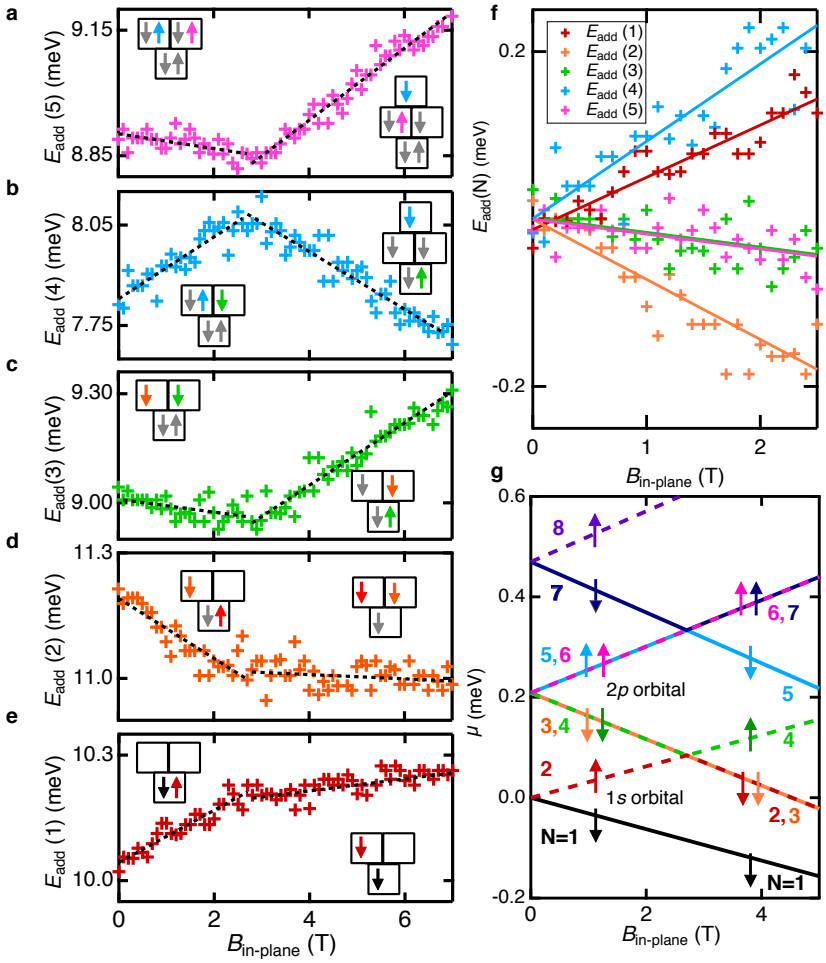

Figure 3.11: **Spin filling sequence and orbital structure:** (**a-e**) Addition energy for the first six holes as a function of in-plane magnetic field. Black dashed lines are a linear fit to the raw data over the region |B|<2.7T (low field) and |B|>2.7T (high field). The left and right inset shows the inferred ground state spin filling for the low and high magnetic field regions respectively, where vertical stacking of the squares represents the orbital structure Each colored arrow corresponds the N^{th} hole (as depicted by the colored text in **g**). Since $E_{\rm add}(N)$ measures the spacing between the μ_{N+1} and μ_N, only the two states relevant to the respective addition energy measurement are shown in color, all other states are gray. (**f**) The first five addition energies plotted over the low field region (|B|<2.5T) with data offset to clarify the linearity of the data, with slopes either positive, negative, or close to zero. Solid lines are the same least squares fit to the data. The difference in the slope of $E_{\rm add}(1)$ and $E_{\rm add}(4)$ is due to the different orbital g^*-factors. (**g**) Model of the hole orbital shell structure and energy levels for the first eight holes (ignoring Coulomb charging energy), extracted directly from the data in (**a-e**). Each line corresponds to the hole charge occupations in (**a-e**), and the color of each line corresponds to the color of the numbers on the left and right of the figure. Experimental parameters are; V_R = -3.50V, $V_{\rm C}$ = +0.55V, $V_{\rm G1}$ = -3.50V, $V_{\rm G2}$ = -0.73V and $V_{\rm G4}$ = -0.10V.

3.5.2 Determining the g* from magnetospectroscopy measurements

In Figure 3.11(f) we show the low field region of the first five addition energy measurements. Given the linear data in Figure 3.11(a-e) and the evidence for orbital structure

of the dot presented in section 3.4 it is possible to extract the effective g-factor, g^*, for holes occupying different orbitals. We have extracted g^* from Figure 3.11 to be $g^*_{1s} = 1.1$ and $g^*_{2p} = 1.4$. The effective g-factor for the orbital occupied by the 7^{th} hole ($N = 7$) is $g^*_{N=7} = 1.6$, and can be extracted from the slope of Figure 3.11(b) for $|B|$ larger than 2.7T. The orbital dependence of g^* provides further evidence for the observed orbital structure and is due to the strong spin-orbit coupling of holes [126, 127]. We observe that holes occupying states with larger orbital momentum have larger effective g-factors.

3.5.3 Details of the orbital shell structure and spin filling

The full orbital and spin filling sequence can be determined from the measurements presented in Figures 3.11(a-e). In Figure 3.11(g) we present the orbital structure of the single hole MOS quantum dot. Here we will discuss the full spin and orbital filling sequence in detail, beginning with the low field orbital spin filling. The first and second holes form a Pauli spin pair in a two-fold degenerate orbital, labeled $1s$. The third and fourth holes fill the $2p_x$ and $2p_y$ states with spins parallel to each other. The fifth and sixth holes fill the $2p_x$ and $2p_y$ states with spins parallel to each-other, but opposite to the third and fourth holes. We are confident in the assignment of the second orbital as a four-fold degenerate $2p$ orbital consistent with the expected spectrum of a symmetric 2D quantum dot. We can rule out the possibility that the apparent four-fold degeneracy arises from an accidental degeneracy of adjacent orbitals by considering together; (i) the addition energy measurements of Figure 3.8(b), (ii) the evidence of corresponding tunnel rate shifts of Figure 3.9(a), and (iii) the distinct effective g-factors extracted from Figure 3.11(f).

We now discuss the spin filling sequence for high field region, $|B| \geq$ 2.7T. The change in slope of $E_{\mathrm{add}}(1)$, $E_{\mathrm{add}}(2)$ and $E_{\mathrm{add}}(3)$ at B=2.7T can be attributed to a magnetic field induced crossing of the $1s$ and $2p$ orbitals, as shown in Figure 3.11(g). By calculating the Zeeman energy at the $1s$ and $2p$ crossing we determine the singlet-triplet energy spacing E_{ST} for the two hole dot is 0.2meV.

To understand the change in slope of $E_{\mathrm{add}}(4)$ and $E_{\mathrm{add}}(5)$, we must first consider the

spin filling and orbital degeneracy for the 7^{th} and 8^{th} holes. Although the addition energy for the 7^{th} and 8^{th} holes is not directly measured, it is possible to determine the spin filling and orbital degeneracy based on the high field slope of $E_{\mathrm{add}}(4)$ and $E_{\mathrm{add}}(5)$ in Figures 3.11(a) and (b). In Figure 3.11(b), for B>2.7T $E_{\mathrm{add}}(4)$ decreases with $|B|$, demonstrating that the 5^{th} hole ground state is spin down for B>2.7T. Addition energy measurements in Figure 3.8(b) show that the second orbital is full for six holes. Thus, for five holes there are no remaining spin down states available in the $2p$ orbital. Therefore we conclude that the change in spin filling sequence at B=2.7T of the 5^{th} hole is due to Zeeman induced crossing between the 2p orbital and the next highest orbital. We conclude that the 7^{th} and 8^{th} holes occupy a two-fold degenerate orbital. This two-fold degeneracy is supported by the observation that the 5^{th} and 6^{th} holes fill with opposite spin at high field, as opposed to the 6^{th} and 7^{th} holes, which fill with spin aligned to the high field due to the four-fold degeneracy of the $2p$ orbital.

The change in slope around 2.7T for $E_{\mathrm{add}}(4)$ and $E_{\mathrm{add}}(5)$ can be now be attributed to a crossing between the $2p$ orbital and the next highest orbital level. The next highest orbital level above the $2p$ orbital is two-fold degenerate and is occupied by the 7^{th} and 8^{th} holes as depicted by the solid gray and dashed purple lines in Figure 3.11(g). For circular 2D confinement the orbital level above $2p$ is expected to be six-fold degenerate. We suspect that the two-fold degenerate orbital above the $2p$ orbital may result from a loss of circular symmetry of the dot due to for higher hole occupations, or many body effects [1].

In Figure 3.11(g) we present the hole orbital spectrum extracted directly from the measurements of E_{add} in Figures 3.11(a−e). Whereas previous studies of silicon hole quantum dots typically show alternating spin filling [76, 104, 128, 129] ($\uparrow\downarrow,\uparrow\downarrow$), a key result of this work is the observation of consecutive filling of holes with the same spin orientation ($\downarrow\downarrow$, $\uparrow\uparrow$), which occurs in the $2p$ orbital. The consecutive spin-orientation shell filling observed here is consistent with studies of 2D electrons in high quality GaAs quantum dots [1, 9]. Further, the degeneracy of the $2p_x$ and $2p_y$ orbital levels at B=0 demonstrates that the quantum dot has remarkably circular confinement. The results in Figure 3.11(g) provide a clear demonstration of the orbital shell spin structure of the first eight holes

in a surface-gated silicon quantum dot. In particular, we highlight the observation that holes have spin polarized filling of the $2p$ orbital, analogous to Hund's first rule of orbital shell filling in atomic physics. This is the first demonstration of holes in silicon quantum dots obeying Fock-Darwin orbital spectrum. The Fock-Darwin orbital spectrum is well defined and has been well characterised, hence these results demonstrate a highly suitable system for hole based spin qubits.

3.6 Estimating the dot size and orbital energy

In this section we use the addition energy measurements to estimate the physical size and the orbital energy of the hole quantum dot. We consider a simple model of a 2D circular dot. In order to estimate the dot diameter we approximate the dot-gate system as a parallel plate capacitor and use the measured N=1 to N=2 addition energy, $E_{\text{add}} = 12$ meV shown in Figure 3.8(b) in section 3.4. The parallel plate capacitance is given by,

$$C = \frac{\epsilon_r \epsilon_0 A}{d} \tag{3.5}$$

where A is the equivalent capacitor area, and d is the oxide thickness. The capacitance is equated to the standard single dot charging energy,

$$E_{\text{C}} = E_{\text{add}} = \frac{C}{e} \tag{3.6}$$

Taking the oxide thickness, d, to be 5.9nm and relative permitivity, ϵ_r to be 3.9 we find the equivalent parallel plate capacitor Area, A, to be 2.28x10^{-15}m^2. For a circular dot this gives a radius of (27±3)nm[1]. A dot radius of 27nm is smaller than previous silicon MOS hole quantum dots operating in the few hole regime [27, 29, 88]. Hence this result is consistent, since we would expect this device to be physically smaller than other devices that did not reach the last hole.

The approximate excited state energy is calculated by modeling the dot as an isotropic

[1]Uncertainty is introduced due to standard deviation in the fit to the lever arm (α=0.174±0.008) and uncertainty in the peak spacing used to extract E_{add}.

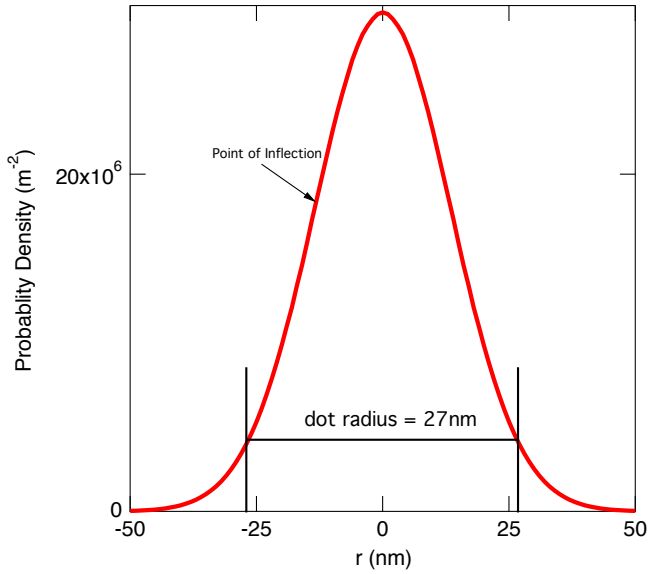

Figure 3.12: **Probability density of wavefunction:** Shows ψ^2 for the wavefunction given in Equation 3.7. The point of inflection is where the second derivative is zero and is set to be half the physical radius of the dot. The point of inflection occurs at r = $(\frac{\hbar}{m^*\omega})^{\frac{1}{2}}$. For a dot radius of 27nm this allow an estimate of $\hbar\omega$. Given the wavefunction of Equation 3.7 the hole has a 95% probability of being located in the region |r|<27nm.

two dimensional harmonic oscillator. We use the ground state Fock-Darwin wavefunction given by

$$\psi_0(r) = (\frac{m^*\omega}{2\pi\hbar})^{\frac{1}{4}} e^{\frac{-m^*\omega r^2}{4\hbar}} \tag{3.7}$$

where r is the radial dimension, and m^* is the effective mass of heavy holes in silicon. We take the in effective heavy hole mass to be m^*=0.21m_0 using Luttinger parameters for silicon [130]. To evaluate the excited state energy, $\hbar\omega$, we solve the probability density function, $\langle\psi|\,|\psi^*\rangle$, and set the point of inflection to be half the calculated dot radius.

$$\frac{d^2}{dr^2}\psi^2 = 0 \tag{3.8}$$

The value of r at the point of inflexion is given by $r = \sqrt{\frac{\hbar}{m^*\omega}}$. Equating $r = \frac{27nm}{2}$ gives $\omega = 4 \times 10^{12}\mathrm{s}^{-1}$, corresponding to an excited state energy of $\hbar\omega$ = 3meV. Figure 3.12 shows the probability density function of the Fock-Darwin ground state wavefunction.

3.7 Pulse-spectroscopy of excited states

In section 3.6 we have approximated dot to be a 2D circular dot with a radius of 27nm. If we assume the confinement is harmonic and isotropic we can calculate an expected orbital spacing of 3meV. In this section, first we present a series of measurements that demonstrate we are able to observe the excited state spectrum of the quantum dot. We then perform detailed spectroscopy measurements of the excited states for a quantum dot with one hole, and a quantum dot containing two holes. The quantum dot containing only one hole allows us to observe the single particle excited state spectrum, while the quantum dot with two holes can provide insight into interaction effects. For the quantum dot with only one hole we find the orbital spacing to be 3.5meV, which is comparable to the predicted energy of 3meV (see section 3.6). We then show that strong hole-hole Coulomb interactions has a strong effect on the excited state spectrum when the dot is occupied by two holes.

3.7.1 Observation of excited states

To experimentally study the orbital shell structure and the nature of the confinement potential, we examined the excited state spectrum of the quantum dot. In Figure 3.13 we present the excited state energy spectrum measurements. Figure 3.13(a) shows the charge stability diagram of a single hole quantum dot. However, the charge transition lines are significantly broader compared to previous stability diagrams (such as in Figure 3.9(a)). The charge transition lines are broadened by increasing V_{pulse} to 40mV (V_{pulse} was 3mV in Figure 3.9(a)). The broadened charge transition window allows single hole tunneling to occur via either the ground state or, when energetically accessible, via an excited state. The excited state spectrum can be resolved by observing the additional structure of I_{pulse} within the broadened charge transition lines.

As V_C increases, the tunnel rate decreases between the dot and the reservoir. In the region where the tunnel rate is comparable to the measurement pulse frequency, f_{pulse}, the signal is very sensitive to additional tunneling mechanisms. Excited states become visible in the broadened I_{pulse} charge transition signal, since they offer an additional

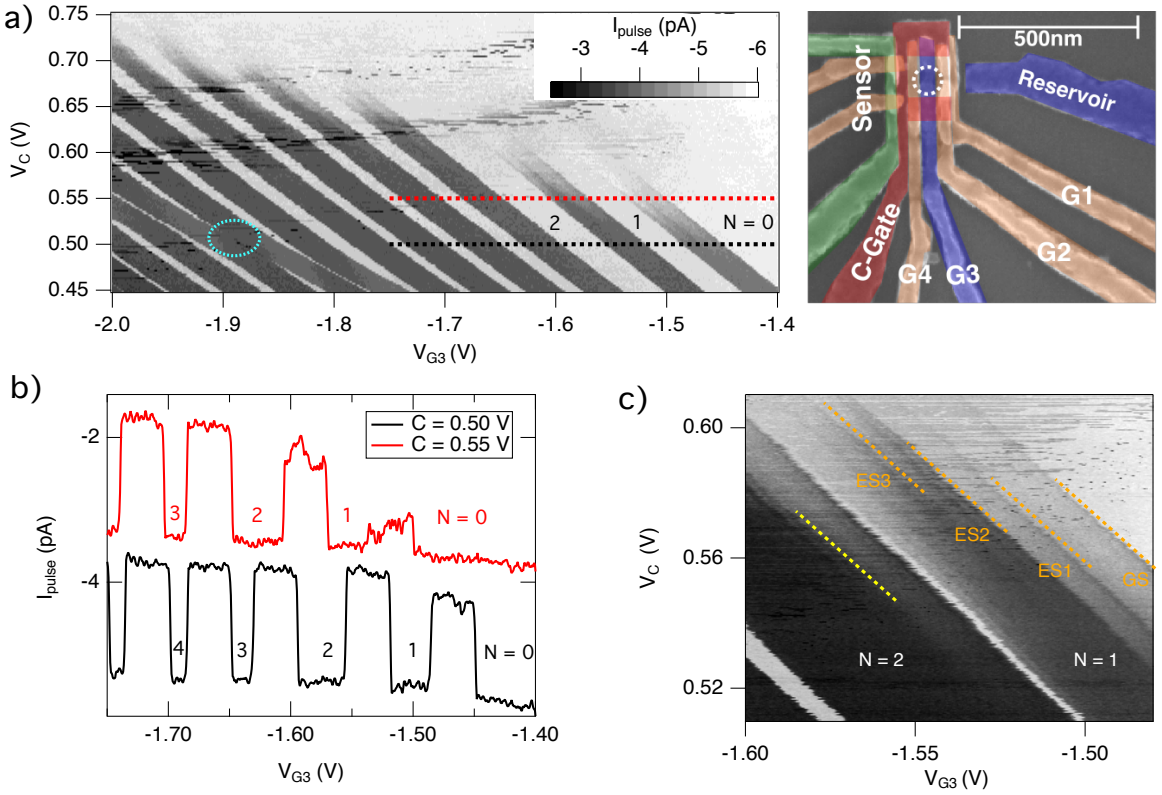

Figure 3.13: **Observing excited states using high bias spectroscopy: (a)** Charge stability diagram for V_{pulse} = 40mV. The charge transition lines are broadened compared to the previous stability diagrams due to the larger pulse amplitude. Additional structure appears in each broadened transition as V_C is made more positive. The region indicated by the blue ellipse, is not a double dot feature. This is a bending of the transitions, due to nearby charge trap similar to what was observed in Figure 3.9(a). **(b)** Line cuts measuring I_{pulse} for two different V_C voltages, corresponding the the black and red dashed line in (a). Data for V_C = -0.55V has been offset by +2pA for clarity. For V_C = 0.50 the tunnel rate for all transitions is large compared to f_{pulse}. However, for V_C = 0.55 the tunnel rate for the first and second transition are comparable to f_{pulse} and additional structure can be observed in the broad I_{pulse} signal due to excited states. **(c)** High resolution image of the N=1 transition. The N=1 excited state spectrum can be observed in the I_{pulse} signal, and is labeled with dashed orange lines adjacent, but parallel to the signal. An excited state for the N=2 transition can also be observed, and this is highlighted by the yellow dashed line.

tunneling pathway, and thus increase the I_{pulse} signal. Figure 3.13(b) shows two line-cuts of the I_{pulse} signal for two different V_C, shown as red and black dashed lines in Figure 3.13(a). For the black data V_C is more negative (V_C = +0.5V), hence the tunnel rate between the dot and the reservoir is larger than f_{pulse}, and all except the first transition show approximately constant signal amplitude. The N=0 to N=1 transition for V_C = +0.5V (black data) shows some reproducible structure, which results from the excited state spectrum of the dot. This excited state structure becomes easier to observe when the tunnel rate of all transitions is decreased. The red data in Figure 3.13(b) is for V_C =

+0.55V and reproducible structure can be clearly observed in the first two transitions. The 3^{rd} and 4^{th} transitions do not yet show any structure since the 3rd and 4th holes occupy a p-shell orbital, and have a stronger coupling to the reservoir

In Figure 3.13(c) we present a high resolution map of the N=1 transition in the region where visibility of the N=1 charge transition is lost. The ground state (GS) and a series of excited states (ES) are labeled with orange text and dashed lines. The angle of the lines is due to the capacitive coupling of V_C to the single quantum dot chemical potential. We note that the excited states of the N = 2 transition can also be observed in Figure 3.13(c), and we have labeled one of the observed ES levels with a yellow dashed line. This Figure demonstrates the high visibility of the excited states using the pulse bias measurement technique. In the following section we will use these measurements to extract the quantitative excited state energy spectrum.

3.7.2 Excited state spectroscopy measurements

We now present detailed spectroscopy measurements of the single hole quantum dot. These measurements are performed using the techniques described in the previous section. Figure 3.14(a) shows a charge stability diagram of the last hole regime. The horizontal dashed lines in Figure 3.14(a) indicate the region where the visibility of the N=1 (b) and N=2 (c) charge transitions begin to lose visibility. Figure 3.14(a) highlights the relative regions in the charge stability diagram that are used to extract the excited state spectrum of the single hole occupied (N=1), and two hole occupied (N=2) quantum dot.

Figure 3.14(b) shows the excited state spectrum for the dot with single hole occupation. This spectrum is obtained from a high resolution cut of I_{pulse} vs. V_{G3} along the dashed white line labeled (b) in Figure 3.14(a). The x-axis in Figure 3.14(b) is converted to energy using the lever arm and the ground state is referenced as the zero in energy. Peaks in Figure 3.14(b) correspond to the single hole tunneling into different orbital states in the unoccupied quantum dot (0→1 transition).

The extracted orbital energies are plotted as black circles in Figure 3.14(d), and show

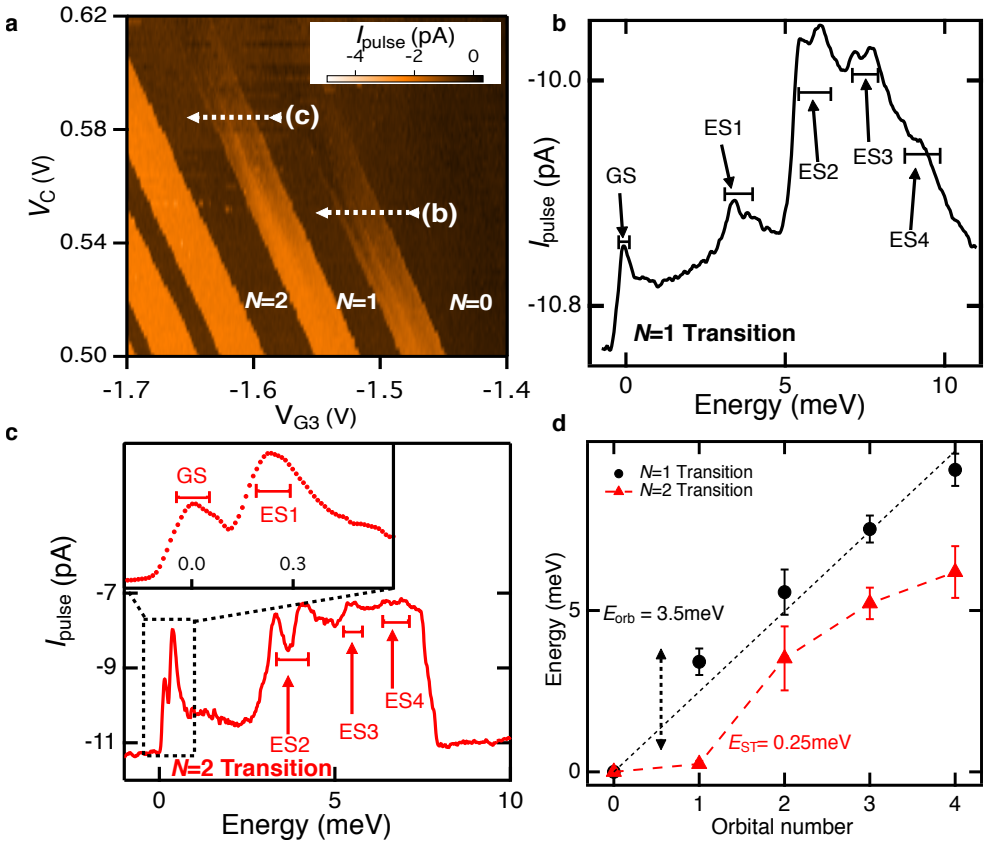

Figure 3.14: **Excited state spectroscopy:** (**a**) Charge stability diagram for V_{pulse} = 40mV and f_{pulse} = 333Hz. The white dashed lines labeled (b) and (c) correspond to cut taken to obtain the data in **b** and **c** respectively. (**b**) Measurement of I_{pulse} over the N=0→1 Coulomb peak. The x-axis has been converted to energy using the lever arm. The ground state (GS) and excited states (ES1-4) for the one hole system are labeled, with the brackets indicating the experimentally determined width of each peak. Additional structure is observed for ES2 and ES3, see text. (**c**) Same as (**b**) for the N=1→2 Coulomb peak. The inset demonstrates that the ground state and first excited state are resolvable. Each dot represents a single data point. (**d**) Plot of the extracted excited state energies for the one (black) and two (red) hole system. The black dashed line is a straight line fit to the N=1 data, highlighting the linear dependence of the excited state energies on the orbital number. The black and red error bars correspond to the width of the black and red brackets in Figures **b** and **c** respectively.

a linear dependence on orbital number. This linearity suggests that the confinement of the dot is parabolic. We note that additional structure can be observed in I_{pulse} for the second excited state (ES2) and the third excited state (ES3) in Figure 3.14(b). This additional structure is likely due to orbital splitting resulting from ellipticity of the dot for higher energy orbitals, consistent with the results for the 7^{th} and 8^{th} hole shell filling in section 3.5[1].

[1]ES2 will be occupied by the 7^{th} and 8^{th} holes. In section 3.5 we show that the 7th and 8th holes depart from the expected spin filling of a circular 2D quantum dot. This is consistent with ES2 orbital level having its six-fold degeneracy lifted.

We now briefly discus the case where the quantum dot confinement is not parabolic, but rather has a different spatial profile. For parabolic confinement the spacing between consecutive orbital levels is constant ($\hbar\omega$). For a square well the orbital energies are given as $E_n = (n^2\pi^2\hbar^2)/(2ma^2)$, where a is the width of the square confinement and n is orbital number. In this case the spacing between consecutive orbital levels will increase with n. We do not observe this trend. For a triangular confinement the orbital levels are given by $E_n = c_n(e^2F^2\hbar^2/(2m))^{\frac{1}{3}}$ where F defines the electric field and $c_1 \approxeq 2.32$, $c_2 \approxeq 4.01$, $c_3 \approxeq 5.52$...[50]. For triangular confinement the spacing between consecutive orbital levels decreases with n. This trend of decreasing orbital confinement can be partially observed in Figure 3.14(d), where orbital level one is slightly higher in energy than the trend-line, while orbital level 4 is slightly lower in energy than the trend-line (data for N=1). This highlights that although the orbital energy levels fit reasonably well to the parabolic confinement (linear trend), the experimental confinement is unlikely to be perfectly parabolic, and it is reasonable to observe some variations from the linear trend.

We now discuss the expected excited state energy scales in order to compare with the experiment. The quantum dot radius was estimated to be ∼27nm, using the charging energy of 12meV for the one to two hole charge occupation (see section 3.6). The expected orbital spacing for a 2D artificial atom with 27nm radius is ∼3meV (see section 3.6). In Figure 3.14(b) we find that the orbital spacing between the Ground State (GS) and the first Excited State (ES) is 3.5meV, and that the first four excited states fit to a linear trend with slope 2.5meV per orbital. The experimentally observed orbital spacing is consistent with the expected orbital spacing for a 27nm radius circular quantum dot.

Finally, we investigated the energy spectrum of the two hole quantum dot. We can determine the strength of hole-hole interactions within the quantum dot by comparing the two-hole energy spectrum with the one-hole energy spectrum. Figure 3.14(c) shows the excited state spectrum for the two-hole quantum dot, which is a cut along the dashed white line labeled (c) in Figure 3.14(a). A key feature of the two hole dot is that the first excited state is now only 0.25meV above the ground state (inset of Figure 3.14(c)), while the separation between excited states remains comparable to the N=1 transition excited state energy separation of ∼3meV. The reduction in the spacing between the

ground state and first orbital state (3.5meV for the one hole system, and 0.25meV for the two hole system) results from the additional Coulomb interaction energy when one hole already occupies the lowest energy orbital[1]. The observation of a 0.25meV excited state spacing for the two-hole dot is consistent with the 0.2meV Zeeman energy required to induce a singlet-triplet ground state transition in Figure 3.11(e). Based on the change in first orbital energy spacing, we estimate that the hole interaction energy is ∼3.25meV, which is ∼90% of the orbital energy. The measured hole-hole interaction energy is much larger than the electron-electron Coulomb interaction energy measured in GaAs and silicon [49] lateral quantum dot devices[2]. Large hole-hole interaction energies (compared to the orbital energy) have also been observed in laterally defined GaAs hole quantum dots [122] and in InAs hole quantum dot devices [103].

The observation of this large Coulomb interaction provides strong motivation for operating hole spin qubits in the single hole (N=1) regime. In the single hole regime the qubit basis states are isolated from the additional energy levels by the orbital spacing. However, when more than one hole is present, strong hole-hole interactions can complicate the energy spectrum and decrease the isolation of the basis states from potential leakage states. Finally, we note that the large Coulomb interaction provides additional insight into the analysis of the orbital shell filling. In InAs quantum dots the enhanced Coulomb interaction has been observed to non-standard shell filling of the Fock-Darwin orbital states [103]. Therefore the large Coulomb interaction may provide an explanation for why the 7^{th} and 8^{th} holes depart from the Fock-Darwin magic numbers in this device (see section 3.5).

3.8 Conclusion and outlook of Chapter Three

In this Chapter we have presented the first experimental evidence of the orbital shell structure and spin filling sequence of holes in a silicon MOS quantum dot. The orbital

[1] See section 1.3.2.

[2] For both GaAs [47] and Si [49] lateral quantum dots the electron-electron Coulomb interaction energy has been observed to be around 50% of the orbital energy. This has been extracted by comparing the difference between the N=1 single particle energy spectrum and the N=2 excited state spectrum.

level spacing and the spin filling suggests that the confinement potential is close to parabolic. We have extracted the ground state spin filling for N=1 to 6 holes. These results show that holes in a planar circular quantum dot follow the standard 2D artificial atom spectrum observed in high quality GaAs electron based devices [1, 9]. We emphasize that this spectrum is achieved due to the tight confinement provided by the surface gate structure of the device. Finally, we observe polarized spin filling and determine that strong hole-hole interactions affects the two-hole energy spectrum. These results highlight the unique physics of 2D hole artificial atoms, and clearly demonstrates that spin properties and energy scales are very different to nanowire and electron artificial atoms [6, 76, 104, 128]. This Chapter demonstrates a step forwards for p-type silicon MOS quantum devices, by providing experimental evidence for energy structure of a device in a known and reproducible charge configuration.

A promising result is the observation of the orbital dependence of the hole g-factor. We observe that the g-factor for an in-plane magnetic field orientation varies from 1.1 to 1.6 across three distinct orbital states. Engineering the g-factor has many applications in spin based quantum electronics. Variation in the g-factor allows holes in different orbitals to experience a different Zeeman splitting. This could be used to individually manipulate hole spins, by tuning the resonance frequency to the Zeeman energy of a specific state. Further, the change in g-factor for different orbitals suggests the hole g-factor is dependent on the orbital angular momentum (s-orbital or p-orbital). This has been observed in other semiconductors with strong spin-orbit coupling, where electric fields allow fine control over the g-factor [73, 131, 132]. In addition to tuning the g-factor, an oscillating electric field will produce an oscillating g-factor, allowing local electric spin manipulation equivalent to ESR [62]. In order to assess the suitability of exploring these interesting experimental regimes, it would first be important to fully characterise the g-tensor, and gain some further insight into how the g-tensor is related to the hole orbital confinement.

Chapter 4

Electric control of the single hole g-tensor

Abstract

Studies of the g-tensor are valuable for characterising the spin physics of semiconductor systems. Hole spins confined in silicon MOS quantum dots are a promising platform for spin-based electronic applications, however there are only limited studies regarding the physics of hole spins in these structures. In this Chapter we isolate a single hole in a quantum dot, place it in a known orbital state, and then study the full 3D anisotropic g-tensor. We find that the orientation of the g-tensor can be electrically tuned, and that the components of the g-tensor be electrically controlled by more than a factor of two by changing the gate voltage by just 0.2V. These results show that both the magnitude and orientation of the hole g-tensor is strongly electrically tunable. We have developed a 3D Luttinger model to support these results, which suggests that spatial dependence of the hole g-factor results from the symmetry of the quantum dot orbital confinement. The strong electric modulation of the g-factor demonstrates that hole spins in silicon MOS quantum dots are a promising candidate for spin-qubit applications.

4.1 Publication

The results presented in this chapter are in preparation for publication. Liles, S. D., Martins, R., Miserev, D. S., Thorvaldson, I. D., Rendell, M., Hudson, F. E., Veldhorst, M., Sushkov, O. P., Dzurak, A. S., Hamilton, A. R. (2019). Electric control of the single hole g-tensor. *Article in preparation.*

4.2 Introduction

In 1896 P. Zeeman observed that the atomic spectral lines of sodium could be broadened by the presence of an external magnetic field. The explanation of this experiment, now known as the Zeeman effect, was provided by H.A. Lorentz, and both physicists jointly received the Nobel prize in 1902. Electrons in atomic shells posses a magnetic dipole moment, which arises from both the orbital and spin angular momentum[1]. This dipole moment can interact with magnetic fields, giving rise to a *Zeeman splitting* of the atomic orbital spectrum. The Hamiltonian for the Zeeman effect can be written as

$$H_Z = \mu_B(\boldsymbol{L} + 2\boldsymbol{S}) \cdot \boldsymbol{B} \tag{4.1}$$

where $\boldsymbol{L}$ is the orbital angular momentum, $\boldsymbol{S}$ is the spin angular momentum, and $\boldsymbol{B}$ is the applied magnetic field. However, it is more convenient to work with the total angular momentum ($\boldsymbol{J} = \boldsymbol{L} + \boldsymbol{S}$), and Equation 4.1 is conventionally simplified to the form

$$H_Z = g\mu_B \boldsymbol{J} \cdot \boldsymbol{B} \tag{4.2}$$

by using $g\boldsymbol{J} = (\boldsymbol{L} + 2\boldsymbol{S})$, where g is the Landé g-factor[2].

[1] Historically the influence of the orbital magnetic moment has been known as the *normal* Zeeman effect, and could be described by the theory of H.A. Lorentz. At the time, it was not known that electrons posses an intrinsic spin magnetic dipole, and so the spectral splitting due to spin was known as the *anomalous* Zeeman effect.

[2] For a free spin-state the Landau g-factor is given by

$$g = \frac{J(J+1) + S(S+1) - L(L+1)}{2J(J+1)}. \tag{4.3}$$

The g-factor is typically extracted by observing the Zeeman splitting of an energy level. Spin-orbit coupling can give rise anisotropic Zeeman splitting, and this anisotropy is best described by an anisotropic g-tensor. In this framework, the g-tensor is a 3x3 matrix, which is diagonal in a suitable choice of coordinate axes. The simplest form of the g-tensor is written as

$$g = \begin{pmatrix} g_1 & 0 & 0 \\ 0 & g_2 & 0 \\ 0 & 0 & g_3 \end{pmatrix} \tag{4.4}$$

where g_1, g_2 and g_3 are the principal g-factors and the co-ordinate axes that diagonalize the g-tensor are known as the principal axes, or the principal magnetic axes [57, 133][1]. For an arbitrary magnetic field orientation the observed Zeeman splitting is given by the effective g-factor

$$g^*(\boldsymbol{B}) = \frac{\sqrt{g_1^2 B_1^2 + g_2^2 B_2^2 + g_3^2 B_3^2}}{|\boldsymbol{B}|} \tag{4.5}$$

where B_1, B_2, B_3 are the components of the magnetic field along the three mutually orthogonal principle axes.

The Landé g-factor is the central parameter that characterizes the response of a spin to an applied magnetic field. In semiconductors, variations of the Landé g-factor from the free electron g-factor value arise due to coupling between the spin and orbital degrees of freedom. The strength of the spin-orbit coupling can be varied through means such as material composition, crystal orientation or confinement, and these effects can be observed in the Landé g-factor. Studies of the modulation of the g-factor can therefore provide detailed insight into the underlying spin physics of electrons and holes semiconductor devices.

A motivation for characterising the Landé g-factor is that in-situ modulation of an electron or hole spin state has wide applications for spin based electronics. In low dimensional systems such as quantum dots, the electrically defined confinement profile can result in

This gives a Landé g-factor of 2 for a free electron in a vacuum ($L = 0$, $S = 1/2$, and $J = L + S = 1/2$).

[1] Conventionally the axes are chosen such that $g_3 > g_2 > g_1$.

an anisotropic and tunable g-factor [51, 127]. Electrical modulation of the g-factor provides a mechanism for local electric spin manipulation [61, 62], while in-situ control of the spin-splitting can facilitate selective addressability of single spin states in devices with multiple adjacent quantum dots. These properties are particularly appealing for implementation in spin-qubits. As such, localized spins in semiconductors with electrically tunable g-factors are attracting attention for use in spin-based quantum information applications [5, 20, 21, 23, 26, 72, 122, 125, 132].

Hole spins in silicon quantum dots are a promising platform for spin-based qubits. While electrons in silicon MOS quantum dots are one of the most successful spin qubit systems [6, 55], electron spin manipulation requires additional device fabrication such as ESR strip lines [13] or micro-magnets [63]. For holes, the inherently strong spin-orbit coupling allows electrical spin manipulation and recent experiments have confirmed that hole spins exhibit rapid all-electric spin manipulation [20, 23, 26]. However, challenges remain for hole spin qubits. The spin coherence times for holes has been found to be short, on the order of hundreds of nanoseconds, and since there are only a limited number of studies of hole spin properties, identifying the exact mechanism driving the spin manipulation and decoherence has proven to be challenging [21]. Studies presented in Chapter 2 and Chapter 3 have shown it is possible to reach the last hole in silicon MOS quantum dots. Detailed characterisation of the hole g-factor anisotropy in a known charge and orbital state will provide valuable insight into the underlying properties of the hole spin-states.

4.3 Literature review of g-tensor modulation in semiconductors

In this chapter there are two primary motivations for characterising the g-factor of hole spins confined in silicon MOS quantum dots. The first motivation is that studies of the g-tensor provide detailed insight into the underlying spin physics. The second motivation arises since the ability to electrically control the g-tensor demonstrates that a spin system is highly suitable in various spintronic applications, such as spin-qubits. The aim of this

literature review is to place these two motivations in the context of recent literature[1].

There is a wide range of g-factor studies in the research literature, which covers various semiconductor systems and uses a variety of experimental techniques. However, the spin physics of holes in silicon quantum dots is still not well understood. To begin this review, in section 4.3.1 we present the main physical mechanisms that are known to cause g-tensor anisotropy and modulation in semiconductor devices. These mechanisms will serve as the basis for analysis of our experimental results later in this chapter. Finally, in section 4.3.6 we describe the relationship between electrical modulation of the g-factor and the ability to perform all electric spin manipulation.

4.3.1 Mechanisms for g-tensor modulation

The Landé g-factor is an experimentally accessible parameter that characterizes the response of spins to a magnetic field. Experimental studies of the g-factor are therefore a powerful tool for extracting and understanding the underlying spin physics of a system. In this section we review experimental studies in order to describe the main physical mechanisms known to influence the g-factor[2]. In section 4.3.2 we describe the effect of semiconductor material composition on the g-factor. In section 4.3.3 we discuss the effect of the crystal orientation on the g-tensor anisotropy. In section 4.3.4 we show that orbital confinement in systems with strong-spin orbit coupling significantly influences the g-factor. Finally, in section 4.3.5 we discuss the effect the that Heavy-Hole Light-Hole mixing has on the hole g-tensor.

[1] In that sense, this section is a review of the main physical concepts with support from appropriate literature, rather than a review of all g-factor literature. See chapter 2 for a literature review of silicon MOS quantum dot devices, and chapter 3 for a review of spectroscopic measurements of hole quantum dots.

[2] This review focuses on providing context and understanding of the key physical mechanisms. Particularly, in the context of the experimental work that is presented in this chapter. The research selected in this review is mostly electrical studies of the g-factor in quantum confined semiconductor systems.

4.3.2 Material composition

The variation of the Landé g-factor from the free value of 2.0 is due to spin-orbit coupling [134]. For this reason material composition plays an important role in defining the Landé g-factor in semiconductor devices [135]. The spin-orbit coupling in semiconductors is mediated by factors including the atoms occupying the lattice, the distinct lattice symmetry, and the band-gap energy [51, 127, 135, 136](see section 1.3.5). Therefore devices composed of different semiconductor materials can exhibit g-factors that can vary significantly in both magnitude and sign[1]. In addition to inter-device material differences, variations of the semiconductor material within a single device can significantly impact the g-factor.

Quantum electronic devices commonly employ heterostructures in order to confine electrons (or holes). The specific materials forming the heterostructure play an important role in determining the g-factor. This is because the active charge states are typically confined near the heterointerface. For example, in GaAs/AlGaAs heterostructures electrons are often confined in a GaAs region at or near an AlGaAs interface. This interface impacts the electron effective g-factor since the g-factor is -0.44 in GaAs, while in AlGaAs the electron g-factor is +0.4. When electric fields are used to tune the overlap of the electron wavefunction into the AlGaAs region it is possible to achieve a weak modulation of the electron g-factor [137].

Jiang & Yablonovitch [137] studied the electric tunability of the electron g-factor using the device shown in Figure 4.1(a). This device is an AlGaAs/GaAs heterointerface device with a top and back gate. Figure 4.1(b) shows the measured g-factor as a function of the top gate and back gate voltage. The inset in Figure 4.1(b) schematically shows the effect of the gate voltage, which shifts the wavefunction with respect to the interface. The main result of Figure 4.1(b) is that the g-factor is weakly tuned to be more like the AlGaAs value (+0.4) or the GaAs value (-0.44) consistent with the voltage induced shift in the wavefunction position.

Building on the results of a composition based g-factor modulation, Salis *et al.* [61]

[1]Interested readers can see Figure 1 in [136], which shows the the electron g-factor in various III-V materials.

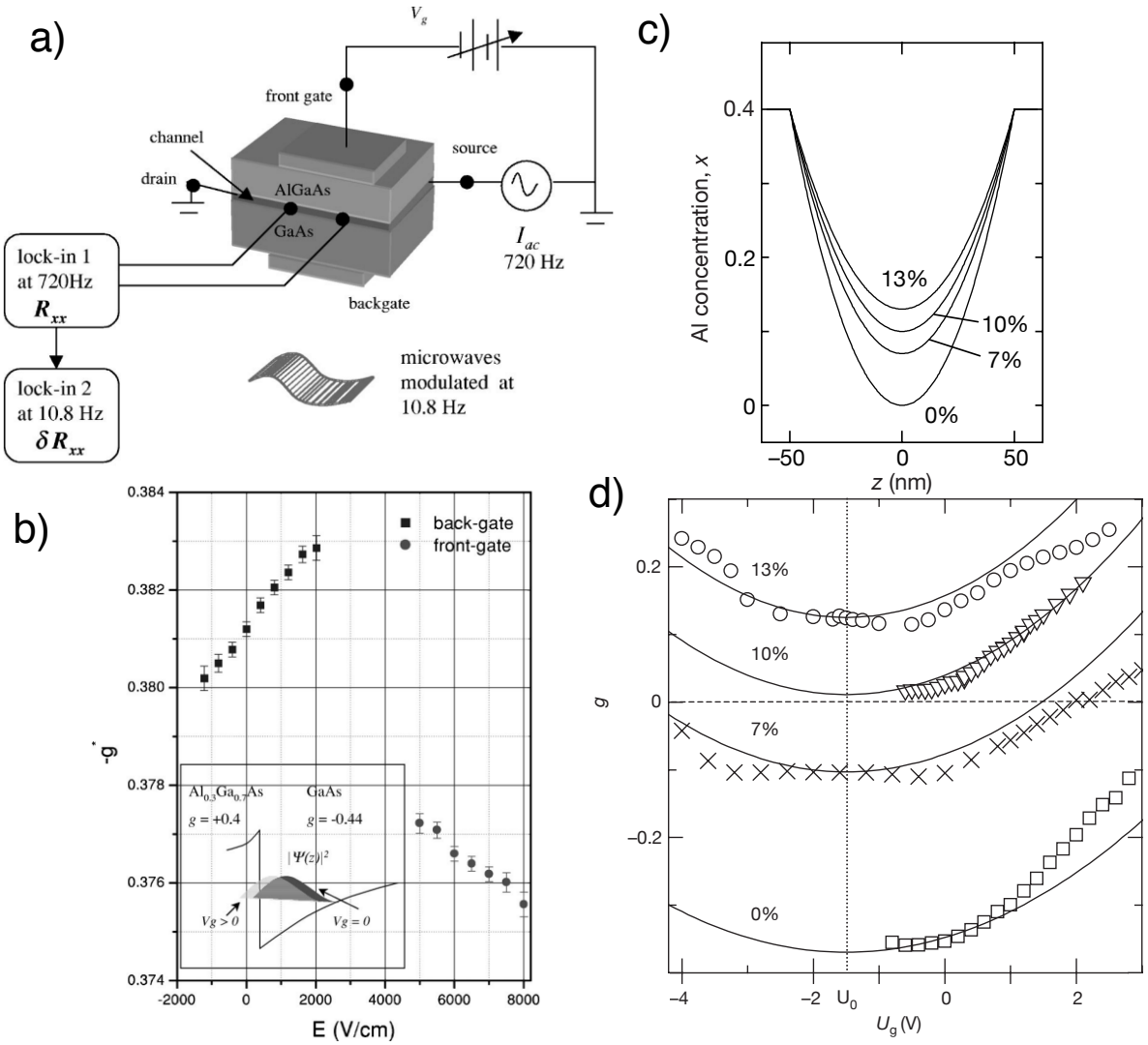

Figure 4.1: **Electron g-factor modulation in AlGaAs/GaAs heterostructures:** (**a**) Shows the schematic outline of the AlGaAs/GaAs device studied by Jiang & Yablonovitch [137]. (**b**) Results of the electron g-factor measured in device (a) as a function of the front (circle) or back (square) gate voltage. The inset indicates how the front and back gate control the overlap of electrons wavefunction into the AlGaAs region. (**c**) Shows the vertical profile of the Al concentration in the samples studied by Salis *et al.* [61]. The Al concentration of the AlGaAs quantum well is varied quadratically from the well center (z=0) up to 0.4 at the barriers. Labels indicate the Al concentration at z=0. (**d**) Tunability of the g-factor measured in [61] as a function of the voltage difference between the front and back gate voltages U_g. The symbols are the measured values for four different Al concentration profiles and solid lines are weighted average fits to the data. A particularly interesting result is that for $x_o = 7\%$ it is possible to electrically tune the g-factor to 0 (at $U_g = 2$V), thereby electrically 'turning off' the spin response.

showed that it is possible to substantially increase the electric tunability of the electron g-factor by specifically engineering the composition of an AlGaAs/GaAs/AlGaAs quantum well device. The devices studied by Salis *et al.* are grown by Molecular Beam Epitaxy (MBE) and have an $Al_{x_o}Ga_{1-x_o}As$ quantum well embedded between two $Al_{0.4}Ga_{0.6}As$

barriers, where x_o is the Al concentration at the center of the $Al_{x_o}Ga_{1-x_o}As$ quantum well. The Al concentration is increased quadratically from x_o to 0.4 from the center of the well to the barrier. Figure 4.1(c) shows examples of the Al concentration along the vertical axis of the quantum well. Figure 4.1(d) shows electric modulation of the g-factor due to bias between the front and back gate (U_g) for different x_o values. There are two clear results here: (1) Salis *et al.* observed that the g-factor shows and approximately parabolic trend, tending towards the AlGaAs value of +0.44 as larger fields displace the wavefunction further from the center of the well; (2) the g-factor at the minima (vertical dashed line) increases towards the AlGaAs value as the Al concentration is increased. While Salis *et al.* observed an electrical modulation of the g-factor up to around 75% (using a specially engineered heterostructure), in the case of a of typical heterojunction Jiang & Yablonovitch observed a change in the g-factor of only around 1%. This is typical, and strong electric modulation of the g-factor due to material composition tends to only occur in specially engineered situations[1].

Material composition is most significant when comparing the g-factor of similar quantum devices fabricated in different materials. However, as we have discussed both Jiang & Yablonovitch [137] and Salis *et al.* [61] observed the material based modulation of the g-factor for electrons within a AlGaAs/GaAs heterojunction device. In the experimental results of this chapter we study hole spins in a silicon MOS quantum dot. The quantum dot is formed at the Si/SiO_2 interface, and is defined by a lateral gate structure. The wavefunction is not expected to overlap strongly into the oxide, and so material gradient effects are expected to be extremely weak.

4.3.3 Crystal orientation

It is possible for the g-tensor to be sensitive to the crystal orientation. This can occur when the crystal structure gives rise to anisotropic spin-orbit coupling. The most common example of this is Bulk Inversion Asymmetry (BIA), which can introduce a Spin-Orbit Interaction (known as the Dresselhaus effect) that is anisotropic with respect

[1] In situations where strong electric modulation of the g-factor is observed in standard devices, the explanation is typically one of the mechanisms discussed in the following sections.

to the crystallographic axes [138]. Since the g-factor is directly linked to the spin-orbit coupling, Bulk Inversion Asymmetry (BIA) introduces anisotropy to g-tensor based on the crystal orientation. Effects of BIA are strong in III-V semiconductors, in contrast, the effects of BIA are extremely weak in bulk silicon due to the diamond lattice.

Due to the suppression of spin-orbit interactions, the Landé g-factor in bulk silicon is isotropic and close to the vacuum value. However, in MOS silicon quantum devices the Si/SiO_2 necessarily terminates the crystal along a specific atomic plane. This Si/SiO_2 interface therefore breaks the inversion asymmetry, and gives rise to a Dresselhaus type spin orbit interaction [139, 140]. Electrons confined near the Si/SiO_2 interface will have an anisotropic g-tensor, that is defined by the crystal orientation[1].

Tanttu *et al.* [52] studied the g-factor anisotropy of electrons in a silicon MOS quantum dot. A schematic vertical profile of the device is shown in Figure 4.2(a) where quantum dots can be formed under the metal gates as indicated by QD1 and QD2. In these devices the electrons are confined extremely close to the Si/SiO_2 interface. Since the sample is grown in the [001] direction, the Si/SiO_2 interface lifts the degeneracy of the in-plane $[1\bar{1}0]$ and [110] orientations. Figure 4.2(b) shows measured the g-factor of QD1 as a function of the crystal orientation. The red data corresponds to the effective g-factor measured along the lattice directions indicated in the upper axis of the figure. Despite the g-factor only changing by $\approx$1.5%, the observed g-factor anisotropy is consistent with an interface defined g-tensor anisotropy, with maxima and minima occurring along the $[1\bar{1}0]$ and [110] crystal orientations respectively .

Tanttu *et al.* [52] are able to clearly observe the weak effect of the crystal orientation on the electron g-factor in silicon. This is achievable since the other spin-orbit interaction effects (such as Structural Inversion Asymmetry) are strongly suppressed. In the experimental results presented later in this chapter we study a silicon MOS device with nearly identical lithography to that of Tanttu *et al.*. However, we study hole spin states, which will experience an additional spin-orbit interaction due to the valence band *p*-orbital nature (see section 1.5.2). If the crystal orientation is the single strongest component contributing to the hole g-tensor, we would expect to find that the principal magnetic

[1]Since all the other spin-orbit interaction effects are weak.

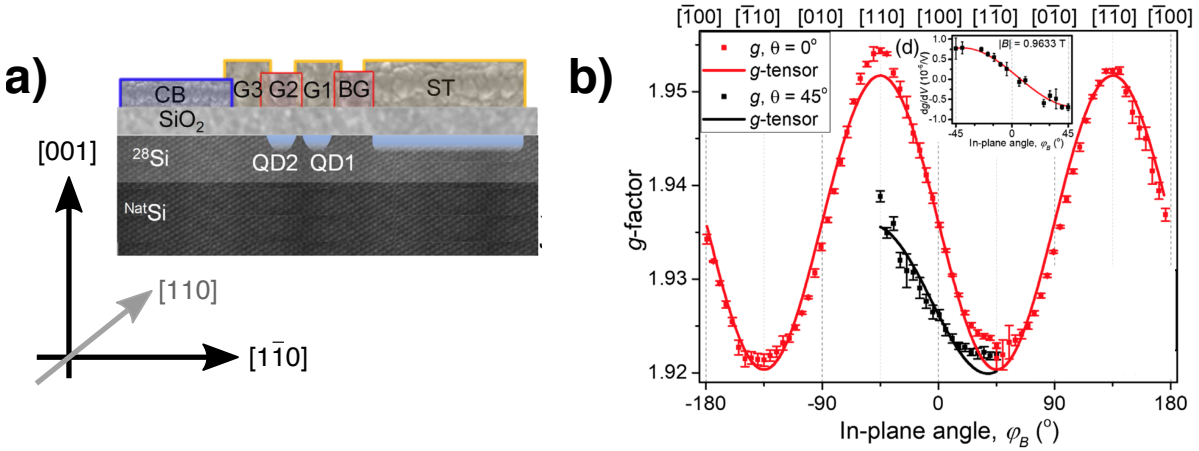

Figure 4.2: **g-factor modulation in a Si quantum dot:** (**a**) Schematic vertical cross section of the Si MOS quantum dot studied by Tanttu *et al.* [52] showing the location of two quantum dots (QD1 and QD2). The sample plane is the axes parallel to the Si/SiO_2 interface. The co-ordinates indicate the relevant crystal axes, where grey arrow indicates the direction into the page. (**b**) Shows the g-factor measurements for QD1. Red data shows the results for an in-plane magnetic field rotation, while the black data shows the results for an in-plane magnetic rotation where the out-of-plane angle is fixed at 45deg. The angled measurement (black data) was performed to obtain off-diagonal g-tensor elements for additional analysis. Inset shows the dg/dV (top) as a function of in-plane field orientation. Reproduced from [52].

axes are fixed by the crystal axes, and cannot be rotated with electric fields.

4.3.4 Orbital confinement

In this section we discus the effects of confinement on the g-tensor. Variations in the Landé g-factor are mediated by coupling between the spin and orbital angular momentum. Quantum confinement significantly influences the orbital angular momentum of electrons and holes. Therefore, confinement leads to a modulation of the g-factor, which is mediated by the strength of the spin-orbit coupling [51, 127]. Confinement effects can be especially significant in quantum dots with strong spin-orbit coupling [127]. This is because quantum dot confinement is three dimensional, often electrically defined, and often anisotropic. This gives rise to electrically tunable, three dimensional, anisotropic g-tensors. In the following review we present results of electrical studies of the g-tensor anisotropy in semiconductor quantum dots. The main purpose of presenting these results is to demonstrate the g-factor modulation and anisotropy in systems with some similar

properties to holes in planar MOS quantum dots[1], which are experimentally studied in this chapter.

Semiconductors such as InAs and InSb are ideal for investigating the consequences of orbital confinement on the g-factor since these heavy elements have small band-gaps leading to strong spin-orbit coupling [51]. Takahashi *et al.* [141] have studied the full three dimensional g-factor anisotropy of electrons confined in self-assembled InAs quantum dots. Figure 4.3(a) shows an SEM image of the device studied by Takahashi *et al.*. The device contains a single self assembled quantum dot that is 30nm high with a 100nm base. The 100nm base provides weak confinement, allowing the in-plane confinement to be primarily controlled using electric fields applied by the side gate.

Takahashi *et al.* characterised the g-factor anisotropy by performing measurements of the g-factor as the magnetic field orientation was stepped in increments around the x-y, y-z and x-z sample axis. The results of the x-y, y-z and x-z rotations are shown in Figure 4.3(b),(c) and(d) respectively. The solid red lines in Figure 4.3(b-d) show the best fit of the raw data and the dashed black lines indicate the orientation of the principal magnetic axes with respect to the sample x, y and z axes. The principal magnetic axes define the orientation of the g-tensor. Takahashi *et al.* studied the g-tensor orientation for multiple charge occupations and found that the magnitude and orientation of the g-tensor varied for each case. Since different charge states will occupy different quantum dot orbital levels, this result suggests that the g-tensor is primarily defined by the symmetry of the orbital confinement [127].

To demonstrate that it is the orbital confinement symmetry which primarily influences the spin-states, Takahashi *et al.* studied the g-factor anisotropy for different confinement symmetries. The confinement of the quantum dot can be tuned using side gate voltage V_{sg}. Figure 4.3(e) shows the x-z anisotropy profile for three distinct side gate voltages. In each case both the magnitude and the orientation of the g-tensor is different (highlighted

[1]We begin by discussing electrons in InAs. For electrons in InAs the spin-orbit length has been measured to be 127nm [67], while for holes in silicon MOS quantum dots it has been measured as 110nm [28], which is comparable. However, there are distinct differences, for example electrons in InAs are spin 1/2, while the ground state holes in silicon MOS quantum dots are spin 3/2. In addition, we discuss InAs self assembled and nanowire quantum dots, which have different lithographic confinement to MOS quantum dots.

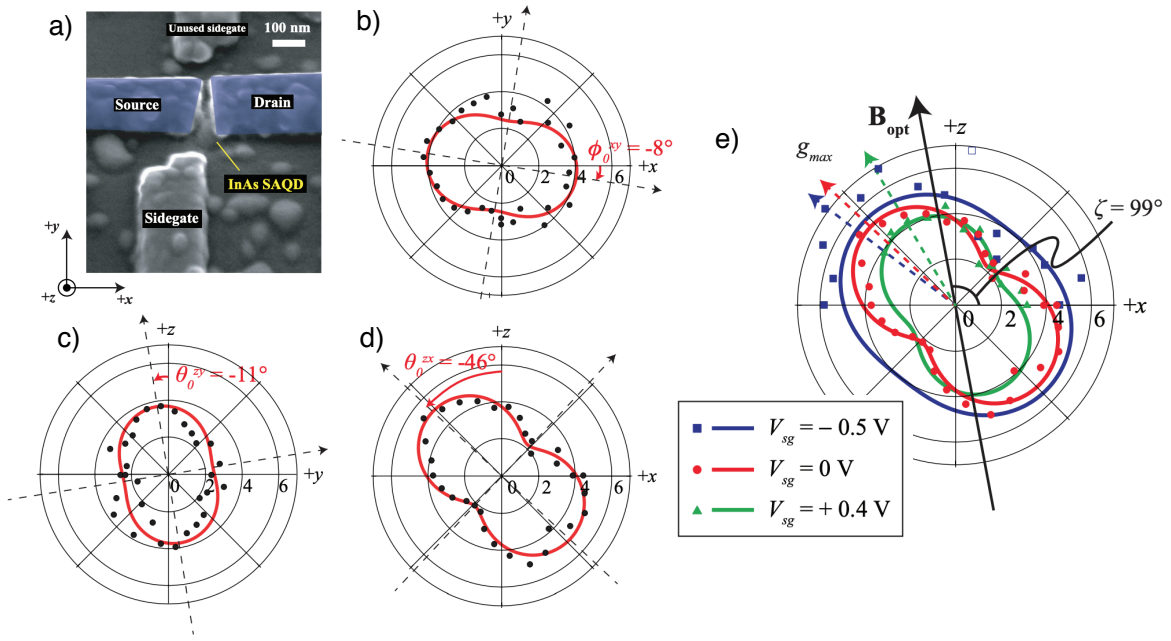

Figure 4.3: **3D g-factor anisotropy in InAs SAQD:** (**a**) Shows a false color SEM image of an InAs Self Assembled Quantum Dot (SAQD) on a (001) semi-insulating GaAs substrate. The side gate controls the confinement symmetry (**b-d**) Measurements of the g-factor around the x-y, y-z and x-z sample axes respectively, with dots for data and red solid lines for the best fit. The dashed arrows indicate the orientation of the principal magnetic axes extracted from the best fit. (**e**) The g-factor anisotropy in the x-z sample plane is measured for three different side gate voltages. The orientation of the principal magnetic axes, g_{max} is shown as a colored arrow and is electrically tunable. Further, the magnitude of anisotropy is clearly different between each V_{sg} measurement. $\mathbf{B}_{opt}$ and ζ indicate the optimum external magnetic field orientation to achieve the fastest g-TMR spin manipulation. Reproduced from [141].

by the dashed colored arrows), demonstrating that the g-factor anisotropy is sensitive to orbital confinement profile.

It could be expected that the crystal confinement axes of the Self Assembled Quantum Dot (SAQD) may define the orientation of the orbital states and therefore the g-factor anisotropy. However, the result presented in Figure 4.3(e) shows that g-factor anisotropy is very sensitive to the electric field confinement, even in a Self Assembled Quantum Dot. One challenge in furthering the analysis of Takahashi *et al.* is that the device was in an unknown charge and orbital state. This prevents the ability to reproduce results, or apply a more detailed model to gain a deeper understanding.

Nanowire quantum dots similarly have a hard radial confinement due to the crystal growth. Schroer *et al.* [142] have studied the g-tensor of electrons in InAs nanowires and show that the g-factor anisotropy is extremely sensitive to electrically defined confine-

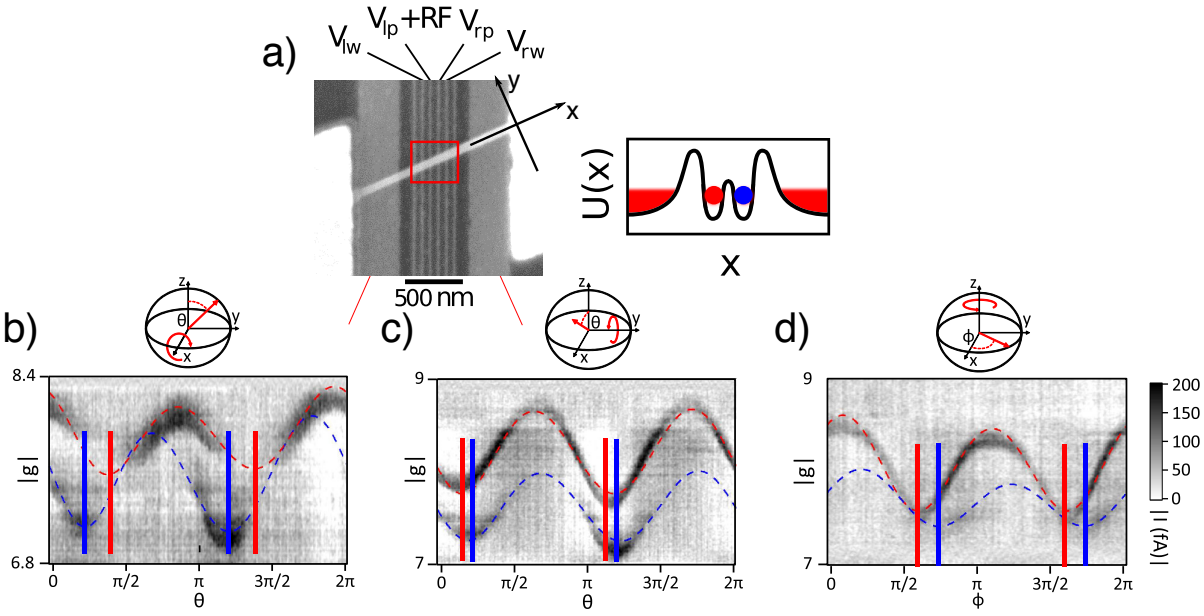

Figure 4.4: **Electron g-factor anisotropy in an InAs nanowire quantum dot:** (**a**) This SEM image shows a nanowire placed on top of an array of gates. The schematic to the right shows the potential profile in the region indicated by the red square in the SEM. This profile indicates the device mode when tuned to form a double quantum dot. (**b-d**) Schroer *et al.* [142] study g-factor as a function of magnetic field orientation for a rotation around the y-z, x-z and x-y axes as indicated by the insets. Two distinct trends can be observed and these are highlighted with red and blue dashed lines. Solid vertical lines indicate the difference in phase between the red and blue trends. The two g-factor trends result from the two distinct quantum dots in the double dot device. Reproduced from [142].

ment, and is only weakly related to the crystal growth axes. In Figure 4.4(a) we show the SEM of a nanowire quantum dot with the a schematic showing the device in the double quantum dot regime. Figures 4.4(b-d) show the results of g-factor anisotropy, which is measured by observing the g-TMR resonance frequency as a function of magnetic orientation. These measurements were performed in the (1,1) charge regime. Two trends are present (red and blue dashed lines), which are the distinct g-factor of the left and right quantum dot in the schematic of Figure 4.4(a). The red and blue trend lines shows that even for two electrons confined in the same nanowire, separated by only tens of nanometers, the g-tensor has a different symmetry and magnitude (indicated by the colored lines to mark the phase). The difference between the g-tensor for two adjacent quantum dots results from the small differences in the local electric confinement.

The hole g-tensor has been studied in silicon nanowires by Voisin *et al.* [73] and Crippa *et al.* [21]. A false color SEM image of the CMOS nanowire device used by Crippa *et al.* is shown in Figure 4.5(a). Using this device a double quantum dot can be formed directly

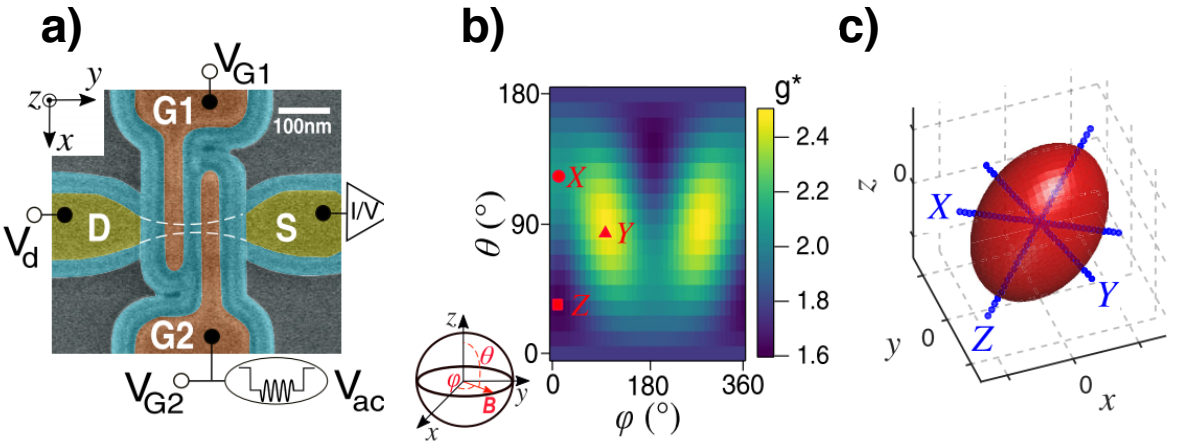

Figure 4.5: **Hole g-factor anisotropy in a Si CMOS nanowire quantum dot:** (**a**) Shows a false colour SEM image of a silicon CMOS nanowire device. The nanowire channel runs underneath G1 and G2, allowing the formation of single or double quantum dots in nanowire channel. The nanowire is aligned with the y axis as shown in the upper left corner. (**b**) Shows the g-factor as a function of the in-plane (ψ) and out-of-plane (θ) angles. The red text indicates the extracted orientation of the g-tensor axes. While the Y axis is close to the lithographic y-axis $(\psi, \theta) = (90^o, 90^o)$, the X and Z axes are not aligned with the lithography. (**c**) Shows the isosurface $\Delta E^2 = (g^* \mu_B B)^2$ with respect to the sample axes (x, y, z), highlighting the arbitrary orientation of the g-tensor with respect to the nanowire. Reproduced from [21].

under gates G1 and G2. Figure 4.5(b) shows a color map of the 3D hole effective g-factor (g^*). The red text (X, Y, Z) indicates the orientation of the principal axes of the g-tensor. The principal magnetic axes are aligned arbitrarily to the nanowire axes (see caption). This is highlighted in Figure 4.5(c), which shows the isosurface of of $\Delta E^2 = (g^* \mu_B B)^2$ with respect to the (x,y,z) lithographic axes. Similar to the previous results of this section Crippa *et al.* find that the hole g-tensor is strongly defined by the symmetry of the confinement potential. The results of Crippa *et al.* allow a major advance in the understanding of the spin physics of holes in silicon quantum dots, which can be built upon with further study. Particularly, since the charge and orbital state studied by Crippa *et al.* is unknown, it would be valuable to perform 3D g-tensor characterisation using a device capable of reaching the last hole.

In this section we have discussed the effects of quantum confinement on the g-tensor[1]. In systems with strong spin-orbit coupling the the orbital confinement symmetry plays a

[1]In this review we focus primarily on the g-tensor for electrons in InAs. This selection is due to the similar spin-orbit coupling strength of InAs electrons to holes in silicon. In addition InAs electrons have had success as spin-orbit qubits [143]. Interested readers can review the g-factor modulation of holes in GaAs [108, 122], holes in silicon nanowires [20, 21, 73], holes in SiGe quantum dots [125, 132], or holes in germanium hut wires [22, 72]. Many of these results have been reviewed in the literature review of Chapter 3.

major role in determining the spin physics of the system. In particular, the orientation of the g-tensor is not fixed by a crystal or lithographic axes. This can be demonstrated by showing that the g-tensor orientation can be electrically tuned.

4.3.5 Heavy-hole light-hole mixing

In the previous section we discussed the effects of orbital confinement on the quantum dot g-factor. Intuitively this effect can be understood in terms of how the orbital confinement influences the coupling between the orbital states of a quantum dot. In this section we introduce the effects of heavy-hole light-hole mixing on the quantum dot g-factor.

Studies of SiGe quantum dots have enhanced the understanding of how heavy-hole light-hole mixing contributes to the hole g-factor modulation. Ares *et al.* [132] investigated the electric modulation of the hole g-factor in SiGe quantum dots in order to characterise the suitability of SiGe quantum dots for g-TMR spin manipulation [125]. Figure 4.6(a) shows a schematic of the device, which is a self assembled SiGe quantum dot with a metal top gate that can be used to control the vertical confinement. Ares *et al.* results in Figure 4.6(b) show that the hole g-factor can be modulated over a range from 2.5 to 0.5. This giant electric tunability demonstrates the SiGe hole quantum dots are a promising candidate for g-TMR based spin qubits with predictions of Rabi frequencies up to 100MHz [125]. However, despite the range of literature studying the g-factor modulation with and many mechanisms proposed[1], Ares *et al.* found that the experimentally observed giant g-factor modulation required a new, and so-far overlooked mechanism for theoretical predictions to match the experimental results.

The results of Ares *et al.* [132] g-factor modulation can be explained by analyzing the effect of the heavy-hole light hole mixing in the 2D Luttinger model. The mixing between the heavy and light hole states can be tuned by varying the strength of the vertical electric field. The insets in Figure 4.6(b) show schematically how the vertical confinement tunes relative displacement of the heavy-hole (red) and light-hole(blue) distributions, and thus influences the mixing. This effect had not been fully studied due to the limited number

[1]These mechanisms for g-factor modulation include material composition effects [61, 131], variations in the spin-orbit coupling strength [144] and orbital confinement [127, 145].

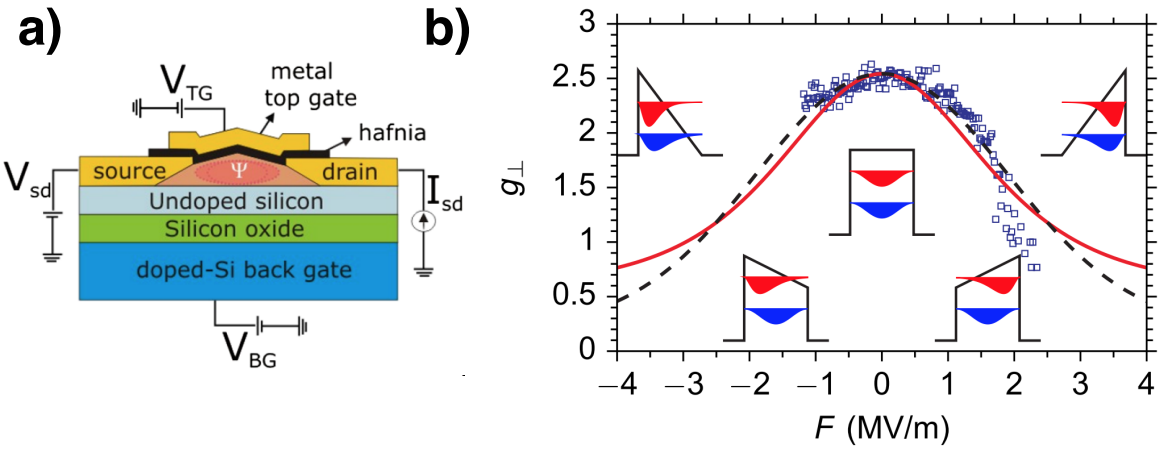

Figure 4.6: **g-factor modulation in SiGe quantum dots:** (**a**) Schematic of the self assembled SiGe quantum dot studied by Ares *et al.* [132]. (**b**) Experimental results (blue squares) and the theoretical predictions (red solid line) for the Heavy-Hole Light-hole induced g-factor modulation in SiGe quantum dots. The y-axis is the g-factor measured for a magnetic field oriented perpendicular to the sample interface and the x-axis is the magnitude of the electric field applied perpendicular to the sample interface (due to the top (V_{TG}) and back gate (V_{BG} in a). Insets indicate the Heavy Hole (red) and Light Hole (blue) wavefunctions at different vertical electric fields. Reproduced from [132].

of investigations into the hole g-factor modulation in quantum dots. The solid line in Figure 4.6(b) shows the theoretical predictions of the g-factor when the heavy-hole light-hole correction is included, showing that the model fits well to the data[1]. The heavy-hole light hole mixing can be controlled by the confinement strength of the quantum dot[2]. In this sense, intuitively the heavy-hole light-hole mixing can be thought of as a confinement effect specific for hole quantum dots.

Conclusion of g-tensor modulation mechanisms

In the preceding sections we have presented a review of the main physical mechanisms related to g-tensor modulation and anisotropy. In each case we have included a brief discussion of how each mechanism is expected to relate to holes in silicon MOS quantum dots.

[1]The dashed line shows an improved fit to the data. The model for the dashed line in Figure includes the heavy hole light hole mixing correction, then adds an addition field gradient across the sample due to the source and drain electrodes.

[2]Since the difference in effective mass leads to a splitting of the HH and LH energy states when asymmetric confinement is introduced. See section 1.5.1.

4.3.6 All-electric spin manipulation

The ability to electrically control the Landé g-factor is particularly useful for spin based applications. Spin qubits are one of the main applications that motivates the ongoing research into quantum dot spin states. All-electric spin manipulation is highly desirable, and can help improve the scalability and operation speed of spin qubits (see section 1.4). In section 4.3.7 we cover the novel spin manipulation technique known as g-Tensor Modulation Resonance (g-TMR), which allows electric spin manipulation as a direct consequence of g-factor modulation. In section 4.3.8 we discuss a second mechanism that allows electric spin manipulation known as Electric Dipole Spin Resonance (EDSR). We conclude this section by discussing the complications that can occur when both the g-TMR and EDSR mechanisms are present.

4.3.7 g-Tensor Modulation Resonance

We begin by describing the basic formalism of magnetically driven Electron Spin Resonance (ESR). We then follow the argument of Kato *et al.* [62] to describe g-Tensor Modulation Resonance (g-TMR) in the same frame as ESR.

The general Hamiltonian used to describe spin dynamics is

$$H = \vec{S} \cdot \vec{\Omega}, \tag{4.6}$$

where $\vec{S}$ is the spin angular momentum operator, $\vec{\Omega}$ is the spin-precession vector,

$$\vec{\Omega} = \frac{\mu_B}{\hbar} \left(\vec{g} \cdot \vec{B} \right), \tag{4.7}$$

μ_B is the Bohr magneton, $\vec{g}$ is the Landé g-tensor, and $\vec{B}$ is the magnetic field vector. If the applied magnetic field has a static and oscillating component it can be given by $\vec{B}(t) = \vec{B}_0 + \vec{B}_1 \sin(\omega t + \phi)$. In this case the Hamiltonian can be broken into the time

independent and time dependent components, such that

$$H = \left(\frac{\mu_B}{\hbar}\right)\vec{S}\cdot\vec{g}\cdot\vec{B}_0 + \left(\frac{\mu_B}{\hbar}\right)\vec{S}\cdot\vec{g}\cdot\vec{B}_1\sin(\omega t+\phi) \tag{4.8}$$

$$H = \vec{S}\cdot\vec{\Omega}_0 + \vec{S}\cdot\vec{\Omega}_1(t) \tag{4.9}$$

where $\vec{\Omega}_0$ defines the spin eigenstates, $\vec{\Omega}_1(t)$ defines the time dependent modulation to the spin projection and ω gives the frequency of the modulation. The primary effect of $\vec{\Omega}_1(t)$ is to produce spin resonance[1] when $\omega = |\vec{\Omega}_0|$.

Traditionally, in Electron Spin Resonance (ESR) experiments the time dependent term $\vec{\Omega}_1(t)$ is introduced by the oscillating magnetic field. However, if the g-tensor is electrically controllable ($\vec{g}(V_0)$), it is possible to introduce an $\vec{\Omega}_1(t)$ term by periodically modulating the g-tensor. If we take the case of $V(t) = V_0 + V_1\sin(\omega t+\phi)$) then the time dependent g-tensor is given by

$$\vec{g}(t) = \vec{g}(V_0) + \frac{d\vec{g}(V_0)}{dV}V_1\sin(\omega t+\phi)). \tag{4.10}$$

In this case the Hamiltonian for the spin dynamics becomes,

$$H = \left(\frac{\mu_B}{\hbar}\right)\vec{S}\cdot\vec{g}(V_0)\cdot\vec{B}_0 + \left(\frac{\mu_B}{\hbar}\right)\vec{S}\cdot\frac{d\vec{g}(V_0)}{dV}\cdot\vec{B}_0(V_1\sin(\omega t+\phi)) \tag{4.11}$$

$$H = \vec{S}\cdot\vec{\Omega}_0(V_0) + \vec{S}\cdot\vec{\Omega}_1(t) \tag{4.12}$$

In the case of Equation 4.12 spin resonance can be driven by electric g-tensor modulation, known as g-Tensor Modulation Resonance (g-TMR) [62]. As a final note we highlight that the time independent term, $\vec{\Omega}_0(V_0)$, has a dependence on the static voltage. Hence it is possible to characterise the expected g-TMR effects, since $\frac{d\vec{g}(V_0)}{dV}$ can be extracted from the voltage dependence of the Zeeman energy.

[1]Specifically it is the component of $\vec{\Omega}_1$ which is perpendicular to $\vec{\Omega}_0$ that can give rise to spin resonance. The component of $\vec{\Omega}_1$ which is parallel to $\vec{\Omega}_0$ modulates the Larmor spin precession frequency.

4.3.8 Electric-Dipole Spin Resonance (EDSR)

In the previous section we have discussed the mechanism by which an electrically tunable g-tensor ($\vec{g}(V_0)$) allows for electric spin manipulation. In this section we introduce a second mechanism for electric spin manipulation. This second mechanism is based purely on spin-orbit coupling, and is known as Electric-Dipole Spin Resonance (EDSR). Finally, we will discuss the relationship between these two mechanisms (g-TMR and EDSR).

We begin by providing a simple example to demonstrate how spin-orbit coupling can be used to enable Electric-Dipole Spin Resonance (EDSR) [146]. The aim is to present a Hamiltonian describing EDSR, which is analogous to the ESR and g-TMR Hamiltonian (Equations 4.9 and 4.12 respectively). We can consider a simple spin-orbit Hamiltonian[1]

$$H_{SO} = \alpha k_x \sigma_y. \tag{4.13}$$

Including the spin-orbit coupling in the spin dynamics gives the Hamiltonian

$$H = \vec{S} \cdot \vec{\Omega_0} + \alpha k_x \sigma_y. \tag{4.14}$$

We now consider a voltage source $V(t) = V_0 + V_1 \sin(\omega t + \phi)$, which produces an electric field that periodically displaces the electron (or hole) along the x-axis such that

$$x(t) = x_0 + (x_1)\sin(\omega t + \phi) \tag{4.15}$$

$$= x_0 + (\gamma V_1)\sin(\omega t + \phi), \tag{4.16}$$

where x_1 defines the amplitude of the oscillations along the x-axis. For small V_1 we have approximated $x_1 = \gamma V_1$, where $\gamma = \frac{\mathrm{d}x}{\mathrm{d}V}$. In the presence of $V(t)$, $k_x(t)$ is given by

$$k_x(t) = \left(\frac{m\omega\gamma V_1}{\hbar}\right)\cos(\omega t + \phi). \tag{4.17}$$

[1]This is a simplified version of the Rashba spin-orbit coupling Hamiltonian $H_R = \alpha(\vec{\sigma} \times \vec{k}) \cdot \hat{E}$ where α is a spin-orbit parameter, and $\hat{E}$ is a unit vector oriented along the electric field gradient [51, 146]. We can then simplify further by considering $\hat{v} = \hat{z}$ and that the motion is only along the x-axis, giving Equation 4.13.

Combining Equation 4.14 with Equation 4.17 gives the Hamiltonian

$$H = \vec{S} \cdot \vec{\Omega_0} + \quad \sigma_y \Omega_1(t) \tag{4.18}$$

where,

$$\Omega_1(t) = \left(\frac{\alpha m \omega \gamma V_1}{\hbar} \right) \cos(\omega t + \phi) \tag{4.19}$$

The form of Equation 4.18 is analogous to the ESR Hamiltonian (Equation 4.9) and the g-TMR Hamiltonian (Equation 4.12). EDSR relies on an A.C electric field oscillating the wavefunction back and forth in the presence of an external static magnetic field ($\vec{S} \cdot \vec{\Omega_0}$). Given these conditions, the displacement oscillations induce coherent spin rotations due to the spin-orbit coupling [60, 85, 146]. The time dependent term ($\Omega_1(t)$) is determined by the strength of the intrinsic spin-orbit coupling (α), the displacement amplitude of the electron ($x_1 = \gamma V_1$), and the frequency (ω). It is important to note that the expected magnitude of the EDSR effects cannot be extracted by observing the Zeeman energy dependence on the applied voltage[1].

Experiments with both g-TMR and EDSR

Both the g-TMR and EDSR effects arise due to spin orbit coupling, and are driven by electric fields. In this section we compare the two effects, and discuss the consequence when both are simultaneously influencing the spin dynamics. Electric spin manipulation via g-TMR is mediated by electric modulation of the g-tensor, and was originally observed by Kato *et al.* [62] in 2D GaAs/AlGaAs heterostructures [61]. Electric spin manipulation via EDSR is mediated by the motion of the wavefunction through the spin-orbit effective magnetic field, and was originally observed in III-V semiconductor quantum dots [59, 143]. However, in semiconductor quantum dots with strong spin-orbit coupling, electric modulation of the g-tensor is typically possible due to confinement effects (see section 4.3.4). For this reason g-TMR and EDSR can both simultaneously contribute to the electrically driven spin resonance. The key distinction is that g-TMR can be calculated by observing the voltage dependence of the g-tensor using basic Zeeman energy measurements, while EDSR cannot [21]. For this reason purely spin-orbit medi-

[1]Unlike the g-TMR, which can be calculated from Zeeman energy dependence.

ated spin resonance has become known as Iso-Zeeman Electric Dipole Spin Resonance (IZ-EDSR) [21, 60], to make the distinction clear.

A key study that demonstrates the coexistence of g-TMR and EDSR has been performed by Crippa *et al.* [21] using holes in silicon nanowires (see Figure 4.5(a)). Crippa *et al.* have performed detailed characterisation of the hole g-tensor[1]. Based on the measured g-factor modulation Crippa *et al.* were able to make a prediction for the spatial dependence of the pure g-TMR spin manipulation frequency (Rabi frequency). Figure 4.7(a) shows the calculated Rabi frequency as a function of magnetic field orientation. Figure 4.7(b) shows the experimentally observed Rabi frequency as a function of magnetic field orientation. Interestingly Crippa *et al.* found that the experimental Rabi frequency was much larger than that calculated from the pure g-TMR model, and the dependence on the magnetic field orientation was significantly different to the prediction.

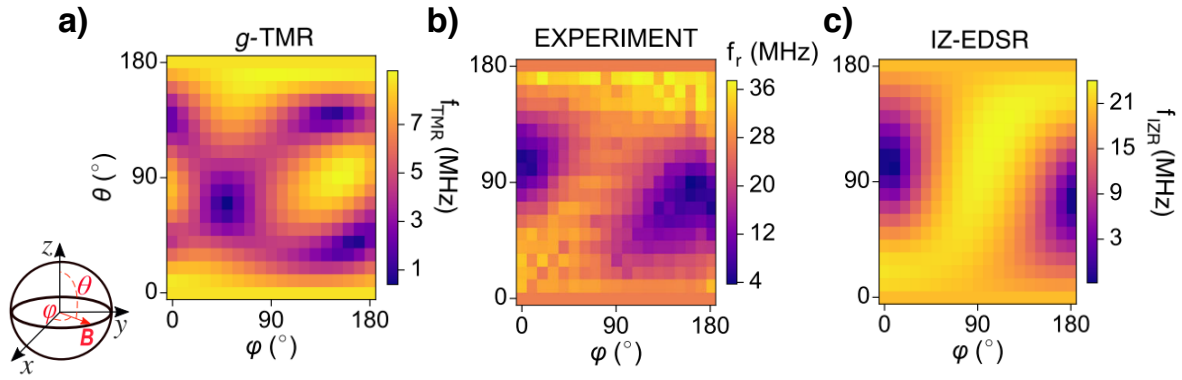

Figure 4.7: **g-TMR and EDSR of holes in silicon nanowires:** (**a**) Shows the calculated Rabi frequency of g-TMR as a function of magnetic field orientation (see inset in bottom left for axes). This has been calculated by observing the g-tensor anisotropy using measurements of the Zeeman energy. (**b**) Shows the experimentally observed Rabi frequency. Here the experimental Rabi frequency shows a different spatial profile and has a significantly larger magnitude than what is calculated by pure g-TMR. (**c**) Crippa *et al.* have extracted the Iso-Zeeman contribution to the Rabi frequency by comparing the difference between the calculated g-TMR map in (a) and the experimentally observed map in (b).

The discrepancy between the calculated and observed Rabi frequency shows that an additional mechanism for electrically driven spin resonance must be present to explain the anomalously high Rabi frequency. This additional mechanism was considered by Crippa *et al.* [21] to be the Iso-Zeeman spin manipulation effect, which results from the spin-orbit coupling[2]. The Iso-Zeeman effect can only be observed in time domain measurements

[1]The g-tensor measurements of Crippa *et al.* have been previously discussed in section 4.3.4.
[2]The Iso-Zeeman effect is the pure spin-orbit mediated Electric Dipole Spin Resonance (EDSR)

of the Rabi frequency, however the complication is that time domain measurements will have a combination of contributions from the Iso-Zeeman and g-TMR effects. By considering the difference between the experimental spatial Rabi frequency (which contains both the g-TMR and Iso-Zeeman contributions) and the pure g-TMR spatial Rabi frequency (calculated based on g-factor anisotropy measurements), Crippa *et al.* were able to determine both the magnitude and spatial dependence Iso-Zeeman spin manipulation frequency. Figure 4.7(c) shows the spatial dependence of the Rabi frequency for pure IZ-EDSR. Thus by including detailed g-factor anisotropy measurements Crippa *et al.* were able to deduce the physical properties of a spin mechanism that was not otherwise observable[1].

4.3.9 Conclusion of literature review

Variations of the observed Landé g-factor from the vacuum value are due to spin-orbit coupling. Detailed characterisation of the g-tensor has the potential to provide a deep understanding of the underlying spin-orbit physics of a semiconductor device. We have covered four mechanisms that primarily influence the g-tensor in semiconductor quantum dot devices. These are material composition, crystal orientation, orbital confinement and Heavy-Hole Light-Hole mixing. Understanding the typical influence of each of these effects (in terms of magnitude and spatial dependence) provides the foundation for interpreting results of g-tensor studies. When the spin physics are well characterised it is possible to develop new spin-based applications. One of the most relevant of these applications is all-electric spin manipulation. In this review we have covered the main concepts related to electric spin manipulation, and discussed how these are related to the g-tensor.

described in [60, 85] and has been described above.

[1]Based on these results Crippa *et al.* can predict the spatial dependence of the Rabi frequency, allowing optimal choice of magnetic orientation for fast spin qubit operation. In addition this can be used to characterise the spin-orbit magnitude and orientation.

4.4 Presentation of results in Chapter 4 and Appendix A

In Chapter 4 we present the key results from the experimental and theoretical study of the hole g-factor anisotropy. In order to clearly present these results, details regarding the characterisation of the device under study are presented in Appendix A. These characterisation measurements include confirmation of the absolute charge occupation (section A.3.1), and characterisation of the higher energy orbital shell structure (section A.4.1). Where relevant, the reader is referred to corresponding characterisation sections throughout the text.

4.5 Credits for sample fabrication

All measurements presented within Chapter 4 are performed on a device fabricated by M. Veldhorst and F.E. Hudson in June 2015. The device studied in Chapter 4 has the same design as the device studied in Chapter 2 and Chapter 3, however it was fabricated on a different processing run. This is important since it emphasises that the results obtained when studying a single device in Chapter 2 and 3 are reproducible using a different device, fabricated during a separate processing run.

During the processing run, 12 devices were fabricated and stored in a nitrogen rich environment. In addition, the devices were further protected from degradation by spinning a thin layer of PMMA onto the surface. Testing of devices for chapter 4 began three years after fabrication, in June 2018. Four individual devices have been tested at 4K, three of these worked perfectly and were characterised as described in chapter 1. Following the characterisation, the best device was selected and studied. All testing and characterisation was performed by S.D. Liles (thesis author).

4.6 Device under study

In Figure 4.8(a) we show a false colour SEM image of a device identical to the device studied in this Chapter. A schematic of the vertical profile of the active region of the device is shown in Figure 4.8(b). The device can be operated as a single hole quantum dot, with G2 acting as the plunger gate. Confinement of the dot in the y-axis is controlled by the voltage applied to the C-gate (V_C), while confinement in the x-axis is controlled by the voltages applied to G1 (V_{G1}) and G4 (V_{G4}). Since V_{G1} also controls the tunnel rate to the reservoir, we use V_{G4} to control the x-axis confinement profile. Absolute charge occupation of the dot can be obtained since the device employs a charge sensor adjacent to the quantum dot. The charge sensor is operated using standard low frequency dual lock-in techniques, with dynamic feedback employed to improve signal-to-noise [40] (see section A.2.1 for full details).

A stability diagram of the quantum dot device is presented in Figure 4.8(c). Starting from the top of the measurement data-set, at V_{G4} = -0.6V, we observe a series of Coulomb peaks consistent with single quantum dot charge transitions. Beyond the region labeled N=0 we observe no further charge transitions, allowing us to confirm the absolute hole occupation. The total number of holes occupying the dot, N, can then be determined by counting the number of observed charge transitions, as shown in the black text in Figure 4.8(c). For further measurements providing confirmation of the ability to reach the last hole see section A.3.1.

As V_{G4} is made more negative we observe a distinct change in the nature of the charge stability diagram. Around V_{G4} = -1.2V we observe the single dot charge transitions break into a honeycomb pattern consistent with a double dot charge stability diagram. We highlight the double dot honeycomb structure with red dashed lines in the lower right corner of Figure 4.8(c). This honeycomb pattern indicates that V_{G4} has been made sufficiently negative to accumulate a second quantum dot under G4. The absolute occupation of the double quantum dot system is represented by the text (N,M), where N is the number of holes occupying the dot controlled by G2, and M is the number of holes occupying the dot controlled by G4.

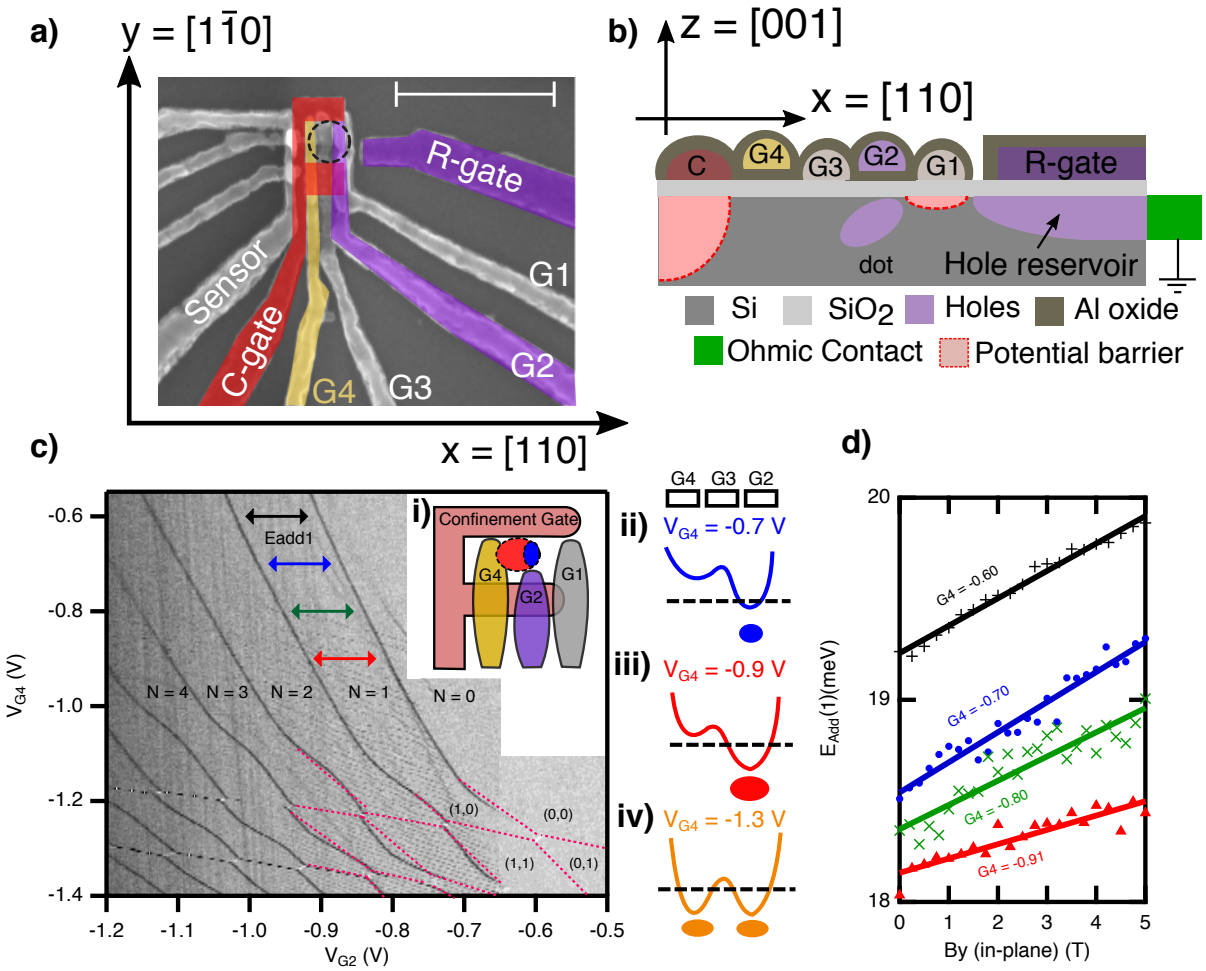

Figure 4.8: **Operation of the single hole quantum dot:** (**a**) A false color SEM image of a device identical to the device under study, with crystal orientations labeled (z=[0,0,1]). The adjacent charge sensor is labeled, and the white scale bar is 500nm. (**b**) Schematic (not to scale) of the vertical profile of the single quantum dot. (**c**) Charge stability diagram showing control of the device from a single to double quantum dot regime Here the x-axis is the voltage applied to the plunger gate G2 (V_{G2}), the y-axis is the voltage applied to the gate G4 (V_{G4}), and the color scale is the charge sensor signal. Inset i) shows a schematic of the device, with blue (V_{G4} = -0.7V) and red (V_{G4} = -0.9V) ellipses schematically indicating that V_{G4} can control the size and shape of the quantum dot. Insets ii) to iv) schematically show the effect of V_{G4} on the energy profile. The horizontal dashed line indicates the fixed chemical potential of the reservoir. See section A.3.2 for more details regarding the charge stability diagram features. (**d**) Measurements of the first addition energy as a function of in-plane magnetic field. The addition energy is extracted by converting the N=1 and N=2 charge transition spacing from ΔV_{G2} into energy using the lever arm. The lever arm has been confirmed to be independent of V_{G4} (see section A.2.2 for further details regarding the lever arm calculation). For each V_{G4} we observe a different g-factor (slope) and charging energy (intercept).

These results suggest that the confinement profile of the quantum dot is highly tunable. Based on the device geometry we would expect that V_{G4} primarily influences the confinement in the x-axis. This is shown schematically in inset (i) of Figure 4.8(c), where

the blue dashed ellipse indicates the single dot tightly confined at V_{G4} = -0.7V, while the red dashed ellipse indicates a physically larger[1] dot due to the weaker x-axis confinement when V_{G4} = -0.9V. Insets (ii)-(iv) present a schematic illustration of the energy profile of the quantum dot at various V_{G4}. As V_{G4} is made more negative the minimum of the G2-controlled dot falls further below the reservoir chemical potential (dashed black line), the dot increases in size then finally forms into a double dot structure. The system forms into a double dot rather than a larger single dot since V_{G3} is tuned such that G3 is partially depleting.

We now investigate how the addition energy and effective g-factor are influenced by the nature of the quantum dot confinement. The N^{th} addition energy, $E_{add}(N)$, is the energy required to add the $(N+1)^{th}$ charge to a dot containing N holes, and is analogous to the addition energy in atomic physics. $E_{add}(1)$ can be extracted by measuring the spacing between the first two charge transitions. The g-factor can then be obtained from the slope $dE_{add}(1)/dB = g\mu_B$, and the Coulomb charging energy can be extracted from the B=0 intercept of $E_{add}(1)$. We measure the first addition energy, $E_{add}(1)$, of the dot as a function of an in-plane magnetic field oriented along the y-axis, B_y. The results are shown in Figure 4.8(d) for four different dot confinement profiles. The different dot confinement profiles are achieved by changing V_{G4}, where the different colors correspond to the V_{G4} indicated by the colored arrows in Figure 4.8(c).

There are two key results obtained from the measurements of $E_{add}(1)$ presented in Figure 4.8(d). The first key result is the change in the $\mathbf{B}$=0 intercept of the four measurements. We attribute this to a change in the physical size of the dot. As V_{G4} becomes more negative the dot becomes larger, reducing the Coulomb repulsion between the two confined holes. This causes the $\mathbf{B}$=0 addition energy to decrease as V_{G4} is made more negative. The addition energy changes by $\sim 5\%$ suggesting the area of the dot also changes by $\sim 5\%$ (see section A.2.5 for more details). The second key result is the difference in the slopes of the four measurements. A difference in slope (dE_{add}/dB_y) corresponds to a difference in the effective g-factor. The values of the addition energy and g-factors are presented in Table 4.1.

[1]This increase in physical size is confirmed by addition energy measurements discussed in the next paragraph.

V_{G4} (V)	E_{add} (1) (meV)	g_y^*
-0.60	19.2 ±0.1	2.3 ±0.1
-0.70	18.5 ±0.1	2.6 ±0.1
-0.80	18.4 ±0.1	2.1 ±0.2
-0.91	18.0 ±0.1	1.2 ±0.1

Table 4.1: **Addition energy and g-factor from Figure 4.8(d)**: The addition energy is extracted from the intercept of the respective linear fit in Figure 4.8(d), and the g-factor is extracted from the slope.

These results demonstrate strong electric tunability of the hole g-factor, allowing a doubling of g_y^* over a small range of V_{G4}. In conclusion, the results of Figure 4.8 and Table 4.1 show strong evidence of fine control of the confinement profile of the quantum dot. Further, we have presented preliminary evidence for an electrically tunable effective hole g-factor.

In our analysis we have assumed the main effect of V_{G4} is to change the electrostatic confinement profile of the quantum dot. This is an intuitive assumption, which is consistent with the trends observed in the addition energy in Table 4.1. The confinement profile of the quantum dot defines the orbital shell structure. In section A.4.1 we present an investigation of orbital shell structure for V_{G4} = -0.9V and V_{G4} = -0.7V. We show that the orbital spectrum is distinctly different for the two different V_{G4} voltages. This provides further support for the assumption that V_{G4} significantly impacts the quantum dot confinement.

4.7 Experimental measurement of the g-tensor

This section presents the first experimental study of the hole g-tensor for a silicon MOS quantum dot containing just one hole. We compare the hole g-tensor for two different confinement profiles. These results are then used to discuss the electrical tunability of the hole g-factor anisotropy and show that the anisotropy is strongly related to the confinement profile of the quantum dot.

The hole g-factor is extracted by measuring the change in addition energy as a function of

magnetic field. We use a superconducting vector magnetic system capable of producing an arily oriented magnetic field. The anisotropy of the single hole g-factor is characterised by rotating a 1T magnetic field around the sample x-z, y-z and x-y axes [141, 142]. The g-factor is extracted in increments of $\pi/12$ giving a total of 144 measurements of the hole g-factor for each confinement profile.

Figure 4.9 shows the results of the g-factor anisotropy measurement. In each data set the y-axis is the effective g-factor measured for the specific magnetic orientation shown on the x-axis. The first column shows the results when V_{G4} = -0.9V (in red, Figures 4.9(a)-(c)), while the second column shows the results when V_{G4} = -0.7V (in blue, Figures 4.9(a)-(c)). The three rows are the results for the x-y, x-z and y-z rotations of the magnetic field orientation respectively. The orientation of the magnetic field rotation is indicated by the orange axes in the insets of Figure 4.9(a), (b), and (c). In all cases we observe π periodic behavior in the hole g-factor anisotropy, consistent with the g-factor anisotropy arising due to the quadrapole moment of the confinement.

We use the results of the rotations presented in Figure 4.9 to extract the magnitude and orientation of the principal axes of the g-tensor. A 3D anisotropic g-factor can be described by three mutually orthogonal g-vectors, which define the principal axes[57, 141]. Therefore, the hole g-tensor can be described by a diagonal 3x3 matrix with components g_1^*, g_2^* and g_3^*. Here g_1^*, g_2^* and g_3^* are the effective g-factors measured when the magnetic field is oriented along the respective principal axes. Since the experimental frame of reference (x,y,z) does not necessarily align with the principal magnetic axes, we fit the measured g-factor anisotropy to a rotated diagonal matrix in order to determine (g_1^*, g_2^*, g_3^*) and the orientation of the principal magnetic axes [57]. The experimental g-factor anisotropy is fit to the equation,

$$g_{exp}^* = R_y(\phi)R_z(\theta)\begin{pmatrix} g_1^* & 0 & 0 \\ 0 & g_2^* & 0 \\ 0 & 0 & g_3^* \end{pmatrix} R_y^{-1}(\phi)R_z^{-1}(\theta) \tag{4.20}$$

where g_1^*, g_2^* and g_3^* define the principal g-factors, $R_{y,z}$ are corresponding rotation ma-

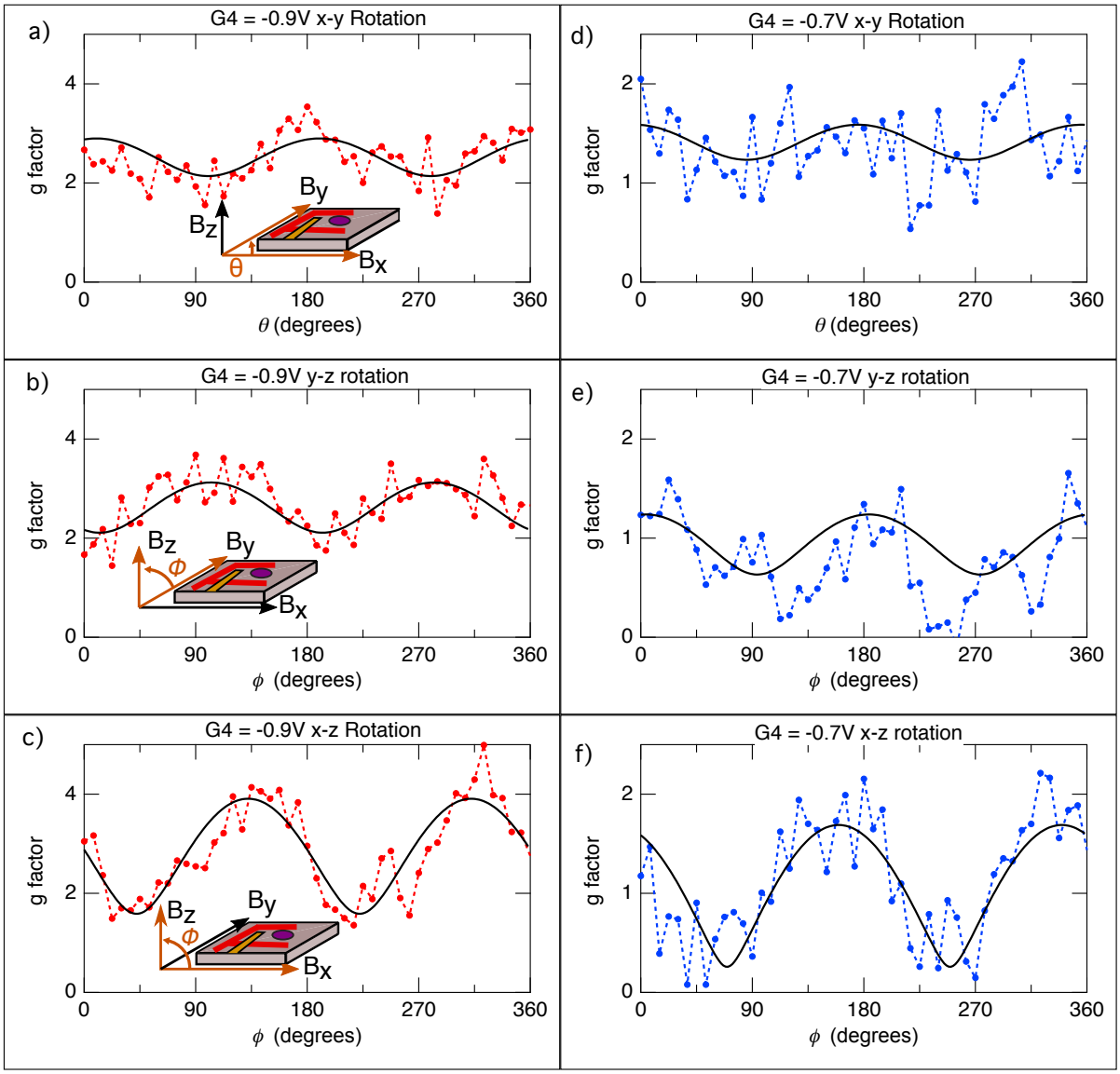

Figure 4.9: **Electrical control of the g-factor anisotropy:** Panels (**a-f**) show the experimentally measured g-factor as a function of magnetic field orientation. Panels (**a-c**) (red) show the measurements for V_{G4} = -0.9V, and panels (**d-f**) (blue) show the measurements for V_{G4} = -0.7V. Solid black lines are the results of a best fit of all data for a specific V_{G4} to Equation 4.20. Insets for each row indicate the plane of rotation. In each inset the axes of rotation are highlighted in orange. θ is the in-plane angle, with $\theta = 0$ corresponding to B_x. ϕ is the out-of-plane angle with ϕ=90 corresponding to B_z. The inset includes a sample schematic where the red region represents the orientation of the C-gate, the orange rectangle indicates G4, and the purple ellipse indicates the quantum dot.

trices[1], θ defines the in-plane orientation of the principal magnetic axes, while ϕ defines the out-of-plane orientation of the principal magnetic axes the with respect to sample (x,y,z) axes. The angles are defined such that if θ=0 and ϕ=0 then the orientation of g_1^*, g_2^* and g_3^* would align with the sample (x,y,z) axes respectively.

[1]See section A.2.3 for definitions of these matrices.

We fit all 144 data points of the measured g-factor anisotropy to Equation 4.20 to extract the the principal g-factors and their orientation. For V_{G4} = -0.9V we find the diagonal g-tensor and orientations to be,

$$\begin{aligned} g^*_{0.9} &= \begin{pmatrix} 1.6 \pm 0.2 & 0 & 0 \\ 0 & 2.1 \pm 0.2 & 0 \\ 0 & 0 & 3.9 \pm 0.2 \end{pmatrix} \\ \theta_{0.9} &= (8 \pm 4)^o \\ \phi_{0.9} &= (-43 \pm 5)^o \end{aligned} \tag{4.21}$$

The components of the diagonal g-tensor are (g^*_1, g^*_2, g^*_3) in the reference frame of the principal magnetic axes.

Similarly for G4 = -0.7V we find the diagonal g-tensor and orientations to be,

$$\begin{aligned} g^*_{0.7} &= \begin{pmatrix} 0.4 \pm 0.4 & 0 & 0 \\ 0 & 1.2 \pm 0.3 & 0 \\ 0 & 0 & 1.7 \pm 0.2 \end{pmatrix} \\ \theta_{0.7} &= (-5 \pm 6)^o \\ \phi_{0.7} &= (-70 \pm 5)^o \end{aligned} \tag{4.22}$$

The solid black lines in Figure 4.9(a)-(f) is the best fit of the measured g-factors to Equation 4.20. The best fit lines reproduce the experimental data well for both V_{G4} profiles. This shows that the hole g-factor anisotropy is well characterised by the 3D anisotropic g-tensor in Equation 4.20.

We begin the analysis of these results by first considering the orientation of the principal magnetic axes (g-axes). We find that both $\theta_{0.7}$ and $\theta_{0.9}$ are within experimental uncertainty of θ=0[1]. This indicates that the principal axis g^*_2 is aligned with the y-axis of the sample for both V_{G4} = -0.9V and V_{G4} = -0.7V (see Figure 4.8(a-b) for lithography axes and crystal orientation). Confinement in the y-axis is provided by the C-gate, while

[1]Experimental misalignment of the sample with respect to the x and y magnetic axes is ± 5 degrees. Given the experimental misalignment and the standard deviation in the fitting, we find that $\theta = 0$ is within both experimental uncertainty ranges of both V_{G4} = -0.9V and V_{G4} = -0.7V.

the only parameter that is changed between the two measurements is V_{G4}. Further, the C-gate is both the largest and the closest gate to the Si/SiO_2 interface. It is therefore consistent that the y-axis confinement is strongly determined by the orientation of the C-gate, and therefore it is unchanged between the two V_{G4} measurements. We can confirm that the hole g-tensor orientation is not defined by the crystal orientation since ϕ is tunable with electric fields.

The main difference in the g-factor anisotropy between V_{G4}=-0.9V and V_{G4}=-0.7V can therefore be understood in terms of the out-of-plane angle ϕ. Given that θ=0, ϕ defines the orientation of the g_1^* and g_3^* principal axes in the x-z plane. In Figure 4.10 we plot the experimental g-factor measured for the rotation around the x-z plane[1]. The dashed black lines indicate the orientation of the principal $\vec{g_1^*}$ and $\vec{g_3^*}$ axes based on the experimentally determined ϕ. For V_{G4} = -0.9V we find the $\vec{g_3^*}$ axis is rotated by $\phi = -43 \pm 2$ degrees from the z-axis [0,0,0], while for V_{G4} = -0.7V we find the $\vec{g_3^*}$ axis is rotated by $\phi = -70 \pm 3$ degrees from the z-axis [0,0,1].

The g_3^* axis is expected to be aligned with the direction of strongest confinement[2]. For a *disk-like* quantum dot this would give the largest effective g-factor oriented in the direction perpendicular to the Si/SiO_2 interface. In the case of V_{G4} = -0.9 we find $\vec{g_3^*}$ is oriented at 43 degrees to the interface. This suggests that as the dot reaches the last hole, confinement in the x, y and z axes becomes comparable, so that the axis of strongest confinement is defined primarily by the electric fields of the applied gates, rather than the interface. This is consistent with observations in self assembled and nanowire quantum dots [21, 141, 142, 144], where electric fields have stronger effects on the g-tensor alignment than the respective crystallographic or lithographic confinement.

When V_{G4} is set to -0.7V we find the $\vec{g_3^*}$ tilts ever further away from the Si/SiO_2 interface. This is consistent with the assumptions made above regarding the case when V_{G4} = -0.9V. Since we suggest that the dot is already tightly confined when V_{G4} = -0.9V, then by making V_{G4} more positive (-0.7V) the confinement in the plane of the 2D hole gas can

[1]Since the g_2^* axis is aligned with the y-axis of the sample, an x-z magnetic field rotation passes through the principal g_1^* and g_3^* axes.

[2]Based on the theoretical model in section 4.7. Note that we have taken convention to define $g_3 > g_2 > g_1$.

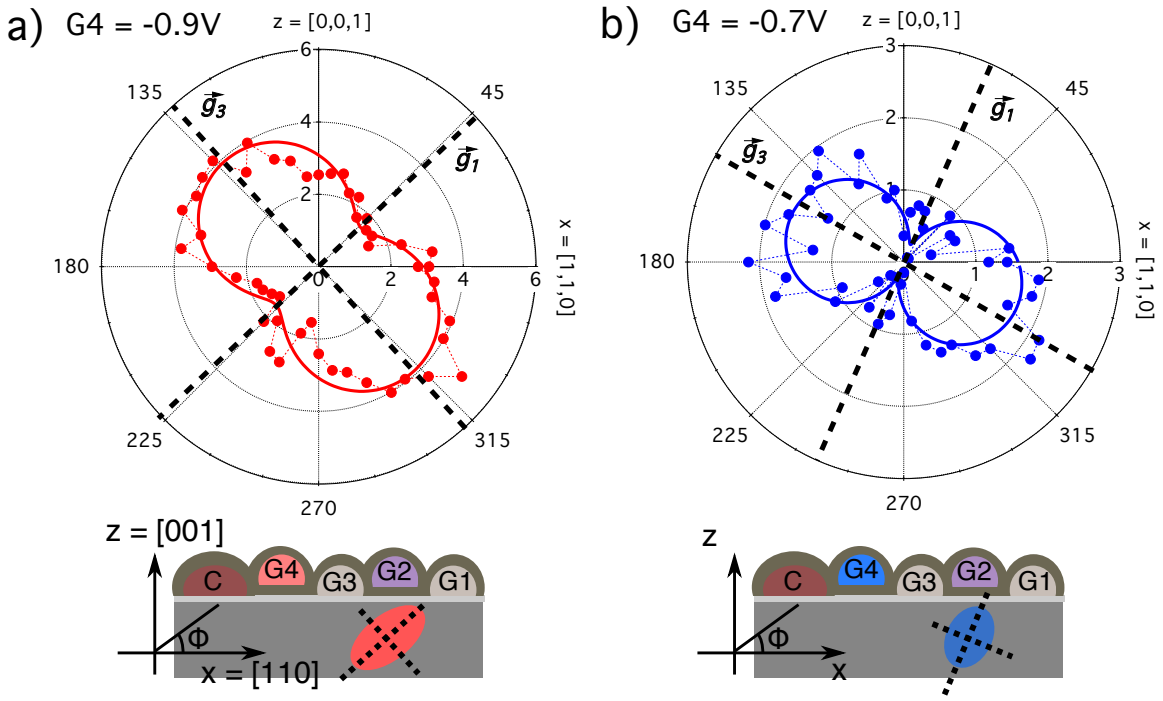

Figure 4.10: **Electrical control of the orientation of the principal g-axes:** Polar plots of the x-z magnetic field rotation measurements for (**a**) V_{G4} = -0.9V (red) and (**b**) V_{G4} = -0.7V (blue). The radial axis is the g-factor and the angular position is the angle ϕ in the x-z plane ($\theta = 0$) of the measured data point. Solid lines are the results of a best fit of respective V_{G4} data to Equation 4.20. Dashed black lines indicate the orientation of the principal g_1^* and g_3^* axes as extracted in the best fit. Below each figure an inset shows a sample schematic, and a rotated quantum dot with principal g_1^* and g_3^* axes indicated by dashed lines. Data is reproduced from Figure 4.9(c) and (f). Note that the radial scale of (a) is double the scale of (b).

become tighter still, resulting in the axis g_3^* tilting even further into the 2D hole gas plane. Finally we note that we have presented quantitative evidence (see Figure 4.8(d)) that the physical size of the quantum dot decreases as V_{G4} is made more positive. This leads to a somewhat surprising conclusion; these preliminary results suggest that the hole quantum dot confinement can be tuned to be 3 dimensional, rather than 2 dimensional (*disk-like*) as one might have expected for a MOS device. Since the confinement shape is linked to the energy scales and spin interactions in quantum dots, this result is valuable for those interested in hole spin based technology. At this point however, the results regarding the confinement dimensions are preliminary, and future work involving electrostatic modeling would be valuable in order to confirm the expected confinement dimensions.

Finally, we discuss the magnitudes of the g-factors. The maximum g-factor observed was 3.9±0.2 and the minimum g-factor was 0.4±0.4. This demonstrates that with control

of both the magnetic field orientation and the electric field[1], it is possible to achieve a wide range of effective hole g-factors. For the case of stronger electric confinement (V_{G4} = -0.7V) we observe that the range g-factors is $\Delta g = 1.7 \pm 0.2$, while for weaker electric confinement (V_{G4} = -0.9V) range g-factors is $\Delta g = 3.3 \pm 0.2$. This effect of confinement strength on Δg is consistent with previous hole quantum dot devices, where the weaker confinement reduces the Heavy-Hole Light-Hole mixing and gives rise to larger g-tensor anisotropy [73, 122].

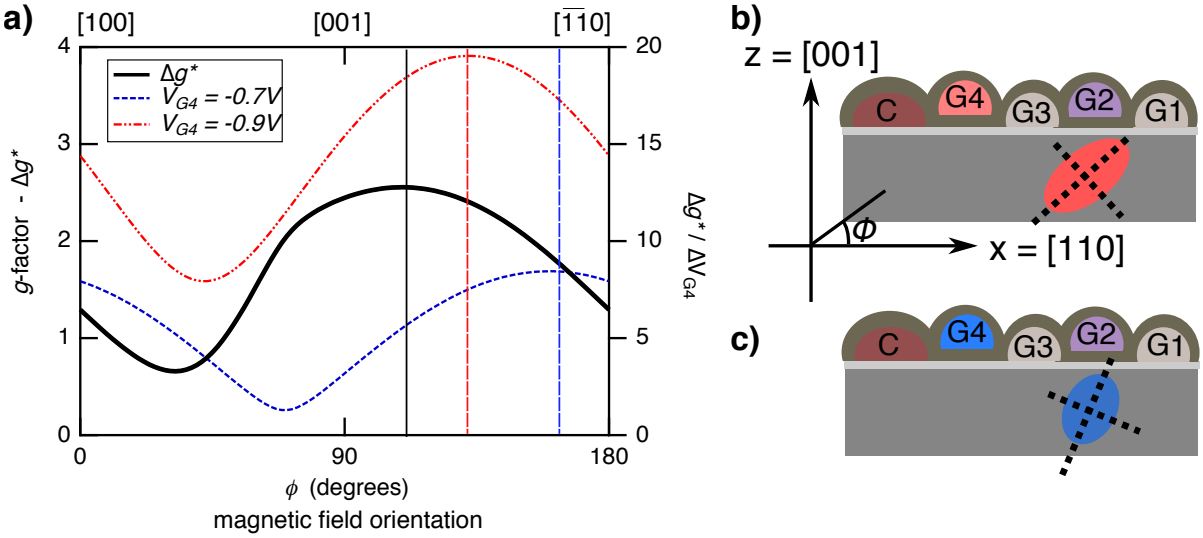

Figure 4.11: Δg^* **in x-z plane:** (**a**) The graph shows the value of Δg^* (black) for magnetic fields oriented around the x-z plane. Δg^* is calculated by taking the difference between the g-factor at V_{G4} = -0.7V (dashed blue) and V_{G4} = -0.9V (broken red), which are reproduced from Figure 4.10 for reference. The vertical lines show the position of the maximum value ($\vec{g}_3^*$) of the respective data sets. The right axis shows the respective $\Delta g/\Delta V_{G4}$. All data sets are the best fit values. (**b**) Shows the sample schematic and indicates the respective lithographic/crystal axes with respect to the angle ϕ. The red ellipse is a schematic of the quantum dot for V_{G4} = -0.9V. (**c**) Shows a schematic of the quantum dot for V_{G4} = -0.7V. (b-c) reproduced from Figure 4.10.

In most applications, the aim is to set a fixed magnetic field, and electrically modulate the g-factor (for example in g-TMR experiments [62]). In Figure 4.11(a) we show the calculated Δg^* as a function of magnetic field orientation in the x-z plane. For a fixed magnetic field orientation the largest Δg observed is 2.6 for ΔV_{G4}=0.2 (corresponding to $\delta g/\delta V_{G4}$ = 13). The largest value of δg occurs for magnetic field oriented at ϕ = 110^o. This is not surprising since this occurs near the orientation of the largest g-factor ($\vec{g}_3^*$, vertical red line) for V_{G4} = -0.9V. As V_{G4} is changed the orientation of $\vec{g}_3^*$ rotates to larger ϕ, producing the largest $\Delta g/\Delta V_{G4}$. Finally, we note that $\Delta g/\Delta V_{G4}$ is useful

[1]In this case over a relatively small range of ΔV_{G4} = 0.2V.

to characterise since the g-TMR Rabi frequency is proportional to $\mathrm{d}g/\mathrm{dV}$ (see section 4.3.7)[1].

In this section we have studied the full 3D g-factor anisotropy of a single hole confined in a silicon MOS quantum dot. Experimental results show that the g-factor is strongly anisotropic and can be characterised by three principal g-factors, g_1^*, g_2^*, and g_3^* oriented along mutually perpendicular directions. The g-factor anisotropy is compared for two distinct values of V_{G4}. This demonstrates that the magnitude of the principal g-factors can be strongly modulated by electric fields, with the g-factor changing over a range from 0-4 using as the magnetic field orientation is varied. Further, we find that the orientation of the principal g-factors can be rotated by electric fields. The rotation of the principal magnetic axes is qualitatively consistent with a rotation of the electrically defined quantum dot confinement profile.

4.8 Theoretical model for hole g-factor anisotropy

The experimental results presented in section 4.7 show strong electric control of the magnitude and orientation of the hole g-tensor. Analysis of these results suggests that the electric g-factor modulation is linked to the electric control of the quantum dot confinement profile. In this section we introduce a simple theoretical model of the g-factor anisotropy for a single hole quantum dot. The model considers the case where the confinement is an anisotropic 3D harmonic oscillator and includes full crystal anisotropy. The only free parameters included in the model are the orientation, and strength of the 3D confinement. Due to the clear and simple parameter choices, this model has great explanatory power.

The model corroborates our conclusion that the g-factor anisotropy is directly linked to the confinement profile. Using the model we demonstrate that the orientation of the principal magnetic axes are defined by the orientation of the confinement. In addition, we show that the magnitude of the principal g-factors can be varied based on the

[1] As a rough estimate for a driving voltage of 2mV and magnetic field of 1T at $\phi = 110^o$, the g-TMR spin manipulation frequency for this device is predicted to be around 30MHz. See Equation 4.12.

strength of the confinement. We conclude this section by discussing the quantitative discrepancies between the model and the experiment. These discrepancies motivate future work, which would be the development of a numeric model that includes full electrostatic considerations.

4.8.1 Details of the theoretical model

In this section we provide details of the theoretical model used explain electric modulation of the hole g-factor in silicon MOS quantum dots. This model was developed in collaboration with D. S. Miserev[1] and O. P. Sushkov[2]. This model is general to any hole system provided appropriate Luttinger parameters are included. It can therefore be used to model holes in Ge or GaAs hole based quantum dots.

$\boldsymbol{k}\cdot\boldsymbol{p}$ theory can successfully provide theoretical models of semiconductor band structure including non-parabolically, spin-splitting, and electric and magnetic field induced effects. These models are also computationally expensive, with the extended Kane Hamiltonian producing a 14x14 matrix. Often it is convenient to consider smaller $\boldsymbol{k}\cdot\boldsymbol{p}$ models that only include certain (adjacent) bands. The Luttinger Hamiltonian is the simplest $\boldsymbol{k}\cdot\boldsymbol{p}$ model for describing the four-fold degenerate topmost valence band [51, 66].

In order to model the g-factor of a single hole quantum dot in silicon we start from the 3D Luttinger Hamiltonian[3],

$$\begin{aligned} H_L &= (\text{Kinetic}) + (\text{Spin-orbit}) + (\text{Crystal Symmetry}) + (\text{Zeeman}) \\ H_L &= (\gamma_1 + \frac{5}{2}\gamma_2)\frac{\boldsymbol{\pi}^2}{2m} \\ &\quad -\frac{\gamma_2}{m}(\pi_x^2 J_x^2 + \pi_y^2 J_y^2 + \pi_z^2 J_z^2) \\ &\quad -\frac{\gamma_3}{2m}(\{\pi_x,\pi_y\}\{J_x,J_y\} + \{\pi_x,\pi_z\}\{J_x,J_z\} + \{\pi_y,\pi_z\}\{J_y,J_z\}) \\ &\quad -2\kappa\mu_B \boldsymbol{B}\cdot\boldsymbol{J} \end{aligned} \tag{4.23}$$

[1]Department of Physics, University of Basel, Klingelbergstrasse 82, CH-4056 Basel, Switzerland.
[2]School of Physics, University of New South Wales, Sydney NSW 2052, Australia.
[3]See background section 1.5.2 for details on the structure of the Luttinger Hamiltonian. The version of the Luttinger Hamiltonian in Equation 4.23 has been expanded to highlight the γ_2 and γ_3 terms.

where γ_i and κ are Luttinger parameters[1], $\boldsymbol{\pi} = \boldsymbol{p}$ - e$\boldsymbol{A}$ is the long momentum, $\boldsymbol{A}$ is the vector-potential, axes *x, y* and *z* are oriented along the crystal axes [1,0,0], [0,1,0] and [0,0,1] respectively, m is the bare electron mass, $\boldsymbol{J} = (J_x, J_y, J_z)$ is the 4x4 hole spin 3/2 matrix, μ_B is the Bohr magneton, $\boldsymbol{B}$ is the magnetic field and brackets {A,B} = AB + BA denote the anti-commutator.

We model the quantum dot confinement by introducing an arbitrarily oriented 3D harmonic potential, V(*X',Y',Z'*), with principal axes of the harmonic oscillator defined by *X', Y'* and Z'. The harmonic oscillator potential in its own reference axes is given by,

$$V(X', Y', Z') = \frac{m}{2}(\omega_{X'}^2 X'^2 + \omega_{Y'}^2 Y'^2 + \omega_{Z'} Z'^2) \tag{4.24}$$

where $\omega_{X'}$, $\omega_{Y'}$ and $\omega_{Z'}$ define the harmonic oscillator confinement along the X', Y' and Z' principal axes. The principal axes of the harmonic oscillator X', Y' and Z' can be arbitrarily oriented with respect to the crystal axes[2]. One can transform between these axes and the crystal axes using the appropriate rotation matrices (See Equation A.5 in section A.2.3 for full details).

The model of Equations 4.23 and 4.24 takes into account the full crystal symmetry and orientation, bulk Zeeman contributions, orbital effects (through $\boldsymbol{\pi} = \boldsymbol{p} - e\boldsymbol{A}$), and Heavy-hole Light-hole effects (since it is a 4-band model). Further, the chosen $V(X', Y', Z')$ allows us to model the effects of an arbitrarily oriented 3D harmonic confinement. The quantum dot confinement is defined by the three principal axes, with harmonic confinement($\omega_{X'}$, $\omega_{Y'}$, $\omega_{Z'}$). Experimentally this confinement is electrically controlled using the voltage applied to the metallic gates. The model initially has six free parameters. These free parameters are the three confinement parameters ($\omega_{X'}$, $\omega_{Y'}$, $\omega_{Z'}$), and three angles (Ψ, Θ, Φ) used to define the orientation of the 3D harmonic oscil-

[1]Luttinger parameters for silicon are $\gamma_1 = 4.29$, $\gamma_2 = 0.34$, $\gamma_3 = 1.45$ and κ =-0.42 [51].

[2]We have now introduced three different co-ordinate systems. To clarify:
· Lower case italic (*x,y,z*) are directed along the primary crystal axes [1,0,0], [0,1,0] and [0,0,1] respectively. These are not mentioned again, and are only used in the model.
· It is more convenient to discuss a co-ordinate system that is aligned with the device lithography. Lower case non-italic (x,y,z) are aligned with [1,1,0], [1,$\bar{1}$,0] and [0,0,1] respectively as shown in the SEM of Figure 4.8.
· Finally, as a mathematical convenience we refer to the co-ordinates oriented along the principal axes of a 3D harmonic oscillator. The harmonic oscillator axes are referred to as capitalised italic and prime (X', Y', Z')

lator (See section A.2.3 for more details regarding Θ, Φ, and Ψ).

4.8.2 Investigations into the 3D Luttinger g-tensor properties

In section 4.3.1 of the literature review we introduced the main mechanisms that can influence the g-tensor in semiconductor quantum dots. The experimental results in sector 4.7 have suggested that it is the orbital confinement that has the main effect on the g-tensor. This conclusion is supported by the observation that the g-tensor can be electrically tuned, and electrically oriented.

In this section we present the results of a theoretical study of the hole g-tensor properties in silicon. We study the 3D Luttinger model with an anisotropic harmonic confinement described in Equations 4.23 and 4.24. For this study we have numerically simulated the g-factor anisotropy for certain combinations of parameters ($\omega_{X'}$, $\omega_{Y'}$, $\omega_{Z'}$) and (Ψ, Θ, Φ). In each case the relevant parameters are clearly indicated in the Figure insets or Table columns.

The main results of this section are concisely summarized in section 4.8.3.

1 - Orbital Contributions

The theoretical model of Equations 4.23 and 4.24 predicts that orbital corrections play a significant role in determining the magnitude of the g-factor. In Figure 4.12 we have present the calculated g-factor as a function of magnetic field orientation (ϕ). The broken black line shows the calculated g-factor anisotropy when orbital contributions have been ignored[1]. This gives the g-factor anisotropy resulting purely from the spin effects. The solid red line shows the g-factor anisotropy when orbital contributions have been included. We show that when orbital corrections are ignored the calculated g-factor decreases by a factor of approximately two. This shows that both the pure spin and the orbital contributions are comparable in magnitude, and we cannot ignore either.

This result is particularly important when considering that the maximum g-factor observed experimentally was 4. If we only consider pure spin contribution the maximum

[1]The orbital corrections are included in the Hamiltonian through the long momentum $\boldsymbol{\pi} = \boldsymbol{p} - e\boldsymbol{A}$ in Equation 4.23. Orbital corrections are removed from the model by setting $\boldsymbol{\pi} = \boldsymbol{p}$.

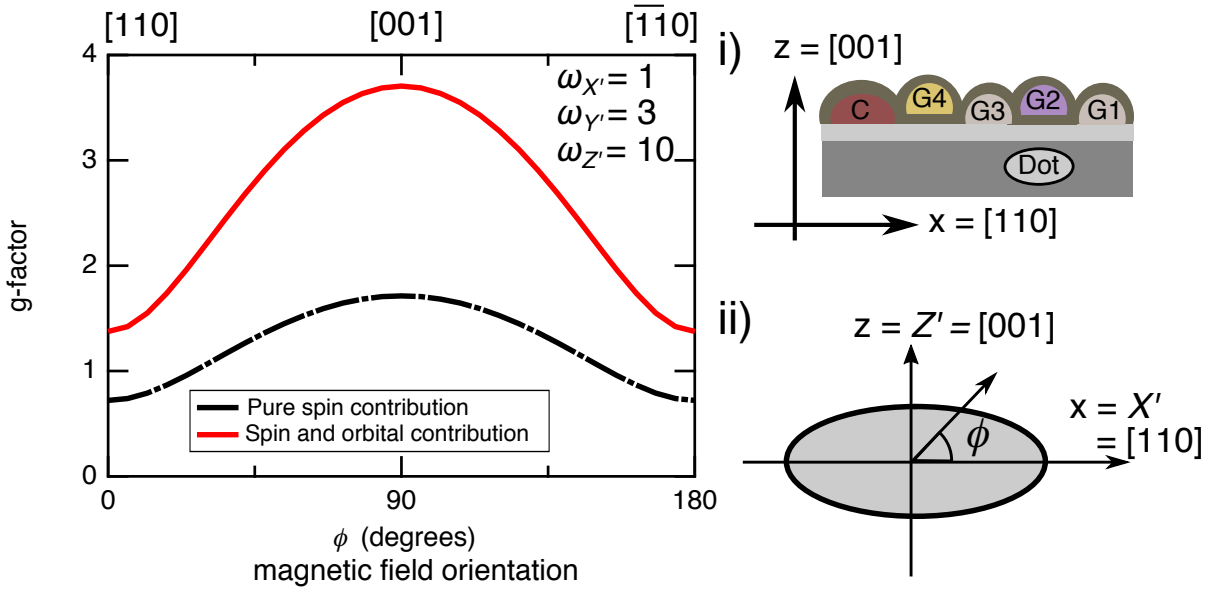

Figure 4.12: **Effects of orbital contributions on the hole g-tensor:** The graph shows the calculated effective g-factor as a function of magnetic field orientation (ϕ). Inset (i) shows a schematic of the sample orientation with respect to the crystal axes x and z. The upper axis of the graph indicates the orientation of the field with respect to the crystal axes for a given ϕ. Inset (ii) shows a schematic of the quantum dot shape for the confinement defined by $(\omega_{X'}, \omega'_Y, \omega'_Z)$ = (1,3,10). The principal axes of the confinement (X', Y', Z') are aligned with the sample axes (x,y,z). The broken black line shows the calculated g-factor when orbital contributions are ignored ($\boldsymbol{\pi} = \boldsymbol{p}$), and the solid red line shows the calculated g-factor when orbital contributions are included ($\boldsymbol{\pi} = \boldsymbol{p} - e\boldsymbol{A}$) in the model.

g-factor possible is the bulk value of $|6\kappa| = 2.52$. Therefore this shows that orbital corrections must be included to obtain the experimentally observed g-factor magnitudes. It is also important to note that the phase (angle ϕ of the maxima and minima) of the g-factor anisotropy is the same for both the pure spin and orbital contributions. This is important since it means the pure spin and orbital terms add together in phase, rather than competing in some random way, which would complicate the analysis[1]. For the following simulations we always include the orbital contributions.

2 - Confinement Orientation

The theoretical model of Equations 4.23 and 4.24 predicts that the orientation of the g-tensor is defined by the orientation of the confinement. In Figure 4.13 we show the calculated g-factor anisotropy for two different confinement orientations. The broken black line is the g-factor for the confinement profile indicated in inset (i), where the (X', Y', Z') axes of the harmonic confinement have been chosen to align with the (x,y,z) axes of the device lithography. The extrema of the g-factor correspond to the orientation

[1] We have confirmed this is the case for all orientations of the confinement.

of the principal axes of the confinement. We have identified the g-factor maxima as $g^*_{Z'}$(i) with a solid black circle and the minima as $g^*_{X'}$(i) with an open black circle in Figure 4.13[1].

The dashed red line in Figure 4.13 shows the g-factor anisotropy calculated for confinement profile shown in inset (ii). Figure 4.13 demonstrates that if the confinement profile is rotated the g-tensor principle axes are similarly rotated. Finally, we note that the two curves (red and black) have different amplitudes. This is due to the small effect of the crystal orientation with respect to the confinement axes. The effects of crystal orientation are discussed in part 4 of this section.

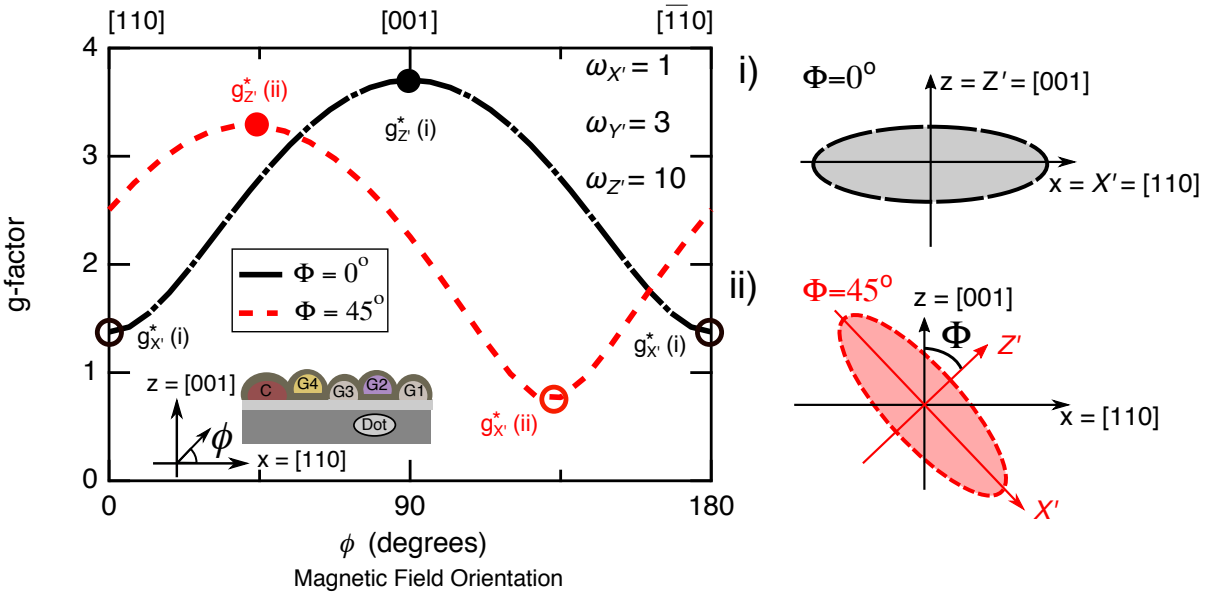

Figure 4.13: **Effects of confinement orientation on the hole g-tensor:** The graph shows the calculated g-factor as a function of magnetic field orientation, for a rotation around the x-z plane. The inset in the graph indicates the relative sample and crystal axes. The broken black line shows the g-factor anisotropy calculated for the confinement indicated in inset (i). For inset (i) the principal axes of confinement are aligned with the sample (x,y,z) axes. The dashed red line shows the g-factor anisotropy calculated for the confinement indicated in inset (ii). For inset (ii) the principal axes of confinement have been rotated by $\Phi = 45^o$ in the x-z plane. The extrema of the g-factors occur along the principal axes of confinement in all cases. For both confinement profiles (i) and (ii) the values of $(\omega_{X'}, \omega'_Y, \omega'_Z)$ are (1,3,10).

The alignment of the principal g-factors with the principal confinement axes is clearly demonstrated by comparing the calculated g-factor anisotropy for two different confinement orientations. In We demonstrate that the dashed red line has maxima labeled

[1]We have not shown rotations into the y-axis since the behavior is qualitatively similar. An extrema occurs in the g-factor anisotropy along the Y' principal axis and the g-factor at the Y' extrema can be labeled $g^*_{Y'}$.

$g^*_{Z'}$(ii) occurring along the rotated Z' axes, and minima labeled $g^*_{X'}$(ii) occurring along the rotated X' axes.

3 - Confinement anisotropy

We now discus the predicted relationship between the g-tensor anisotropy (g_1, g_2, g_3) and the confinement anisotropy $(\omega_{X'}, \omega_{Y'}, \omega_{Z'})$. First we highlight that the theoretical model with harmonic oscillator confinement is scale invariant. This scale invariance occurs since we are considering only the quadratic Hamiltonian and the linear response in magnetic field. Due to the scale invariance only the ratio of the frequencies effects the g-factor.

In Figure 4.14 we show the calculated g-factor anisotropy for different confinement profiles. The black dashed line in Figure 4.14 is for $(\omega_{X'}, \omega_{Y'}, \omega_{Z'}) = (0.1,0.3,1)$, while the solid red line is for $(\omega_{X'}, \omega_{Y'}, \omega_{Z'}) = (1,3,10)$. In each of these cases the ratios of $\omega_{X'}/\omega_{Y'}$ and $\omega_{Z'}/\omega_{Y'}$ is the same and the model therefore predicts identical g-factors. The broken blue and green lines show the calculated g-factors for two different confinement profiles. Figure 4.14 serves two main points; (1) to highlight the scale invariance and (2) to generally show that $(\omega_{X'}, \omega_{Y'}, \omega_{Z'})$ have a large impact on the g-tensor.

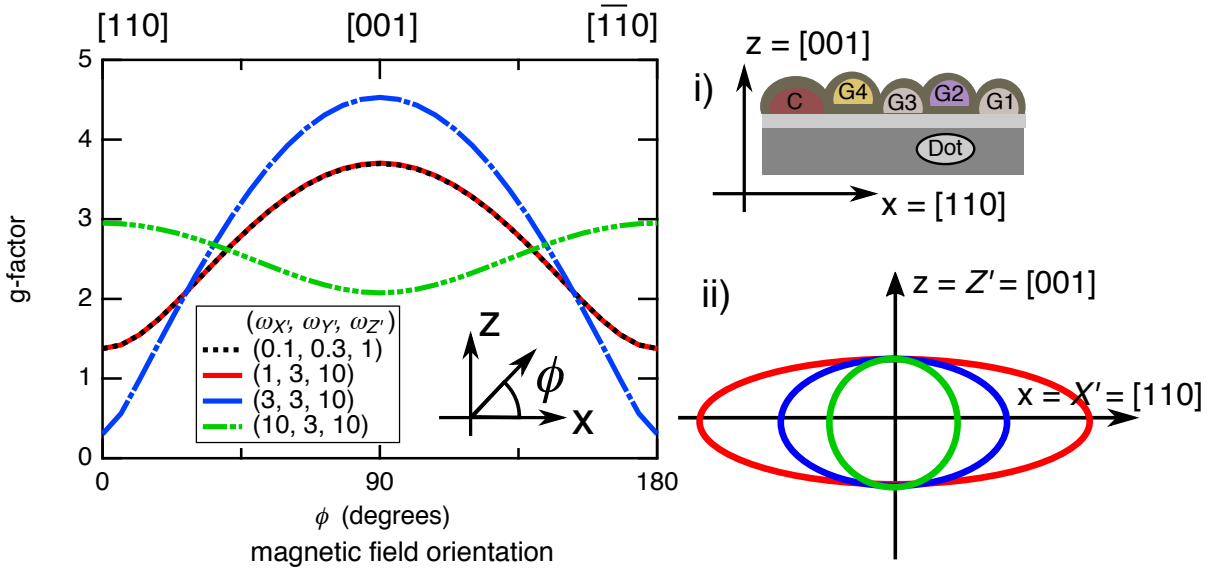

Figure 4.14: **Effects of orbital confinement on the hole g-tensor:** The graph shows the g-factor anisotropy for four distinct confinement profiles. Inset (i) shows the relative orientation of the sample and crystal. Inset (ii) schematically indicates the quantum dot shape for the three confinement profiles (respective colour to the graph caption). In each case the principal axes of confinement (X', Y', Z') are aligned with the sample axes (x,y,z), and therefore the principle g-factors are aligned with (x,y,z).

We now consider a more systematic approach to demonstrate the effects of the confine-

ment profile $(\omega_{X'}, \omega_{Y'}, \omega_{Z'})$. Due to the scale invariance only the ratio of the frequencies effects the g-factor. This allows us to consider the effect of confinement with respect to two parameters, $\omega_{X'}/\omega_{Y'}$ and $\omega_{Z'}/\omega_{Y'}$. Conveniently these two parameters simply define the anisotropy of the confinement profile. In Table 4.2(a) we show the calculated principal g-factors for a range of specific confinement profiles. We consider three intuitive cases: (1) the symmetric 2D *disk-like* case, where there is strong confinement along one axis and isotropic confinement in the other two axes; (2) the asymmetric 2D *disk-like* case, where there is strong confinement in one axis, and anisotropic confinement in the other two axes; and (3) the 1D *needle-like* case, where there is strong confinement in two axes, and weak confinement along the remaining axis. The specific $(\omega_X, \omega_{Y'}, \omega_{Z'})$ that represents each of these cases is shown in brackets in Table 4.2, with bold text to highlight the distinct difference between the similar confinement situations.

The results presented in Table 4.2(a) demonstrate the predicted trends of the g-factor anisotropy based on the confinement anisotropy. For the 2D circular *disk-like* case the model predicts the largest g-factor is oriented along the axis of strongest confinement (indicated by bold text). In the case of the elliptic *disk-like* confinement the largest g-factor is still oriented along the direction of strongest confinement, and the second largest g-factor is oriented along the axis of second strongest confinement (indicated with the bold text). Finally, for *needle-like* confinement we find that the smallest g-factor is oriented along the axis of weakest confinement (see the non-bold text). Analysis of Table 4.2(a) allows insight into how the confinement anisotropy and g-factor anisotropy are linked. The model demonstrates an intuitive trend between the magnitudes of the g-factors and the confinement anisotropy. This general trend is highlighted by the bold text in Table 4.2(a).

4 - Crystal Anisotropy

The orientation of the confinement profile with respect to the crystal symmetry plays a role in determining the magnitude of the g-factors $(g^*_{X'}, g^*_{Y'}, g_{Z'})$. A simple example of this can be observed in the extrema points of Figure 4.13. The confinement profile in Figure 4.13 (i) and (ii) have identical confinement parameters with $\omega_{X'} = 1$, $\omega_{Y'} = 3$ and $\omega_{Z'} = 10$. However, the principal axes have been rotated by $\pi/4$ around Y' for profile

Situation	$\omega_{X'}$	$\omega_{Y'}$	$\omega_{Z'}$	$g_{X'}$	$g_{Y'}$	$g_{Z'}$
(**a**) - Confinement aligned with x, y, z axes.						
Circular *disk*	1	1	**5**	0.22	0.22	**4.8**
Circular *disk*	1	**5**	1	0.55	**3.3**	0.97
Circular *disk*	**5**	1	1	**3.3**	0.55	0.97
Elliptic *disk*	1	**3**	5	1.3	**2.6**	2.7
Elliptic *disk*	**3**	1	5	**2.6**	1.3	2.7
1D *needle*	**10**	**10**	1	**3.3**	**3.3**	1.1
1D *needle*	**10**	1	**10**	**3.0**	1.1	**2.1**
1D *needle*	1	**10**	**10**	1.1	**3.0**	**2.1**
(**b**) - Arbitrary confinement orientation.						
Circular *disk*	1	1	**5**	0.4	0.2	**3.4**
Circular *disk*	1	**5**	1	0.8	**3.3**	0.8
Circular *disk*	**5**	1	1	**3.4**	0.1	0.3
Elliptic *disk*	1	**3**	**5**	1.9	**2.2**	3.1
Elliptic *disk*	**3**	1	**5**	**1.4**	0.7	3.3
1D *needle*	**10**	**10**	1	**2.3**	**2.1**	1.8
1D *needle*	**10**	1	**10**	**2.5**	1.1	**2.5**
1D *needle*	1	**10**	**10**	1.9	**2.3**	**2.5**

Table 4.2: **g-Tensor anisotropy for different confinement profiles**: (**a**) Shows the calculated g-tensor anisotropy for several intuitive confinement profiles. In (a) the g-factors are calculated when the confinement is aligned with the (x,y,z) sample axes. This is a special orientation since x = [110], y = [1$\bar{1}$0], and z = [001], which gives rise to the symmetry in the magnitude of the principal g-factors along the x and y axes. Bold text is included to indicate the trends within the similar confinement profiles. (**b**) Shows the calculated g-tensor anisotropy for the same confinement anisotropy as (a), except now the confinement is arbitrarily aligned with respect to the crystal axes. For this specific case we took the confinement $(\Psi, \Theta, \Phi) = (0, 45^o, -43^0)$, which corresponds to the experimental alignment when V_{G4} = -0.9V. However, the choice of angle is arbitrary for the purposes of this table. The main result is that the general trend of the principal g-factors remains the same as in (a) (shown in bold), however the values of each g-factor are changed due to the new alignment with respect to the crystal.

(ii). We note that rotating the confinement axes does not simply result in a phase shift of the calculated g-factor anisotropy. This can be seen by comparing $g^*_{Z'}$ and $g^*_{X'}$ for two confinement orientations of (i) and (ii). For the two rotated confinement orientations $g^*_{Z'}(i) \neq g^*_{Z'}(ii)$ and $g^*_{X'}(i) \neq g^*_{X'}(ii)$. This demonstrates that the calculated g-factors are

influenced by the silicon cubic crystal anisotropy.

In Table 4.2(a) we have considered the g-tensor anisotropy for various confinement profiles. However, in each case of Table 4.2(a) the confinement is oriented such that $X' = [110]$, $Y' = [1\bar{1}0]$ and $Z' = [001]$, which is a special orientation[1]. If we consider the g-tensor values for the circular *disk-like* case, we see that the magnitude of the largest g-factor is different $(\omega_{X'}, \omega_{Y'}, \omega_{Z'}) = (1,1,\mathbf{5})$ and $(1,\mathbf{5},1)$. This is due to the effects of the crystal orientation. In addition, we can notice that the values of $g_{X'}$ and $g_{Y'}$ are swapped between $(1,\mathbf{5},1)$ and $(\mathbf{5},1,1)$. This is due to the degeneracy of the $[110]$ and $[1\bar{1}0]$ crystal orientations for bulk silicon.

In Table 4.2(b) we show the g-factor anisotropy for the circular and elliptic *disk-like* case. However the confinement is now arbitrarily orientated with respect to the crystal axes (see caption). We emphasise that the symmetry between the g-tensor components that was present in Table 4.2(a) is lost now that the confinement is not aligned with a special crystal axes. In addition, for the arbitrary confinement orientation the value of $g^*_{Z'}$ is dependent on the values of $\omega_{X'}$ and $\omega_{z'}$. Despite these effects, the general trend of the g-factor magnitudes remains the same, as indicated by the bold text. The conclusion is that the confinement profile $(\omega_{X'}/\omega_{Y'}, \omega_{Z'}/\omega_{Y'})$ defines the g-tensor anisotropy profile, and the crystal orientation influences the magnitudes of the relative g-factors.

4.8.3 Properties of the theoretical g-tensor

Based on the studies in section 4.8.2 we have four major conclusions regarding the calculated g-tensor for holes in silicon quantum dots:

(1) - Orbital contributions are significant and must be included in the model to obtain g-factors consistent with the experiment.

(2) - The orientation of the g-tensor is defined by the orientation of the confinement, defined as (Ψ, Θ, Φ).

(3) - The g-tensor anisotropy $(g_{X'}, g_{Y'}, g_{Z'})$ is defined by the confinement anisotropy ($\omega_{X'}$, $\omega_{Y'}$, $\omega_{Z'}$). In addition, the confinement profile is scale invariant and can be described by

[1]Since the crystal axes [110] and $[1\bar{1}0]$ are degenerate in the 3D Luttinger model.

two parameters $\omega_{X'}/\omega_{Y'}$, and $\omega_{Z'}/\omega_{Y'}$.

(4) - The g-tensor anisotropy $(g_{X'}, g_{Y'}, g_{Z'})$ is moderately influenced by the orientation of the confinement with respect to the silicon crystal axes.

Here we briefly summarize the consequences of these four conclusions. The most significant consequence is the ability to reduce the number of free parameters in the model down to just two free parameters. The theoretical model initially contains six free parameters, which are (Ψ, Θ, Φ) and $(\omega_{X'}, \omega_{Y'}, \omega_{Z'})$. The parameters (Ψ, Θ, Φ) define the orientation of the anisotropic harmonic oscillator with respect to the crystal axes[1]. However, the orientation of the harmonic oscillator can be determined based on the orientation of the experimentally observed g-tensor. Therefore, in the case of our experiments we can fix the three angles[2] as $(\Psi, \Theta, \Phi) = (0,\ 45^o,\ \phi(V_{G4}))$, where $\phi(V_{G4})$ is the V_{G4} dependent ϕ defined in Equation 4.22 and 4.21. Further, since the 3D Luttinger model is scale invariant we can reduce the three remaining free parameters $(\omega_{X'}, \omega_{Y'}, \omega_{Z'})$, down to just two $(\omega_{X'}/\omega_{Y'})$ and $(\omega_{Z'}/\omega_{Y'})$. Reducing the model to just two free parameters is valuable for fitting the model to the experimental results. In addition, we note that the two free parameters define the relative confinement anisotropy.

4.8.4 Comparison of experimental results and the theoretical model

In the final section of this theoretical study, we compare the observed g-tensor anisotropy with the theoretically calculated g-tensor anisotropy. We have shown that it is possible to extract the confinement orientation based on the experimental g-tensor orientation[3]. The aim of this section is to determine if it is possible to extract the quantitative quantum dot confinement anisotropy $(\omega_{X'}/\omega_{Y'}, \omega_{Z'}/\omega_{Y'})$ from the experimental g-tensor data.

In Figure 4.15 we show the theoretical predictions for the principal g-factors $(g^*_{X'}, g^*_{Y'}, g^*_{Z'})$

[1] See section 4.8 for the full details.

[2] We can set $\Theta = 45^o$ because the y-axis of the sample is aligned with the $[1,\bar{1},0]$ crystal axes. However in general $\Theta = \theta(V_{G4}) + 45^o$, where $\theta(V_{G4})$ is the V_{G4} dependent in-plane angle. We have found that $\theta(V_{G4}) = 0$ for both V_{G4}=-0.7V and -0.9V, hence we set $\Theta = 45^o$. Note that Θ= 0 corresponds to the crystal [100] axes, while $\theta = 0$ corresponds to the sample y-axis $[1\bar{1}0]$.

[3] See section 4.8.2 for full details.

as a function of the two free parameters ($\omega_{X'}/\omega_{Y'}$) and ($\omega_{Z'}/\omega_{Y'}$). Figure 4.15(a)-(c) shows the predictions for the confinement orientation when V_{G4}=-0.7V where $(\Psi, \Theta, \Phi) = (0, 45^o, -70)$, and Figure 4.15(d)-(f) shows the predictions for the confinement orientation when V_{G4}=-0.9V where $(\Psi, \Theta, \Phi) = (0, 45^o, -43)$. The contour lines in each panel indicate regions of the theoretical model that correspond to the experimentally observed principal g-factors (see caption of Figure 4.15 for experimental values and uncertainty).

We begin by discussing the general trends that can be observed in Figure 4.15. Figure 4.15 provides a visual demonstration of how the confinement anisotropy ($\omega_{X'}/\omega_{Y'}$ and $\omega_{Z'}/\omega_{Y'}$) influences the magnitude of the g-factors ($g^*_{X'}, g^*_{Y'}, g^*_{Z'}$). We highlight three general results based on these simulations. **(1)** The model predicts that the hole g-factor in a silicon quantum dot can take any value between 0 and 4. This is consistent with the experimental results where we find the g-factor can be tuned over a range of 0 to 4. **(2)** The model predicts that the relative magnitudes of the g-factors are particularly sensitive to the confinement anisotropy[1]. When one confinement axis is much stronger than the others, the g-factor is largest along the axis of strongest confinement. This is clear by considering the red regions of the color scale with respect to the axis $\omega_{X'}/\omega_{Y'}$ and $\omega_{Z'}/\omega_{Y'}$. **(3)** In the regions where the confinement is comparable along two or more axes, the g-factors are extremely sensitive to small changes in the confinement profile. This can be observed in the regions around the contour lines, where the color scale changes rapidly.

Finally, we discuss the ability to quantitatively predict the confinement anisotropy ($\omega_X, \omega_{Y'}, \omega_{Z'}$) using the experimental g-factors. Contour lines are included in Figure 4.15 to indicate the regions in the $\omega_{X'}/\omega_{Y'}$ and $\omega_{Z'}/\omega_{Y'}$ parameter space where the calculated g-factors are similar to the respective observed g-factor. In order to quantitatively fit the model to the experiment, it is required to find a unique $\omega_{X'}/\omega_{Y'}$ and $\omega_{Z'}/\omega_{Y'}$ that can reproduce the experimental results. Black rectangles in Figure 4.15 indicate the regions in the parameter space that best reproduce the experimental results[2]. These regions are defined in the caption of Figure 4.15. A white circle is included in Figure 4.15 to indicate

[1] This is discussed in more detail in section 4.8.2.

[2] The black rectangles indicate the regions where at least two of the three experimental g-factors can simultaneously obtain for a single value of ($\omega_{X'}/\omega_{Y'}$, $\omega_{Z'}/\omega_{Y'}$).

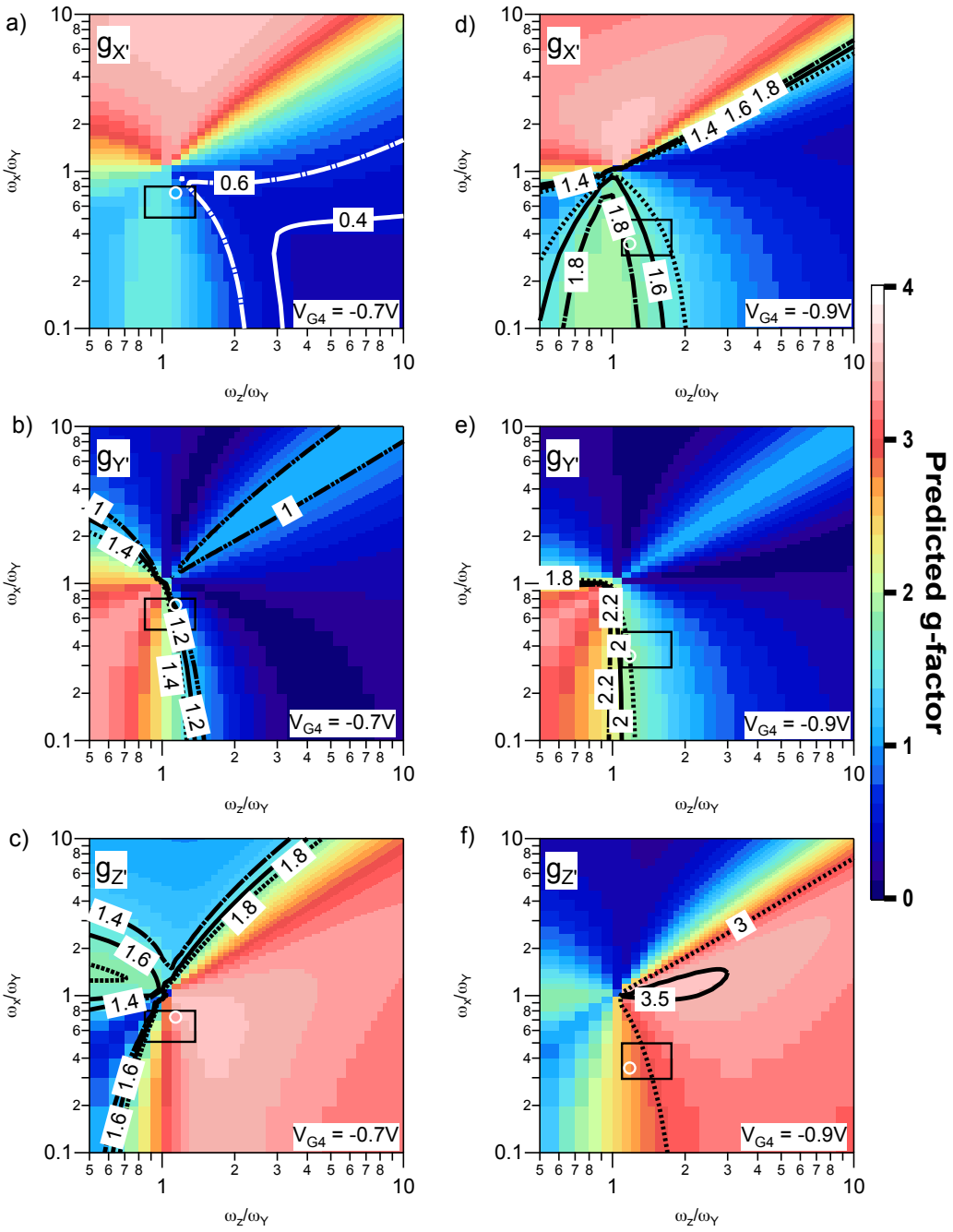

Figure 4.15: **Fitting g-factor anisotropy to the Luttinger harmonic oscillator model:** (**a-c**) Shows the calculated values of the principal g-factors $g^*_{X'}$ (a), $g^*_{Y'}$ (b), $g^*_{Z'}$ (c) for V_{G4} = -0.7V. (**d-f**) Shows the calculated values of the principal g-factors for V_{G4} = -0.9V. Contour lines indicate the regions of each figure where the theoretical value is close to the experimental value. Black rectangles indicate the region where a reasonable fit to at least 2 experimental g-factors can be obtained. For V_{G4} = -0.7V the black rectangle is defined by the region $(\omega_{Z'}/\omega_{Y'}, \omega_{X'}/\omega_{Y'})$ = ([0.85-1.35], [0.55-0.75]). For V_{G4} = -0.9V the black rectangle is defined by the region $(\omega_{Z'}/\omega_{Y'}, \omega_{X'}/\omega_{Y'})$ = ([1.15-1.75], [0.35-0.50]). A white circle is placed at the best fit within the black rectangle, see Table 4.3(a). The experimental values of $(g^*_{X'}, g^*_{Y'}, g^*_{Z'})$ for V_{G4} = -0.9V are $(1.6, 2.1, 3.9)\pm(0.2, 0.2, 0.2)$ and for V_{G4} = -0.7V are $(0.4, 1.2, 1.7)\pm(0.4,0.2,0.2)$).

the unique best fit of the parameters for each V_{G4} respectively.

(**a**) - Compare experiment and theory

Situation	$\omega_{X'}/\omega_{Y'}$	$\omega_{Z'}/\omega_{Y'}$	$g_{X'}$	$g_{Y'}$	$g_{Z'}$
Experiment - $V_{G4} = -0.9V$	NA	NA	1.6 ± 0.2	2.1 ± 0.2	3.9 ± 0.2
Model Fit - $V_{G4} = -0.9V$ (1.4, 4.0, 4.6)	0.35	1.15	1.8	2.0	2.8
Experiment - $V_{G4} = -0.7V$	NA	NA	0.4 ± 0.4	1.2 ± 0.3	1.7 ± 0.2
Model Fit - $V_{G4} = -0.7V$ (3.0, 4.0, 4.6)	0.75	1.15	1.0	1.2	3.3

Table 4.3: **Table summarizing main results of Figure 4.15**: (**a**) Compares the experimental principal g-factors with the best fit regions from the theoretical model. The column $\omega_{X'}/\omega_{Y'}$ and $\omega_{Z'}/\omega_{Y'}$ indicates the location of the white circle in Figure 4.15. This is the location of the best fit of the calculated g-tensor to the experimental data. The values for $g^*_{X'}$, $g^*_{Y'}$, and $g^*_{Z'}$ are the values at the white circle in Figure 4.15.

In Table 4.3(a) we have indicated the best fit of the model to the experimental g-factor anisotropy. The values of $(g_{X'}, g_{Y'}, g_{Z'})$ presented in Table 4.3(a) are the principal g-factors at the position indicated by the white circles in Figure 4.15. Based on best fit we find the confinement[1] for V_{G4} = -0.9V is $(\omega_{X'}, \omega_{Y'}, \omega_{Z'})$ = (1.4, 4.0, 4.6), while for V_{G4} = -0.7V the confinement is $(\omega_{X'}, \omega_{Y'}, \omega_{Z'})$ = (3.0, 4.0, 4.6).

The best-fit confinement profile is consistent with what was deduced from the experimental trends. First we note that in both cases the confinement is not *disk*-like, but rather has similar confinement in all dimensions. Further, the only difference between the best-fit confinement profiles is the value of the $\omega_{X'}$ confinement. These results are consistent with the predictions from the experimental results and the analysis of orientation dependence. The difference between the confinement profile for V_{G4} = -0.9V and V_{G4} = -0.7V is a enhancement of the x-axis confinement ($\omega_{X'}$), and a rotation around of ϕ by -25^o.

There is consistency between the theoretical and experimental results. Thanks to this consistency, the theoretical model provides reliable insight into the expected effects that various mechanisms (such as crystal orientation, confinement strength, and confinement

[1]Here were present the confinement anisotropy with respect to the values $(\omega_{X'}, \omega_{Y'}, \omega_{Z'})$. Since the confinement is spatially invariant (section 4.8.2) only the ratio of these values are relevant ($\omega_{X'}/\omega_{Y'}$ and $\omega_{Z'}/\omega_{Y'}$). However, for the purpose of discussion we find it more intuitive to present representative values of $(\omega_{X'}, \omega_{Y'}, \omega_{Z'})$.

orientation) have on the g-tensor. We now briefly discuss the potential directions for future modeling and theoretical research. Firstly, we note that the uncertainty in the parameters $\omega_{X'}/\omega_{Y'}$ and $\omega_{Z'}/\omega_{Y'}$ is quite large (given by the black rectangles in Figure 4.15). This is a consequence of the fact that the confinement is comparable in all three dimensions. We find that the g-factor varies quite widely within the best fit regions, and therefore the calculated g-factors are extremely sensitive to fine changes in the confinement profile[1]. Therefore, care should be taken to select a realistic confinement profile[2]. This could be achieved by undertaking 3D electrostatic modeling of the device, to determine a realistic shape of the quantum dot for the given gate lithography and applied voltages.

The most significant discrepancy between the calculated and experimental g-tensor is in the value of $g^*_{Z'}$. We note that for both V_{G4} = -0.9V and V_{G4} = -0.7V the calculated value of $g^*_{Z'}$ is well outside the uncertainty range of the experimental data. We have seen that additional effects, such as crystal orientation can lead to a change in the g-factor magnitudes. Hence, this discrepancy suggests that additional mechanisms may be required in order for the model to quantitatively reproduce the experimental g-tensor. One particular mechanism that is interesting for future study is the effect of strain. Strain has not been included in the Luttinger model that we have studied. It is known that strain can introduce shifts in the wavefunction and g-tensor of electrons in silicon quantum dots [147–151]. In silicon MOS quantum dots strain can be introduced due to intrinsic stress caused by different thermal properties of the gate and the substrate material[3]. It would be interesting to include strain into the 3D Luttinger model, in-order to determine the magnitude of the effect of strain on the g-tensor.

In the experimental results of section 4.7 we showed that the g-tensor orientation and magnitude could be manipulated with electric fields, and we hypothesized this was due

[1]This is clear when considering the regions in Figure 4.15 close to $\omega_{X'}/\omega_{Y'} = \omega_{Z'}/\omega_{Y'} = 1$. In these regions the g-factor changes rapidly since the confinement is finely balanced

[2]The 3D anisotropic harmonic confinement was selected for this study, since it is intuitive and reasonable as a first assumption. It is possible to easily tune the parameters $(\omega_{X'}, \omega_{Y'}, \omega_{Z'}, \Psi, \Theta, \Phi)$ and systematically observe the effects.

[3]In this case the gate is Al and the substrate is Si. Al has a linear thermal expansion coefficient α = 23.1×10^{-}6 K^{-1} while for Si α = 2.56×10^{-}6 K^{-1}. This is an order of magnitude difference, so large strain is possible [147].

to the confinement profile rotating and becoming comparable in all three dimensions. In section 4.8.1 we introduced a 3D Luttinger model with a set of intuitive parameters for investigation. In this final section we have shown that the model confirms the hypothesis of the experimental results. By systematically studying the free parameters of the model we have learned that the g-tensor orientation is defined by the confinement orientation. Similarly we determine that the confinement anisotropy and crystal orientations play a role in determining the g-factor magnitudes. Interestingly the model and experiment suggest that the confinement is comparable in all three dimensions, which is surprising for MOS-based quantum dots. Finally, we have concluded this section by indicating directions for future modeling and theoretical research.

4.9 Conclusion and outlook of Chapter Four

Studies of the Landé g-factor allow insight into the spin-properties of a system. In addition, the ability to modulate the g-factor leads to potential applications, particularly for spin-qubits. This chapter focuses on characterising the hole g-tensor modulation in silicon MOS quantum dots. To this end, we have study one single hole confined by a quantum dot device in a known orbital state.

The main result of this Chapter is the full 3D characterisation of the anisotropic hole g-tensor. These experimental results show that the hole g-tensor can be strongly tuned using electric fields. The experimental and theoretical results suggest that the quantum dot confinement is best described as 3 dimensional, rather than 2 dimensional (*disk*-like) as may have be expected for MOS quantum dots. This is a key result since it is common to model MOS quantum dots in the 2D limit. The 3D confinement will give distinctly different spin and orbital physics, particularly since the 3D confinement will effect the Heavy-Hole Light hole mixing.

The effective hole g-factor can be tuned from 3.9±0.2 to 0.4±0.4 over the range of voltages and magnetic orientations. These results show that hole spins in silicon MOS quantum dots have high potential for use in spin-based electronics. The magnitude of the electric g-factor modulation ($\Delta g/\Delta V$) is found to be comparable to spin systems

that have been successfully used as fast all-electric spin-qubits [21, 132]. Future work would be to study all-electric spin manipulation of holes in a known orbital state. It would be particularly interesting to compare experimental Rabi frequencies with the Rabi frequency calculated from g-factor modulation calculations, similarly to Crippa *et al.* [21]. In addition, it would be interesting use spin manipulation techniques to investigate the time-domain spin properties (T_2^* and f_{Rabi}) of holes in distinctly different orbital shells [152].

In this chapter we have studied the g-tensor properties calculated by a 3D Luttinger model. The model includes the orbital confinement and crystal anisotropy. We have modeled the quantum dot confinement with an idealized 3D anisotropic harmonic oscillator, which provides 6 intuitive free parameters for investigation. We use this model to investigate the leading mechanisms that influence the hole g-tensor. We have shown that the confinement orientation and anisotropy is the primary factor that determines the g-tensor orientation and anisotropy of a hole quantum dot in silicon. This is consistent with other quantum dot systems where the spin-orbit coupling is strong [5, 21, 141, 142]. Further, these conclusions are consistent with the experimentally observed hole g-tensor properties presented in section 4.7. In addition, we have used the model to show that the crystal anisotropy has an influence on the magnitude of the hole g-factor.

Finally, we comment on the prospects for future work on the theoretical model. We show that the g-tensor is extremely sensitive to small changes in $(\omega_{X'}, \omega_{Y'}, \omega_{Z'})$ when the confinement strength is comparable in all 3 dimensions. Since the device under study has comparable confinement in all three dimensions, we find it is difficult to determine an exact best fit to $(\omega_{X'}, \omega_{Y'}, \omega_{Z'})$. In general, this is to be expected since we include an intuitive but simplified confinement profile. For future work we propose including a more realistic confinement profile based on an electrostatic model of the MOS device. Electrostatic modeling has proven valuable in uncovering underlying spin physics of electrons in silicon quantum dots [153]. We expect that by including a more realistic confinement profile for the three dimensional confinement it can be possible to achieve a full quantitative fit to the experimental g-factor. With a full electrostatic model the g-factor anisotropy can be used to determine the spatial profile of the hole wavefunction. In

addition, we suggest future work should include the effects of strain in the model. It will be interesting to predict the extent that strain can perturb the hole wavefunction, and modify the g-tensor. This would provide valuable information regarding the fundamental physics of hole states, and also for determining the suitability of hole spins for spin qubit applications.

Chapter 5

Conclusions

The feeling is not so much that this is an ending
but rather, this is just another starting point.

5.1 Summary of results

In this section we briefly summarize the principal findings of this thesis. There were three major aims which we set-out to address in this thesis:
(1) - Determine if it is possible to isolate a single hole in a silicon MOS quantum dot.
(2) - Characterise the orbital shell structure of holes in a silicon MOS quantum dot.
(3) - Study the spin physics of a single hole in a silicon MOS quantum dot.

In Chapter 2 we present measurements of a planar p-type silicon MOS quantum dot device with an adjacent charge sensor. We confirm the device is capable of operating down to the last hole in both the single quantum dot and double quantum dot configurations. This ability to isolate a single hole in a silicon quantum dot is significant for two reasons. The first is that this allows spectroscopy measurements of silicon based holes in a known and reproducible orbital state. The second is that the most successful spin qubit devices have been operated in the regime of the last few charges [17, 19, 30, 55, 154].

In Chapter 3 we present spectroscopic measurements of a planar p-type silicon MOS quantum dot device in a known and reproducible charge configuration. We extract the

confinement energy and the orbital energy levels using excited state and magnetic spectroscopy measurements. We find that the quantum dot shell structure is consistent with the Fock-Darwin spectrum expected for 2D artificial atoms, with hole spin filling obeying Hunds rules. Interestingly, we find that the hole-hole Coulomb interaction is quite large, and can significantly influence the orbital shell structure, even in a dot containing just two holes. This provides motivation for using singly occupied hole quantum dots for spin qubit applications.

In Chapter 4 we characterise the anisotropic Landé g-tensor of a single hole in a known orbital state. We demonstrate strong modulation of the g-tensor by using electric fields to control the confinement anisotropy and orientation. This shows that hole spins are strongly influenced by the orbital confinement due to strong spin-orbit coupling. Since we find that the g-tensor is linked to the confinement, our results suggest that the quantum dot confinement can be tuned to be three dimensional. This is a surprising result since it has been typical to consider MOS based quantum dots as 2D disk-like structures [30]. We support the experimental findings by studying a 3D Luttinger model with an intuitive confinement profile. Finally, we discus the potential for future theoretical work since the effects of strain have not yet been included in the model.

5.2 Outlook

In the final section we present an outlook on future research that is motivated by the results presented in this thesis. Where appropriate we comment on what would be involved, what has already began and the feasibility.

Improved charge sensing for hole quantum dots

In this thesis we presented measurements of a hole quantum dot with an adjacent p-type charge sensor. Typically in experiments using p-type charge sensors we must employ integration times of 100-300ms. This has prevented access to single shot measurements[1], which are standard for n-type charge sensors [6, 30]. Single shot measurements would

[1]Single shot measurements require acquisition times shorter than the tunneling time of an electron. Using averaging we demonstrated tunnel times on the order of several mili-seconds (see section 2.7.2).

allow access to time domain measurements of the hole spin properties. The challenge is primarily due to the reduced mobility of the holes in silicon, which limits the maximum transconductance of the p-type charge sensor.

As an outlook for future work, a potential solution is to use ambipolar devices. Devices that include a p-type quantum dot, and an adjacent n-type charge sensor could allow the advantages of highly sensitive and successful single electron transistor charge sensing for studies of a hole quantum dot. This would not necessarily require any changes in the device lithography. Rather, the only design charge would be to invert the polarity of the charge sensor ohmic contacts, so that they are both n-type. Prospects for ambipolar devices are the promising, and there have already been preliminary work by other research groups [114] towards this goal. We have began tests of ambipolar devices in collaboration with F.E. Hudson and I.K. Jin. In Figure 5.1 we show a schematic of a potential ambipolar device design, which allows a n-type charge sensor adjacent to a p-type quantum dot.

Investigation of T_1 and T_2^* in the single hole regime

A major motivation for future work is to characterise the hole spin relaxation (T_1) and decoherence time (T_2^*) in the single hole regime. Previous research by Maurand *et al.* [20] has found T_2^*=60ns for holes in silicon nanowire quantum dots. These results are a stunning breakthrough for p-type CMOS technology. However, the measurements were performed in the few hole regime, so the orbital state was not known. It has been shown that the specific configuration of the orbital levels can cause T_2^* to vary over several orders of magnitude [75]. Further, in this thesis we have shown that spin-orbit interaction and hole-hole interactions can complicate the orbital structure when several holes occupy a quantum dot. It would therefore be valuable to use the devices in this thesis to characterise T_1 and T_2^* in a known and reproducible charge and orbital state.

We now briefly discuss the feasibility of performing T_1 and T_2^* characterisation. Measurements of spin coherence and relaxation typically require the application of MHz to GHz electrical signals. The hardware and software required to implement these high frequency measurements was not available in my research group at the beginning of this postgraduate program. During this PhD program I have worked with R. Li, F. Mar-

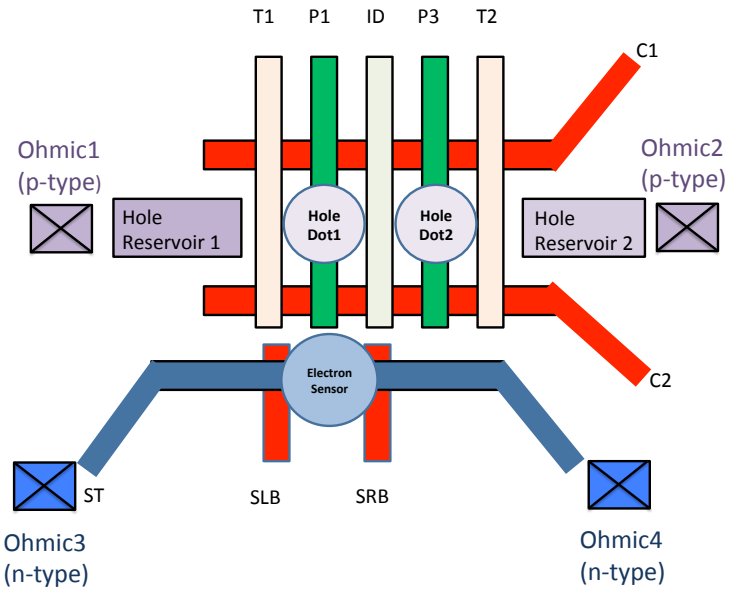

Figure 5.1: **Schematic of ambipolar device design:** The top region is a p-type (purple) double quantum dot with two tunnel barriers (T1 and T2), two confinement gates (C1 and C2), two plunger gates (P1 and P2), and inter-dot coupling control (ID). This design allows transport of holes through the double quantum dot from Ohmic 1 to Ohmic 2. In addition if T2 is made fully depleting and the Reservoir 2 is depleted, then the device acts as a single lead quantum dot. The bottom region (blue) is the n-type charge sensor, where a single electron quantum dot can be formed between the barrier gates. The sensor is offset with respect to the hole double dot to allow different capacitive coupling between Dot 1 and Dot 2 with the sensor.

tins and I. Vorreiter to install and characterise high frequency measurement hardware[1]. In addition, I have worked with I. Thorvaldson to develop the software environment required for these measurements.

A significant technical achievement resulting from this PhD program has been the successful implementation of a high frequency measurement ensemble in our groups laboratory. To demonstrate operation we have implemented high frequency pulse sequences to characterise tunnel rates up to 100MHz. In Figure 5.2(a) we present a characterisation of the hole tunnel period, measured at different points (2,0) to (1,1) region of the double dot charge stability. These tunnel rates are determined by observing the averaged response of the charge sensor to microsecond duration pulses on the quantum dot gates. We observe the tunnel time onto the G2 dot is much faster than the G4 dot, consistent with the respective distances between the each dot and the reservoir as

[1]This includes cryogenic high frequency coax on the dilution refrigerators, reflectometry circuits, and acquisition of arbitrary waveform generators IQ capable microwave sources.

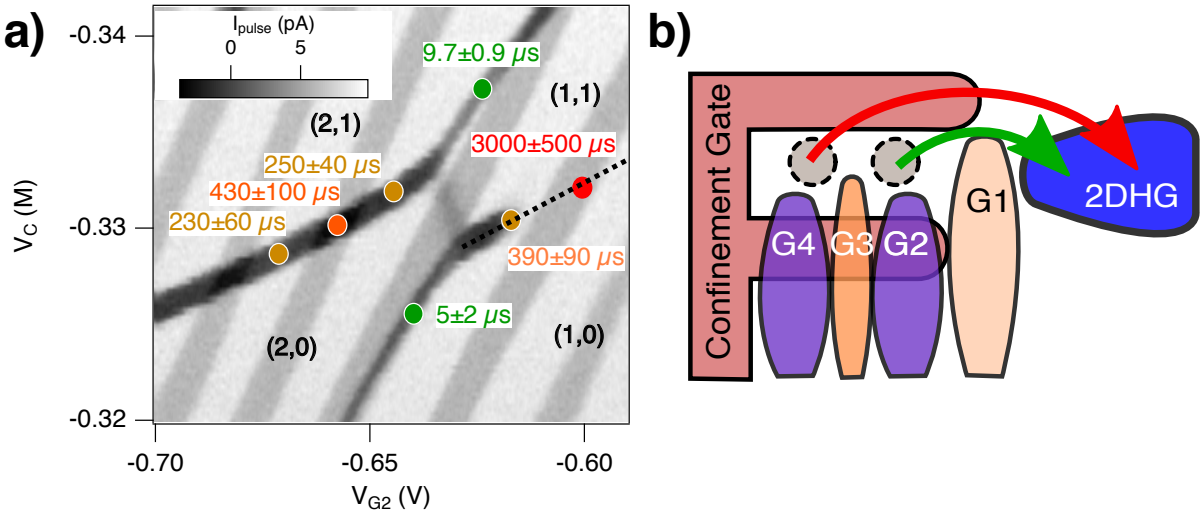

Figure 5.2: **Characterising fast hole tunnel rates:** (**a**) Shows a charge stability diagram of the device studied in chapter 4. The device is tuned to the last hole regime. Grey diagonal stripes are the non-interacting *accidental* background quantum dot transitions (Discussed in Appendix A.3.2). The clear double dot charge transition can be observed in black. Measurement of the hole tunneling times have been performed at different location in the stability diagram. The measured tunnel times are shown in text, with the colour indicating the relative rate (red for slow, green for fast). (**b**) Shows a schematic of the device, and provides an explanation for the trend in the tunnel rates. The time to load the G4 dot, horizontal transition in (a) is much longer since the G4 dot is further from the reservoir.

shown schematically in Figure 5.2(b). Finally, the high frequency experimental set-up has been used by other members of our research group to achieve EDSR of holes in a different quantum dot device[1]. Since the EDSR measurements and fast pulse sequences are typical techniques used to extract T_2^* and T_1, this demonstrates that characterising T_1 and T_2^* is a realistic prospect for future work.

Investigation of hole spins in higher momentum orbital states

In this thesis we have performed a detailed study of the g-tensor of holes in the lowest energy orbital state. Holes that occupy higher energy orbitals (such as p or d orbital) will have larger angular momentum. This may give rise to exotic non-trivial spin-orbit phenomenon [152]. The devices presented in this thesis are suitable for studies of the higher orbital states, since it is possible to determine the exact charge and orbital state. Particularly it can be interesting to characterise the Landé g-factor and other spin properties (such as T_1 and T_2^*) for the higher orbital states. Interpretation and understanding of the higher orbital hole spin physics could be further theoretically investigated by extending the 3D Luttinger model developed in section 4.8.

[1]Unpublished research of M. Rendell.

Thank you for your time and consideration,

Scott Liles.

"Here was the secret of happiness, about which philosophers had disputed for so many ages, at once discovered; happiness might now be bought for a penny, and carried in the waistcoat-pocket; portable ecstasies might be had corked up in a pint-bottle; and peace of mind could be sent down by the mail"

Thomas De Quincey.

Appendix A

Supporting experimental results for Chapter 4

"I spent the day running full diagnostics on every system in the Hab. It was tedious, but my survival depends on these machines, so it had to be done. I can't just assume an explosion did no long term damage"

The Martian, Andy Weir.

A.1 Appendix Introduction

In this Appendix we present results and analysis that supports the conclusions drawn in Chapter 4. These supporting results are presented in the Appendix so that the main conclusions of Chapter 4 can be clearly and concisely developed.

In section A.2 we present supporting details related to the device and the analysis. These details are relevant since the device studied in Chapter 4 is a different device to the one studied in Chapters 2 and 3. A key result of this section is the demonstration that the lever arm is independent of V_{G4}, which is important for the analysis of addition energies. In addition, we present details of the fitting algorithms used in Chapter 4.

A fundamental aspect of the results presented in Chapter 4 is that the g-tensor has been characterised for a single hole in a known orbital state. In section A.3 we present

results demonstrating that the last charge has been reached. In addition, we have found that a background structure can be observed in the single hole charge stability diagrams presented in Chapter 4. In section A.3.2 we demonstrate that this structure results from the presence of a secondary *accidental* quantum dot. We confirm that this *accidental* quantum dot does not interact with the primary quantum dot, and discuss the likely origin of the *accidental* quantum dots. This analysis provides details relevant for future device design, which can aim to eliminate the source of *accidental* quantum dots.

One of the main assumptions of Chapter 4 is that V_{G4} controls the quantum dot confinement profile. In section A.4.1 we show that the orbital shell structure is dependent on V_{G4}. Since the orbital structure is determined by the quantum dot confinement profile, this section demonstrates that V_{G4} does control the quantum dot confinement profile.

Finally, in section A.5 we present the full data set taken during this experiment. This data set is presented in two figures, and much of the data presented has not yet been fully analyzed. This provides insight into the data-set of experimental results that is available for future work, either by our research team, or by interested collaborators.

A.2 Experimental details

A.2.1 Experimental set-up and methods

All measurements in Chapter 4 were undertaken using a BlueFors XLD250 dilution refrigerator with a base temperature around 100mK. The system has a vector magnet capable of producing 5T along one axis, and 1T along the other two axes. The charge sensor is operated in the same way as described in section 2.6.3 of Chapter 2. During standard measurements of the charge sensor we add a 1mV DC voltage to a 50μV AC voltage at 77Hz and apply these signals to the source ohmic contact of the charge sensor. Pulse bias sensing [38] of the quantum dot charge state is achieved by applying a symmetric square pulse of amplitude 4mV at 177Hz to G2. The output signal of the charge sensor drain ohmic-contact is filtered at 3kHz and amplified by a Basel current pre-amplifier (Basel SP 0983).

We simultaneously record three measurements, the AC sensor conductance, the DC sensor conductance, and the charge sensor signal (transconductance). The AC charge sensor conductance is measured with a lock-in at 77Hz, and is monitored so that a feedback mechanism can keep the sensor at optimal sensitivity [40]. The DC charge sensor conductance is monitored in order to perform tunnel rate independent measurements of the quantum dot charge state (see section A.3.1). Finally, the charge sensor signal is a measurement of the charge sensor transconductance and is measured by observing the modulation of the DC current due to the square pulse applied to G2. This is measured with a second lock-in operating at the frequency of the square pulse (177Hz). The charge sensor signal is sensitive to the changes in the hole occupation of the quantum dot. See Chapter 2 section 2.6.3 for further details of this charge sensing method.

A.2.2 Lever arm calibration

In Chapter 4 we compare the addition energies and g-factors measured for different V_{G4}. These measurements rely on using a known lever arm (α) to convert ΔV_{G2} into ΔE. We assume that V_{G4} has the potential to shift the confinement profile of the quantum dot[1]. Shifting the confinement profile could result in a change in the lever arm, which would complicate the comparison of addition energies and g-factors measured at different V_{G4}. In this section we show that the lever arm is independent of V_{G4}.

The lever arm is extracted by observing the thermal broadening of a charge transition peak. Thermal broadening is produced by heating the mixing chamber stage of the BlueFors XLD250 dilution refrigerator. In Figure A.1(a) we show a charge transition peak measured when the mixing chamber temperature (T_{MC}) was 28mK (blue) and 793mK (red). The charge transition peak shape is given by the derivative of the Fermi-Dirac distribution,

$$I_{signal} = \frac{\alpha e}{k_B T} \frac{A e^{\frac{\alpha e(V_{G2}-V_0)}{k_B T}}}{1 + e^{\frac{\alpha e(V-V_0)}{k_B T}}} \tag{A.1}$$

where α is the lever arm, e is the electron charge, k_B is the Boltzmann constant, V_0 is the

[1]This assumption is confirmed in section A.4.1.

G2 voltage at the peak center[1], V_{G2} is the voltage applied to G2, A gives the amplitude of the peak, and T is the temperature of the system given by $T = \sqrt{T_{MC}^2 + T_H^2}$. Here the temperature, T, is defined by the mixing chamber temperature (T_{MC}), and the hole-bath temperature (T_H).

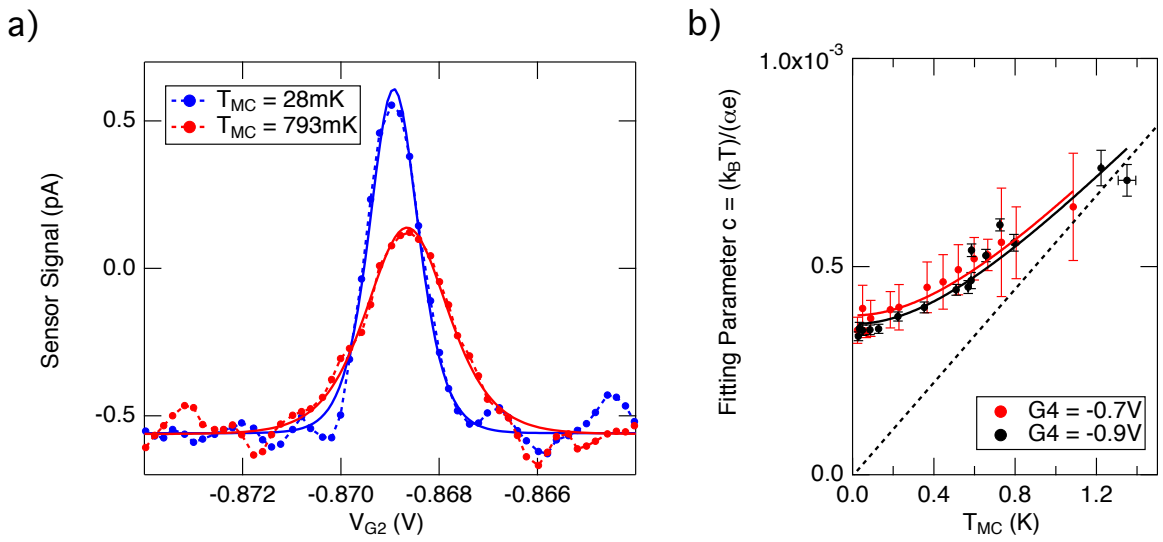

Figure A.1: **Lever Arm Calculation:** (**a**) The first Coulomb blockade charge transition for V_{G4} = -0.7V measured at two different temperatures of the BlueFors XLD250 mixing chamber temperature T_{MC}. The peak is broadened due to the change in temperature. Solid lines are the fit of Equation A.2 to the data points, and dashed lines connect the measured points. (**b**) The fitting parameter c of Equation A.2 is plotted as a function of the T_{MC}. This is repeated for two different V_{G4} and shows c is independent of V_{G4}. Solid lines are the fit to Equation A.3 allowing the extraction of the lever arm α. The dashed line shows asymptote of the fits, which intercepts $T_{MC} = 0$. Error bars come from standard deviation in fitting to charge transitions and variations in the temperature over the measurement

We extract the lever arm by fitting the Coulomb peaks to a simplified form of Equation A.1,

$$I_{signal} = \frac{Ae^{\frac{(V_{G2}-b)}{c}}}{c(1+e^{\frac{(V_{G2}-b)}{c}})} \tag{A.2}$$

$$c = \frac{k_B}{\alpha e}T$$

$$c = \frac{k_B}{\alpha e}\sqrt{T_{MC}^2 + T_H^2} \tag{A.3}$$

In Figure A.1(b) we show the value of the fitting parameter c as a function of mixing chamber temperature. Comparing the red and black data in Figure A.1(b) we show that

[1]Where the Fermi energy of the dot matches the Fermi energy of the reservoir.

the lever arm is independent of V_{G4}. Solid lines in Figure A.1(b) show the fitting of each data set to Equation A.3. We extract the lever arm to be $\alpha_{0.9} = (0.167 \pm 0.007)$eV/V and $\alpha_{0.7} = (0.166 \pm 0.007)$eV/V for $V_{G4} = -0.9$V and $V_{G4} = -0.7$V respectively. These values are comparable to the previous lever arm of 0.174eV/V in Chapter 3 section 3.3, which is reasonable since the devices have identical lithography.

Fitting gives the constant offset in temperature $T_H = 700 \pm 50$mK. Previous measurements of the hole and electron bath temperature on this BlueFors XLD250 system have given results around 100mK. These previous tests we performed with no high frequency coaxial lines connected. In this measurement two SMA coax lines were connected via cold bias tees[1]. The bandwidth of the coax lines is around 10GHz, which could explain the anomalously large T_H for this measurement.

A.2.3 Rotating between co-ordinate systems

In Chapter 4 section 4.8 we introduce the principal confinement axes of the Harmonic oscillator as X', Y' and Z'. These coordinates are arbitrarily oriented with respect to the crystal axes x = [1,0,0], y =[0,1,0] and z = [0,0,1]. One can transform between the two co-ordinate systems by rotating the crystal axes (x,y,z) around z by angle Φ, then rotating around the new x-axis by angle Ψ, and finally rotating around the new y-axis by angle Θ. Mathematically the transform from the crystal axes (x,y,z) to the harmonic oscillator axes (X, Y, Z) is achieved using the following equation,

$$\begin{pmatrix} X' \\ Y' \\ Z' \end{pmatrix} = R_y(-\Phi) \cdot R_x(-\Psi) \cdot R_z(-\Theta) \cdot \begin{pmatrix} x \\ y \\ z \end{pmatrix} \tag{A.4}$$

[1]Bias-tee is on sample board connected to the BlueFors mixing chamber. Parameters are 330kΩ and 4.7nF.

where R_x, R_y, and R_z are the rotation matrices defined as,

$$R_x(\theta) = \begin{pmatrix} 1 & 0 & 0 \\ 0 & \cos\theta & -\sin\theta \\ 0 & \sin\theta & \cos\theta \end{pmatrix} R_y = \begin{pmatrix} \cos\theta & 0 & \sin\theta \\ 0 & 1 & 0 \\ -\sin\theta & 0 & \cos\theta \end{pmatrix} R_z = \begin{pmatrix} \cos\theta & -\sin\theta & 0 \\ \sin\theta & \cos\theta & 0 \\ 0 & 0 & 1 \end{pmatrix} \quad \text{(A.5)}$$

A.2.4 Extracting the position of the Coulomb peaks

In this section we provide details for how the Coulomb peak center and amplitude is extracted from large data sets. In Figure A.2(a) we show data for an example charge transition. Here, the Coulomb peak maximum occurs at V_{G2} = -0.8096V. We can then extract the addition energy by measuring the spacing between consecutive Coulomb peaks. In Figure A.2(b) we show $E_{add}(1)$, measured for different in-plane magnetic field magnitudes. The spacing between the first and second charge transitions has been extracted by finding the maximum point of each Coulomb peak. We then extract the g-factor from the slope dE_{add}/dB. In Figure A.2(b) the g-factor was found to be $g^* = (2.72 \pm 0.24)$.

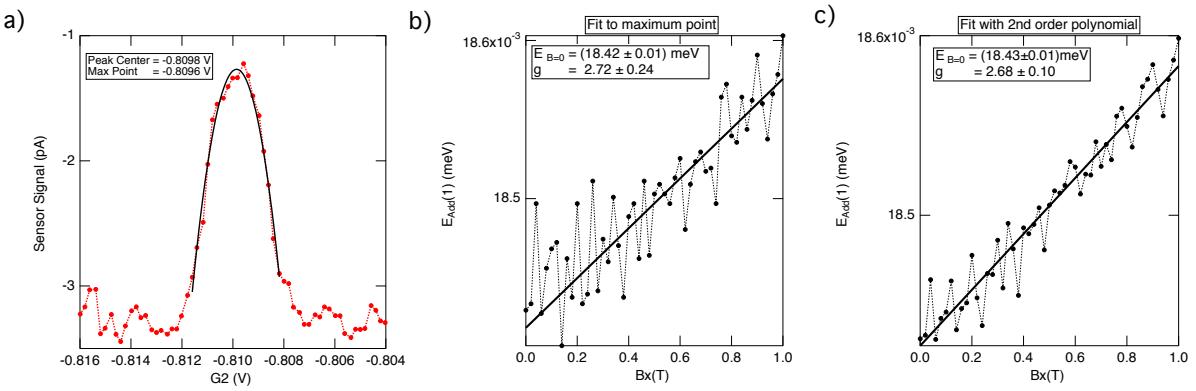

Figure A.2: **Fitting to Coulomb peaks and extracting g-factors:** (**a**) An example of a Coulomb peak measured with the charge sensor. Solid black line is a the result of fitting a second order polynomial to 20 points centered at the maximum reading. (**b**) The first addition energy calculated by finding the spacing between the maximum data point of the first and second Coulomb peaks. Solid black line is a linear fit to the data, with the slope and intercept presented in the inset with standard deviation. (**c**) Same as (b) except the addition energy is calculate by finding the spacing between the maximum points of the parabolic fits. In all panels dots indicate measured data points and dashed lines connect all data points.

For more accurate measurement of the Coulomb peak center and amplitude we fit a

second order polynomial to a region of points around the peak maximum. An example of this fitting is shown as the solid black line in Figure A.2(a), where 20 data points around the peak maximum point were used for fitting. In this case the parabolic fit gives the peak center as V_{G2} = -0.8098V , which is different to the peak maximum by 0.2mV. In Figure A.2(c) we show $E_{add}(1)$ extracted from the same data set as Figure A.2(b), however the peak center is now found using a parabolic fit. When parabolic fitting is used we extract the g-factor to be $g^* = (2.68 \pm 0.10)$. We find that the standard deviation in the g-factor is reduced by half when using the parabolic fitting.

We have tested using different fitting functions and find that the standard deviation is not changed whether we use a Gaussian, Lorentzian, or the derivative of the Fermi Dirac distribution given in Equation A.1. Given this, we use a second order polynomial to fit around the peak maximum for programming convenience. In summary, we have demonstrated the method we use to extract coulomb peak amplitudes and centers, and shown that this method allows for a reduction in the standard deviation of the g-factor compared to simply finding the peak maximum.

A.2.5 Estimate of the dot size as a function of G4 voltage

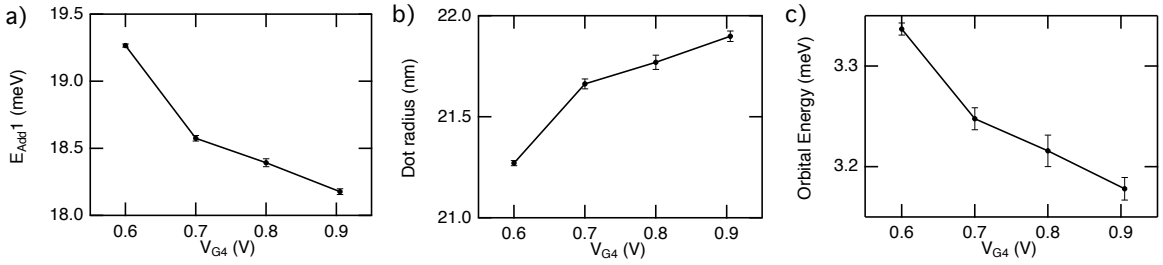

Figure A.3: **Estimate of the dot size and orbital energy for different confinement potentials:** (**a**) Shows the addition energy, $E_{add}1$ for four different V_{G4}. These values are extracted from the intercept of the linear fits in Figure 4.8(d). (**b**) The approximate radius of a 2D circular quantum dot for the given charging energies, as in Equation A.6. (**c**) The single particle orbital energy of a dot given the sizes calculated in (b).

In this section we provide rough estimates of how the dot size and orbital energies are changed by V_{G4}. In section 4.6 we showed that the first addition energy $E_{add}(1)$ varies as V_{G4} is changed. This was used as evidence to suggest that V_{G4} is strongly influencing the

confinement strength of the quantum dot. The energy required to add the second hole, $E_{add}(1)$, can be related to the capacitance of the dot. We model the dot and plunger gate (G2) as a circular parallel plate capacitor in order to estimate the dot radius using the charging energy,

$$E_{\mathrm{C}} = E_{\mathrm{add}} = \frac{C}{e} = \frac{\epsilon_r \epsilon_0 \pi r^2}{de} \tag{A.6}$$

Taking the oxide thickness, d, to be 5.9nm and relative permitivity, ϵ_r, of silicon oxide to be 3.9, we can calculate the dot radius, r, for the different charging energies. In Figure A.3(a) we show the B=0 $E_{add}(1)$ extracted from the measurements in Figure 4.8(d). Using Equation A.6 we estimate the corresponding dot radius, assuming the dot is a 2D circular quantum dot. These estimates suggest the dot radius changes by approximately 3% over the range of V_{G4}. We are also interested in an approximate calculation of the orbital energy and the change in orbital energy. If we assume the dot is a 2D harmonic potential we can estimate an orbital energy using the relation,

$$r = \sqrt{\frac{4\hbar}{m^*\omega}} \tag{A.7}$$

where ω describes the harmonic confinement strength (see Chapter 3 section 3.6). In Figure A.3(c) we show the approximate orbital spacing for the estimated dot radius. These estimates suggest that the orbital energy could be around 3meV, and changes by around 5%. We acknowledge that 2D parallel plate and harmonic oscillator models are not realistic models for this device, especially since the g-factor anisotropy results in Chapter 4 section 4.7 suggest that V_{G4} rotates the dot confinement in the z-x plane, and the confinement is comparable in all three spatial dimensions. However, the results presented in Figure A.3(b)-(c) provide a general estimate of the dot size and orbital spacing, which can be used rough guide when considering the physical properties of this device.

A.3 Confirmation of the charge occupation

A.3.1 Confirmation of the absolute hole occupation

In Chapter 4 all charge stability diagrams and Coulomb charge transitions are measured using pulse bias charge sensing (see section A.2.1). This charge sensing technique is sensitive to the tunnel rate between the quantum dot and the reservoir of holes. For tunnel rates smaller than than the pulse frequency (177Hz in this experiment), visibility of the charge transition is lost. This can be clearly seen in the Figure A.4(a), where at V_{G2} = -0.6V the transitions lose visibility. This is due to the effect of G2, which acts as both a plunger gate and a partial tunnel barrier. In this section we present charge sensing measurements that are insensitive to the tunnel rate, allowing confirmation of the absolute charge occupation of the device studied in Chapter 4.

Tunnel rate independent charge sensing is performed by monitoring the DC current through the charge sensor. When monitoring the DC current the amplitude of the square pulse is set to 0V and no sensor feedback is applied[1]. Figure A.4(b) shows the DC sensor current monitored in the upper black dashed rectangle of A.4(a). The last charge transition can be observed running parallel to the dashed white indicator line. With these measurements we can observe many transitions in the region where $V_{G2}<$-0.9, however we observe no additional transitions when $V_{G2}>$-0.82, confirming the device has been depleted of all holes.

In Figure A.4(c) we present the DC charge sensor measurement of the region indicated by the bottom right dashed rectangle in Figure A.4(a). In this region the tunneling rate onto the dot has dropped such that charge transitions are no longer observable in pulse bias charge sensing. However, this region can be identified as the expected location for the (1,0) to (1,1) crossing, since the (0,1) to (1,0) inter-dot transition is visible as a white diagonal line[2]. Since the DC sensor current is independent of the tunnel rate, all charge transition of the double dot crossing, including the inter-dot transition are clearly

[1]Here the source-drain DC voltage was 1mV.

[2]Although the standard charge transitions cannot be resolve, the (1,0) to (0,1) inter-dot charge transition can be seen in A.4(a) since the inter-dot tunnel rate is much larger than the dot-to-reservoir tunnel rate.

resolved in A.4(c). The measurement of Figure A.4(c) is consistent with the expected double dot charge stability diagram, and provides clear evidence that we have reached the last charge regime.

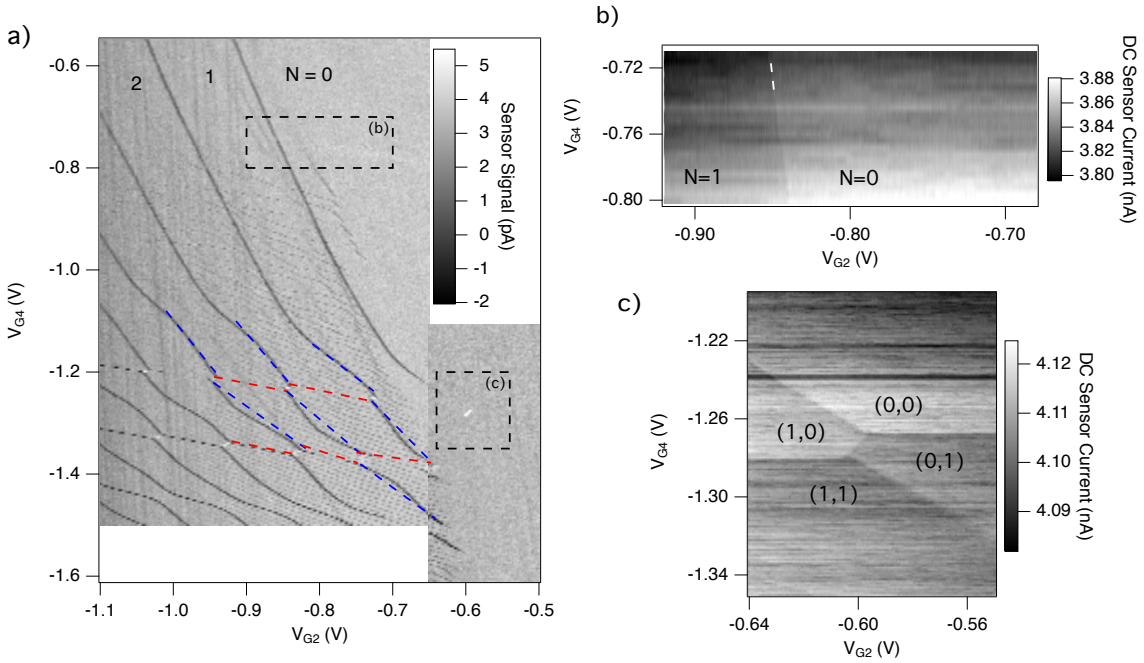

Figure A.4: **Confirming the absolute hole occupation:** (**a**) For clarity we reproduce the charge stability diagram of Figure 4.8(c) with a colour scale indicating the magnitude of the sensor signal. The measurement is made using the pulse bias technique [38, 40], which is sensitive to tunnel rate, hence the charge transitions are not visible beyond V_{G2}>-0.6V. Red and blue dashed lines indicate the formation of the double dot features, with red indicating the G4 coupled dot, and blue the G2 coupled dot. (**b**) Measurement of the DC sensor current for the region indicated by the top dashed rectangle in (a). The last charge transition runs parallel to the white dashed line (guide to eye). (**c**) Measurement of the DC sensor current for the region indicated by the bottom dashed rectangle in (a). Although the visibility of the charge transitions has been lost for this region in (a), a clear double dot charge stability digram can be observed in (c) exactly where it is projected to occur based on extending the lines in (a). This demonstrates the DC sensor current is working independent of the tunnel rate. In all cases V_{SD} is 1mV.

A.3.2 Background structure in charge stability diagrams

The charge stability diagram of the device studied in this chapter shows a clear single dot structure, that forms into a double dot honeycomb pattern as V_{G4} is made more negative. However, in addition to the main charge transitions, we have observed a series of background signals, which are consistent with an accidental quantum dot. In this section we present measurements of the main quantum dot and the accidental quantum dot charge transitions, and show that these two systems are independent and do not

interact. We conclude by providing evidence that suggests these accidental quantum dots form under the accumulating plunger gate away from the main region of the device.

The charge stability diagram of the device is shown in Figure A.5(a). Starting for V_{G4}=-0.7V we observe five strong charge transition signals running parallel to the dashed red line. These are the charge transitions of the main single quantum dot. The main dot forms into a double quantum dot around V_{G4}=-1.2V, as indicated by the distinct avoided crossing of the charge transitions. The white inter-dot signals connecting the avoided crossings are the inter-dot tunneling signals.

In addition to the strong charge transitions of the primary dot, additional background structure can be observed. Within the dashed blue rectangle in Figure A.5(a) the main dot charge transition is highlighted in red, while a series of periodic additional signals can be observed. These additional signals are reproducible and are consistent with an additional *accidental* quantum dot structure. The charge transition of the accidental-dot have a different amplitude and coupling to G2, suggesting that the primary and accidental quantum dots are located in different positions within the device.

In Figure A.5(b) we show a zoom of a region where the main dot and accidental dot charge transitions cross. The *accidental* dot charge transitions are outlined with blue dashed lines, and the main quantum dot charge transitions are outlined with red dashed lines. We note that as the accidental-dot transitions approach each other, they experience avoided crossings. This is consistent with the accidental-dot acting as a double (or multiple) quantum dot. The avoided crossing of the blue transitions is due to the wavefunction overlap as two interacting states are brought to the same energy. In contrast, we highlight that the accidental (blue) and main quantum dot (red) charge transitions overlap and shown no evidence of interaction. Based on these investigations we are justified in ignoring the accidental quantum dot in our analysis of the main quantum dot spin states.

The accidental quantum dot introduces a series of additional peaks in the charge sensor signal. In Figure A.5(c) we show a line cut of the sensor signal when V_{G4}=-0.9V. The main charge transition peaks can be identified by their amplitude, and by their coupling to V_{G4} in the stability diagram as in Figure A.5(a). When extracting the Coulomb peaks

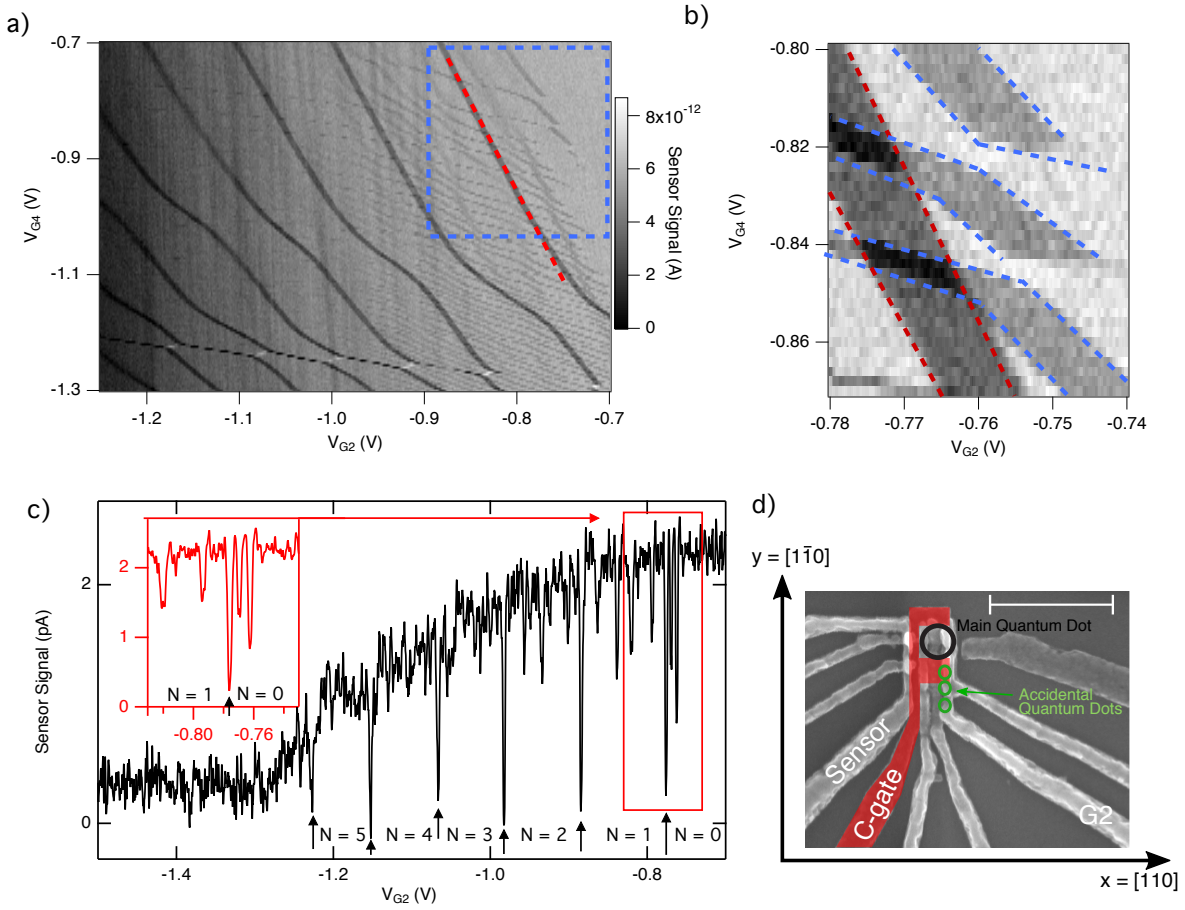

Figure A.5: **Accidental background dot structure:**(**a**) Charge stability diagram of the device highlighting the primary quantum dot transitions (parallel to red dashed line) and the accidental quantum dot transitions (most clearly visible withing the blue dashed rectangle). (**b**) Shows an image of the charge stability diagram where the accidental quantum dot charge transitions (blue) cross the primary quantum dot charge transitions (red). The blue lines anti-cross since they are coupled, while the blue and red lines simply cross, indicating there is no coupling between the primary and accidental quantum dot systems. (**c**) The sensor signal for a sweep of the plunger gate, V_{G2} across multiple charge transitions. The charge occupation of the primary quantum dot, N, is indicated with arrows and text. Inset shows a region where the primary and background charge transitions are close together. Slight tuning of V_{G4} at B=0T can ensure no transitions overlap or cross over the range of magnetic field sweeps. (**d**) False colour SEM indicating the potential location of the accidental quantum dots in green ellipses. The white scale bar is 500nm.

for g-factor analysis we take detailed measurements to ensure the accidental quantum dot transitions do not interfere with the amplitude or shape of the main quantum dot charge transition. This can be achieved by fine tuning V_{G4}. The primary quantum dot transitions are labeled with black arrows in Figure A.5(c) and the absolute hole occupation of the main quantum dot is shown in text as N.

Finally we comment on the likely location of the accidental quantum dot. The device

lithography has a depleting C-gate placed closest to the SiO_2 interface, with plunger gates placed on top of the C-gate. However, the C gate does no extend under the entire length of the gates G1-G4 as shown in Figure A.5(d). Since V_{G2} is operating in accumulation mode, it is possible accidental quantum dots can form under G2 in the regions indicated as green ellipses in Figure A.5(d) due to the disorder introduced by the SiO_2 interface. In support of this hypothesis we note that the sensor signal in Figure A.5(c) shows a decay and plateau as V_{G2} is made more negative. This can be explained by a accidental hole states forming under G2, which can then screen the charge sensor signal (as described in Chapter 2 section 2.6.3). Similar effects have been observed in n-type silicon MOS devices, and the solution was to extend the C-gate in the negative y-direction all the way out to the field oxide region in order to prevent accidental quantum dot states [155].

A.4 Control and Characterisation of the orbital structure

A primary conclusion of Chapter 4 is that the g-factor anisotropy is determined by the symmetry and orientation of the quantum dot confinement profile. This conclusion is supported by the observation that the g-factor anisotropy is strongly tuned by the voltage applied to the local gates (specifically V_{G4}). However, this conclusion rests on the assumption that the quantum dot confinement can in fact be strongly electrically tuned[1]. In this section we present experimental evidence showing that the confinement profile can be strongly tuned by electric fields.

A.4.1 Control of the orbital energy spectrum

In this section we use magnetospectroscopy to study the orbital spectrum of the hole quantum dot in Chapter 4. As holes are added to a quantum dot they fill into distinct orbital shells, much like the shell structure of an atom [9]. This shell structure is sensitive

[1]Rather than the confinement being strongly defined by the SiO_2 interface orientation or crystal axes.

to the symmetry of the quantum dot confinement [44, 49]. In this section we use ground state magnetospectroscopy to observe the orbital shell structure when V_{G4} = -0.9V and when V_{G4} = -0.7V. We observe a distinct change in the shell structure, providing evidence that the dot confinement profile is different between the two V_{G4} configurations.

The orbital shell structure can be deduced by observing the spin filling sequence of holes into the dot. We extract the relative spin orientation of the $(N+1)^{th}$ hole by observing the slope of the N^{th} addition energy with respect to an applied magnetic field. The first five addition energies have been measured for V_{G4} = -0.9V and for V_{G4} = -0.7V. The key results are presented in Figure A.6 (see section A.5 for full set of addition energy measurements).

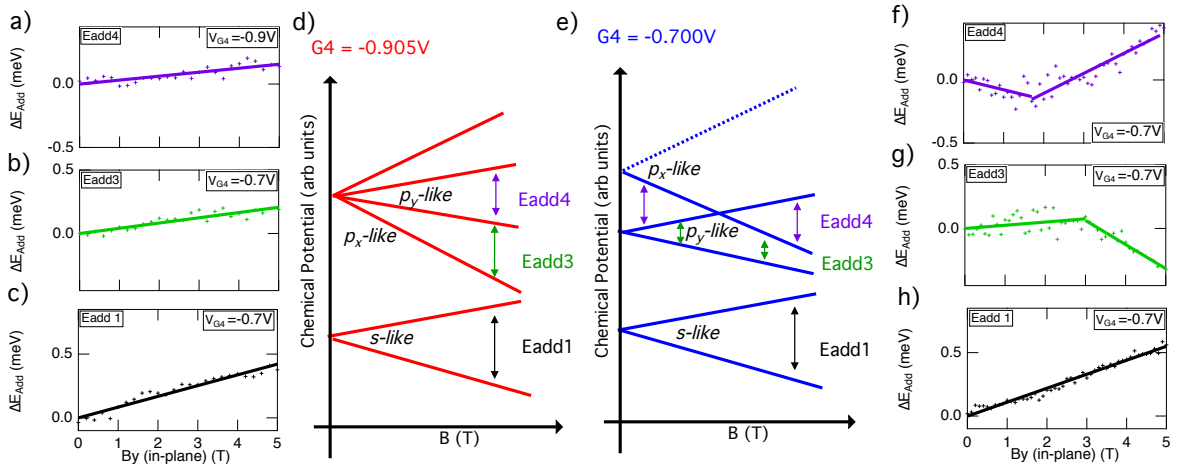

Figure A.6: **Orbital shell structure for V_{G2} = -0.9V and -0.7V:** (**a-c**) Measurements of the addition energy as a function of B_y for $E_{add}(4)$ (purple), $E_{add}(3)$ (green), and $E_{add}(1)$(black) respectively. (**d**) Orbital shell structure of the first 6 holes for V_{G4} = -0.9V. The orbital structure is constructed from the slopes of the addition energy measurements (see section A.5 for full measurements). The respective addition energies are the spacing between consecutive charge states, as indicated with colored vertical arrows in (d). Since $E_{add}(1)$ (purple), $E_{add}(3)$ (green), and $E_{add}(4)$ (black) all increase with B_y we obtain the displayed orbital spectrum. (**e**) Orbital shell structure for V_{G4} = -0.7V, with key addition energy measurements shown in (**f-h**). We find $E_{add}(3)$ (green) slightly increases then decreases, while $E_{add}(4)$ (purple) slightly decreases then increases with B_y. These observations support the orbital structure of (e) (see section A.5 for full measurements). We use an arbitrary energy scale in (d) and (e) since supplementary excited state spectroscopy measurements were not possible to confirm absolute energy scales. Excited state spectroscopy was not possible on this device due to the accidental quantum dot signals complicating analysis of broad peaks (see section A.3.2).

In Figure A.6(a)-(c) we show the key addition energy measurements that allow us to reconstruct the orbital structure of the dot when G4 = -0.9V. We note that in each case of Figure A.6(a)-(c) the addition energy is increasing, and a positive slope is observed.

Based on these results[1] we can infer the quantum dot orbital structure, which we present in Figure A.6(d). The key features we observe are that the first two holes fill a two-fold degenerate spin pair. Holes 3, 4, 5, and 6 occupy a four-fold degenerate state at zero magnetic field. We observe that these holes split into two spin-pairs with distinct and different effective g-factors, which we label as p_x-like and p_y-like orbitals[2].

In Figure A.6(f)-(h) we show the key addition energy measurements that allow us to reconstruct the orbital structure of the dot when V_{G4} = -0.7V[3]. The orbital shell structure is presented in Figure A.6(e). We find that the first two holes form a two-fold degenerate Pauli spin-pair. For the higher energy orbitals, we find that the 3^{rd} and 4^{th} holes form a spin-pair, while the 5^{th} and 6^{th} holes form another spin pair. This spin structure is confirmed by the observation of a distinct change in slope in Figures A.6(f) and A.6(g) around B_y = (2.3±0.5)T. The change in slope indicates a change in the spin filling sequence caused by a Zeeman induced crossing of the orbital levels. Based on the g-factor extracted from dE_{add}/dB we can use the Zeeman energy at the crossing to estimate that the p_x-like and p_y-like orbital levels are separated by (0.5±0.2)meV[4].

Here we directly compare the orbital structure for the two different V_{G4} values presented in Figure A.6(d) and A.6(e). The orbital structure for V_{G4} = -0.9V is consistent with the magic number shell filling expected for close to circular 2D quantum dots. In circular quantum dots the 3^{rd} and 4^{th} holes fill with spin down into the degenerate p_x and p_y orbitals, and the 5^{th} and 6^{th} fill with spin up. Based on the experimental evidence presented in Figure A.6(a)-(e) we cannot confirm that the apparent four-fold degeneracy of the 3^{rd} to 6^{th} holes is due to circular confinement and degeneracy of the p_x-like and

[1] See section A.5 for all measurements of E_{add}. These results obtain a negative slope dE_{add}/dB for $E_{add}(2)$, and a positive slope for $E_{add}(5)$.

[2] Justification and discussion regarding the label assigned to these orbital states is presented later in this section.

[3] See section A.5 for all measurements of E_{add}. These results obtain a negative slope dE_{add}/dB for $E_{add}(2)$. The slope for $E_{add}(5)$ is not resolvable due to noise. In Figure A.6 we show the sixth holes chemical potential as dotted to indicate that this is inferred spin filling. We can infer that the sixth hole is not spin down base on the high field addition energy of $E_{add}(4)$.

[4] The change in slope for $E_{add}(4)$ occurs at By = (1.9±0.5)T. The change in slope for $E_{add}(3)$ occurs at By = (2.7±0.4)T. Although the uncertainty ranges overlap, it seems that the change in slope occurs at lower B_y for $E_{add}(4)$ than for E^3_{add}. This may be due to a change in the dot shape as V_{G2} is made more negative. For more negative V_{G2} the dot may become larger, thus reducing the orbital splitting, which is consistent with what we observe.

p_y-like orbitals[1]. However, we can clearly resolve that there are three distinct orbital states based on the different g-factors. For convenience of discussion we label the lowest energy orbital as the s-like orbital, the higher orbital with largest g-factor as p_x-like, and the higher orbital with smaller g-factor as p_y-like.

When V_{G4} is set to -0.7V we observe a lifting of the four fold degeneracy of the two higher orbitals. These two orbitals are again labeled p_x-like and p_y-like. As V_{G4} is made more positive the confinement of the dot along the x-axis is expected to become stronger. This stronger confinement can cause the dot to become more elliptical and lift the degeneracy of the p_x-like and p_y-like orbitals[2]. Since confinement has become stronger in the sample x-axis we find it consistent that the p_x-like orbital is at higher energy than the p_y-like orbital.

In conclusion, this section presents the results of a study of the orbital shell structure for the silicon MOS hole quantum dot. The motivation for this section is to provide supporting evidence that V_{G4} strongly influences the confinement profile of the quantum dot. This supporting evidence is important since in section 4.7 we related the difference in the g-factor anisotropy at V_{G4}=-0.7V and V_{G4}=-0.9V to a change in the confinement symmetry caused by V_{G4}. We observe spin filling into three distinct orbital levels, each with a unique g-factor[3]. The key results of Figure A.6(d)-(e) is that we demonstrate electrical control over the degeneracy of the 2^{nd} and 3^{rd} orbital level (labeled p_x-like and p_y-like). This provides strong evidence that the voltage applied to G4 has significant control over the confinement profile of the quantum dot. Finally, we note that this is the first demonstration of control of the orbital energy spectrum for hole quantum dot with a known charge occupation.

[1]In particular we note that the distinct g-factors may suggest this four fold degeneracy is due to an accidental degeneracy of two different orbitals. In Chapter 3 we found all four states of the degenerate p-orbitals to have similar g-factors. However in Chapter 2 the dot confinement appeared to be 2D and circular, while for Chapter 4 we have tuned the confinement to be three dimensional (see section 4.7).

[2]This argument remains consistent in the case that the orbitals are not p-like orbitals, but are rather two distinct orbitals. In this case, as the confinement changes between V_{G4}=-0.9V and V_{G4}=-0.7V the orbital with larger momentum will move to higher energy, thereby lifting the degeneracy reproducing the orbital structure in Figure A.6(e).

[3]We note that the use of labels s-like and p-like are primarily for discussion purposes, and detailed excited state spectroscopy(cite) or 3D tunnel rate spectroscopy(cite) would be required to confirm the orbital symmetry. However, this distinct orbital symmetry is not the key result.

A.5 Full experimental data-set

This section presents the full data set of addition energy measurements used to extract the g-factor anisotropy and to deduce the orbital structure. The main purpose of including this section is for completeness and transparency of the data analysis. Further, this section provides preliminary insight into the rich physics of hole spin states in the energy higher orbital states.

We show the full set of the first five addition energy measurements for V_{G4} = -0.7V in Figure A.7, while Figure A.8 shows the results for V_{G4} = -0.9V. Each panel (a)-(e) shows the measurements for $E_{add}(1)$ to $E_{add}(5)$ respectively. The N^{th} addition energy, $E_{add}(N)$ is extracted by measuring the spacing between the N^{th} and $(N+1)^{th}$ Coulomb peak. Each individual panel has four distinct x-axes, from left to right these respective axes are the in-plane magnetic field B_x, the in-plane (x-y) angle for a 1T magnetic field rotation θ, the out-of-plane angle for a 1T magnetic field rotation ϕ, and the in-plane magnetic field B_y.

The measurements of $E_{add}(N)$ in each panel were performed in order of left to right. First $E_{add}(N)$ was measured for B_x = 0T to 1T, following this and starting from $\vec{B}$= (1,0,0), a 1T magnetic field rotation of 2π is performed about x-y plane. Following this, starting from $\vec{B}$= (1,0,0), $E_{add}(N)$ is measured for a 1T magnetic field rotation of 2π about x-z plane[1]. Finally the magnetic field was ramped to 0T and $E_{add}(N)$ was measured for B_y = 0T to 5T. We have checked that the measurements are symmetric about B=0T and show here only the positive B measurements for linear sweeps.

The results of a linear fit to each region with a distinct slope is shown in Figure A.7 and Figure A.8 as a solid black line (solid red for $E_{add}(5)$ in panel (e)). The text in the corresponding figures panels shows the values of the E_0 and the g-factor. The parameter E_0 is the B=0 intercept and the g-factor is extracted from the slope. In cases where there is a distinct change in the slope we refer to the Low Field g-factor as g_{LF}, and the High Field g-factor as g_{HF}.

These results are the full measurement data set and as such, some of this data has already

[1]For $E_{add}(1)$ a rotation was also performed about the y-z plane.

been presented in the Thesis. The results of $E_{add}(1)$ in Figure A.7(a) and Figure A.8(a) have been presented and discussed in detail in the analysis of the g-factor anisotropy in Chapter 4 section 4.7. The slopes of $E_{add}(1)$ to $E_{add}(5)$ for both B_x and B_y in Figure A.7 and Figure A.8 have been used to determine the orbital shell filling structure ($E_{add}(1)$, $E_{add}(3)$, and $E_{add}(4)$ for B_y are reproduced in Figure A.6 of section A.4.1).

Figure A.7 and Figure A.8 present a full data-set of the experimental results used to extract the g-factor anisotropy and to determine the spin filling sequence of holes into orbital shells. The experimental results of this chapter have primarily focused on the spin physics of a single hole occupying the first orbital. The full set of rotation measurements for higher orbitals remains open for future theoretical and experimental investigation. In particular we highlight that in some cases such as in Figure A.8(d) we see very large amplitude oscillations in the out-of-plane magnetic field rotation. Another interesting feature is the measurement of $E_{add}(3)$ in Figure A.8(c) shows strong out-of-plane oscillation and weak in-plane oscillation, while $E_{add}(5)$ in Figure A.8(e) shows strong in-plane oscillation and weak out-of-plane oscillation. Understanding the distinct results for higher hole orbitals will require further research and is a focus of future work.

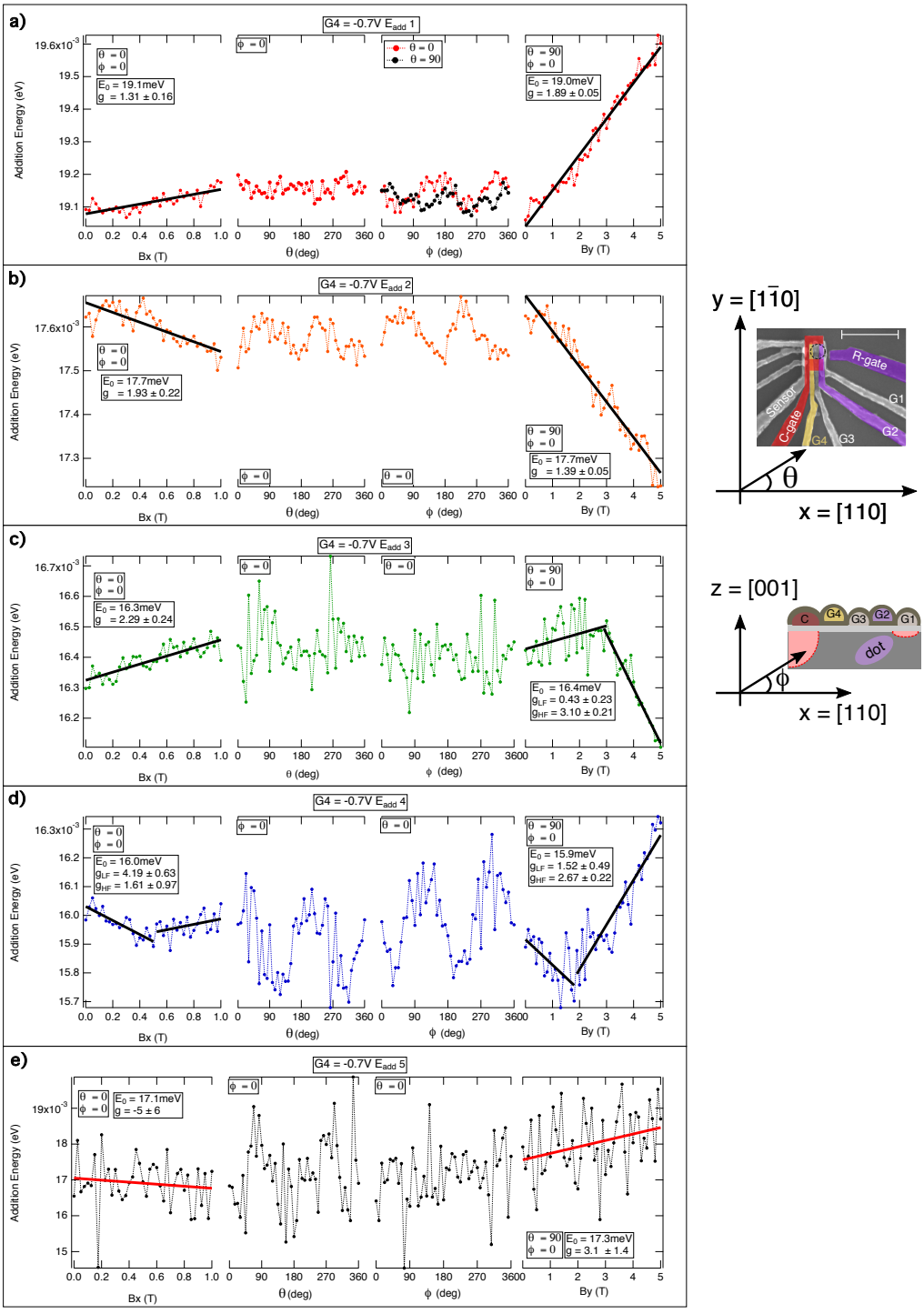

Figure A.7: **Raw Addition energy Measurements for G4 = -0.7V:** (**a-e**) Shows the full set of measurements of the first five addition energies used in the analysis of the orbital shell structure of section A.4.1. Each panel shows four distinct measurements of a respective addition energy. From left to right these are the addition energy for steps in B_x, steps of the in-plane angle θ for $|B| = 1T$, steps of the out-of plane angle ϕ for $|B|=1T$, and steps of B_y up to 5T. Insets for each measurement indicate the relevant angles, and results of respective best fits (solid lines). In panel (a) for $E_{add}(1)$ two data sets are shown for the third measurement. These two measurements are for x-z rotation of magnetic field (red, θ=0) and a y-z rotation of magnetic field (black, θ=90). These results are presented for completeness and reference for interested readers. In cases where the slope changes over the magnetic field sweep we present the fit parameters for the low field region.

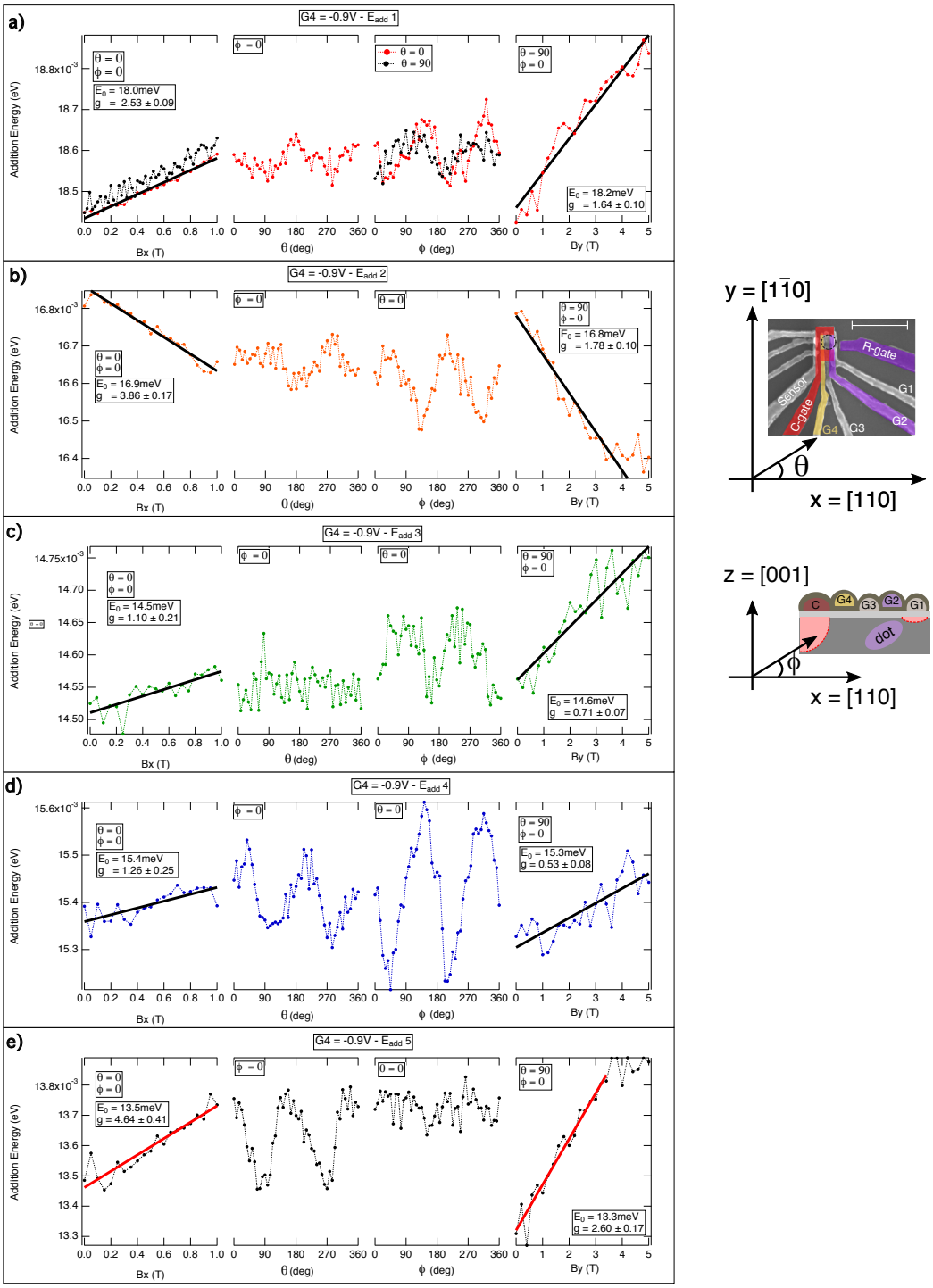

Figure A.8: **Raw Addition energy Measurements for G4 = -0.9V:** (**a-e**) Shows the full set of measurements of the first five addition energies used in the analysis of the orbital shell structure of section A.4.1. Each panel shows four distinct measurements of a respective addition energy. From left to right these are the addition energy for steps in B_x, steps of the in-plane angle θ for |B| = 1T, steps of the out-of plane angle ϕ for |B|=1T, and steps of B_y up to 5T. Insets for each measurement indicate the relevant angles, and results of respective best fits (solid lines). In panel (a) for $E_{add}(1)$ two data sets are shown for the third measurement. These two measurements are for x-z rotation of magnetic field (red, θ=0) and a y-z rotation of magnetic field (black, θ=90). These results are presented for completeness and reference for interested readers.

Bibliography

1. Ciorga, M *et al.* Addition spectrum of a lateral dot from Coulomb and spin-blockade spectroscopy. *Physical Review B* **61,** R16315 (2000).
2. Fuechsle, M. *et al.* A single-atom transistor. *Nature nanotechnology* **7,** 242 (2012).
3. Mo, Y.-W., Savage, D., Swartzentruber, B. & Lagally, M. G. Kinetic pathway in Stranski-Krastanov growth of Ge on Si (001). *Physical Review Letters* **65,** 1020 (1990).
4. Katsaros, G *et al.* Hybrid superconductor–semiconductor devices made from self-assembled SiGe nanocrystals on silicon. *Nature nanotechnology* **5,** 458 (2010).
5. Nadj-Perge, S *et al.* Spectroscopy of spin-orbit quantum bits in indium antimonide nanowires. *Physical review letters* **108,** 166801 (2012).
6. Zwanenburg, F. A. *et al.* Silicon quantum electronics. *Reviews of modern physics* **85,** 961 (2013).
7. Lu, W., Ji, Z., Pfeiffer, L., West, K. & Rimberg, A. Real-time detection of electron tunnelling in a quantum dot. *Nature* **423,** 422 (2003).
8. Loss, D. & DiVincenzo, D. P. Quantum computation with quantum dots. *Physical Review A* **57,** 120 (1998).
9. Tarucha, S., Austing, D., Honda, T, Van der Hage, R. & Kouwenhoven, L. P. Shell filling and spin effects in a few electron quantum dot. *Physical Review Letters* **77,** 3613 (1996).
10. Stafford, C. A. & Sarma, S. D. Collective Coulomb blockade in an array of quantum dots: a Mott-Hubbard approach. *Physical review letters* **72,** 3590 (1994).
11. Mukhopadhyay, U., Dehollain, J. P., Reichl, C., Wegscheider, W. & Vandersypen, L. M. A 2× 2 quantum dot array with controllable inter-dot tunnel couplings. *Applied Physics Letters* **112,** 183505 (2018).
12. Elzerman, J. *et al.* Single-shot read-out of an individual electron spin in a quantum dot. *nature* **430,** 431 (2004).
13. Koppens, F. H. *et al.* Driven coherent oscillations of a single electron spin in a quantum dot. *Nature* **442,** 766 (2006).
14. Koppens, F., Nowack, K. & Vandersypen, L. Spin echo of a single electron spin in a quantum dot. *Physical Review Letters* **100,** 236802 (2008).

15. Petta, J. R. *et al.* Coherent manipulation of coupled electron spins in semiconductor quantum dots. *Science* **309,** 2180–2184 (2005).

16. Lim, W. *et al.* Observation of the single-electron regime in a highly tunable silicon quantum dot. *Applied Physics Letters* **95,** 242102 (2009).

17. Veldhorst, M *et al.* An addressable quantum dot qubit with fault-tolerant control-fidelity. *Nature nanotechnology* **9,** 981–985 (2014).

18. Kloeffel, C. & Loss, D. Prospects for spin-based quantum computing in quantum dots. *Annu. Rev. Condens. Matter Phys.* **4,** 51–81 (2013).

19. Veldhorst, M. *et al.* A two-qubit logic gate in silicon. *Nature* **526,** 410 (2015).

20. Maurand, R *et al.* A CMOS silicon spin qubit. *Nature communications* **7,** 13575 (2016).

21. Crippa, A. *et al.* Electrical spin driving by g-matrix modulation in spin-orbit qubits. *Physical review letters* **120,** 137702 (2018).

22. Watzinger, H. *et al.* Hole spin resonance in Ge double quantum dots. *arXiv preprint arXiv:1802.00395* (2018).

23. Watzinger, H. *et al.* A germanium hole spin qubit. *Nature communications* **9,** 3902 (2018).

24. Vukusic, L., Kukucka, J., Watzinger, H. & Katsaros, G. Fast hole tunneling times in germanium hut wires probed by single-shot reflectometry. *Nano letters* **17,** 5706–5710 (2017).

25. Hendrickx, N., Franke, D., Sammak, A, Scappucci, G & Veldhorst, M. Fast two-qubit logic with holes in germanium. *arXiv preprint arXiv:1904.11443* (2019).

26. Hendrickx, N. *et al.* Gate-controlled quantum dots and superconductivity in planar germanium. *Nature communications* **9,** 2835 (2018).

27. Li, R., Hudson, F. E., Dzurak, A. S. & Hamilton, A. R. Single hole transport in a silicon metal-oxide-semiconductor quantum dot. *Applied Physics Letters* **103,** 163508 (2013).

28. Li, R., Hudson, F. E., Dzurak, A. S. & Hamilton, A. R. Pauli spin blockade of heavy holes in a silicon double quantum dot. *Nano letters* **15,** 7314–7318 (2015).

29. Spruijtenburg, P. C. *et al.* Single-hole tunneling through a two-dimensional hole gas in intrinsic silicon. *Applied physics letters* **102,** 192105 (2013).

30. Hanson, R., Kouwenhoven, L. P., Petta, J. R., Tarucha, S. & Vandersypen, L. M. Spins in few-electron quantum dots. *Reviews of Modern Physics* **79,** 1217 (2007).

31. Liu, H. *et al.* Pauli-spin-blockade transport through a silicon double quantum dot. *Physical Review B* **77,** 073310 (2008).

32. Prance, J. *et al.* Single-shot measurement of triplet-singlet relaxation in a Si/SiGe double quantum dot. *Physical review letters* **108,** 046808 (2012).

33. Morello, A. *et al.* Single-shot readout of an electron spin in silicon. *Nature* **467,** 687 (2010).

34. Van der Wiel, W. G. *et al.* Electron transport through double quantum dots. *Reviews of Modern Physics* **75,** 1 (2002).

35. Elzerman, J. *et al.* Few-electron quantum dot circuit with integrated charge read out. *Physical Review B* **67,** 161308 (2003).

36. Ashoori, R. *et al.* Single-electron capacitance spectroscopy of discrete quantum levels. *Physical review letters* **68,** 3088 (1992).

37. Field, M *et al.* Measurements of Coulomb blockade with a noninvasive voltage probe. *Physical Review Letters* **70,** 1311 (1993).

38. Elzerman, J., Hanson, R, Willems van Beveren, L., Vandersypen, L. & Kouwenhoven, L. Excited-state spectroscopy on a nearly closed quantum dot via charge detection. *Applied physics letters* **84,** 4617–4619 (2004).

39. Schoelkopf, R., Wahlgren, P, Kozhevnikov, A., Delsing, P & Prober, D. The radio-frequency single-electron transistor (RF-SET): A fast and ultrasensitive electrometer. *Science* **280,** 1238–1242 (1998).

40. Yang, C., Lim, W., Zwanenburg, F. & Dzurak, A. Dynamically controlled charge sensing of a few-electron silicon quantum dot. *AIP Advances* **1,** 042111 (2011).

41. Fock, V. Bemerkung zur Quantelung des harmonischen Oszillators im Magnetfeld. *Zeitschrift fur Physik A Hadrons and Nuclei* **47,** 446–448 (1928).

42. Darwin, C. G. *The diamagnetism of the free electron* in *Mathematical Proceedings of the Cambridge Philosophical Society* **27** (1931), 86–90.

43. Kouwenhoven, L. P., Austing, D. & Tarucha, S. Few-electron quantum dots. *Reports on Progress in Physics* **64,** 701 (2001).

44. Amasha, S *et al.* Electrical control of spin relaxation in a quantum dot. *Physical review letters* **100,** 046803 (2008).

45. Camenzind, L. C. *et al.* Spectroscopy of Quantum Dot Orbitals with In-Plane Magnetic Fields. *Physical review letters* **122,** 207701 (2019).

46. Kittel, C. *et al. Introduction to solid state physics* (Wiley New York, 1976).

47. Hanson, R *et al.* Semiconductor few-electron quantum dot operated as a bipolar spin filter. *Physical Review B* **70,** 241304 (2004).

48. Ando, T., Fowler, A. B. & Stern, F. Electronic properties of two-dimensional systems. *Reviews of Modern Physics* **54,** 437 (1982).

49. Yang, C. *et al.* Orbital and valley state spectra of a few-electron silicon quantum dot. *Physical Review B* **86,** 115319 (2012).

50. Davies, J. H. *The physics of low-dimensional semiconductors: an introduction* (Cambridge university press, 1998).

51. Winkler, R. Spin-orbit coupling effects in two-dimensional electron and hole systems. *Springer Tracts in Modern Physics* **191,** 153–156 (2003).

52. Tanttu, T. *et al.* Controlling spin-orbit interactions in silicon quantum dots using magnetic field direction. *Physical Review X* **9,** 021028 (2019).

53. Fujisawa, T., Hayashi, T., Jung, S. W., Jeong, Y.-H. & Hirayama, Y. in *Quantum Computing in Solid State Systems* 279–287 (Springer, 2006).

54. Hayashi, T., Fujisawa, T., Cheong, H.-D., Jeong, Y. H. & Hirayama, Y. Coherent manipulation of electronic states in a double quantum dot. *Physical review letters* **91,** 226804 (2003).

55. Huang, W *et al.* Fidelity benchmarks for two-qubit gates in silicon. *Nature* **569,** 532 (2019).

56. Malinowski, F. K. *et al.* Notch filtering the nuclear environment of a spin qubit. *Nature nanotechnology* **12,** 16 (2017).

57. Slichter, C. P. *Principles of magnetic resonance* (Springer Science & Business Media, 2013).

58. Golovach, V. N., Khaetskii, A. & Loss, D. Phonon-induced decay of the electron spin in quantum dots. *Physical review letters* **93,** 016601 (2004).

59. Nowack, K., Koppens, F., Nazarov, Y. V. & Vandersypen, L. Coherent control of a single electron spin with electric fields. *Science* **318,** 1430–1433 (2007).

60. Golovach, V. N., Borhani, M. & Loss, D. Electric-dipole-induced spin resonance in quantum dots. *Physical Review B* **74,** 165319 (2006).

61. Salis, G. *et al.* Electrical control of spin coherence in semiconductor nanostructures. *Nature* **414,** 619 (2001).

62. Kato, Y *et al.* Gigahertz electron spin manipulation using voltage-controlled g-tensor modulation. *Science* **299,** 1201–1204 (2003).

63. Pioro-Ladriere, M *et al.* Electrically driven single-electron spin resonance in a slanting Zeeman field. *Nature Physics* **4,** 776–779 (2008).

64. Hamilton, A. *et al.* The 0.7 anomaly in one-dimensional hole quantum wires. *Journal of Physics: Condensed Matter* **20,** 164205 (2008).

65. Kane, E. O. Band structure of indium antimonide. *Journal of Physics and Chemistry of Solids* **1,** 249–261 (1957).

66. Luttinger, J. Quantum theory of cyclotron resonance in semiconductors: General theory. *Physical review* **102,** 1030 (1956).

67. Fasth, C., Fuhrer, A., Samuelson, L., Golovach, V. N. & Loss, D. Direct measurement of the spin-orbit interaction in a two-electron InAs nanowire quantum dot. *Physical review letters* **98,** 266801 (2007).

68. Lodari, M *et al.* Light effective hole mass in undoped Ge/SiGe quantum wells. *arXiv preprint arXiv:1905.08064* (2019).

69. Kloeffel, C., Trif, M. & Loss, D. Strong spin-orbit interaction and helical hole states in Ge/Si nanowires. *Physical Review B* **84,** 195314 (2011).

70. Betz, A., Gonzalez-Zalba, M., Podd, G & Ferguson, A. Ambipolar quantum dots in intrinsic silicon. *Applied Physics Letters* **105,** 153113 (2014).

71. Hao, X.-J. *et al.* Strong and Tunable Spin- Orbit Coupling of One-Dimensional Holes in Ge/Si Core/Shell Nanowires. *Nano letters* **10,** 2956–2960 (2010).

72. Watzinger, H. *et al.* Heavy-hole states in germanium hut wires. *Nano letters* **16,** 6879–6885 (2016).

73. Voisin, B *et al.* Electrical control of g-factor in a few-hole silicon nanowire MOSFET. *Nano letters* **16,** 88–92 (2015).

74. Yoneda, J. *et al.* A quantum-dot spin qubit with coherence limited by charge noise and fidelity higher than 99.9%. *Nature nanotechnology* **13,** 102 (2018).

75. Yang, C. *et al.* Spin-valley lifetimes in a silicon quantum dot with tunable valley splitting. *Nature communications* **4,** 2069 (2013).

76. Hu, Y., Kuemmeth, F., Lieber, C. M. & Marcus, C. M. Hole spin relaxation in Ge-Si core-shell nanowire qubits. *Nature nanotechnology* **7,** 47–50 (2012).

77. Higginbotham, A. P. *et al.* Hole spin coherence in a Ge/Si heterostructure nanowire. *Nano letters* **14,** 3582–3586 (2014).

78. Szumniak, P, Bednarek, S, Partoens, B & Peeters, F. Spin-Orbit-Mediated Manipulation of Heavy-Hole Spin Qubits in Gated Semiconductor Nanodevices. *Physical review letters* **109,** 107201 (2012).

79. Kloeffel, C., Trif, M., Stano, P. & Loss, D. Circuit QED with hole-spin qubits in Ge/Si nanowire quantum dots. *Physical Review B* **88,** 241405 (2013).

80. Bulaev, D. V. & Loss, D. Spin relaxation and anticrossing in quantum dots: Rashba versus Dresselhaus spin-orbit coupling. *Physical Review B* **71,** 205324 (2005).

81. Keane, Z. *et al.* Resistively detected nuclear magnetic resonance in n-and p-type GaAs quantum point contacts. *Nano letters* **11,** 3147–3150 (2011).

82. Brunner, D. *et al.* A coherent single-hole spin in a semiconductor. *science* **325,** 70–72 (2009).

83. De Greve, K. *et al.* Ultrafast coherent control and suppressed nuclear feedback of a single quantum dot hole qubit. *Nature Physics* **7,** 872 (2011).

84. Pribiag, V. *et al.* Electrical control of single hole spins in nanowire quantum dots. *Nature nanotechnology* **8,** 170 (2013).

85. Flindt, C., Sorensen, A. S. & Flensberg, K. Spin-orbit mediated control of spin qubits. *Physical review letters* **97,** 240501 (2006).

86. Dennis, E., Kitaev, A., Landahl, A. & Preskill, J. Topological quantum memory. *Journal of Mathematical Physics* **43,** 4452–4505 (2002).

87. Jones, C. *et al.* Logical qubit in a linear array of semiconductor quantum dots. *Physical Review X* **8,** 021058 (2018).

88. Yamaoka, Y., Iwasaki, K., Oda, S. & Kodera, T. Charge sensing and spin-related transport property of p-channel silicon quantum dots. *Japanese Journal of Applied Physics* **56,** 04CK07 (2017).

89. Scott-Thomas, J., Field, S. B., Kastner, M., Smith, H. I. & Antoniadis, D. Conductance oscillations periodic in the density of a one-dimensional electron gas. *Physical review letters* **62,** 583 (1989).

90. Meirav, U, Kastner, M. & Wind, S. Single-electron charging and periodic conductance resonances in GaAs nanostructures. *Physical review letters* **65,** 771 (1990).

91. Ono, K, Austing, D., Tokura, Y & Tarucha, S. Current rectification by Pauli exclusion in a weakly coupled double quantum dot system. *Science* **297,** 1313–1317 (2002).

92. Bluhm, H. *et al.* Dephasing time of GaAs electron-spin qubits coupled to a nuclear bath exceeding 200 μs. *Nature Physics* **7,** 109 (2011).

93. De Lange, G, Wang, Z., Riste, D, Dobrovitski, V. & Hanson, R. Universal dynamical decoupling of a single solid-state spin from a spin bath. *Science* **330,** 60–63 (2010).

94. Simmel, F, Abusch-Magder, D., Wharam, D., Kastner, M. & Kotthaus, J. Statistics of the Coulomb-blockade peak spacings of a silicon quantum dot. *Physical Review B* **59,** R10441 (1999).

95. Angus, S. J., Ferguson, A. J., Dzurak, A. S. & Clark, R. G. Gate-defined quantum dots in intrinsic silicon. *Nano letters* **7,** 2051–2055 (2007).

96. Fujiwara, A. *et al.* Single electron tunneling transistor with tunable barriers using silicon nanowire metal-oxide-semiconductor field-effect transistor. *Applied Physics Letters* **88,** 053121 (2006).

97. Lim, W. *et al.* Electrostatically defined few-electron double quantum dot in silicon. *Applied Physics Letters* **94,** 173502 (2009).

98. Lim, W., Yang, C., Zwanenburg, F. & Dzurak, A. Spin filling of valley–orbit states in a silicon quantum dot. *Nanotechnology* **22,** 335704 (2011).

99. Lai, N. *et al.* Pauli spin blockade in a highly tunable silicon double quantum dot. *Scientific reports* **1,** 110 (2011).

100. Leobandung, E., Guo, L. & Chou, S. Y. Single hole quantum dot transistors in silicon. *Applied physics letters* **67,** 2338–2340 (1995).

101. De Almeida, A. *et al.* Single-charge occupation in ambipolar quantum dots. *arXiv preprint arXiv:2001.05045* (2020).

102. Tracy, L. A., Hargett, T. & Reno, J. Few-hole double quantum dot in an undoped GaAs/AlGaAs heterostructure. *Applied Physics Letters* **104,** 123101 (2014).

103. Reuter, D *et al.* Coulomb-interaction-induced incomplete shell filling in the hole system of InAs quantum dots. *Physical review letters* **94,** 026808 (2005).

104. Zwanenburg, F. A., van Rijmenam, C. E., Fang, Y., Lieber, C. M. & Kouwenhoven, L. P. Spin states of the first four holes in a silicon nanowire quantum dot. *Nano letters* **9,** 1071–1079 (2009).

105. Ishikuro, H. & Hiramoto, T. On the origin of tunneling barriers in silicon single electron and single hole transistors. *Applied physics letters* **74,** 1126–1128 (1999).

106. Mueller, F., Konstantaras, G., Spruijtenburg, P. C., van der Wiel, W. G. & Zwanenburg, F. A. Electron–Hole Confinement Symmetry in Silicon Quantum Dots. *Nano letters* **15,** 5336–5341 (2015).

107. Mueller, F., Konstantaras, G., van der Wiel, W. G. & Zwanenburg, F. A. Single-charge transport in ambipolar silicon nanoscale field-effect transistors. *Applied physics letters* **106,** 172101 (2015).

108. Wang, D., Hamilton, A., Farrer, I, Ritchie, D. & Klochan, O. Double-layer-gate architecture for few-hole GaAs quantum dots. *Nanotechnology* **27,** 334001 (2016).

109. Wang, D. Q. *et al.* Anisotropic Pauli spin blockade of holes in a GaAs double quantum dot. *Nano letters* **16,** 7685–7689 (2016).

110. Barraud, S *et al.* Performance of omega-shaped-gate silicon nanowire MOSFET with diameter down to 8 nm. *IEEE Electron Device Letters* **33,** 1526–1528 (2012).

111. Bohuslavskyi, H. *et al.* Pauli blockade in a few-hole PMOS double quantum dot limited by spin-orbit interaction. *Applied Physics Letters* **109,** 193101 (2016).

112. Hardy, W. J. *et al.* Single and double hole quantum dots in strained Ge/SiGe quantum wells. *Nanotechnology* **30,** 215202 (2019).

113. Deal, B. E. Standardized terminology for oxide charges associated with thermally oxidized silicon. *IEEE Transactions on Electron Devices* **27,** 606–608 (1980).

114. Berg, T. *Ambipolar charge sensing in silicon quantum dots* MA thesis (University of Twente, 2018).

115. Bogan, A. *et al.* Single hole spin relaxation probed by fast single-shot latched charge sensing. *Communications Physics* **2,** 17 (2019).

116. Culcer, D., Cywiński, Ł., Li, Q., Hu, X. & Sarma, S. D. Realizing singlet-triplet qubits in multivalley Si quantum dots. *Physical Review B* **80,** 205302 (2009).

117. Malkoc, O., Stano, P. & Loss, D. Optimal geometry of lateral GaAs and Si/SiGe quantum dots for electrical control of spin qubits. *Physical Review B* **93,** 235413 (2016).

118. Recher, P., Sukhorukov, E. V. & Loss, D. Quantum dot as spin filter and spin memory. *Physical review letters* **85,** 1962 (2000).

119. Khaetskii, A. V. & Nazarov, Y. V. Spin-flip transitions between Zeeman sublevels in semiconductor quantum dots. *Physical Review B* **64,** 125316 (2001).

120. Raith, M., Stano, P. & Fabian, J. Theory of single electron spin relaxation in Si/SiGe lateral coupled quantum dots. *Physical Review B* **83,** 195318 (2011).

121. Klochan, O *et al.* Fabrication and characterization of an induced GaAs single hole transistor. *Applied Physics Letters* **96,** 092103 (2010).

122. Bogan, A *et al.* Consequences of spin-orbit coupling at the single hole level: Spin-flip tunneling and the anisotropic g factor. *Physical review letters* **118,** 167701 (2017).

123. Van der Heijden, J. *et al.* Probing the spin states of a single acceptor atom. *Nano letters* **14,** 1492–1496 (2014).

124. Marx, M. *et al.* Spin–orbit assisted spin funnels in DC transport through a physically defined pMOS double quantum dot. *Japanese Journal of Applied Physics* **58,** SBBI07 (2019).

125. Ares, N *et al.* SiGe quantum dots for fast hole spin Rabi oscillations. *Applied Physics Letters* **103,** 263113 (2013).

126. Nenashev, A., Dvurechenskii, A. & Zinovieva, A. Wave functions and g factor of holes in Ge/Si quantum dots. *Physical review B* **67,** 205301 (2003).

127. Pryor, C. E. & Flatte, M. E. Lande g factors and orbital momentum quenching in semiconductor quantum dots. *Physical review letters* **96,** 026804 (2006).

128. Roddaro, S. *et al.* Spin states of holes in Ge/Si nanowire quantum dots. *Physical review letters* **101,** 186802 (2008).

129. Brauns, M., Ridderbos, J., Li, A., Bakkers, E. P. & Zwanenburg, F. A. Electric-field dependent g-factor anisotropy in Ge-Si core-shell nanowire quantum dots. *Physical Review B* **93,** 121408 (2016).

130. Lawaetz, P. Valence-band parameters in cubic semiconductors. *Physical Review B* **4,** 3460 (1971).

131. Deacon, R. *et al.* Electrically tuned g tensor in an InAs self-assembled quantum dot. *Physical Review B* **84,** 041302 (2011).

132. Ares, N *et al.* Nature of tunable hole g factors in quantum dots. *Physical review letters* **110,** 046602 (2013).

133. Harriman, J. E. *Theoretical foundations of electron spin resonance: physical chemistry: a series of monographs* (Academic press, 2013).

134. Roth, L. M., Lax, B. & Zwerdling, S. Theory of optical magneto-absorption effects in semiconductors. *Physical Review* **114,** 90 (1959).

135. Ivchenko, E. & Kiselev, A. Electron g factor of quantum wells and superlattices. *Soviet physics. Semiconductors* **26,** 827–831 (1992).

136. Kosaka, H., Kiselev, A. A., Baron, F. A., Kim, K. W. & Yablonovitch, E. Electron g factor engineering in IlI-V semiconductors for quantum communications. *Electronics Letters* **37,** 464–465 (2001).

137. Jiang, H. & Yablonovitch, E. Gate-controlled electron spin resonance in G a A s/A l x Ga 1- x As heterostructures. *Physical Review B* **64,** 041307 (2001).

138. Dresselhaus, G. Spin-orbit coupling effects in zinc blende structures. *Physical Review* **100,** 580 (1955).

139. Golub, L. & Ivchenko, E. Spin splitting in symmetrical SiGe quantum wells. *Physical Review B* **69,** 115333 (2004).

140. Ferdous, R. *et al.* Interface-induced spin-orbit interaction in silicon quantum dots and prospects for scalability. *Physical Review B* **97,** 241401 (2018).

141. Takahashi, S *et al.* Electrically tunable three-dimensional g-factor anisotropy in single InAs self-assembled quantum dots. *Physical Review B* **87,** 161302 (2013).

142. Schroer, M., Petersson, K., Jung, M & Petta, J. R. Field tuning the g factor in InAs nanowire double quantum dots. *Physical review letters* **107,** 176811 (2011).

143. Nadj-Perge, S, Frolov, S., Bakkers, E. & Kouwenhoven, L. P. Spin–orbit qubit in a semiconductor nanowire. *Nature* **468,** 1084 (2010).

144. Takahashi, S *et al.* Large anisotropy of the spin-orbit interaction in a single InAs self-assembled quantum dot. *Physical review letters* **104,** 246801 (2010).

145. Jovanov, V *et al.* Observation and explanation of strong electrically tunable exciton g factors in composition engineered In (Ga) As quantum dots. *Physical Review B* **83,** 161303 (2011).

146. Bychkov, Y. A. & Rashba, E. I. Oscillatory effects and the magnetic susceptibility of carriers in inversion layers. *Journal of physics C: Solid state physics* **17,** 6039 (1984).

147. Thorbeck, T. & Zimmerman, N. M. Formation of strain-induced quantum dots in gated semiconductor nanostructures. *AIP Advances* **5,** 087107 (2015).

148. Usman, M. *et al.* Strain and electric field control of hyperfine interactions for donor spin qubits in silicon. *Physical Review B* **91,** 245209 (2015).

149. Huebl, H. *et al.* Phosphorus donors in highly strained silicon. *Physical review letters* **97,** 166402 (2006).

150. Dreher, L. *et al.* Electroelastic hyperfine tuning of phosphorus donors in silicon. *Physical Review Letters* **106,** 037601 (2011).

151. Lovett, B. W. Spin qubits feel the strain. *Physics* **4,** 6 (2011).

152. Leon, R. *et al.* Coherent spin control of s-, p-, d-and f-electrons in a silicon quantum dot. *arXiv preprint arXiv:1902.01550* (2019).

153. Zhao, R *et al.* Coherent single-spin control with high-fidelity singlet-triplet readout in silicon. *arXiv preprint arXiv:1812.08347* (2018).

154. He, Y *et al.* A two-qubit gate between phosphorus donor electrons in silicon. *Nature* **571,** 371–375 (2019).

155. West, A. *et al.* Gate-based single-shot readout of spins in silicon. *Nature nanotechnology,* 1 (2019).